FATIGUE-PROOF AND DAMAGE TOLERANT LIGHTWEIGHT DESIGN OF Ti-6Al-4V FORGINGS

DOCTORAL THESIS

Dipl.-Ing. Bernd Oberwinkler

MONTANUNIVERSITÄT LEOBEN
Chair of Mechanical Engineering
Leoben, Austria

SUPERVISORS

Univ.-Prof. Dipl.-Ing. Dr. Wilfried Eichlseder

Chair of Mechanical Engineering, Montanuniversität Leoben, Austria

Prof. Dr.-Ing. habil. Hans-Jürgen Christ

Department Mechanical Engineering, University of Siegen, Germany

Leoben, April 2010

Editor
Dipl.-Ing. Bernd Oberwinkler
Montanuniversität Leoben
Chair of Mechanical Engineering
A-8700 Leoben
Austria

First printing, April 2010

Printed in Austria

Typesetting: Bernd Oberwinkler, Leoben
Production: Bernd Oberwinkler, Leoben
Bookbinding: Kunst-Buchbinderei Franz Dienbauer, Leoben

To my marvelous mother Gabi,
and to my beloved grandparents Helga and Werner,
who put me on this path,
and who have always been on my side
with their love, support and understanding.

Für meine großartige Mutter Gabi,
und meine Oma Helga und meinen Opa Werner,
die mich auf diesen Weg gebracht
und dabei stets begleitet und unterstützt haben.

AFFIDAVIT

I declare in lieu of oath, that I wrote this thesis and performed the associated research myself, using only literature cited in this volume.

Dipl.-Ing. Bernd Oberwinkler

Leoben, April 2010

Preface

This doctoral thesis originated from my work at the Chair of Mechanical Engineering at the Montanuniversität Leoben (Austria), which I joined in November 2007 as scientific assistant. Before, from 2003 to 2007, I was already student assistant at this Chair. In the past two and a half years I have investigated important aspects of the fatigue behavior of Ti-6Al-4V to afford fatigue-proof and damage tolerant lightweight design of Ti-6Al-4V forgings.

During my employment at the Chair of Mechanical Engineering I had fruitful discussions and conversations with several persons inspiring me in my investigations. First of all I am indebted to four persons:

Univ.-Prof. Dipl.-Ing. Dr. Wilfried Eichlseder, the head of the Chair of Mechanical Engineering, who laid the foundations for these investigations and who is responsible for the successful activities of the Chair. Furthermore, he allowed me already in 2003, at the beginning of my studies, to join the chair as student assistant, which was an important factor for my personal development.

Dipl.-Ing. Dr. István Gódor for his fatherly advices, which were important especially during my employment as student assistant. His hints led to the solution of a number of problems.

Dipl.-Ing. Dr. Martin Riedler from Böhler Schmiedetechnik GmbH & Co KG, who gave me plenty of rope during these investigations and the necessary support for successful completion.

Dipl.-Ing. Dr. Heinz Leitner for his support during my diploma thesis and for the initiation of the research project, which served as the basis for this doctoral thesis.

Furthermore, I want to thank Prof. Dr.-Ing. habil. Hans-Jürgen Christ from the Department Mechanical Engineering of the University of Siegen (Germany) for his willingness to serve as supervisor of my doctoral thesis.

I want to use this opportunity to thank Dipl.-Ing. Dr. Christian Oberwinkler for fruitful discussions, which were the breeding ground for a number of new ideas.

Special thanks to Mrs. Christina Lohner and Mrs. Edith Wolfgruber for their indefatigable work in the office of the Chair of Mechanical Engineering.

Many thanks to Mr. Mario Bichler and Mr. Franz Grabner for sampling and manufacturing of countless fatigue test specimens used for this research.

Moreover, I want to thank Mr. Josip Juric, Mr. Anton Lettner, Dipl.-Ing. Sabine Redik and Ms. Claudia Wagner for carrying out a part of the presented fatigue tests and several other “thankless tasks”.

The investigations presented were driven by cooperation with Böhler Schmiedetechnik GmbH & Co KG, Kapfenberg (Austria). On this way I want to thank Dipl.-Ing. Dr. Martin Stockinger.

I would also like to thank the Austrian Research Promotion Agency (FFG) for funding of this research work within the framework of the FFG’s Bridge Program.

The base for a professional evolution is set in the private environment. On this way, I want to express my deepest thanks to my whole family for always giving me the necessary support and making this education possible for me. Special thanks to Ing. Hans Peter Pirner, who was considerably responsible for my decision to aspire to a technical education.

Bernd Oberwinkler, April 2010

Table of contents

1. Abstract

1.1. Abstract (English)

Titanium alloys and especially Ti-6Al-4V with their excellent properties such as low density, high specific strength or corrosion resistance have a huge range of application, from aerospace and motorsports to medical engineering. Apart from material and processing, fatigue-proof and damage tolerant design is an essential part of the approach to light weighting.

Conventional models for fatigue-proof design, which are predominantly developed based on ferrous and aluminum materials, are currently utilized for titanium components. However, the analyzed titanium alloy Ti-6Al-4V exhibits many characteristics and anomalies regarding fatigue, which cannot be represented by existing models. This thwarts the principle of lightweight design. The thermomechanical processing, in this case forging and subsequent heat treatments, holds additional parameters with respect to the fatigue strength. The aim of this thesis was the development of appropriate models for fatigue-proof and damage tolerant lightweight design of forged Ti-6Al-4V components under consideration of microstructural variation resulting from thermomechanical processing.

For that purpose, specimens were taken from open- and closed-die forgings with different subsequent heat treatments and therefore varying microstructures. The focus was thereby on equiaxed and bimodal microstructures without any precipitations or crystallographic textures. Furthermore, the fatigue and crack growth behavior was thoroughly analyzed with respect to microstructure. Based on these results, phenomenological models were developed to link fatigue and fracture behavior with microstructural parameters. Extensive fatigue tests were additionally performed for the development of fatigue models regarding mean stress and notch sensitivity, damage tolerance (influence of preexisting flaws), influence of multiaxial loading and surface state. The influence of operating temperature on the fatigue strength was discussed based on existing test results and included in a phenomenological model.

All developed models for the lifetime estimation of Ti-6Al-4V forgings were implemented by Böhler Schmiedetechnik GmbH & Co KG in *Fortran* in a postprocessor. Results of the forging simulation (microstructural parameters) and finite element stress analyses (stress tensors) are thereby used as input. Local variations of microstructure, owing to different local cooling rates or the like, can hence be considered. Postprocessing results are the distributions of damage and maximum allowable crack lengths in a component for a given load spectrum.

The developed models for the lifetime estimation of Ti-6Al-4V components contribute in many respects to the approach of lightweight design. On the one hand, they enable an optimized utilization of the material capability of Ti-6Al-4V owing to improved dimensioning of a component (inter alia in combination with topology and shape optimization); on the other hand, they are the basis for a simulation-based optimization of the whole forging process. The result is an optimized component performance under service conditions.

1.2. Abstract (German)

Titanlegierungen und insbesondere Ti-6Al-4V finden aufgrund ihrer guten Eigenschaften wie hoher spezifischer Festigkeit oder Korrosionsbeständigkeit vielfältige Anwendung, wobei das Spektrum von Luft- und Raumfahrt über Motorsport bis hin zur Medizintechnik reicht. Um Leichtbau von Titan-Komponenten zu gewährleisten, spielt neben Werkstoff und Formgebung die betriebsfeste und oftmals auch schadenstolerante Auslegung eine zentrale Rolle.

Konventionelle Berechnungskonzepte für betriebsfeste Auslegung, entwickelt vorwiegend auf Basis von Eisen- und Aluminiumwerkstoffen, finden zurzeit noch Anwendung im Bereich von Titankomponenten. Die in dieser Arbeit betrachtete Titanlegierung Ti-6Al-4V weist jedoch in vielfacher Hinsicht Besonderheiten und Anomalien in Bezug auf Ermüdung auf. Diese können nur unzureichend über bestehende Modelle abgebildet werden und wirken somit dem Prinzip Leichtbau entgegen. Zusätzlich birgt die thermomechanische Fertigung, in diesem Fall Schmieden und nachfolgende Wärmebehandlungen, eine Vielzahl an Einflüssen auf die Schwingfestigkeit von Ti-6Al-4V. Das Ziel dieser Arbeit ist eine Herleitung entsprechender Modelle für eine betriebsfeste und schadenstolerante Auslegung von geschmiedeten Komponenten aus Ti-6Al-4V unter Berücksichtigung der lokalen Mikrostruktur.

Dazu wurden Proben aus gesenk- bzw. freiformgeschmiedeten Teilen mit unterschiedlichen nachfolgenden Wärmebehandlungen entnommen und deren Mikrostruktur analysiert, wobei sich diese Arbeit auf globulare und bimodale Mikrostrukturen frei von möglichen Ausscheidungen und kristallographischen Texturen beschränkte. Danach erfolgte eine umfangreiche Charakterisierung der Schwingfestigkeit und des Rissfortschrittsverhaltens in Abhängigkeit der Mikrostruktur. Die Verknüpfung dieser Ergebnisse lieferte phänomenologische Modelle zur Beschreibung von Schwingfestigkeit und Risswachstum in Abhängigkeit wesentlicher mikrostruktureller Kenngrößen. Weitere umfangreiche Schwingfestigkeitsuntersuchungen bildeten die Basis für eine modellmäßige Beschreibung von Mittelspannungs- und Kerbempfindlichkeit, Schadenstoleranz (Einfluss vorhandener Fehlstellen), Einfluss von Mehrachsigkeit der Beanspruchung sowie Oberflächenbeschaffenheit. Der Einfluss der Betriebstemperatur auf die Schwingfestigkeit wurde anhand bereits vorhandener Versuchsergebnisse diskutiert und ebenfalls modellmäßig erfasst.
Sämtliche im Zuge dieser Arbeit entwickelten Modelle zur Lebensdauerberechnung von geschmiedeten Bauteilen aus Ti-6Al-4V wurden von Böhler Schmiedetechnik GmbH & Co KG in einem Postprozessor in *Fortran* implementiert. Als Input dienen dabei Ergebnisse aus Umformsimulation (Gefügeparameter in jedem Element des Bauteils) sowie Finite-Elemente-Analyse der vorliegenden Spannungsverteilung (Spannungstensor in jedem Knoten des Bauteils). Lokale Unterschiede der Mikrostruktur, z.B. durch lokal unterschiedliche Abkühlraten, können somit simuliert und über entsprechende Materialmodelle in der Lebensdauerberechnung mit berücksichtigt werden. Als Resultat erhält man für ein vorgegebenes Belastungskollektiv die entsprechende Schädigungsverteilung im Bauteil sowie die maximal zulässige Rissgröße an jeder Stelle.

Die entwickelten Modelle zur Berechnung der Schwingfestigkeit von Ti-6Al-4V liefern somit in mehrfacher Hinsicht einen wesentlichen Beitrag zu Leichtbau. Zum einen ermöglichen sie eine optimale Nutzung des Festigkeitspotenzials von Ti-6Al-4V durch exaktere Dimensionierung des Bauteils (unter anderem durch mögliche Verknüpfung mit Topologie- und Gestaltsoptimierung), zum anderen bilden sie die Grundlage für eine simulationsbasierte Optimierung des Schmiedeprozesses inklusive möglicher Wärmebehandlungen.

2. Introduction

2.1. Overview

This doctoral thesis is subdivided into an introduction, the material characterization, the main chapter "Fatigue behavior of Ti-6Al-4V", verification and application of the developed fatigue models, and conclusion and outlook. Finally, the list of publications (chronologically ordered) and the bibliography (alphabetically ordered) are stated. Complementary data and models are discussed in the Appendix.
The chapter "Fatigue behavior of Ti-6Al-4V" includes the most important influences on the crack initiation and crack growth behavior of Ti-6Al-4V, namely microstructure, relative stress gradient, impressed mean stress, multiaxial loading, surface state, flaws, and operating temperature. Owing to the wide variety, the state-of-the-art is separately discussed for each fatigue influence, as well as the developed models.

2.2. Titanium and titanium alloys

2.2.1. Titanium

Titanium is present in the earth's crust at a level of about 0.6% and is therefore the fourth most abundant structural metal after aluminum, iron and magnesium. The most important mineral sources are ilmenite ($FeTiO_3$) and rutile (TiO_2).
Gregor, a clergyman and amateur mineralogist, expressed the first suspicion of a new, unknown element present in a dark, magnetic iron-sand (ilmenite) in Cornwall (UK) in 1791. In 1795, Klaproth, a German chemist, analyzed rutile from Hungary and identified an oxide of an unknown element, the same as the one reported by Gregor. Klaproth named the element titanium after the Titans, the powerful sons of the earth in Greek mythology. Because of the strong tendency of this metal to react with oxygen and nitrogen, it was not until well in to the 20^{th} century (1937-1940) that a commercially attractive process was developed by Kroll in Luxembourg. This process involved the reduction of titanium tetrachloride with magnesium in an inert gas atmosphere. The resulting titanium is called "titanium sponge" because of its porous and spongy appearance. This famous Kroll process remained essentially unchanged and is still the dominant process for titanium production today. [105]

2.2.2. Titanium alloys

The properties of titanium and titanium alloys are significantly influenced by the two phases α and β. In pure titanium and several alloys, a hexagonal close-packed (hcp) phase is existent at low temperatures; the so-called α-phase. The high temperature phase crystallizes in a body-centered cubic (bcc) modification and is called β-phase. The existence and arrangement of these two phases play a major role with respect to the properties of titanium and titanium alloys. Titanium alloys can be classified with respect to their fraction of α- or β-stabilizing elements in (near) α-, (α+β)-, and (metastable) β-alloys. Titanium alloy development in the USA progressed rapidly from about 1950 stimulated by the recognition of the general usefulness of (α-stabilizing) aluminum additions for strengthening. In conventional titanium alloys, the aluminum content is limited to six weight percent to avoid embrittlement, whereas the new titanium aluminides contain approximately 50 atom-% aluminum. A classification of titanium alloys with respect to the aluminum content is shown in Fig. 2.1.

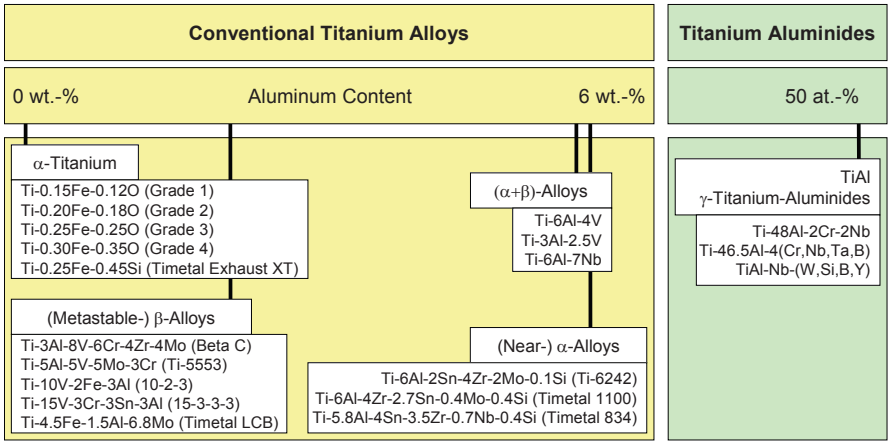

Fig. 2.1: Classification of titanium alloys with respect to the aluminum content [130]

A major breakthrough for titanium alloys was the appearance of the Ti-6Al-4V alloy in the USA in 1954, becoming soon the most important (α+β)-alloy combining excellent properties and good producibility. Today, Ti-6Al-4V is still the most widely used alloy. In countries or regions with major aerospace industry, for example North America or Europe, the commercially pure (CP) titanium accounts for only 26% of the total market. The further breakdown of the remaining 74% for titanium alloys shows that 56% of the market is covered by Ti-6Al-4V. [105], [130]

2.2.3. Applications of Ti-6Al-4V

Titanium alloys and especially Ti-6Al-4V have a huge range of application; from biomedical devices, aircraft and automotive applications to sports equipment and appearance related uses (e.g. jewelry or architectural creations). The reasons for the application of Ti-6Al-4V are the low density (4.3 g/cm³) and high strength, resulting in a high specific strength, the high fatigue strength, the good biocompatibility, high corrosion resistance and the good image in society. [105], [133]

2.2.3.1. Aircraft applications

One major application area of (α+β)–titanium alloys are aircraft structural parts, e.g. engine mounts, pylon fitting and frame parts. For such applications, (α+β)–titanium alloys are selected over other competing metallic materials, such as high strength aluminum alloys, because of higher yield stress and fatigue strength (even on a density normalized basis), better corrosion resistance, higher modulus of elasticity, and higher temperature capability. For large structural parts (e.g. landing gear beams) the most important mechanical property is fatigue crack propagation of macro cracks resulting in a requirement for setting the service time between inspections. Because these large components are located well within the interior of the aircraft structure, considerable disassembly is required for inspection. Thus, good fatigue crack growth characteristics are highly desirable. In addition, high fracture toughness is usually a requirement although the actual fracture toughness value has an insignificant influence on fatigue lifetime and essentially no influence on the inspection intervals. Thus, the high fracture toughness requirement can be viewed as largely redundant. The most economical processing route for large forgings typically consists of forging in the (α+β)–phase field followed by mill-annealing. The resulting microstructure typically consists of nominally equiaxed α with a varying extent of recrystallisation. Other common heat treatments are solution treating, recrystallization annealing, and beta-annealing, respectively.

Ti-6Al-4V is also used in aircraft engines for fan blades and fan disks and for blades and disks in the first four to five rows of the low pressure compressor. Thereby, the maximum operating temperature of 350°C is the limiting factor for application. [105], [130], [133]

2.2.3.2. Automotive applications

Titanium alloys are well suited for use in many components of a passenger car from a property standpoint. However, the high price of titanium has prevented wide realization of these applications in mass-produced passenger cars. In spite of the higher costs, titanium alloys are increasingly used in motor production for reduction of rotating and oscillating masses, especially in sports cars. Ti-6Al-4V connecting rods of the Porsche 911 GT3 or of several Ferrari 12-cylinder engines can be cited as an example. Further applications are inlet valves (Toyota, Nissan), turbocharger wheels (Mercedes-Benz) and wheel rim screws (Porsche, Volkswagen). However, Schauerte [152] notes that if one extrapolates the status of titanium technology based on the historic development of the knowledge bases on other automotive metals (steel, aluminum), the future of titanium use in cars looks quite bright. [65], [68], [105], [133], [152]

2.3. Fatigue-proof damage tolerant lightweight design

2.3.1. State-of-the-art

In the aerospace industry, the realization of lightweight structural components is a top priority. Weight reduction of structures both increases the potential payload of aircraft and decreases their fuel consumption and CO_2 emission. Lightweight design is thereby based on three principal points, namely material, processing and design (Fig. 2.2).

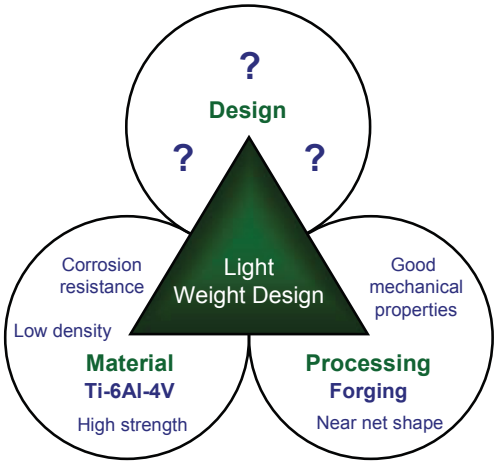

Fig. 2.2: Lightweight design of Ti-6Al-4V forgings

Material

Titanium alloys have become very important materials in the aircraft industry, due to their excellent properties (such as high fatigue strength and good corrosion resistance) and low density; ideal for lightweight design. Titanium components (particularly Ti-6Al-4V) are used in place of heavy steel components (e.g. airfoils, pylon fittings, undercarriage components, and other structural parts).

Processing

Manufacturing parts according to customer specifications by using forming techniques has both cost and quality advantages, compared to cutting and machining parts out of feedstock plates or bars. Because of this, components are increasingly manufactured by forging. Forging results in better utilization of material through near net shape manufacturing, and also reduces manufacturing costs and provides better mechanical properties, such as high fatigue strengths. Therefore forging is suitable for the processing of lightweight titanium components.

Design

Depending on the thermomechanical treatment of a titanium alloy, in this case Ti-6Al-4V, the microstructure and thus the mechanical properties can vary in a wide range. Such influences have been documented in numerous reports in the literature with the problem that a holistic optimization of the whole product development chain (design, thermomechanical processing) is still lacking. Therefore, it is currently not possible to optimize Ti-6Al-4V components with respect to thermomechanical processing and design.

The requirement for tolerance to flaws and damages necessitates the application of damage tolerant (DT) component design. Several DT design principles exist but an exact definition is missing. D.O. Adams [28] mentions: *"Definition of terms is an immediate difficulty in this field. Different sources may use conflicting definitions of common terms. This is due to the simultaneous evolution of fatigue substantiation methodologies in related but independent endeavors over the last 40 years. For example, the term "Damage Tolerance" is deliberately avoided in the FAR 29.571 advisory material, even though most readers think that this is precisely what is being discussed."*

Nevertheless, Damage Tolerance is a common wording; e.g. Lazzeri and Mariani [100] use the following definition: *"Damage Tolerance, as it is called by the fixed-wing community, while it is more often called Flaw Tolerance by the helicopter community; and indeed the regulation uses the term ''fail-safe (residual strength after flaw growth) evaluation". It requires that the structure can retain, after a partial failure, the capability to withstand the limit load; it is based on the use of redundant solutions (fail-safe) or on the slow crack propagation approach (or, preferably, on the no-growth approach). The use of redundant solutions is often possible in stiffened shell structures, and sometimes multiple load paths can be easily introduced. Nevertheless, most dynamic components cannot be other than single load path. In this case, the slow crack growth (or the no-growth) option is the recommended one. Inspection intervals must be determined, in order to ensure that, if a defect is present, this is timely detected and consequent repair actions taken."*

2.3.2. Approach for fatigue-proof damage tolerant lightweight design

A new approach, cf. Fig. 2.3, was developed in this thesis to afford damage tolerant lightweight design of Ti-6Al-4V forgings. With the aid of forging simulation using finite element analysis, it is possible to predict the local microstructure in Ti-6Al-4V forgings in respect of the thermomechanical processing. The thermomechanical processing varies within a component due to local temperature and heating (e.g. at radii or adiabatic heating) during the forging process and thickness dependent cooling rates causing differences in local microstructure. A link between this local microstructure and the fatigue life is necessary to enable an accurate lifetime estimation for forged Ti-6Al-4V components and to optimize their thermomechanical processing.

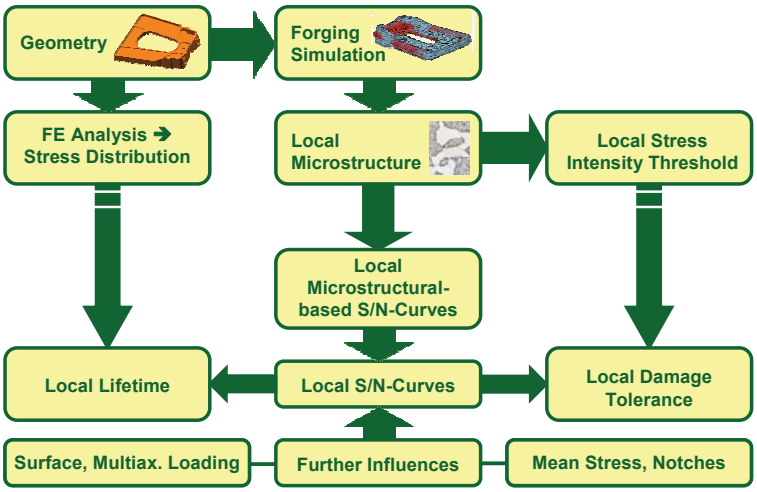

Fig. 2.3: Chosen approach for fatigue-proof damage tolerant lightweight design of Ti-6Al-4V forgings

In the chosen approach (Fig. 2.3), local microstructure results in local microstructural-based S/N-curves and stress intensity factor thresholds. The local microstructural-based S/N-curves can be combined with additional important influences regarding fatigue, e.g. mean stress and relative stress gradient, to local S/N-curves. Due to the anomalous behavior of Ti-6Al-4V with respect to mean stress sensitivity and notch supporting effect, new models were introduced which account for these anomalies. The influence of surface state and operating temperature was additionally examined aside.

The local S/N-curves provide the basis for computation of the local lifetime of forged components based on local stresses. Thereby, a given load spectrum, the local stress distribution in the component (determined with finite element analysis), and the computed local S/N-curves are used as input for a damage accumulation. The damage accumulation consequently results in a local lifetime in every node of the component.

The combination of local S/N-curve and local stress intensity factor threshold leads to an estimation of the local damage tolerance by application of a type of Kitagawa-Takahashi relationship between flaw size and fatigue strength. The allowable crack size distribution for finite life and no-growth can hence be determined.

A closed optimization-loop for the thermomechanical processing of a forged component is hence achieved by linking local lifetime, local damage tolerance and local microstructure (derived from forging simulation). In addition, the geometry of a component can be optimized with shape optimization tools based on the local lifetime estimation. Damage tolerant lightweight design of Ti-6Al-4V forgings is hence enabled.

3. Material characterization

3.1. Material and processing

The material used for this research was provided by Böhler Schmiedetechnik GmbH & Co KG in the form of Ti-6Al-4V V-shape and side-pressed pancake forgings, respectively. Both forgings were (α+β)-forged. Additionally, the used feedstock billet (FB) for the V-shape forgings was analyzed in as-received condition to achieve a higher diversity of microstructure.

3.1.1. Pancakes

Although the forging looks like a ciabatta, the description "pancake forging" is quite widespread, being used not only for upsetting deformation (the upsetting axis of the press is in the same direction as the billet axial direction) but also for side pressing (the upsetting axis of the press is perpendicular to the billet axial direction). Therefore, "pancake" is used from hereon.

3.1.1.1. Forging simulation

The forging process of the pancakes was simulated with finite element analysis in the Deform™ software tool. The obtained effective strain distribution with its typical "forging cross" is shown in Fig. 3.1.

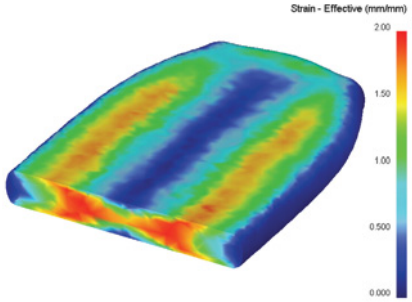

Fig. 3.1: Distribution of the effective strain in a pancake

3.1.1.2. Forging process

The pancakes were forged on a hydraulic press (Fig. 3.2). The diameter of the feedstock was 45 mm. The forging process was done in one heating (furnace temperature 930°C) with one pressing operation with an average ram speed of 15 mm/s. One half of the pancakes were forged with a thickness of 13.5 mm (for as-forged specimens) and the other half with a thickness of 15 mm (for machined specimens). This circumstance will be discussed in the according chapters.

Fig. 3.2: Forging of pancakes

3.1.1.3. Heat treatment

Different types of microstructures were achieved by varying subsequent heat treatments. All pancakes were mill-annealed (720°C / 2h / air-cooling). Some of the pancakes remained in the mill-annealed (MA) state, in part other heat treatments (solution treating, recrystallization-annealing or beta-annealing) followed. Thereby the solution treating (ST) consisted of 950°C / 70 min. / air-cooling and 730°C / 2h / air-cooling. The beta-annealing (BA) included 1030°C / 100 min. / air-cooling and 730°C / 2h / air-cooling. Recrystallization annealing (RA) was achieved by 950°C / 2h with furnace-cooling (~38°C/h) to 730°C and subsequent air-cooling. The corresponding temperature-time-distributions are shown in Fig. 3.3. Finally, sand blasting and chemical milling (~ 0.3 mm surface layer removal) was done for descaling and removal of the α-case. The chemical composition of the bath is shown in Tab. 3.1.

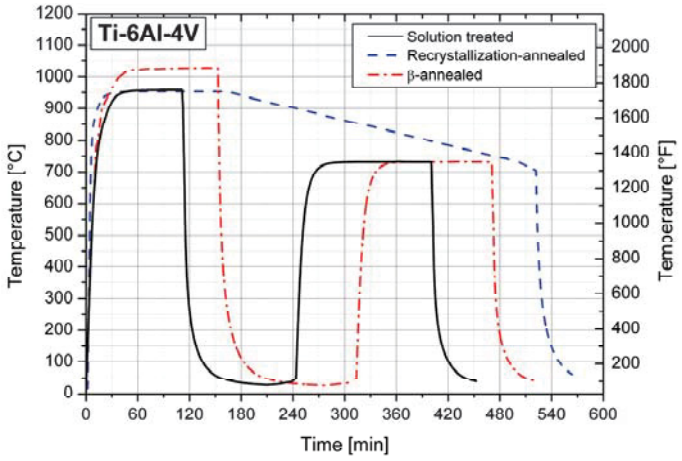

Fig. 3.3: Subsequent heat treatments of the mill-annealed pancakes

Agent	Amount [ml]	Concentr. [%]
HNO_3	15	53
HF	6	75
H_2O	79	-

Tab. 3.1: Composition of the chemical milling bath

3.1.2. V-Shapes

The V-shapes were purpose designed for this research work. The wording V-shape originates from the profile of these special forgings.

3.1.2.1. Forging simulation

The design process was done by Böhler Schmiedetechnik GmbH & Co KG with the finite element tool Deform™. The results of the forging simulation are shown in Fig. 3.4. Thereby, forging was performed in two heats using one blow each heat. One main criterion for the V-shape design was to achieve an effective strain as uniform as possible in the longitudinal direction with different effective strain levels along the transverse axis. This was necessary for the sampling of lateral specimens with a uniform gauge (cf. chapter Sampling). The results of the finite element analysis concerning effective strain and temperature distribution in the V-shape geometry are shown in Fig. 3.5. The residual stresses in the V-shape were also simulated. These results are discussed in the Appendix.

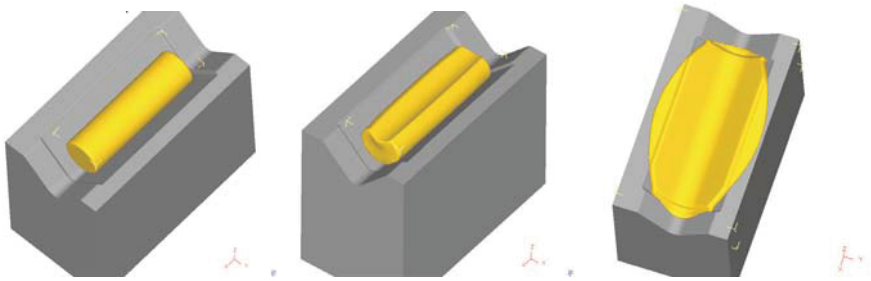

Fig. 3.4: Semi-finished product (l), after first pressing (c) and finished V-shape (r) in the forging simulation

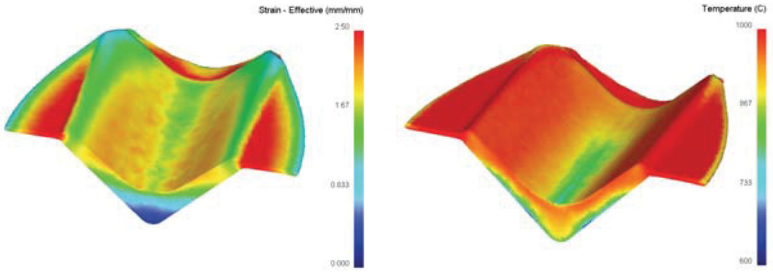

Fig. 3.5: Distribution of effective strain (l) and temperature (r) in a V-shape

3.1.2.2. Forging process

The feedstock billet for the V-shapes had a diameter of 230 mm. It was heated in a furnace up to 940°C and forged with an open die hammer to semi-finished products with a diameter of 100 mm. These were heated in a rotating hearth furnace up to 930°C and forged at a 350MN-screw-press in two heats with one blow each heat (see Fig. 3.6 and Fig. 3.7). The used die was pre-heated to 240°C.

Fig. 3.6: Semi-finished products (l), heating in rotating hearth furnace (c) and the die (r)

Fig. 3.7: 350MN-screw-press (l), manipulator with V-shape (c) und finished V-shape (r)

3.1.2.3. Heat treatment

Subsequent to the forging process a mill-annealing (720°C / 2h / air-cooling) was done. Two of these mill-annealed V-shapes were subsequent solution treated (950°C / 70 min), polymer-quenched and mill-annealed (720°C / 2h / air-cooling). The abbreviation for this type of heat treatment is STPQ. One V-shape was solution treated (ST) at an elevated temperature (980°C / 70 min / air-cooling) and mill-annealed (720°C / 2h / air-cooling). Finally, sand blasting and chemical milling (composition of the bath see Tab. 3.1) was done on all V-shapes for descaling and removal of the α-case.

3.1.3. Summary of performed heat treatments

Different heat treatments were performed on V-shape and pancake forgings, respectively. To gain a better overview, they are summarized in Tab. 3.2. Furthermore, a first assessment of microstructures with regard to the heat treatments is given.

Material	Step 1	Step 2	Microstructure
V-Shape MA	720°C / 2 hours / AC	-	Mill-annealed
V-Shape ST	980°C / 70 min. / AC	720°C / 2 hours / AC	Bimodal
V-Shape STPQ	950°C / 70 min. / PQ	720°C / 2 hours / AC	Bimodal
Pancake MA	720°C / 2 hours / AC	-	Mill-annealed
Pancake ST	950°C / 70 min. / AC	730°C / 2 hours / AC	Bimodal
Pancake RA	950°C / 2 hours	FC to 730°C / AC	Equiaxed
Pancake BA	1030°C / 100 min. / AC	730°C / 2 hours / AC	Lamellar
Feedstock billet	As-received	-	Equiaxed

Abbr.: AC = air-cooling, FC = furnace-cooling, PQ = polymer-quenching

Tab. 3.2: Performed heat treatments

3.2. Microstructural characterization

The analysis of the different microstructures was done with a light optical microscope (Olympus BX51M). The metallographic sections were therefore grinded, polished and etched. The composition of the used etchant can be found in Tab. 3.3. The microstructure becomes thereby visible in a light optical microscope, whereby the α-phase appears bright and the β-phase appears dark.

Agent	Amount [ml]	Concentr. [%]
HNO_3	5	70
HF	10	50
H_2O	85	-

Tab. 3.3: Composition of the used etchant

The micrographs of the different microstructures are hereafter presented as 3D cubes for visualization of possible grain shape textures. With regard to the round specimens, the left front face of the cube is in accordance with the cross section and the right front face with the longitudinal cut (Fig. 3.8). In consideration of V-shape and pancake, the vertical front edge of the cube corresponds with the through-thickness direction.

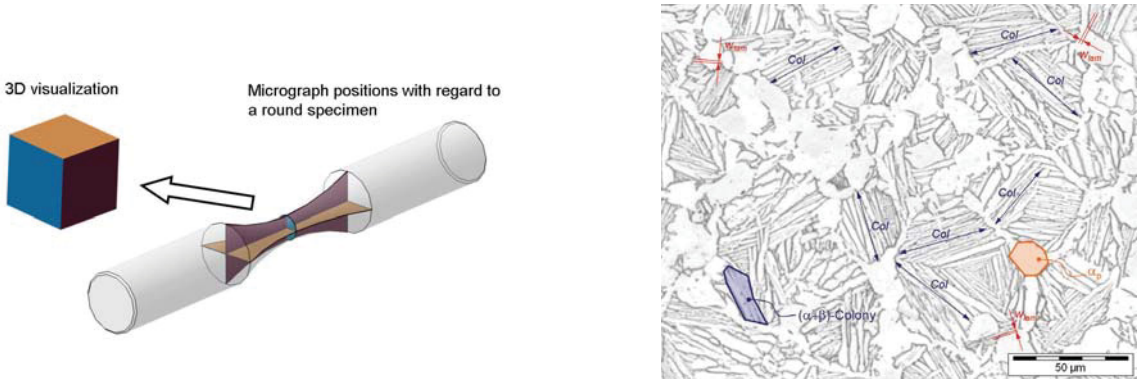

Fig. 3.8: 3D visualization of micrographs (l) and exemplary micrograph of bimodal Ti-6Al-4V (r)

The microstructures were characterized by the parameters average primary α-grain size α_p, (α+β)-content $C_{\alpha+\beta}$, colony length *Col* of the (α+β)-lamellae packages, connectivity *Con* of α-grains, and α-lamellae width w_{lam}, cf. Fig. 3.8 (r). With the exception of colony length and lamellae width, the parameters were determined by an intercept approach. The (α+β)-content is thereby defined as the balance of 100% minus primary α-content. The connectivity is defined as ratio of mean size of interconnected α-regions α_{IC} and mean primary α-grain size α_p, Equ. (3.1).

$$Con = \frac{\alpha_{IC}}{\alpha_p} \cdot 100 - 100 \qquad \text{Equ. (3.1)}$$

For the determination of the colony length, measured data of several larger colonies in a micrograph was averaged. This is necessary because a micrograph is 2D and the colonies are 3D. Therefore, it can be assumed that the larger colonies within a micrograph represent the true colony length, cf. Fig. 3.9. The lamellae width is a mean value of measurements of the smallest lamellae in a micrograph. In this case, a cut under 90° to the lamellae represents the true lamellae width and leads to the smallest lamellae in a micrograph.

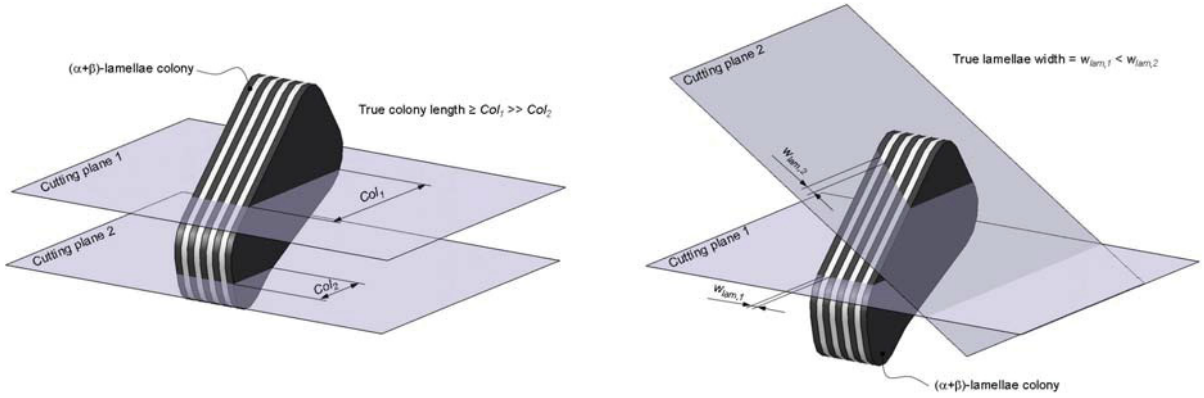

Fig. 3.9: Colony length (l) and lamellae width (r) in respect of the position of the cutting plane

Furthermore, the crystallographic texture of the different materials was measured with X-ray diffraction (XRD) and in part with electron backscatter diffraction (EBSD). For XRD analysis, three peaks of α-Titanium were measured with a Copper K_α-radiation (wavelength 1.5406 angstrom). A direct measurement of 002-orientation of α-Titanium (basal plane of hexagonal α-crystal) was not possible due to the marginal difference between 2θ-values of 002 α-Titanium (38.421°) and 110 β-Titanium (38.481°). Therefore, a retroactive calculation with the measured peaks (Tab. 3.4) was necessary for the generation of 002 pole figures.

hkl	101	102	110
2θ	40.170°	53.004°	62.949°

Tab. 3.4: Measured peaks of α-Titanium

Lütjering [103] observed that the deformation temperature during processing determines the texture type. At relatively low deformation temperatures (below 900°C) where a high volume fraction of α-phase is present during deformation, an α-deformation texture, a so-called basal/transverse type of texture, develops. At high deformation temperatures (above 930°C) in the (α+β)-phase field where a high volume fraction of β-phase is present during deformation, a β-deformation texture develops in which, upon subsequent transformation to α, only one of the six possible variants of the Burgers-relationship, (110)||(0002), is selected, resulting in a so-called transverse type of transformation texture. The deformation degree determines the texture intensity whereas the deformation mode determines the texture symmetry. The resulting textures of α-phase will not change significantly during a subsequent recrystallization step. Forming between 900°C and 930°C does not lead to a crystallographic texture.

3.2.1. Pancake mill-annealed (MA_P)

Mill-annealing does not cause complete recrystallization and leads therefore to a distinct texture of the primary α-grain shapes in respect of the forging process. This can be seen in Fig. 3.10 which shows the microstructure along the cross section of a mill-annealed pancake and in Fig. 3.11 where micrographs are presented in 3D visualization. Two different mean values of primary α-grain size were determined owing to this shape texture, namely the mean α-grain size (7.3 µm) and the average grain size in direction of the grain shape elongation of all three cuts (8.2 µm).

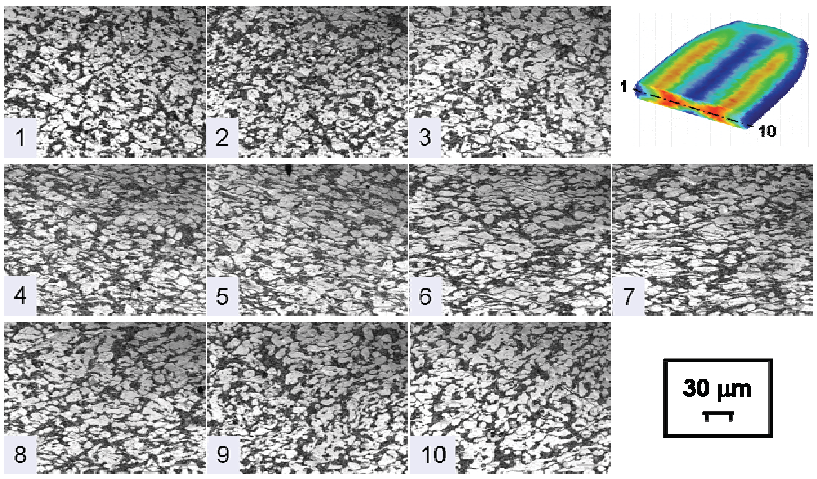

Fig. 3.10: Microstructure along the cross section of a mill-annealed pancake

The microstructure has an average (α+β)-content of 31%. The connectivity of α-grains is relatively high with 45%. The colony length is approximately 7.1 µm and the mean lamellae width is 0.57 µm.

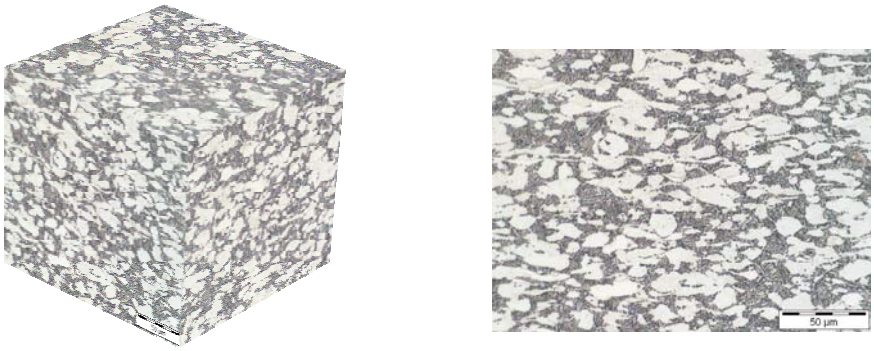

Fig. 3.11: Micrographs of pancake mill-annealed, 3D visualization (l) and cross section (r)

Because of the chosen forging temperature (930°C) no crystallographic texture occurs, cf. [103]. This was confirmed with XRD (Fig. 3.12) measurements.

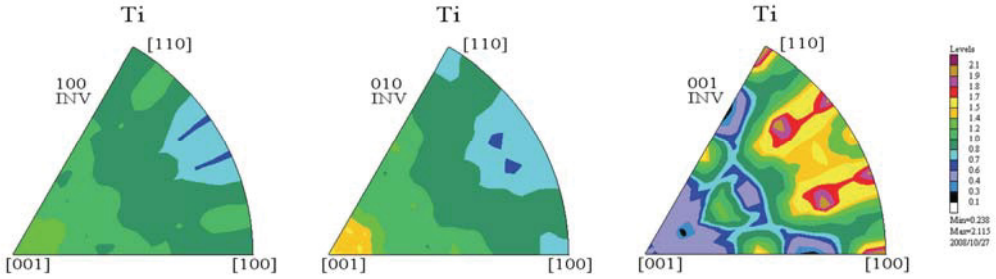

Fig. 3.12: Inverse pole figures of mill-annealed pancake

3.2.2. Pancake solution treated (ST_P)

The solution treatment leads to a bimodal microstructure (Fig. 3.13) with an average α-grain size of 8.9 µm and an (α+β)-content of 51%. Due to the air-cooling, the lamellae width is relatively large, namely 0.74 µm. The colony length approximates 16.1 µm. XRD measurements (Fig. 3.14) showed that the solution treated pancakes are isotropic. This ties in well with the results of the mill-annealed pancake; a formation of a texture owing to the heat treatment is not due.

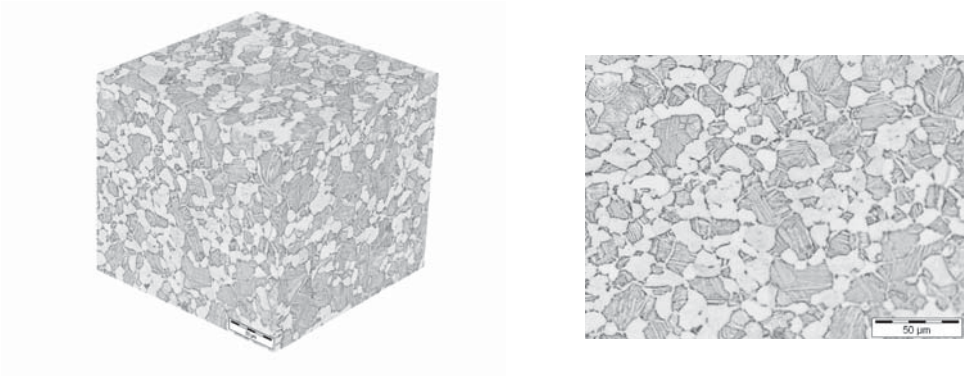

Fig. 3.13: Micrographs of pancake solution treated, 3D visualization (l) and cross section (r)

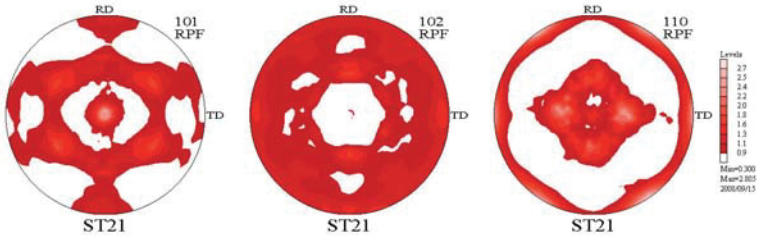

Fig. 3.14: Pole figures of solution treated pancake

3.2.3. Pancake recrystallization-annealed (RA_P)

The recrystallization-annealing leads to a coarse equiaxed microstructure (Fig. 3.15) with an average α-grain size of 10.3 µm and a connectivity of 99%. As mentioned before, the chosen forging temperature of 930°C results in an isotropic material. This was confirmed with XRD measurements (Fig. 3.16).

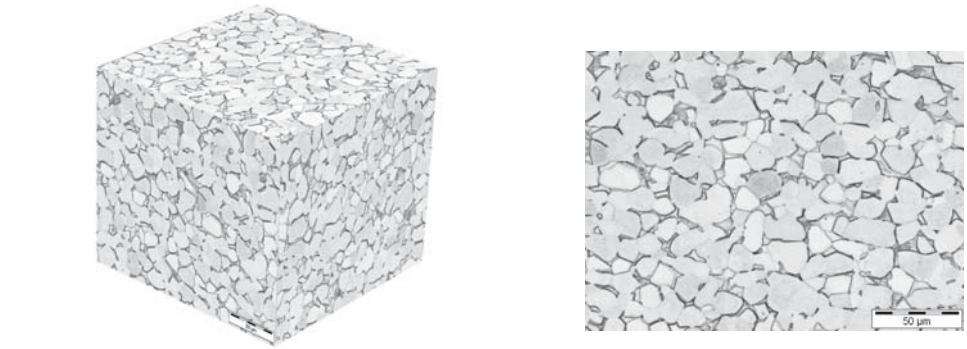

Fig. 3.15: Micrographs of pancake recryst.-annealed, 3D visualization (l) and cross section (r)

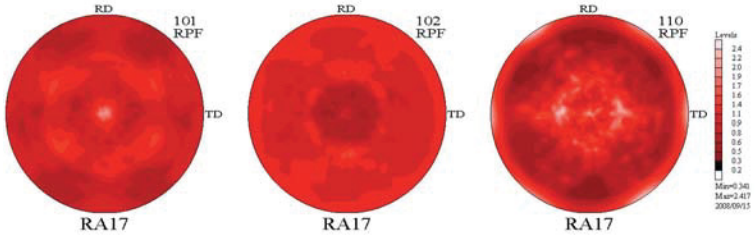

Fig. 3.16: Pole figures of recrystallization-annealed pancake

3.2.4. Pancake beta-annealed (BA_P)

The beta-annealing results in a lamellar microstructure. The mean lamellae width is 0.75 µm. The primary β-grain size approximates 400 µm.

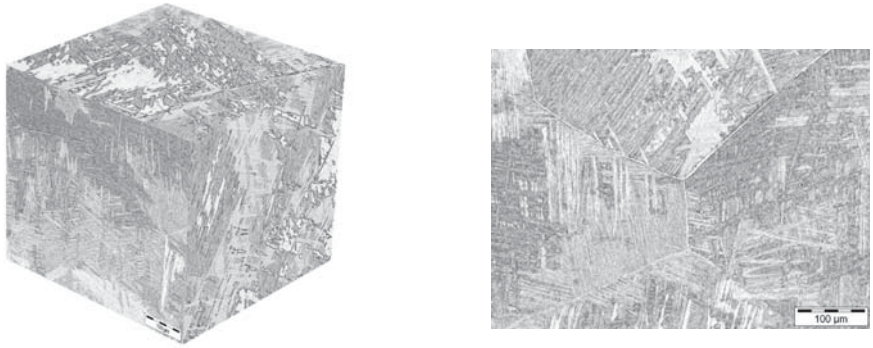

Fig. 3.17: Micrographs of pancake beta-annealed, 3D visualization (l) and cross section (r)

Both, XRD and EBSD measurements confirm the isotropy of this material. Fig. 3.18 shows the EBSD results; orientation imaging microscopy (OIM) map and resulting inverse pole figure. It was observed that parallel lamellae within a colony have the same crystallographic orientation.

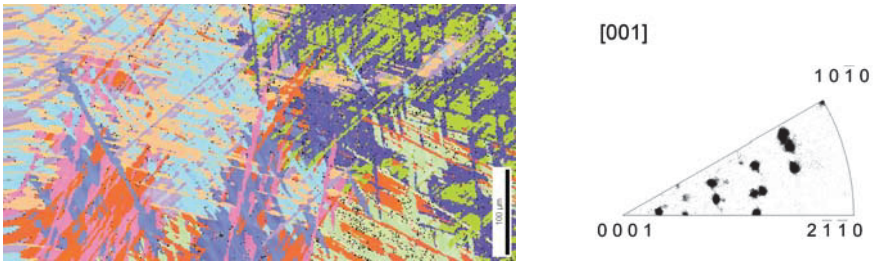

Fig. 3.18: OIM map (l) and pole figure (r) for beta-annealed pancake

3.2.5. V-shape mill-annealed (MA_V)

The mill-annealing of V-shapes results in a so-called mill-annealed microstructure (Fig. 3.19). Due to the missing recrystallization step, a primary α-grain shape texture is identifiable. Again, two different mean values of primary α-grain size were determined, namely the mean α-grain size (8.7 µm) and the average grain size in direction of the grain shape elongation of all three cuts (11.5 µm). The (α+β)-content averages 20%, the colony length 9.2 µm and the lamellae width 0.65 µm.

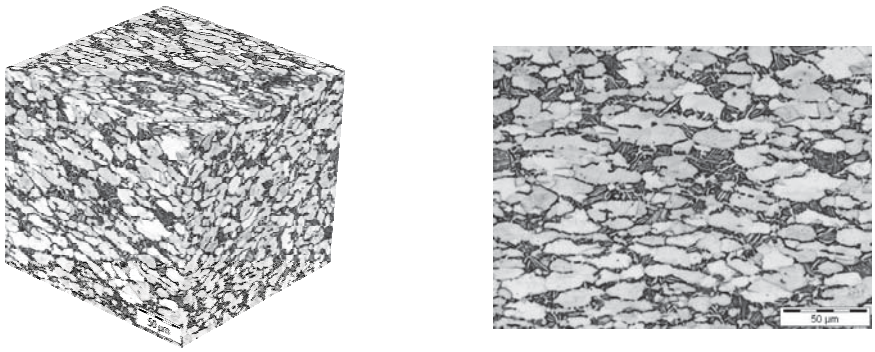

Fig. 3.19: Micrographs of V-shape mill-annealed, 3D visualization (l) and cross section (r)

The influence of mill-annealing on the microstructure of forged Ti-6Al-4V was determined on a V-shape without heat treatment in comparison to a mill-annealed one at the same position, Fig. 3.20. The mill-annealed microstructure exhibits a lower (α+β)-content (30%) than the untreated one (40%). The primary α-grain size decreases during mill-annealing from 7.6 µm to 7.0 µm; the colony length remains the same (7.2 µm). It can be assumed that during mill-annealing a partial recrystallization occurs, which includes transformation from (α+β)- to α-phase. This could be the reason for the decreasing average α-grain size (formation of smaller α-grains) and the increasing (α+β)-content during mill-annealing. Recovery befalls in the primary α-grains, which retain their textured shapes. These findings are based on heavy-duty processing, and have to be confirmed under laboratory conditions.

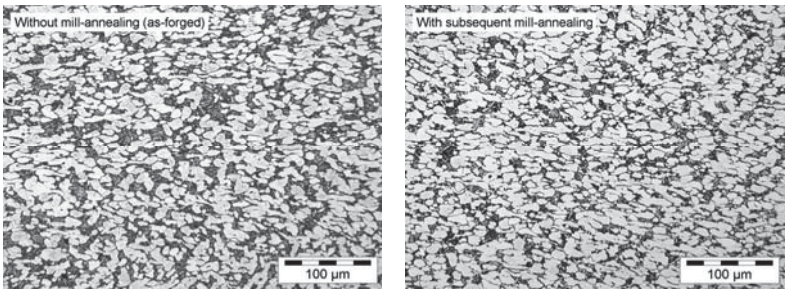

Fig. 3.20: Influence of mill-annealing on the microstructure of forged Ti-6Al-4V

Due to the forging temperature of 930°C no crystallographic texture occurs. This was shown with XRD and EBSD measurements (Fig. 3.21, Fig. 3.22). Remarkable are thereby the different colors within some primary α-grains in the OIM-map. This indicates different crystallographic orientations within one grain and may be attributed to substructures or micro residual stresses, owing to recovery and incomplete recrystallization.

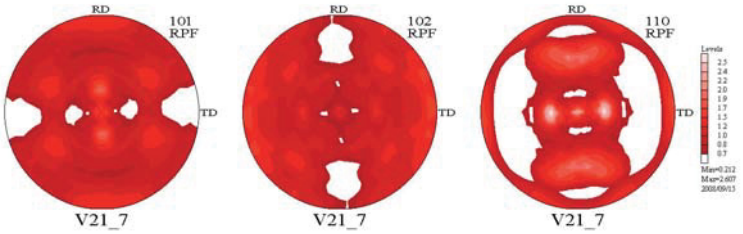

Fig. 3.21: Pole figures of mill-annealed V-shape

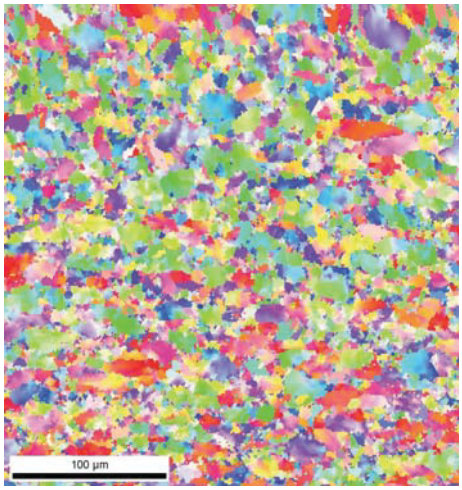

Fig. 3.22: OIM map of mill-annealed V-shape

3.2.6. V-shape solution treated (ST_V)

The solution treating of V-shapes at an elevated temperature (980°C) results in a bimodal microstructure (Fig. 3.23). The primary α-grains were found to be relatively large (9.0 µm) and interconnected (connectivity of 79%). The (α+β)-content averages 67%. Both, the lamellae width (1.2 µm) and the colony length (32.4 µm) are relatively large due to the elevated solution treating temperature and the subsequent air-cooling.

Concerning crystallographic texture, the same applies to the solution treated V-shapes as to the mill-annealed ones. Due to the forging temperature no texture occurs.

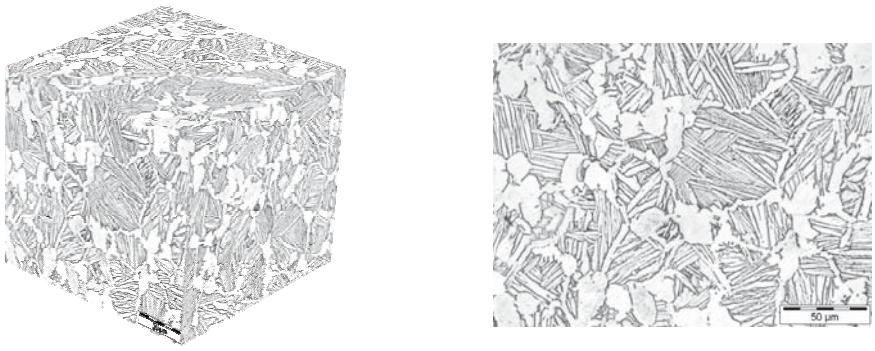

Fig. 3.23: Micrographs of V-shape solution treated, 3D visualization (l) and cross section (r)

3.2.7. V-shape solution treated and polymer-quenched ($STPQ_V$)

The solution treating at 950°C with subsequent polymer-quenching leads to a microstructure with a primary α-grain size of 8.1 µm and a connectivity of 39.5 %, Fig. 3.24. The (α+β)-content averages 61%. A relatively small α-lamellae width of 0.58 µm and a small colony length of 13.4 µm occur, owing to the fast cooling in consequence of the polymer-quenching. The chosen forging temperature of 930°C results in no crystallographic texture.

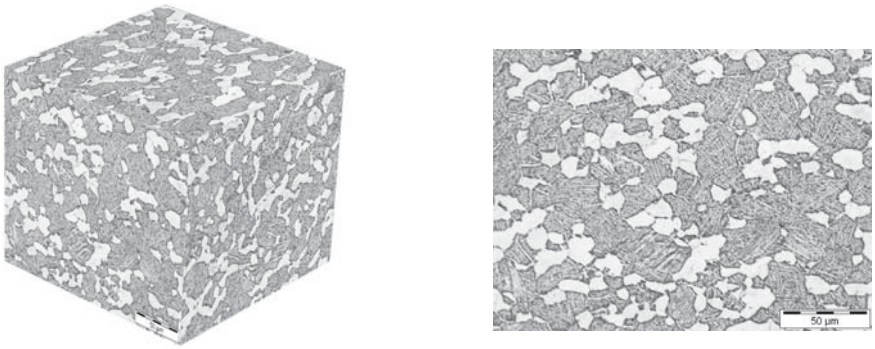

Fig. 3.24: Micrographs of V-shape STPQ, 3D visualization (l) and cross section (r)

3.2.8. Feedstock billet as-received (FB)

The feedstock billet has a coarse equiaxed microstructure with a primary α-grain size of 9.8 µm. Outstanding is thereby the connectivity of zero, owing to the complete separation of the α-grains by a β-seam.

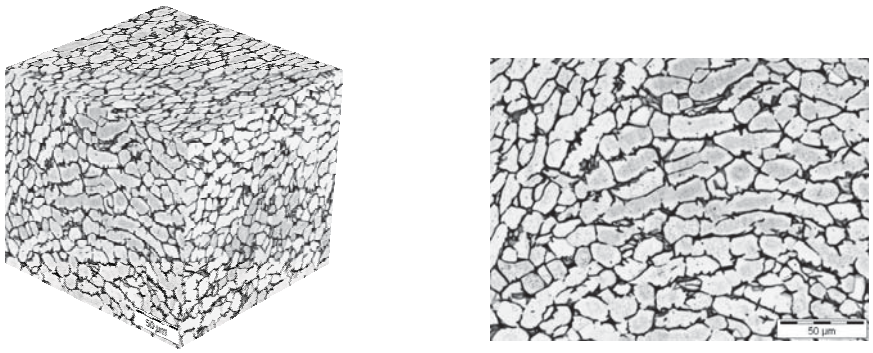

Fig. 3.25: Micrographs of feedstock billet as-received, 3D visualization (l) and cross section (r)

Macrozones were observable in polished unetched micrographs, analyzed with polarized light, Fig. 3.26 (l). The same structure is observable after etching in polarized light (Fig. 3.26, c) and in the primary α-grain shape texture (Fig. 3.26, r). It is believed that these macrozones correlate with prior β-grains. The XRD-analysis showed no distinct crystallographic texture.

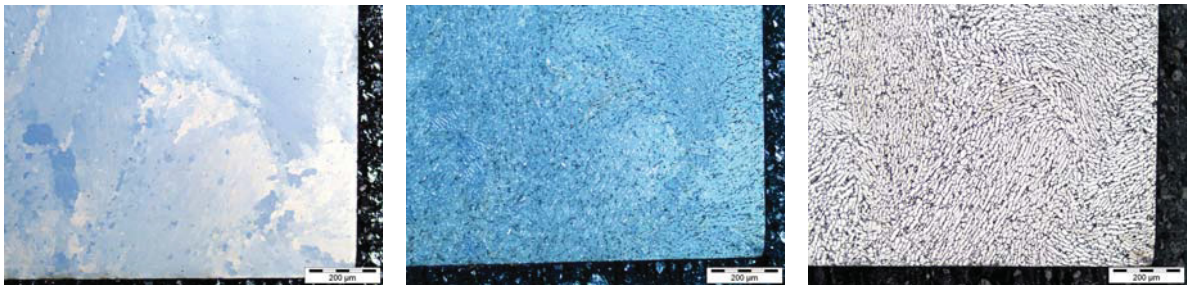

Fig. 3.26: Macrozones in the microstructure of the feedstock billet; unetched (l) and etched (c, r) micrographs

3.2.9. Summary of microstructural characterization

Due to the chosen forging temperature of 930°C, no crystallographic texture occurs in the pancake and in the V-shape forgings. The feedstock billet in the as-received condition shows isotropy too and is therefore comparable to the forgings. However, macrozones were observed in the feedstock billet, which has to be kept in mind. The different subsequent heat treatments (cf. Tab. 3.2) led to a high diversity of microstructure. The focus of this research work was on (α+β)-forged equiaxed and bimodal microstructures, respectively. Primary α-grain sizes between 7.3 µm and 11.5 µm were achieved. The colony length of the different microstructures varies in the range of 9 µm and 32 µm. Distinct differences were also found concerning (α+β)-content, connectivity of primary α-grains and α-lamellae width.

Material	α_p [µm]	$C_{\alpha+\beta}$ [%]	*Con* [%]	*Col* [µm]	*Lam* [µm]
MA_V	11.5*/8.7**	20.3	28.7	9.2	0.65
$STPQ_V$	8.1	61.4	39.5	13.4	0.58
ST_V	9.0	67.0	78.9	32.4	1.21
MA_P	8.2*/7.3**	30.9	45.2	7.1	0.57
ST_P	8.9	50.9	33.7	16.1	0.74
RA_P	10.3	0	99.0	-	-
FB	9.8	0	0	-	-

*Average α-grain size in direction of the grain shape elongation of all three cuts
**Mean primary α-grain size

Tab. 3.5: Summarized microstructural parameters

A linear correlation between the microstructural parameters colony length *Col* [µm] and lamellae width w_{lam} [µm] was found, cf. Fig. 3.27 (l) and Equ. (3.2). This means that the length and the width of a lamella are linked. It can be assumed that this behavior is based on diffusion processes during heat treatment and especially during cooling. A good accordance of linear fit and measured values was determined for microstructures based on the same type of cooling (in this case air-cooling). The polymer-quenching led to slight variance. It can be assumed that a significant difference in cooling rate changes the aspect ratio of the α-lamellae.

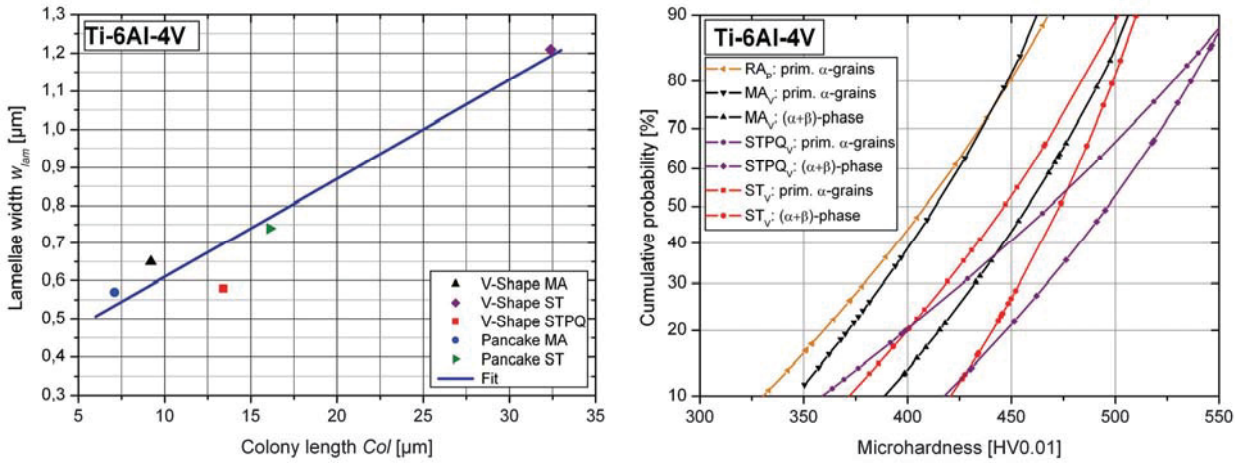

Fig. 3.27: Correlation between colony length and lamellae width (l); microhardness probability distributions (r)

$$w_{lam} = 0.026\,Col + 0.35 \qquad \text{Equ. (3.2)}$$

The microhardness of primary α-grains and (α+β)-phase of three different microstructures were measured (20 values per microstructure and phase) according to Vickers (0.01 kg load), Fig. 3.28. The Weibull-probability function was used in combination with the Gumbel-approach for determination of the probability distributions, Fig. 3.27 (r).

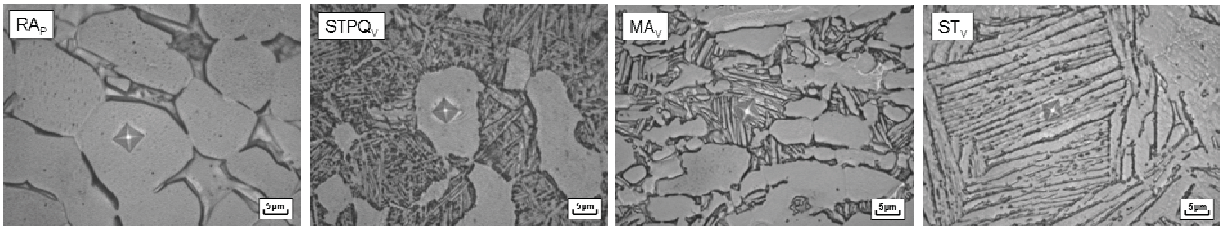

Fig. 3.28: Microhardness indentations in α-grains and (α+β)-phase

It was observed that the primary α-grains of recrystallization-annealed pancake and mill-annealed V-shape exhibit the same microhardness distributions. The microhardness of the primary α-grains increases with increasing (α+β)-content. The (α+β)-phase shows generally the higher microhardness compared with that of the primary α-grains of the same microstructure. The microhardness of the (α+β)-phase increases with increasing (α+β)-content too. It can be assumed that the length and width of the (α+β)-lamellae do not significantly affect the microhardness. However, the scatter seems to be influenced by cooling rate and hence lamellae dimensions.

3.3. Sampling

All used specimen geometries are discussed hereafter. Furthermore, the sampling of these different specimens from forgings and feedstock billet is depicted. All samples were thereby removed from the core thickness of the forgings.

3.3.1. Specimen geometries

3.3.1.1. Specimen geometry used for tensile tests

The specimen geometry for tensile tests was chosen according to DIN 50125 [58].

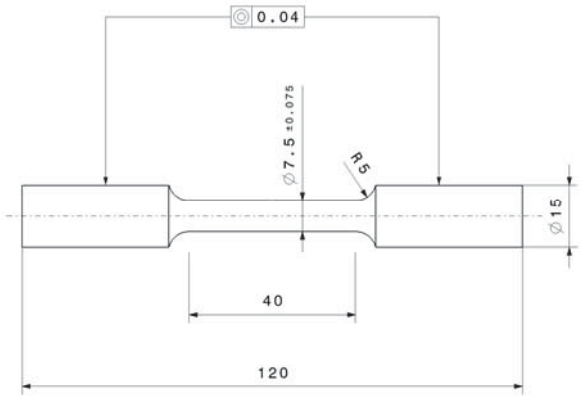

Fig. 3.29: Specimen geometry used for tensile tests

3.3.1.2. Specimen geometry used for low cycle fatigue tests

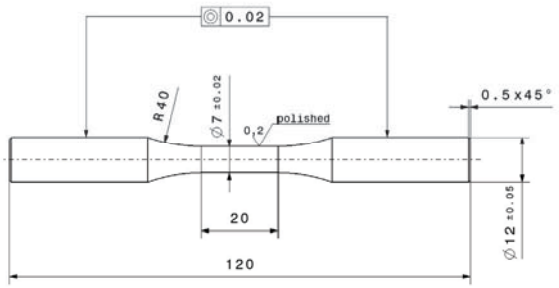

Fig. 3.30: Specimen geometry used for low cycle fatigue tests

3.3.1.3. Specimen geometries used for high cycle fatigue tests

High cycle fatigue test were performed on plane and round specimens with different types of surface states and notches.

Plane four-point-bending specimens

The plane four-point-bending test geometries are shown in Fig. 3.31 (machined gauge) and Fig. 3.32 (as-forged gauge).

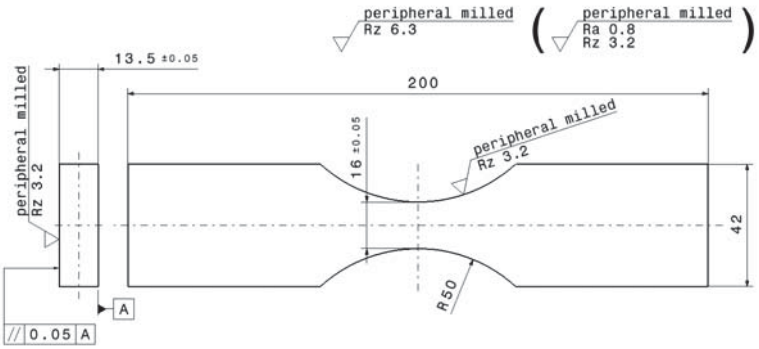

Fig. 3.31: Plane four-point-bending test specimen with machined gauge

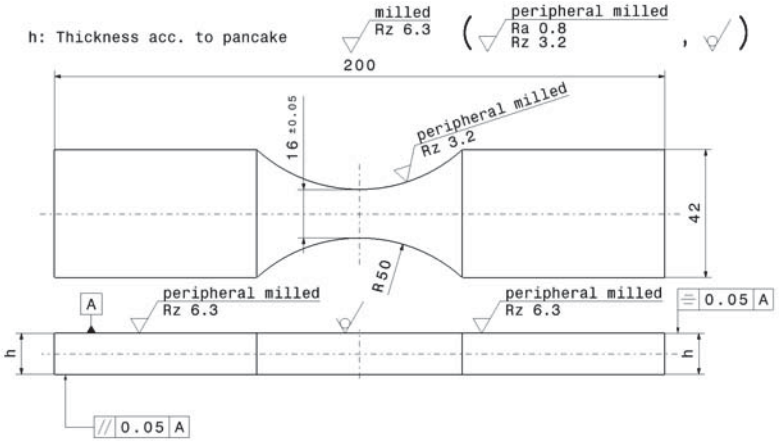

Fig. 3.32: Plane four-point-bending test specimen with as-forged gauge

Flat notched specimens

Tension/compression fatigue tests were performed on flat specimens provided with a reamed center hole (Fig. 3.33). The dimensions of these specimens are customer-specific and not stated.

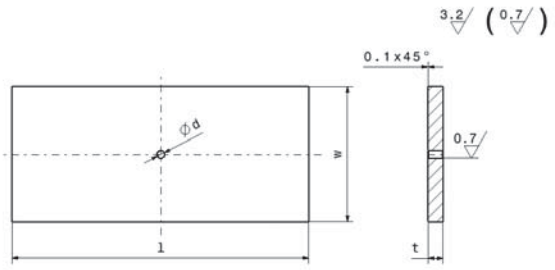

Fig. 3.33: Flat notched specimen for high cycle fatigue tests

Unnotched and notched round specimens

Rotating bending, tension/compression, torsion and multiaxial fatigue tests were performed on round specimens. Unnotched hourglass specimens (Fig. 3.34) and varying notched specimens (Fig. 3.35 - Fig. 3.37) were used, respectively. Thereby, the gauge diameter was consistently 6 mm for all round specimens. The round specimens sampled from pancakes got a smaller fixing shaft with a diameter of 12 mm instead of 15 mm, owing to the low pancake thickness.

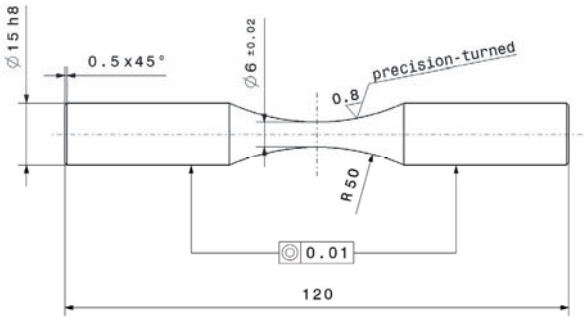

Fig. 3.34: Unnotched hourglass specimen

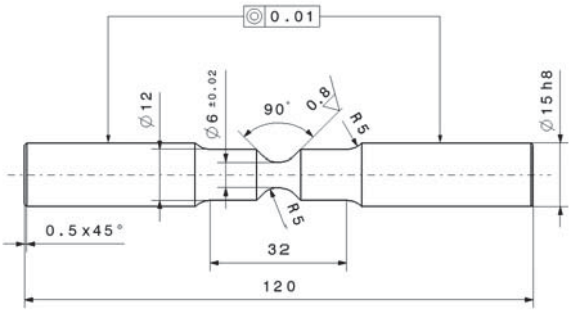

Fig. 3.35: Mild notched round specimen

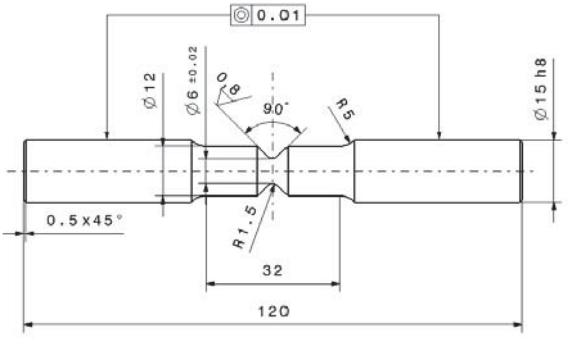

Fig. 3.36: Notched round specimen

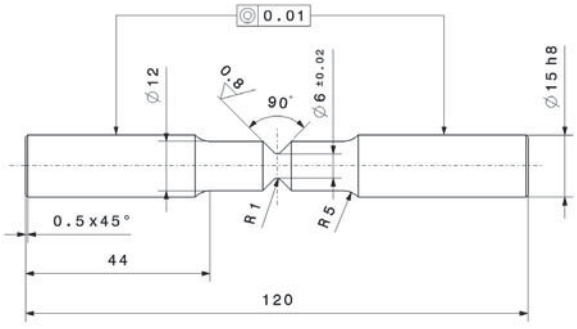

Fig. 3.37: Sharp notched round specimen

Some unnotched hourglass specimens were electrolytically polished (Fig. 3.38) to get a smooth surface for etching and to afford a residual stress free surface layer. Thereby, approximately 0.06 mm were removed from the surface, resulting in a gauge diameter of 5.88 mm. These specimens were used for microstructurally short crack growth tests.

Fig. 3.38: Electrolytically polished hourglass specimen

To evaluate the influence of a residual stress free surface layer on the fatigue behavior some rotating bending specimens were chemically milled (cf. Tab. 3.1) after the precision turning (Fig. 3.39). Thereby a surface layer of approximately 0.36 mm was removed.

Fig. 3.39: Chemically milled rotating bending specimen

3.3.1.4. Specimen geometry used for long crack growth tests

Single edge V-notched bending specimens (SEB) were used for the long crack growth testing (cf. Fig. 3.40).

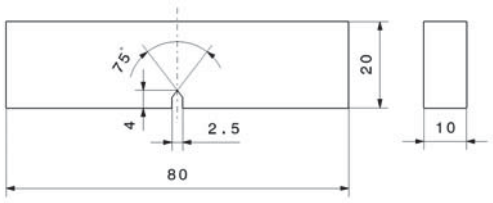

Fig. 3.40: Single edge V-notched bending specimen

3.3.1.5. Specimen geometry for physically short crack growth tests

Plane specimens (Fig. 3.41) were used for the measurement of the physically short crack growth (SCG).

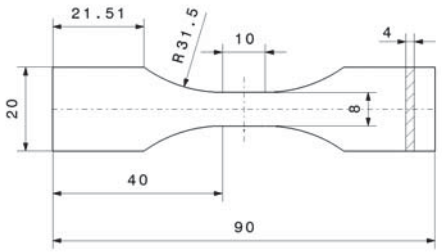

Fig. 3.41: Physically SCG plane specimen

Each specimen was provided with one wire eroded initial crack with a width of ~ 0.04 mm and a length of 0.2 mm or 0.4 mm, respectively.

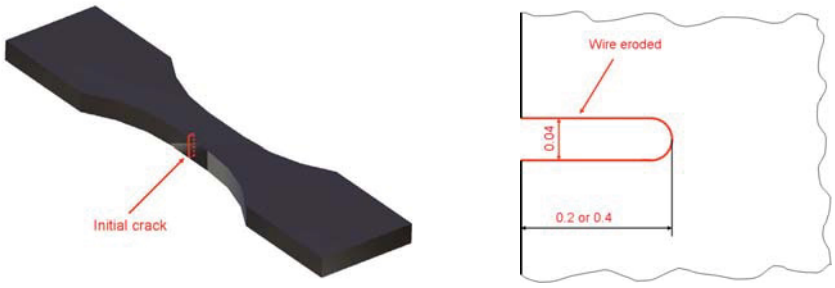

Fig. 3.42: Position (l) and shape (r) of a wire eroded initial crack

3.3.2. Sampling from pancakes

Two plane four-point-bending test specimens were sampled from each pancake in the longitudinal direction (Fig. 3.43). Regarding top surface quality, two different types of specimens were produced; namely as-forged (from pancakes with a thickness of 13.5 mm, cf. Fig. 3.32) and machined (from pancakes with a thickness of 15 mm, cf. Fig. 3.31). The sampling was done by sawing with a band saw, followed by milling.

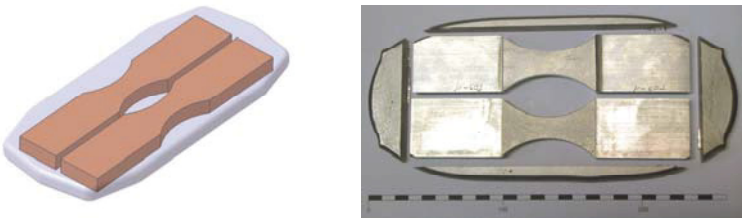

Fig. 3.43: Sampling of two four-point-bending specimens from a pancake

For high cycle fatigue testing, round specimens (five per pancake) were sampled from pancakes with different heat treatments. Single edge bending specimens (four per pancake) were taken for characterization of the long crack growth. The sampling of the hourglass specimens and SEB specimens was done via jet cutting and successive turning or milling, respectively.

Fig. 3.44: Sampling of rotating bending (l) and SEB (r) test specimens (after jet cutting)

3.3.3. Sampling from V-Shapes

Specimens for tensile tests, LCF and HCF tests and short and long fatigue crack growth tests were manufactured from V-shapes in transverse direction (Fig. 3.45). The sampling was done by sawing with a band saw, followed by milling and turning, respectively.

The crack growth direction of long cracks in the SEB specimens was in longitudinal direction of the V-shape. In contrast, the physically short cracks (see specification in Fig. 3.41 and Fig. 3.42) grew in through-thickness direction.

Fig. 3.45: Sampling from a V-shape

3.3.4. Sampling from feedstock billet

The sampling from the feedstock billet with a diameter of 230 mm was done in longitudinal direction (Fig. 3.46). The SEB and rotating bending specimens were taken by band sawing, milling and turning, respectively.

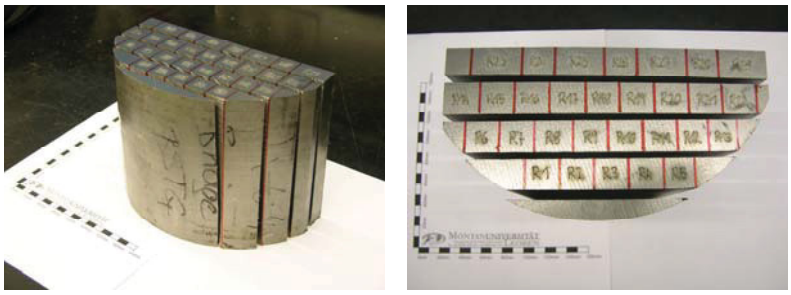

Fig. 3.46: Sampling from feedstock billet

3.4. Specimen characterization

The fatigue test specimens were characterized with respect to geometry (relative stress gradient and stress concentration), roughness and residual stresses. In this chapter, the all-purpose round fatigue test specimens are characterized, which were used for the determination of the influence of microstructure, relative stress gradient, mean stress and multiaxial loading on the fatigue behavior. All other special purpose specimens are discussed in detail in the according chapters.

3.4.1. Surface roughness

The surface roughness of the specimens was measured with a confocal laser scanning microscope (Olympus LEXT OLS3000, cut-off length 131.4 µm), Tab. 3.6. It was observed that the surface roughness is generally low; the maximum center-line average roughness $R_a < 1.5$ µm. Both, the center-line average roughness R_a and the average maximum roughness height R_z increase with decreasing notch radius of the precision turned round specimens. It can be assumed that the influence of these roughness variations on the fatigue behavior is small (< 10%, cf. [76]).

Type of specimen	R_a [µm]	R_z [µm]
Unnotched R50	0.6	1.4
Mild notched R5	0.6	1.6
Notched R1.5	0.9	2.3
Sharp notched R1	1.4	3.6

Tab. 3.6: Measured surface roughness of round specimens

3.4.2. Residual stresses

All residual stress measurements were performed using X-ray diffraction (XRD) in combination with the $sin^2\psi$ method. Fig. 3.47 shows the residual stress distributions for four different types of precision turned round specimens. Graphs of residual stresses are comprised of measured data points (calculated by the average of data in the longitudinal and transversal direction, assuming a homogenous plane stress state), with no smoothing.

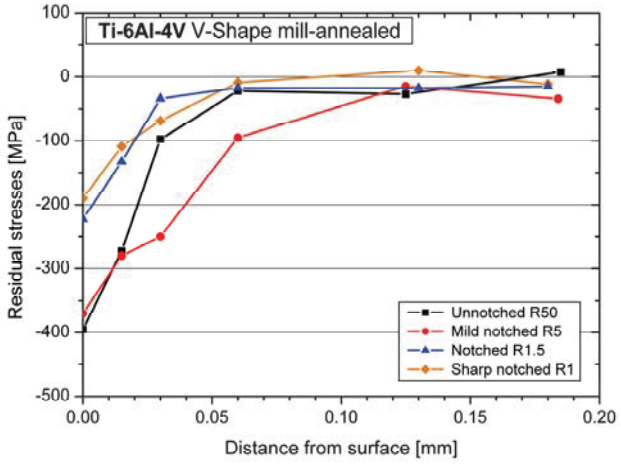

Fig. 3.47: Residual stress measurement on precision turned round specimens

The peak values of the compressive residual stresses are located at the surface for all precision turned specimens. They range between -200 MPa and -400 MPa. The compressive residual stresses reach approximately a depth of 0.05 mm. The anomalous distribution of the mild notched round specimen may derive from measuring inaccuracy.

3.4.3. Notch characterization

The important parameters (theoretical notch concentration factor K_t and relative stress gradient χ^*; achieved by finite element analysis) regarding notch characterization of the used specimens are summarized in Tab. 3.7. The notch characterization is discussed in detail in the chapter "Influence of relative stress gradient on the fatigue behavior".

Type of load	Type of notch	Notch radius [mm]	K_t [-]	χ^* [mm^{-1}]	$K_{t,Mises}$ [-]	χ^*_{Mises} [mm^{-1}]
Tension/Compression	Unnotched	50	1.03	0.04	1.02	0.05
Tension/Compression	Mild notched	5	1.25	0.41	1.17	0.56
Tension/Compression	Sharp notched	1	2.05	2.54	1.84	3.60
Rotating Bending	Unnotched	50	1.02	0.37	1.01	0.38
Rotating Bending	Notched	1.5	1.50	1.58	1.36	2.05
Rotating Bending	Sharp notched	1	1.69	2.11	1.52	2.73
Torsion	Unnotched	50	1.01	0.36	-	-
Torsion	Sharp notched	1	1.37	1.25	-	-

Tab. 3.7: Relative stress gradients and stress concentration factors of all used round specimens

4. Fatigue behavior of Ti-6Al-4V

This chapter contains the discussion of the most important influences on the fatigue behavior of Ti-6Al-4V, namely:

- Microstructure
- Relative stress gradient (notches)
- Impressed mean stress
- Multiaxial loading
- Flaws
- Surface state
- Surface arrangement
- Operating temperature

For each of these influences, the state-of-the-art is reported. Subsequent, the experimental procedure is elucidated and the experimental results are discussed. Developed phenomenological models are explained, in part also the according verification, and finally the conclusion is stated.

4.1. Influence of microstructure on the fatigue behavior

The aim of this part of the research work is to determine the influence of microstructure on the fatigue behavior of Ti-6Al-4V, including crack propagation. The focus is thereby on forgeable and economic microstructures in equiaxed or bimodal condition, respectively. Due to the chosen forging temperature of 930°C (typical for (α+β)-forged components) no crystallographic texture occurs in the analyzed materials. An influence of texture on the fatigue behavior is therefore excluded.

4.1.1. State-of-the-art

The influence of microstructure on the fatigue behavior of titanium alloys and especially Ti-6Al-4V is well documented in literature, with the problem that damage tolerant lightweight design of Ti-6Al-4V forgings is still lacking. The reasons for this circumstance are the multitude of possible processing and the high diversity of microstructure. The research works presented in papers are often limited on one or two (partly crystallographic texture afflicted) microstructures and the used processing is in part entirely uneconomical. Therefore, a quantitative link between microstructural parameters and fatigue strength or stress intensity factor threshold is not available in literature.
Already in 1984, Rüdinger and Fischer [146] concluded, that it must be kept in mind that optimal values for fatigue strength reached on a small dimension like a 30 mm bar, cannot be achieved in the same way for a heavy plate or a large forged part of various section sizes, because the microstructure produced by thermomechanical processing predominates the fatigue strength. Today, with powerful tools like FE forging simulation it is possible to predict the local microstructure for components of any size by the utilization of user-routines, see, for example, [163]. Such a user-routine is currently implemented in Deform™ for Ti-6Al-4V. The necessary quantitative link between local microstructure and fatigue strength will be discussed hereafter.

Lütjering [105] summarized the influence of several microstructural parameters on mechanical properties of (α+β)-titanium alloys (Tab. 4.1). The qualitative trends (+, 0, -) point out the direction in which a specific mechanical property will change when a microstructural feature is changed according to the footnote in Tab. 4.1.

	$R_{p0.2}$	ε_F	HCF	Microcracks ΔK_{th}	Macrocracks			Creep strength 0.2%
					ΔK_{th} R=0.7	K_{IC}	ΔK_{th} R=0.1	
Small α-colonies, α-lamellae [a]	+	+	+	+	-	-	-	+/-
Bimodal structure [b]	+	+	-	+	-	-	-	-
Small α-grain size [c]	+	+	+	+	-	-	-	-
Aging (α_2), Oxygen	+	-	+	-	-	-	+	+
Secondary α in β	+	-	+	+	0	0	0	+
Texture: Stress || c-Axis	+	0	+ Vac - Air	0 Vac - Air	0 Vac - Air	0	0 Vac - Air	+

[a] Compared to coarse lamellar structure.
[b] Compared to fully lamellar structure with same cooling rate.
[c] Compared to large α-grain size of fully equiaxed structures.

Tab. 4.1: Qualitative correlation of microstructural parameters and mechanical properties for (α+β)-alloys [105]

4.1.1.1. Crack initiation and high cycle fatigue

Peters et al. [131] investigated three different microstructures (fine equiaxed, coarse equiaxed, bimodal) with constant basal texture. They found that the fatigue strength of the equiaxed microstructures could be improved by reducing the α-grain size. Furthermore, they observed that it is advantageous for high fatigue strength in aggressive environments to separate the α-grains by fine lamellar portions (bimodal microstructure). They concluded that laboratory air is already a very aggressive environment for Ti-6Al-4V, because a large drop in fatigue strength existed when comparing tests in vacuum and in laboratory air, cf. Fig. 4.1 (l). In contrast, the difference between tests in air and in 3.5% NaCl solution was small.

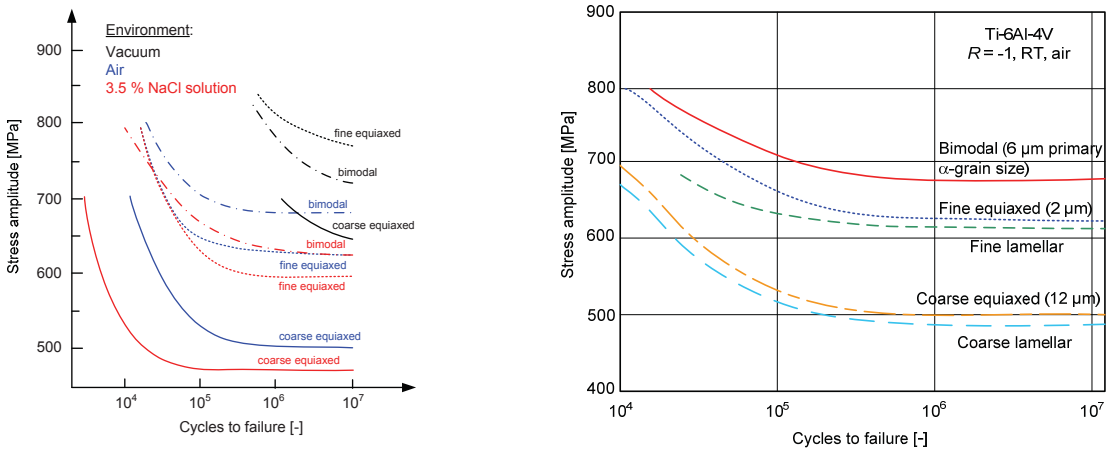

Fig. 4.1: Comparison of fatigue strength in diff. environments (l) [131] and with varying microstructure (r) [104]

Hall [80] summarized later results of Peters et al. [132] concerning influence of texture and environment on the fatigue behavior of Ti-6Al-4V. They found that moist air is an aggressive environment, especially where the stress and crystallographic orientations favor basal plane fracture. In both air and salt-water tests, basal plane cracks were the observed initial crack-like discontinuities. However, little basal plane cracking was observed in vacuum tests. This difference was more obvious at higher fatigue stresses. In all cases, nucleation was reported due to reversible slip over whatever slip distances the microstructure and texture allowed. If texture or coarseness of the structure was favorably arranged for high tensile stress across the basal plane, strong environmental influences were noted. Otherwise, slip on other planes performed the nucleation job. Hydrogen is considered to play a role by promoting slip heterogeneity as postulated by Postans and Jeal [135]. The primary α-grain size in the alloy of this study was very fine (< 2µm). However, the strong texture diminished the advantage of the fine alpha.

Lütjering and Gysler [104] reported the influence of microstructure on the HCF behavior of aged Ti-6Al-4V with basal texture, cf. Fig. 4.1 (r). They found that the bimodal microstructure exhibits the highest fatigue strength in air, because the basal planes of the strongly textured α-grains are separated from each other. The aggressive effect of laboratory air (about 50% relative humidity) was thought to be due to hydrogen, which is most damaging along the basal plane.

Wagner and Gregory [177] discussed the influence of the microstructural parameters lamellae width and α-grain size, cf. Fig. 4.2. They concluded that smaller lamellae width and α-grain size lead to higher fatigue strength. Furthermore, they reported that fatigue cracks nucleate in bimodal microstructures in the lamellar matrix, at the interface between lamellar matrix and primary α-phase, or within the α-phase.

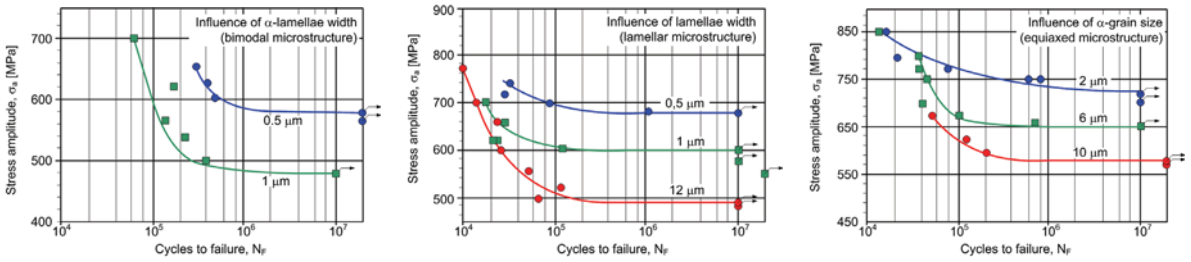

Fig. 4.2: Influence of grain size and lamellae width on the fatigue behavior of Ti-6Al-4V [177]

Benson et al. [39] studied the mechanisms of fatigue of mill-annealed Ti-6A1-4V at 600°F and room temperature. Early crack initiation (< 0.14 N_f) was found to occur in α-grains by a slip-band mechanism under all but the least severe conditions of cyclic stress. Under cyclic stresses near the fatigue limit at room temperature, fatigue cracks initiated later at the interface between α- and (α+β)-grains without detectable slip. Under all conditions, Stage I fatigue crack growth occupied 50% to 80% of the total life. Although mechanical twins were produced in profusion near the growing Stage II fatigue cracks, they appeared to play no role in crack initiation or Stage I crack growth; nor did they facilitate Stage II growth. None of the observations could be interpreted as evidence for a metallurgical instability or strain-induced phase transformation, which might be harmful to the fatigue resistance of the alloy.

Neal and Blenkinsop [121] observed that in the high cycle fatigue region, internal fatigue origins were often present in Ti-6Al-4V with flat alpha facets found at the crack origin. Based on Stroh's analysis [164] they proposed a mechanism for fatigue crack initiation by cleavage along the $(10\bar{1}7)$ plane in equiaxed alpha grains due to the restricted slip. [86]

The work of Freudenthal [64] also emphasized the fact that the pseudoelastic nature of Ti-6Al-4V leads to development of very high stress intensification at the strain incompatibilities. In the same vein, Steel and McEvily [162] suggested that the crack initiation in Ti-6Al-4V differs from that in a "plastic" material, such as copper, in that the internal stress concentration rather than the slip-band roughening is responsible for crack initiation in the high cycle range, possibly by the cleavage cracking, as discussed by Neal and Blenkinsop [121]. [86]

Ivanova et al. [86] tested equiaxed and bimodal Ti-6Al-4V in the finite life and high cycle fatigue regime with a stress ratio of 0.1. In the finite life region, they found crack initiation at the α/β interface and within the primary α-phase. In the high cycle fatigue region the fatigue cracks initiated in α-grains. In the equiaxed microstructure the cracks started thereby at the α/α grain boundary, cf. Fig. 4.3 (l). A close-up of the fractured grain, Fig. 4.3 (c), taken with a field emission microscope, allowed them to see a fan-shaped pattern on the grain surface which is characteristic for cleavage-type fracture, cf. [84]. The percentage of life spent for crack initiation was < 30% in the finite life region and > 80% in the high cycle fatigue region.

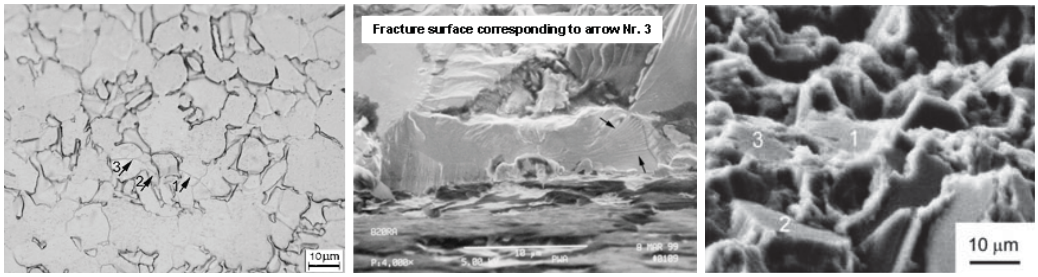

Fig. 4.3: Crack initiation in Ti-6Al-4V acc. to Ivanova et al. [86] (l, c), and acc. to Peters et al. [129] (r)

They concluded that it is very likely that cleavage-type fracture contributes to the crack initiation in Ti-6Al-4V; another observation in support of this point was the absence of slip activity in the alpha phase in the HCF regime. According to Adachi et al. [27], during tension/compression fatigue with impressed mean stress in Ti-6Al-4V, dislocations pile up at the unfavorably-oriented-for-slip α-grains, causing stress concentration ahead of the pile-up. However, on the other hand, the orientation of these grains is such that the easy cleavage plane in Ti-6Al-4V $(10\bar{1}7)$ is nearly perpendicular to the loading direction, maximizing hence the effect of the applied tensile stress. This stress combined with tensile stress caused by dislocation pile-up in the neighboring grain can exceed fracture strength of the easy cleavage plane in this alloy, thereby initiating a fatigue crack by cleavage fracture. It has to be mentioned that Ivanova et al. determined the fatigue cracks with a replica technique. It can be challenged that this method is able to determine fatigue cracks in the lamellar $(\alpha+\beta)$-phase in the bimodal microstructure.

Peters et al. [129] analyzed the fatigue behavior of solution treated and overaged Ti-6Al-4V with residual stress-free smooth specimens under tension/compression loading. They found crack initiation at the specimens surface for fully reversed loading (R = -1), whereas positive load ratios (R = 0.1-0.8) led to subsurface crack initiation. In addition, they found that the crack initiation site moved from regions close to the surface (~ 40-100 µm) to farther into the interior (~ 250-450 µm) with decreasing stress amplitude. Scanning electron microscopy of a subsurface crack initiation site (R = 0.7, N_f = 9.8E7) revealed a facet-type fracture surface, involving crack initiation and early growth along planar slip bands, Fig. 4.3 (r). The facets of fractured α-grains, which were aligned perpendicular to stress axis, were of near-basal orientation, based on electron backscatter diffraction (EBSD) analysis.

Knobbe et al. [94] analyzed fatigue crack initiation in mill-annealed Ti-6Al-4V in the high cycle fatigue region. They found that the fatigue cracks initiate preferentially at grain or phase boundaries. The scanning electron microscopy (SEM) picture in Fig. 4.4 (l) shows an initiated fatigue crack in primary α-phase. With electron backscatter diffraction (EBSD), they ascertained that this crack initiated at an α/α-grain boundary. The center picture in Fig. 4.4 shows an initial crack at an α/β-lamellae boundary. The Schmid factor of the α-lamellae was determined to be high for prismatic slip (~ 0.4) and very low for basal slip (< 0.1). The right SEM picture in Fig. 4.4 shows a fatigue crack initiated at an α/(α+β)-phase boundary and the according Schmid factors. The crack grew into the adjacent primary α-grain with high Schmid factor for basal slip. It can be assumed that the presented fatigue cracks initiated by cleavage fracture.

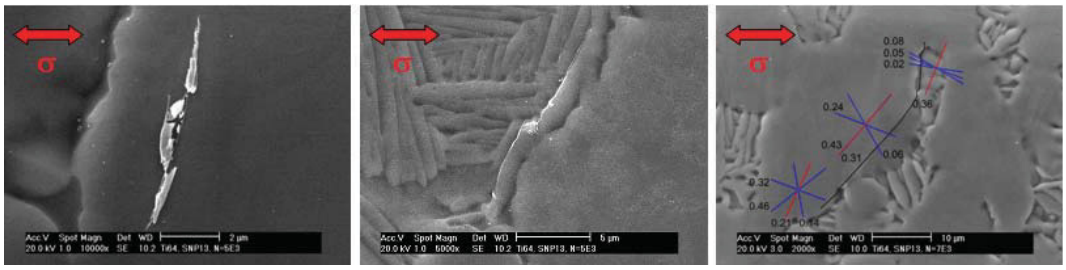

Fig. 4.4: Initiated fatigue cracks in mill-annealed Ti-6Al-4V according to Knobbe et al. [94]

Bridier et al. [43] performed strain-controlled fatigue tests on bimodal Ti-6Al-4V in the finite life region ($R_\varepsilon = 0$, $\varepsilon_a = 0.4\%$, $N_f \approx 20{,}000$) at room temperature in air. They noted that slip traces mostly occurred within primary α-grains, which accommodate the major plastic deformation.
The plastic deformation remained relatively localized, as only a small part (~ 30%) of all the analyzed primary α-grains exhibited single slip traces after the fatigue test. All activated slip bands were identified: 24% of them correspond to prismatic single slip, 5% to basal single slip, and only one grain presented slip traces along a first-order pyramidal slip plane. All cracks were found to form across primary α-grains. Six cracks formed along a prismatic plane and 10 cracks along a basal plane. Most of the observed prismatic cracks remained limited to the initial primary α-grain and were parallel to straight and regularly spaced slip bands. Conversely, basal cracks observed on the sample, i.e. after the same number of cycles, had already propagated through the surrounding microstructure.

They calculated the Schmid factor μ of all potential slip systems from EBSD data. Results concerning gliding activity after failure are summarized in Fig. 4.5 (l). For each prismatic, basal or pyramidal system, one bar corresponds to the percentage of grains presenting slip and associated with a certain Schmid factor on all the grains presenting a Schmid factor in the same range.

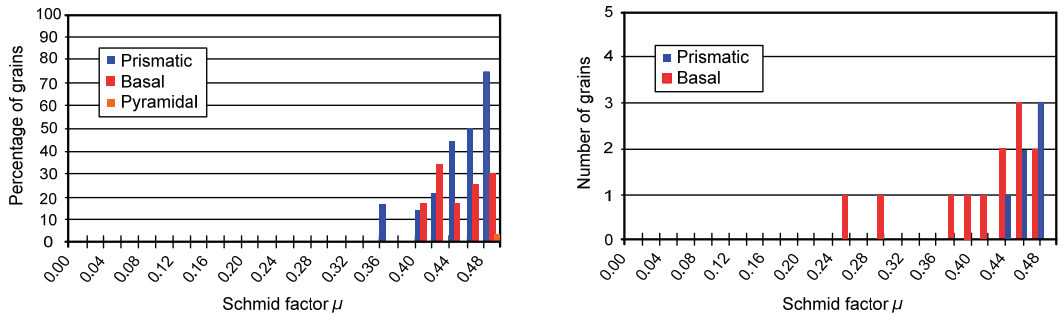

Fig. 4.5: Distribution of gliding (l) from the observation of a 0.1x1 mm² area, and distribution of cracks (r) [43]

It hence displays the relative ease by which each gliding system can be activated. Prismatic slip is, however, more easily activated than the basal one. The only first-order pyramidal gliding case was associated with a very high Schmid factor. Results concerning crack initiation are shown in Fig. 4.5 (r). They observed that two basal cracks have even been formed for much lower Schmid factors than the lowest value concerning basal slip.

To investigate the influence of local crystallographic orientation further, Bridier et al. [43] made a numerical analysis of the EBSD data. The orientation of every analyzed primary α-grain according to the stress axis was projected on inverse pole figures (IPF), Fig. 4.6 (l, c). The domain corresponding to prismatic crack formation appears more concentrated around the highest Schmid factor value than for gliding.
This fact and the strongly marked prismatic slip bands close to prismatic cracks lead to the conclusion, that prismatic crack formation involves a classical surface roughening mechanism. The result is quite different for basal systems. The crystallographic domain favoring plasticity corresponds to a high and relatively high Schmid factor. However, poles concerning crack formation are located mainly in an orientation domain of moderate basal Schmid factors. In particular, this domain is shifted towards the [0001] pole, which corresponds to a very low Schmid factor for prismatic systems and high tensile normal stresses to the basal plane.

They considered the elastic anisotropy of the hcp α-phase on the basis of Hayes formulation [83], and observed that the domains of basal slip or crack formation belong to a high stiffness domain. It can hence be concluded that crack formation in the finite life region requires a combination of a high Schmid factor and a high elastic stiffness, inducing a high tensile stress normal to the basal plane.

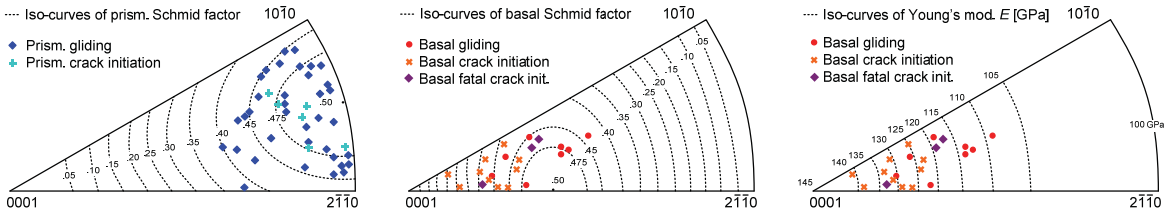

Fig. 4.6: IPFs with experimental poles of grains with prismatic (l) and basal (c, r) slip traces and cracks [43]

Calles [45] analyzed different types of microstructures of forged and rolled Ti-6Al-4V, respectively. He defined the grain size as the mean diameter of the primary α-grains. For lamellar microstructures, he appointed a mean slip length in respect of the mean lamellae dimensions to consider the different orientations of the lamellae with regard to the loading direction. Calles showed with tension/compression fatigue tests (R = -1) for different types of microstructures that the fatigue strength of small specimens (d = 1.9 mm) is lower than for "normal" specimens with common dimensions (d = 8 mm), Fig. 4.7. This finding conflicts with the statistical size effect. For steels, the statistical size effect can be ascribed to the increasing number of potential crack seeds (non-metallic inclusions, pores, etc.) with increasing material volume. Therefore, he suggested that the crack initiation mechanism via intrusions and extrusions on slip bands, known from very homogeneous materials, is negligible for such cases. However, for titanium alloys (almost no impurities due to the manufacturing process) the slip occurrence in the grains is a major influence on the fatigue behavior. The slip occurrence again is affected by the grain size as a quantity for the free dislocation slip length according to the Hall-Petch relationship, which is valid for static loading.

Furthermore, in (α+β)-titanium alloys the α-phase has the lower strength, so this phase is limiting the fatigue strength. The grain boundaries, which have to be passed by slip bands for propagation, are additionally reinforced by β-phase. Therefore, the influence of the α-grain size is intensified by this effect. Calles concluded that for small specimens with a four times higher specific surface compared to specimens with common dimensions, well oriented grains in respect of crack initiation are more likely near the vulnerable surface.

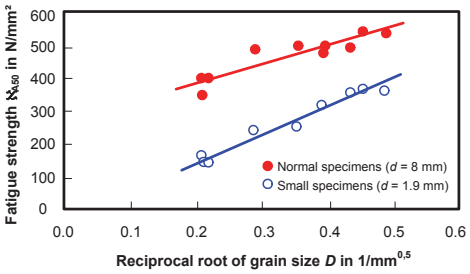

Fig. 4.7: Hall-Petch relationship for small and "normal" specimens [45]

Other authors (e.g. [26], [35], [183]) also concluded that the major influence in respect of crack initiation and fatigue strength is the maximum slip length in the microstructure.

Lucas and Koniezny [102] documented the relationship between α-grain size and crack initiation fatigue strength for Ti-6Al-4V (Fig. 4.8). They found that the fatigue limit increases with decreasing average grain size.

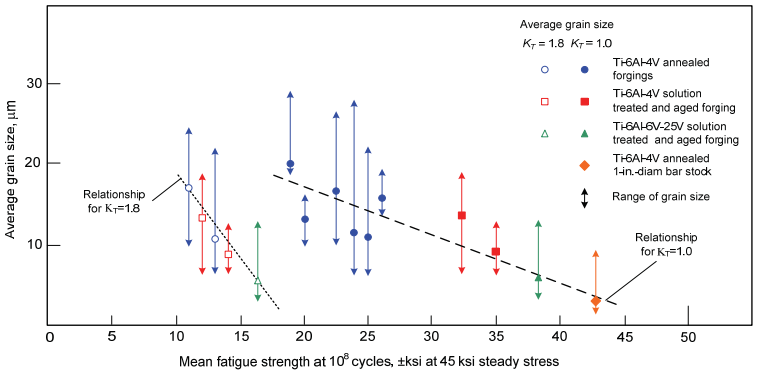

Fig. 4.8: Relationship between α-grain size and crack initiation fatigue strength [102]

In contrast to other authors, Nalla et al. [117] reported that the lamellar microstructure showed higher fatigue strength (at stress ratios 0.1 and 0.5) in the HCF region compared with a bimodal structure. They suggested that this behavior might be related to the fact that the bimodal microstructure had a high percentage (~ 64 %) of interconnected primary α, which leads to large effective slip length. It has to be mentioned at this point that the lamellar microstructure was achieved by an uneconomical heat treatment containing solution treating in vacuum and rapid quenching in high-purity helium gas. Crack initiation was found to occur at both the surface and subsurface regions (~ 40 to 100 µm below surface) of unnotched specimens. Nalla et al. mentioned in their paper that the most critical parameter to increase the HCF strength (resistance against fatigue crack nucleation) is to reduce the maximum dislocation slip length in the microstructure. Generally, fatigue cracks nucleate due to irreversible slip within the longest crystallographic slip bands (i.e. maximum slip length) available in the microstructure.

Zuo et al. [185] analyzed the ultra-high cycle fatigue (UHCF) behavior of Ti-6Al-4V with bimodal and lamellar basketweave microstructure (Fig. 4.9). They found internal crack initiation in the UHCF region caused by microstructural inhomogeneities. The interior cracks initiate at the α-grain boundaries or inside α-grains in bimodal microstructure and at the (α+β)-interfaces or colony boundaries in basketweave microstructure.
They concluded that the S/N-curves of Ti-6Al-4V continue to decrease with increasing number of cycles to failure, and no conventional fatigue limit exists in the regime of 10^5 to 10^9 cycles for Ti-6Al-4V with both bimodal and basketweave microstructure. It has to be mentioned that the fatigue test results of Zuo et al. do not clearly confirm their conclusion.

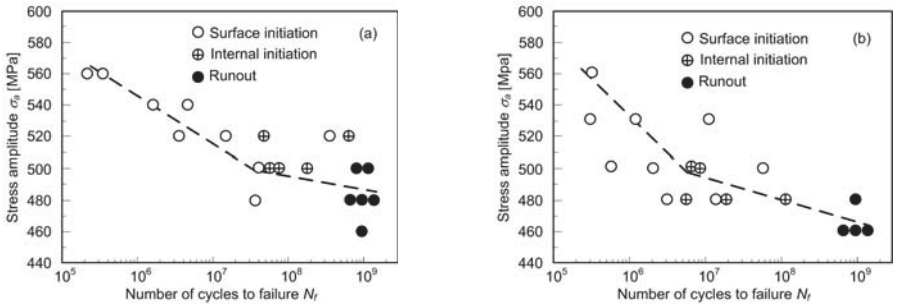

Fig. 4.9: S/N-curves of Ti-6Al-4V with bimodal (a) and basketweave (b) microstructure [185]

Morrissey and Nicholas [113] investigated the fatigue behavior of Ti-6Al-4V with bimodal microstructure in the HCF and UHCF regime. They compared S/N results at ultrasonic and conventional frequencies and found a distinct fatigue limit of 410 MPa (Fig. 4.10). Furthermore, they observed no frequency effects due to the increased strain rate or due to temperature increases caused by internal damping.

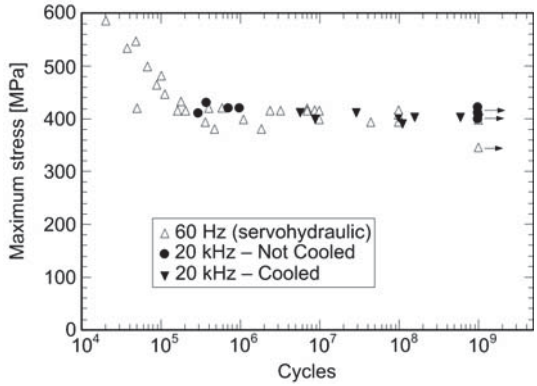

Fig. 4.10: Comparison of S/N-results at ultrasonic and conventional frequencies [113]

Knobbe et al. [94] tested mill-annealed Ti-6Al-4V with a frequency of 760 Hz up to $5 \cdot 10^8$ load cycles and reported a distinct fatigue limit.

Lütjering [103] and Bowen [41] showed that the crystallographic texture has a considerable influence on the fatigue behavior (Fig. 4.11). They observed fatigue limits between 600 MPa and 725 MPa owing to different types of crystallographic textures. Thereby, the basal/transversal texture led to the highest endurance limits.

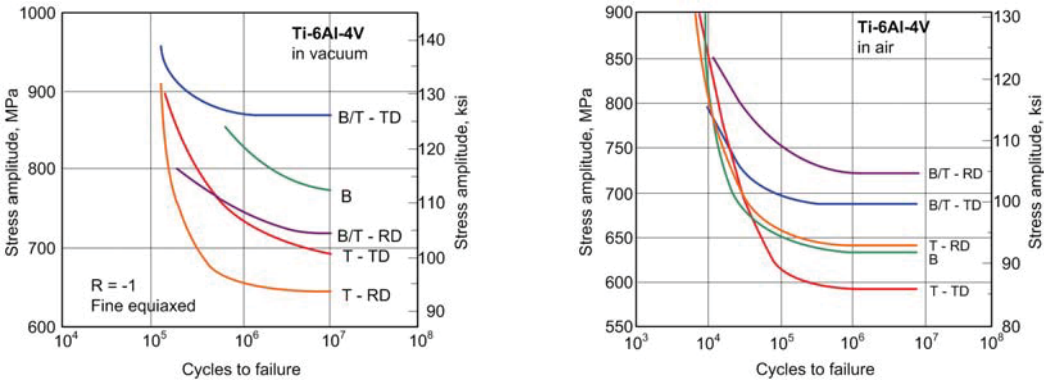

Fig. 4.11: Influence of texture & test direction on the fatigue behavior of Ti-6Al-4V in vacuum (l) and in air (r) [41]

4.1.1.2. Fatigue crack propagation

In 1975, Pearson [127] observed the abnormal behavior of short cracks in commercial aluminum alloys for the first time. Short cracks already propagate beneath the stress intensity range threshold ΔK_{th}. Furthermore, they possibly show significantly higher crack growth rates at equivalent stress intensity ranges ΔK compared with long cracks. The crack growth behavior of short cracks is often explained by the absence of crack closure mechanisms, e.g. [120] or [158]. But Nalla et al. [117] reported that short cracks propagate also beneath the effective stress intensity range threshold $\Delta K_{th,eff}$ which is corrected regarding crack closure effects.

A classification of short cracks can be made with respect to their dimensions, cf. [142] and [156]. Suresh and Ritchie [165] suggested the following classification of short cracks:

- *Microstructurally short cracks*, where crack size is comparable to the scale of some characteristic microstructural dimension (micro-crack limiting obstruction distance d_o) such as grain size.
- *Mechanically short cracks*, where the zone of permanent deformation (plastic zone) around a crack may be comparable to its size.
- *Physically short cracks*, which do not lie in any of the above two categories but are merely smaller than 1–2 mm.
- *Chemically short cracks*, where environmental stress corrosion mechanisms become more active below a certain crack size.

The Kitagawa-Takahashi diagram [93] plots the threshold of cyclic stress (stress amplitude σ_a or stress range $\Delta\sigma$) for growth of existing cracks against initial crack length a. Beneath this limiting curve is the no-growth region and therefore infinite life, above crack propagation and hence finite life, Fig. 4.12.

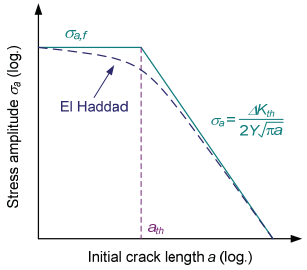

Fig. 4.12: Kitagawa-Takahashi diagram and El Haddad relation

The classical Kitagawa-Takahashi diagram is characterized by two parameters, namely fatigue limit σ_f and stress intensity factor threshold for long crack propagation ΔK_{th}. El Haddad et al. [61] reported differences between Kitagawa-curve and experimental data at the transition region of fatigue limit and stress intensity threshold line, where the threshold of the stress intensity factor depends on the crack length. Therefore, they suggested a new empirical model including these short crack effects, Equ. (4.1). Thereby, the initial crack length a_0 is increased by a notional crack length a_{th}; the crack length at the transition point of the Kitagawa-curve, Equ. (4.2). The El Haddad relation leads to a continuous transition and asymptotical convergence to the fatigue limit.

$$\Delta\sigma = \frac{\Delta K_{th}}{\sqrt{\pi \cdot (a_0 + a_{th})}} \qquad \text{Equ. (4.1)}$$

$$a_{th} = \frac{1}{\pi}\left(\frac{\Delta K_{th}}{2\sigma_{a,f}}\right)^2 \qquad \text{Equ. (4.2)}$$

Chapetti [47] also discussed the fatigue propagation threshold of short cracks under constant amplitude loading, and presented several interesting findings. He assumed that both, the fatigue limit and the high cycle fatigue resistance depend on the effective resistance of the microstructural barriers that has to be overcome by the cracks, Fig. 4.13.

Each of these barriers has a characteristic dimension (d_1, d_2,…) and a critical stress range associated with its resistance to crack propagation. The plain fatigue limit is determined by the strongest microstructural barrier (d), since that resistance is generally greater than the resistance to crack nucleation. On the other hand, above the fatigue limit and for a given stress range, each barrier has an associated number of cycles that is necessary to propagate the crack. A crack is non-damaging with respect to the plain fatigue limit up to a crack size $a = d$.

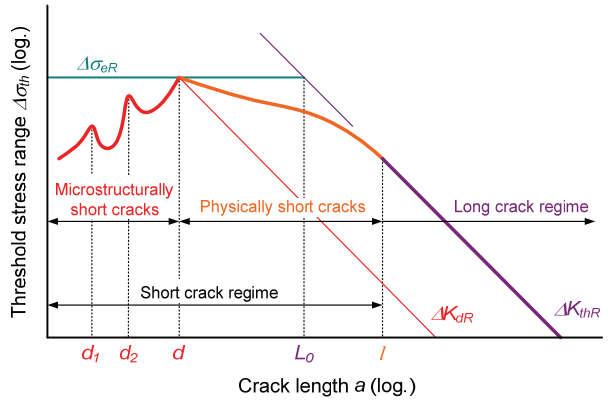

Fig. 4.13: Kitagawa diagram showing the threshold stress for short and long cracks [47]

Chapetti [47] defined an intrinsic resistance to microstructurally short crack propagation (ΔK_{dR}) by using the position d of the strongest microstructural barrier and the (stress ratio dependent) plain fatigue limit $\Delta\sigma_{fR}$. This intrinsic resistance is considered to be a microstructural threshold for crack propagation, Equ. (4.3).

$$\Delta K_{dR} = Y \cdot \Delta\sigma_{fR} \cdot \sqrt{\pi \cdot d} \qquad \text{Equ. (4.3)}$$

For the long crack regime (where crack closure has built up to a steady state level), a total extrinsic component ΔK_{CR} can be defined as the difference between the mechanical threshold for long cracks, ΔK_{thR}, and the microstructural one, ΔK_{dR}. The total extrinsic component of the threshold corresponds to a steady state level and is built up after a given crack length that depends on the material ($a = l$ in Fig. 4.13). In order to obtain an expression to estimate the fatigue crack propagation threshold as a function of crack length, Chapetti [47] defined the development of the extrinsic component ΔK_C by using the expression proposed by McEvily and Minakawa [109], Equ. (4.4). Thereby, k is a stress ratio dependent material constant, and a the crack length.

$$\Delta K_C = \Delta K_{CR}\left(1 - e^{-k \cdot a}\right) \qquad \text{Equ. (4.4)}$$

The material threshold for crack propagation as a function of crack length, ΔK_{th}, is then defined according to Equ. (4.5).

$$\Delta K_{th} = \Delta K_{dR} + \Delta K_C = \Delta K_{dR} + \left(\Delta K_{thR} - \Delta K_{dR}\right)\left(1 - e^{-k \cdot (a-d)}\right) \qquad \text{Equ. (4.5)}$$

Finally, Chapetti proposed an expression for the material parameter k, which defines the development of the extrinsic threshold component, Equ. (4.6).

$$k = \frac{1}{4d} \cdot \frac{\Delta K_{dR}}{\Delta K_{thR} - \Delta K_{dR}} \qquad \text{Equ. (4.6)}$$

Künkler et al. [98] summarized the different crack propagation stages. They reported that crack initiation in polished specimens starts trans- or intercrystalline at positions in the microstructure with elevated stress due to stress raisers (e.g. grain boundaries or inclusions). The following crack propagation in stage I occurs on single-crystallographic slip bands inclined by about 45° to the applied stress axis (tension/compression loading, Fig. 4.14). This means that shear stresses act on the slip planes.

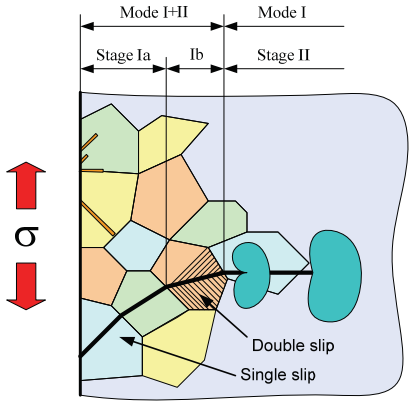

Fig. 4.14: Different stages of crack propagation [98]

After crossing the first grain boundary, the crack can propagate through several grains in stage I, which leads to a zigzag-like crack path. Thus, geometrically induced crack closure can occur. Plasticity induced crack closure known from long cracks seems not possible in stage I as no plastic crack tip opening exists. During the crack growth in stage I, grain and phase boundaries may act as barriers against slip transmission into adjacent grains (depending on the orientation of the respective slip bands). This leads to an oscillating crack growth rate. With increasing crack length and depending on the orientation of the individual grains and the crack path, additional slip bands are activated and the crack propagates alternating on two different slip bands.
At the beginning, the position and the length of the activated slip bands are determined by the microstructure. Due to the propagation on different slip systems, the crack changes from its direction parallel to the maximum shear stress to a path perpendicular to the loading axis (mode I), which is the direction of crack growth in stage II. Because position and length of the activated slip bands are still determined by the microstructure, the crack can be termed "microstructurally short".
With further increase in crack length, the stress intensity in front of the crack increases and more and more slip bands are activated until a larger area at the crack tip is plastically deformed. Now the influence of individual slip band orientation and grain shape on crack propagation decreases. Thus, the crack is no longer microstructurally short and may be described by elastic-plastic or linear-elastic fracture mechanics (stage II).

The fatigue crack propagation behavior of short and long cracks in Ti-6Al-4V is considerably influenced by microstructure. Wagner and Gregory [177] reported the crack growth behavior of microstructurally short cracks (Fig. 4.15, left) and long cracks in coarse lamellar and fine equiaxed microstructure. They found that the coarse lamellar microstructure exhibits a worse short crack growth behavior but – owing to the additional crack growth resistance contributions of crack front geometry and crack closure – a slower long crack propagation compared to the fine equiaxed microstructure (Fig. 4.15, center). Furthermore, they reported a decrease of long crack growth rate with increasing α-grain size owing to the same crack growth resistance contributions mentioned before, Fig. 4.15 (r).

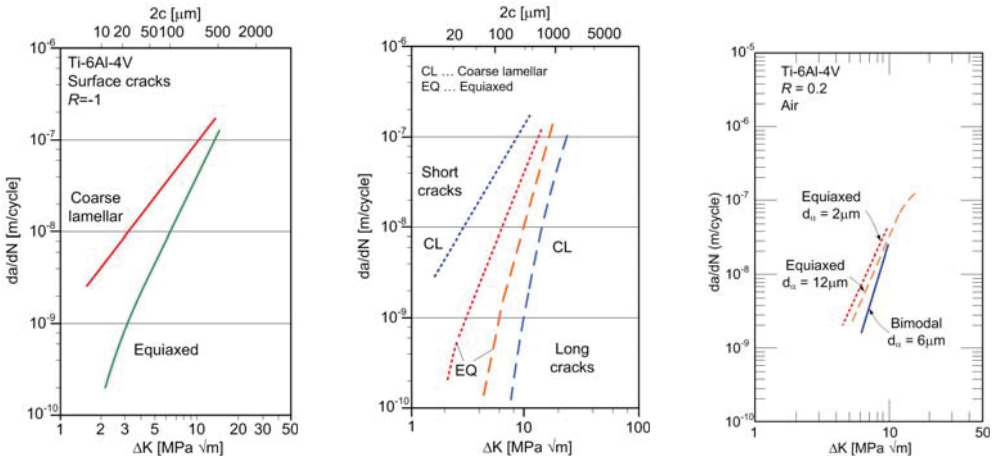

Fig. 4.15: Crack growth of short cracks (l), comparison with long cracks (c) and influence of grain size (r) [177]

Gray and Lütjering [73] also observed that coarsening the equiaxed grain size reduces the fatigue crack propagation rates of Ti-6Al-4V at low stress ratios. They attributed the influence of grain size and the increase in fatigue crack propagation resistance with decreasing stress ratio to roughness-induced crack closure. Furthermore, they observed that the coarse lamellar microstructure possesses (in comparison to equiaxed microstructures) the highest resistance to fatigue crack propagation owing to roughness-induced crack closure.

Testing in a more aggressive environment (ambient air) was found to drastically reduce the crack propagation resistance of Ti-6Al-4V with equiaxed and lamellar microstructure in comparison to experimental results in vacuum (Fig. 4.16).

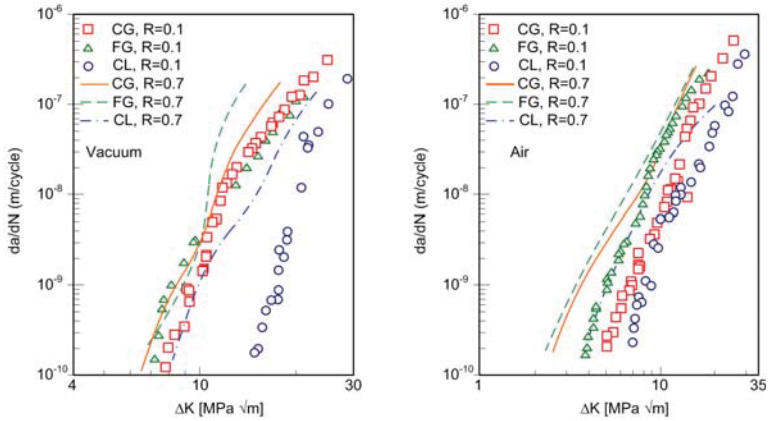

Fig. 4.16: Fatigue crack propagation in respect of microstructure and stress ratio in vacuum (l) and air (r) [73]

Nakajima et al. [116] investigated the early stage of crack growth in mill-annealed Ti-6Al-4V ($C_{\alpha+\beta}$ = 33%, α_p = 7 µm) on notched flat specimens (stress ratio R = 0.1). They found that the fatigue crack initiated as a stage I crack in an α-grain at the notch root surface. The incipient crack grows under 45° to the maximum tensile stress axis. It was also revealed that the small fatigue crack changed its propagation direction at the grain boundary. Nakajima et al. supposed that crack closure develops fast, owing to the relatively large α-grains with planar slip characteristics. At the fatigue limit, non-propagating cracks were not observed. In contrast, Takafuji et al. [166] reported non-propagating crack in Ti-6Al-4V at the notch root of (run-out) V-notched round specimens at 10^7 load cycles.

Knobbe et al. [94] analyzed crack initiation and short crack growth near the fatigue limit in mill-annealed Ti-6Al-4V. They found more initial fatigue cracks in the lamellar (α+β)-phase. The initiated cracks grow intercrystalline; even in lamellae.

Lütjering and Gysler [104] investigated the long crack propagation behavior of Ti-6Al-4V with varying microstructure. The equiaxed and bimodal microstructures had thereby a mixed basal/transversal texture after rolling. They observed that the material with the larger α-grain size exhibited slightly lower long crack propagation rates at both high and low stress ratios. Similar findings are reported by Peters et al. [131].

Lütjering and Williams [105] presented an example for the fatigue crack propagation behavior of fully equiaxed microstructures with an α-grain size of 6 µm. The propagation rates of small, self-initiated surface cracks (microcracks) measured on round smooth specimens and large cracks (macrocracks) measured on fracture mechanics type specimens for two different stress ratios were compared (Fig. 4.17 left). These results indicate that, even for these relatively fine grained equiaxed microstructures, a sufficient large grain size effect on the crack front profile of macrocracks exists which explains the change in grain size ranking between microcracks and macrocracks (cf. Tab. 4.1).

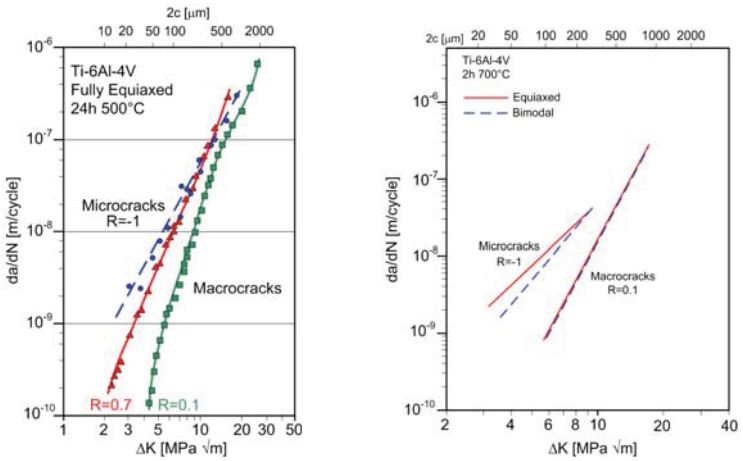

Fig. 4.17: FCP in equiaxed microstructure (l) and comparison of bimodal and equiaxed microstructure (r) [105]

Fig. 4.17 (r) shows the differences in fatigue crack propagation behavior between equiaxed and bimodal microstructures. It was observed that the microcracks in the bimodal microstructure propagate at slower rate as compared to the microcracks in the equiaxed microstructure containing many interconnected α-grains.
The microcracks in the fully equiaxed microstructure showed the tendency to grow through areas containing interconnected α-grains whereas the microcracks in the bimodal microstructure showed the tendency to propagate through the lamellar (α+β)-phase. Although the macroscopic crystallographic texture measured with XRD was similar for both microstructures, the slip length seems to be larger in areas with interconnected α-grains (equiaxed microstructure) than in the lamellar (α+β)-phase of the bimodal microstructure. [105]

Lütjering and Williams [105] reported the influence of texture and environment on the long crack growth, cf. Fig. 4.18. It was observed that there is not much effect of texture on macrocrack propagation in vacuum.
In 3.5% NaCl solution the macrocracks propagated much faster under transverse direction (TD) loading (basal planes perpendicular to the loading direction) as compared to the rolling direction (RD) loading (basal planes parallel to the loading direction).

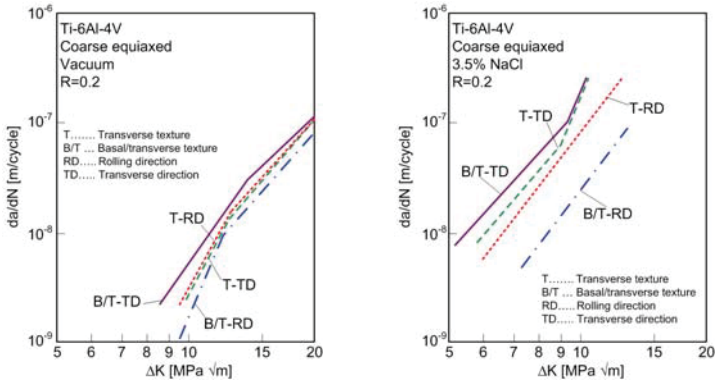

Fig. 4.18: Crack propagation behavior in respect of texture in vacuum (l) and aggressive environment (r) [105]

Tokaji et al. [170] found that in high strength low alloy steels with fine and coarse austenite grain sizes, the surface crack was less than three grain diameters in length. The grain boundaries provided crack arrest or deceleration points. Slightly longer cracks were not strongly influenced by the microstructure. [80]

The longer cracks grew faster than predicted from linear elastic fracture mechanics (LEFM) extrapolations of long crack data until surface lengths exceeded several grain diameters (*d*). They concluded that after a surface crack reached 3*d*, some crack closure began to be effective and that this effect saturated after another 150 µm of growth. Then LEFM adequately described crack growth. From this point, grain boundaries become less important as crack growth inhibitors. Wagner et al. [178] investigated equiaxed Ti-8.6Al in a similar manner and found grain boundaries to provide substantial resistance to growth of very short cracks. They also examined the total shape of surface cracks, finding them not to conform to an expected uniform *a/c* ratio. Slower short crack growth was reported, consistent having more grain boundary arrest points. [80]

4.1.2. Experimental procedure

The test program for the determination of the influence of microstructure on the fatigue behavior of Ti-6Al-4V included rotating bending fatigue tests, single edge bending long crack growth tests, and microstructurally and physically short crack propagation tests. All tests were performed at ambient air and room temperature.

4.1.2.1. High cycle fatigue tests on Ti-6Al-4V with varying microstructure

Fatigue tests were performed on precision turned round hourglass specimens (Fig. 3.34) under rotating bending loading (stress ratio $R = -1$) with a frequency of 70 Hz. The used rotating bending test rig (Fig. 4.19) was developed at the Chair of Mechanical Engineering. The specimens are thereby loaded under four point bending loading.
The evaluation of the S/N-curves in the finite life region was based on the logarithmic normal distribution. The high cycle fatigue strengths at 10^8 load cycles were determined according to the *arcsin*√*P*-method [55]. Due to the limited specimen lot sizes, the high cycle fatigue strength and especially the scatter are not statistically firm. Both, the test results and the literature, e.g. [94] and [113], raise the suspicion that Ti-6Al-4V has a distinct fatigue limit. Therefore, two-line S/N-curves were used with a horizontal high cycle fatigue line.

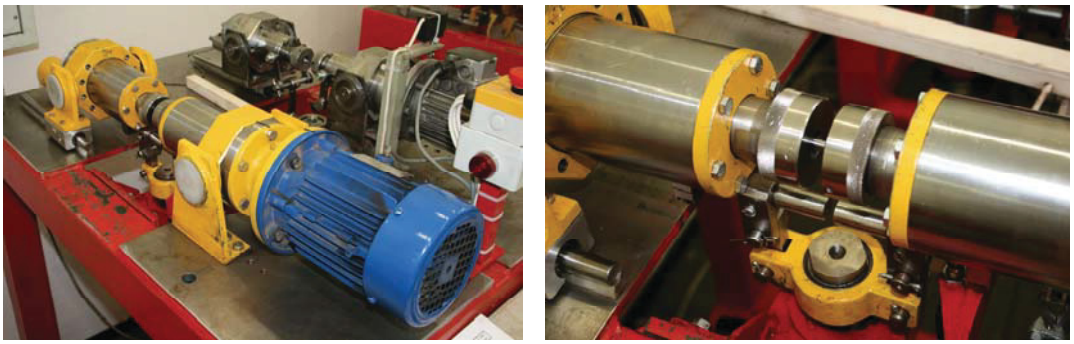

Fig. 4.19: Rotating bending test rig

The fracture surfaces were analyzed with a stereo light optical microscope (Olympus SZX12). Two exemplary pictures of a fracture surface are shown for each microstructure; one overview (16x magnification) and one detailed view of the crack initiation site (64x magnification, except pancake BA). The crack initiation site is located at twelve o'clock position in all pictures. The fatigue cracks initiated from or directly underneath (ca. 50 µm, in accordance to the residual stress distribution, cf. Fig. 3.47) the surface independent of microstructure. It can be assumed that such a subsurface crack initiation directly beneath the surface is caused by machining-induced residual stresses.

Mill-annealed microstructure

The mill-annealed V-shape exhibits a fatigue strength of 580 MPa (Fig. 4.20). The scatter (Tab. 4.2) is relatively low despite the mill-annealed microstructure. This may be caused by the special design of the V-shapes resulting in a uniform gauge with regard to effective strain.

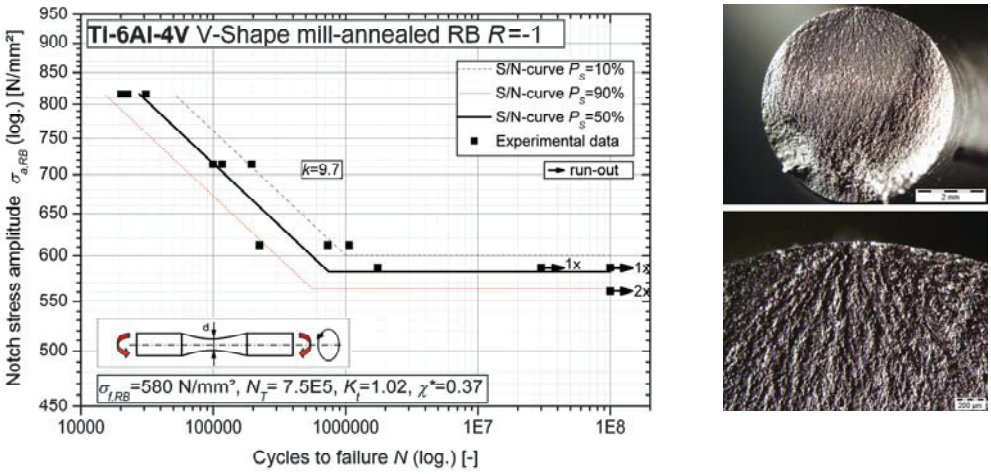

Fig. 4.20: Rotating bending S/N-curve (l) and fracture surface (r) for V-shape mill-annealed unnotched

Symbol	Description	Unit	Value
σ_f	Fatigue strength at N=10^8	MPa	580
N_T	Cycles at transition	-	7.5E5
k	Slope	-	9.7
T_N	Scatter at finite life	-	1:3.4
T_S	Scatter at N=10^8	-	1:1.1

Tab. 4.2: Parameters for RB S/N-curve V-shape mill-annealed unnotched

The mill-annealed pancake exhibits a high fatigue strength in the HCF and in the finite life region. The scatter is markedly higher in comparison to the mill-annealed V-shape. This may arise from the non-uniform effective strain distribution in the cross section of the mill-annealed pancake (cf. Fig. 3.10) and resulting variations in microstructure.

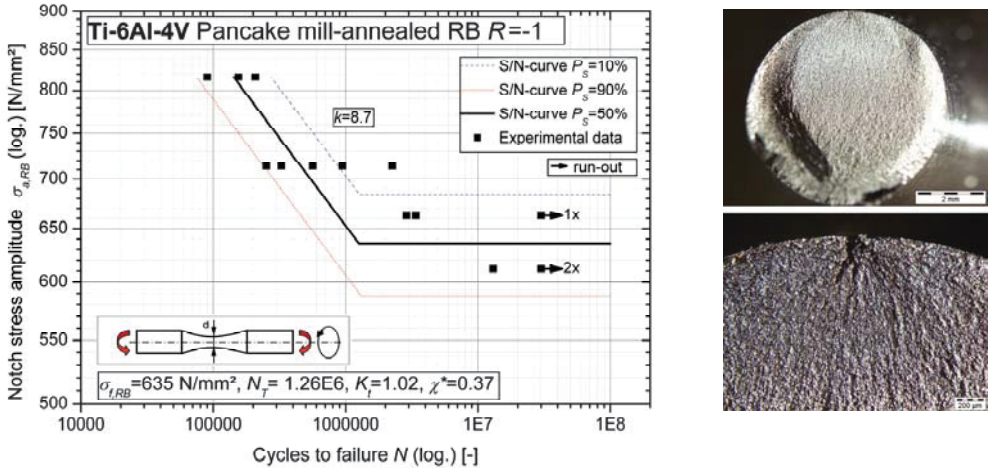

Fig. 4.21: Rotating bending S/N-curve (l) and fracture surface (r) for pancake mill-annealed unnotched

Symbol	Description	Unit	Value
σ_f	Fatigue strength at N=10^8	MPa	635
N_T	Cycles at transition	-	1.3E6
k	Slope	-	8.7
T_N	Scatter at finite life	-	1:3.7
T_S	Scatter at N=10^8	-	1:1.2

Tab. 4.3: Parameters for RB S/N-curve pancake mill-annealed unnotched

Bimodal microstructure

The bimodal microstructure of the solution treated V-shape leads to a relatively low fatigue strength of 465 MPa at 10^8 load cycles (Fig. 4.22). The scatter (Tab. 4.4) is low, owing to the homogenous bimodal microstructure.

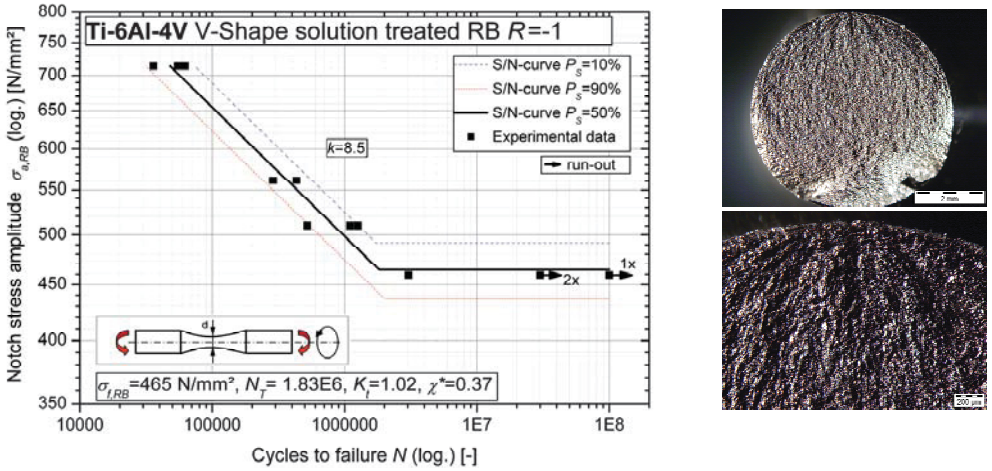

Fig. 4.22: Rotating bending S/N-curve (l) and fracture surface (r) for V-shape solution treated unnotched

Symbol	Description	Unit	Value
σ_f	Fatigue strength at N=10^8	MPa	465
N_T	Cycles at transition	-	1.8E6
k	Slope	-	8.5
T_N	Scatter at finite life	-	1:2.4
T_S	Scatter at N=10^8	-	1:1.1

Tab. 4.4: Parameters for RB S/N-curve V-shape solution treated unnotched

The solution treated and polymer-quenched V-shape shows a significantly higher fatigue strength (Fig. 4.23). The scatter is also very low owing to the complete recrystallization caused by the heat treatment.

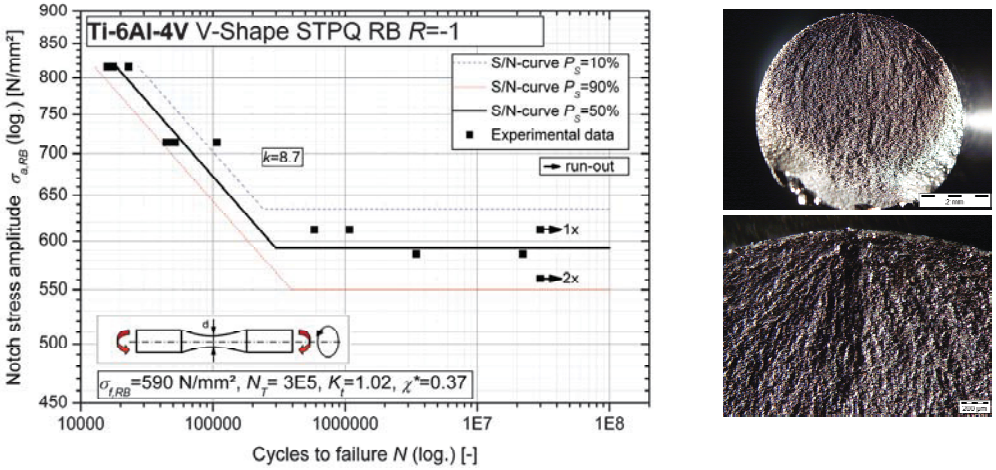

Fig. 4.23: Rotating bending S/N-curve (l) and fracture surface (r) for V-shape STPQ unnotched

Symbol	Description	Unit	Value
σ_f	Fatigue strength at N=10^8	MPa	590
N_T	Cycles at transition	-	3E5
k	Slope	-	8.7
T_N	Scatter at finite life	-	1:2.1
T_S	Scatter at N=10^8	-	1:1.2

Tab. 4.5: Parameters for RB S/N-curve V-shape STPQ unnotched

The solution treated pancake also exhibits a high fatigue limit of 580 MPa, Fig. 4.24. The scatter in the finite life region is higher than those of the solution treated V-shapes and similar to the mill-annealed pancake. This behavior may arise from the inhomogeneous mill-annealed initial microstructure for the subsequent solution treating.

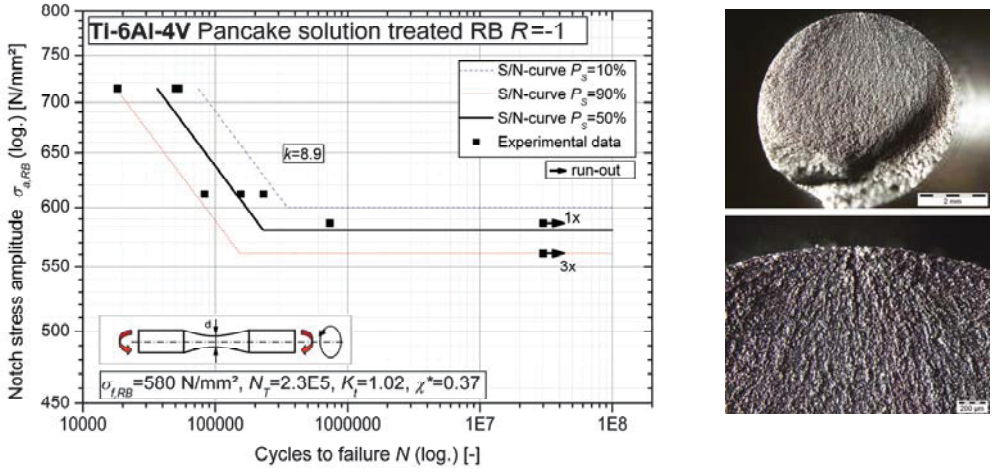

Fig. 4.24: Rotating bending S/N-curve (l) and fracture surface (r) for pancake solution treated unnotched

Symbol	Description	Unit	Value
σ_f	Fatigue strength at N=10^8	MPa	580
N_T	Cycles at transition	-	2.3E5
k	Slope	-	8.9
T_N	Scatter at finite life	-	1:4.2
T_S	Scatter at N=10^8	-	1:1.1

Tab. 4.6: Parameters for RB S/N-curve pancake solution treated unnotched

Equiaxed microstructure

The recrystallization-annealing of pancakes led to a coarse equiaxed microstructure, which results in low fatigue strength, Fig. 4.25. The scatter in the finite life region is high, which is typically for the pancake forgings.

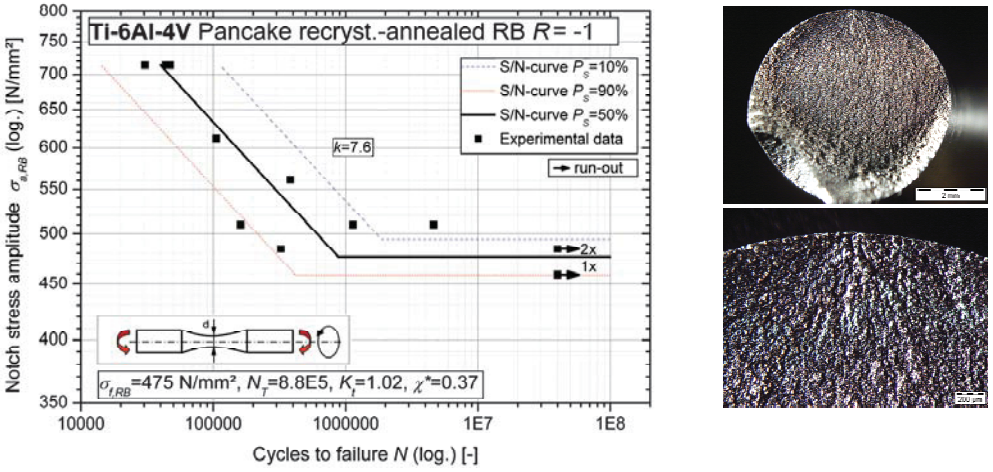

Fig. 4.25: Rotating bending S/N-curve (l) and fracture surface (r) for pancake recryst.-annealed unnotched

Symbol	Description	Unit	Value
σ_f	Fatigue strength at N=10^8	MPa	475
N_T	Cycles at transition	-	8.8E5
k	Slope	-	7.6
T_N	Scatter at finite life	-	1:7.9
T_S	Scatter at N=10^8	-	1:1.1

Tab. 4.7: Parameters for RB S/N-curve pancake recryst.-annealed unnotched

The feedstock billet also exhibits a coarse equiaxed microstructure. The fatigue strength (Fig. 4.26) is hence similar to that of the recrystallization annealed pancake. The scatter is very high for both, finite life and high cycle fatigue region. This arises from the inhomogeneous microstructure of the billet due to missing forming and recrystallization. Furthermore, an anomalous coarse fracture characteristic was observed; similar to those of lamellar microstructures. It can be assumed that this behavior is caused by the macrozones, identified in the micrographs of the feedstock billet, cf. Fig. 3.26.

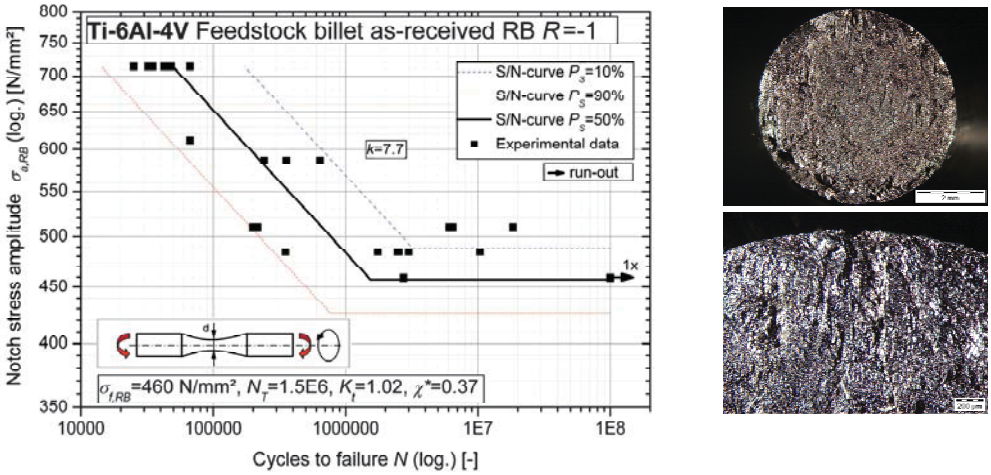

Fig. 4.26: Rotating bending S/N-curve (l) and fracture surface (r) for feedstock billet unnotched

Symbol	Description	Unit	Value
σ_f	Fatigue strength at N=10^8	MPa	460
N_T	Cycles at transition	-	1.5E6
k	Slope	-	7.7
T_N	Scatter at finite life	-	1:12.1
T_S	Scatter at N=10^8	-	1:1.2

Tab. 4.8: Parameters for RB S/N-curve feedstock billet unnotched

Lamellar microstructure

For the purpose of comparison, a beta-annealing was performed on some pancakes, resulting in a lamellar microstructure. It was observed that the fatigue strength is low for both finite and infinite life region, Fig. 4.27. The scatter is comparable to those of pancakes with other heat treatments.

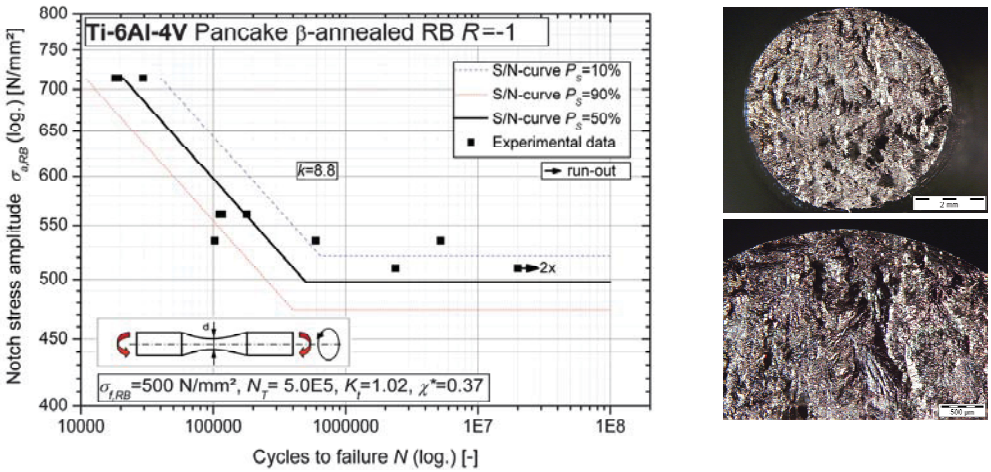

Fig. 4.27: Rotating bending S/N-curve (l) and fracture surface (r) for pancake beta-annealed unnotched

Symbol	Description	Unit	Value
σ_f	Fatigue strength at N=10^8	MPa	500
N_T	Cycles at transition	-	5.0E5
k	Slope	-	8.8
T_N	Scatter at finite life	-	1:3.7
T_S	Scatter at N=10^8	-	1:1.1

Tab. 4.9: Parameters for RB S/N-curve pancake beta-annealed unnotched

Comparison of different microstructures

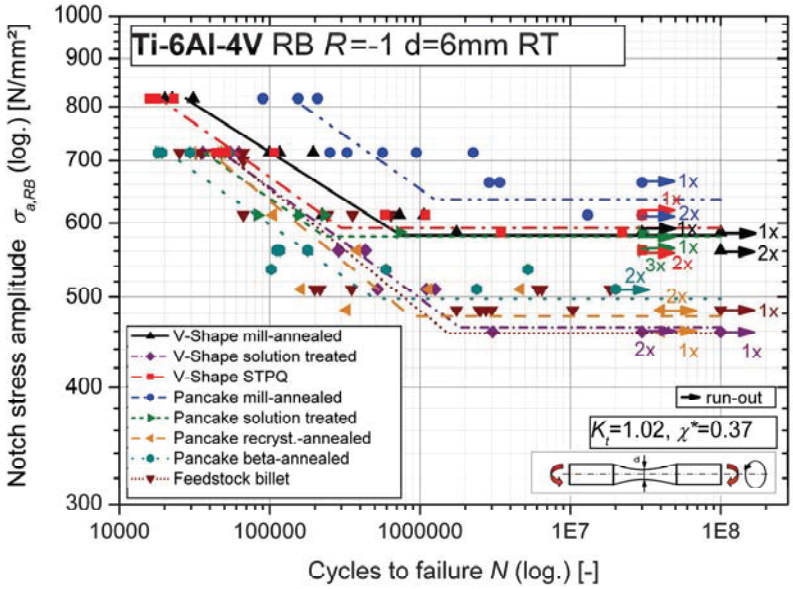

Fig. 4.28: Comparison of rotating bending S/N-curves for Ti-6Al-4V with different microstructures

The comparison of the different rotating bending S/N-curves (Fig. 4.28) shows that the fatigue behavior is noticeably affected by microstructure. All S/N-curves in Fig. 4.28 correspond to a survival probability of 50%. The fatigue strength at 10^8 load cycles varies between 460 and 640 MPa – a difference of 40%. The finite life region also exhibits distinct dependencies with the microstructure. The scatter in the finite life region was different for the two types of forgings. The pancakes exhibit a higher scatter than the V-shapes. This behavior supposably arises from the more homogeneous effective strain distribution and therefore more homogeneous microstructure of the V-shapes at the gauge of the fatigue test specimens. The aim of this research is to define values for local microstructure. Therefore, the scatter for the homogeneous forgings (V-shapes) is taken as a reference. The mill-annealing leads even for the V-shapes to higher scatter due to the incomplete recrystallization. The recommended values for the scatter with respect to the heat treatments are summarized in Tab. 4.10.

Heat treatment	T_N	T_S
Mill-annealing	1:2.8	1:1.15
Solution treating	1:2.4	1:1.15

Tab. 4.10: Scatter in respect of heat treatment

4.1.2.2. SEB fatigue crack growth tests on Ti-6Al-4V with varying microstructure

The characterization of the long crack growth behavior was done with V-notched single edge bending (SEB) specimens (Fig. 3.40) under four-point-bending loading (cf. ASTM E647 [32]) at a Rumul Cracktronic resonant testing rig with a frequency of approximately 140 Hz. The crack length was measured with the potential drop method, cf. Fig. 4.29. Temperature compensation was done with a Pt100 resistance temperature sensor fixed at the specimens near the crack.

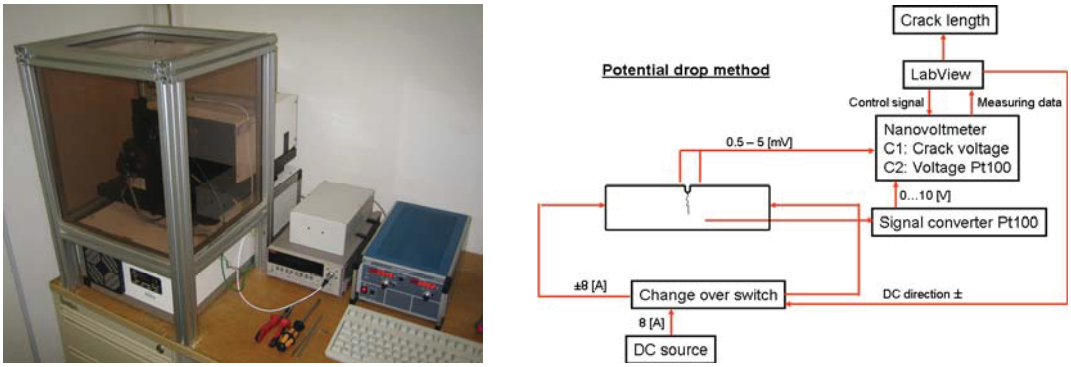

Fig. 4.29: Resonant testing system for long crack growth (l) and scheme of the potential drop method (r)

The measurements were performed for four different stress ratios R (ratio of minimum and maximum stress or stress intensity factor, respectively). The stress intensity factor range ΔK was derived according to linear elastic fracture mechanics for all stress ratios, cf. Equ. (4.7), where $\Delta\sigma$ is the applied stress range, a the crack length and Y the appropriate geometry factor according to Murakami [115].

$$\Delta K = \Delta\sigma\sqrt{\pi\, a}\; Y \qquad \text{Equ. (4.7)}$$

The measurements were finished at 80 MPa√m due to testing rig limitations regarding maximum stress intensity factor range. At least two specimens were tested for each stress ratio and microstructure. The test procedure was constant ΔK-testing for crack initiation up to a crack length of 6 mm, ΔK-decreasing testing from the Paris-region down to the threshold and subsequent ΔK-increasing testing with constant bending moment from the Paris-regime to fracture or testing rig limit. Carboni et al. [46] reported that this testing method could lead to non-conservative threshold values, mainly due to plasticity induced crack closure. Therefore, the size of the plastic zone after the constant ΔK-testing was determined with FE analysis, Fig. 4.30. It was observed that the size of the plastic zone is in the range of the grain size and plasticity-induced crack closure can hence be neglected.

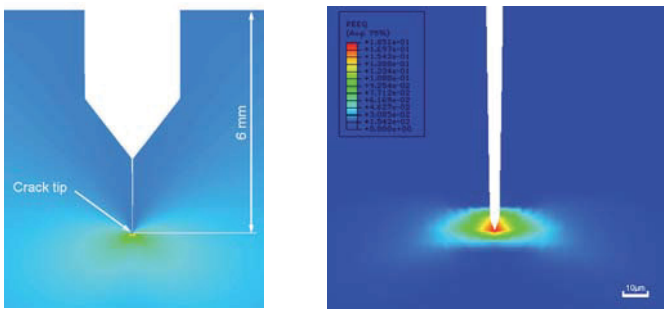

Fig. 4.30: FE analysis of the SEB specimen; stress distribution (l) and plastic equivalent strain at the crack tip (r)

The measured data points were fitted with a new developed four-parametric equation, Equ. (4.8), where a is the crack length, N the number of load cycles, ΔK the range of stress intensity factor and p and q the parameters resulting from the fitting. The value with the lowest crack growth rate was thereby weighted.

$$\log\frac{da}{dN} = \frac{p_1 \cdot \log\Delta K + p_2}{(\log\Delta K)^2 + q_1 \cdot \log\Delta K + q_2} \qquad \text{Equ. (4.8)}$$

This fit results in an ideal representation of the data points in the near-threshold and Paris-region and is hence capable for the visual comparison of the varying microstructures. The fitting parameters for all microstructures and stress ratios are summarized in the Appendix, Tab. 12.2. Due to the high variation and complex interaction of these parameters, they cannot be used for linking crack growth and stress ratio or microstructure. The Paris-region of the different long crack growth curves was fitted with the Paris-Erdogan-equation [126], Equ. (4.9).

$$\frac{da}{dN} = C \cdot \Delta K^m \qquad \text{Equ. (4.9)}$$

Mill-annealed microstructure

The mill-annealed microstructures of V-shape and pancake lead to a relatively fast long crack propagation and low stress intensity factor thresholds, Fig. 4.31.

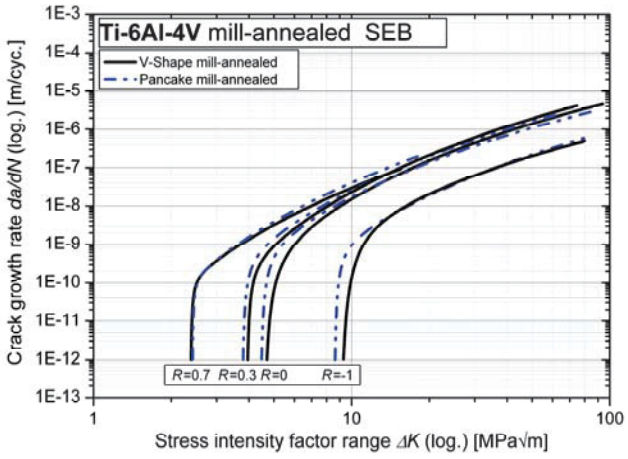

Fig. 4.31: Long crack growth behavior of mill-annealed Ti-6Al-4V

V-Shape MA	R=-1	R=0	R=0.3	R=0.7
C [m/(Cyc. MPa√m)]	4.66E-10	1.34E-10	1.43E-10	2.10E-11
m [-]	1.5	2.3	2.4	3.0
ΔK_{th} [MPa√m]	9.4	5.1	4.0	2.4

Tab. 4.11: Fatigue crack growth parameters for V-shape mill-annealed

Pancake MA	*R*=-1	*R*=0	*R*=0.3	*R*=0.7
C [m/(Cyc. MPa√m)]	7.71E-11	1.25E-10	1.60E-10	1.26E-11
m [-]	2.0	2.3	2.4	3.4
ΔK_{th} [MPa√m]	8.8	4.8	3.8	2.4

Tab. 4.12: Fatigue crack growth parameters for pancake mill-annealed

Bimodal microstructure

All bimodal microstructures show an identical crack propagation behavior at a stress ratio R = -1, Fig. 4.32. At higher stress ratios, a difference in the near-threshold region was observable with respect to microstructure.

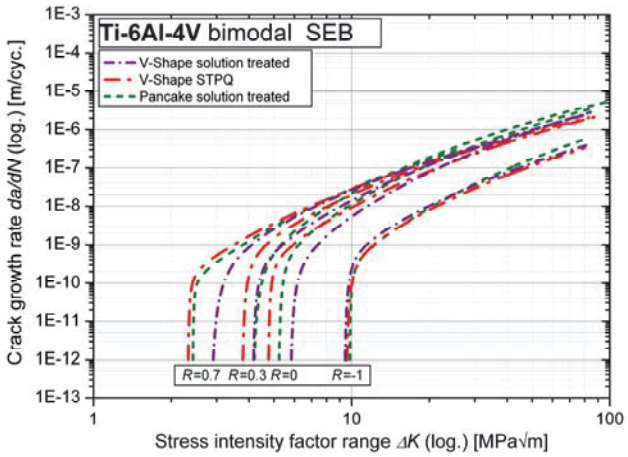

Fig. 4.32: Long crack growth behavior of bimodal Ti-6Al-4V

V-Shape ST	*R*=-1	*R*=0	*R*=0.3	*R*=0.7
C [m/(Cyc. MPa√m)]	1.30E-11	9.96E-11	2.94E-10	1.30E-10
m [-]	2.4	2.3	2.0	2.4
ΔK_{th} [MPa√m]	9.5	5.6	4.1	2.9

Tab. 4.13: Fatigue crack growth parameters for V-shape solution treated

V-Shape STPQ	*R*=-1	*R*=0	*R*=0.3	*R*=0.7
C [m/(Cyc. MPa√m)]	3.20E-11	8.08E-11	1.61E-10	2.30E-12
m [-]	2.1	2.3	2.2	3.8
ΔK_{th} [MPa√m]	9.2	4.9	3.8	2.3

Tab. 4.14: Fatigue crack growth parameters for V-shape STPQ

Pancake ST	*R*=-1	*R*=0	*R*=0.3	*R*=0.7
C [m/(Cyc. MPa√m)]	1.75E-11	1.60E-10	1.98E-10	1.43E-10
m [-]	2.3	2.2	2.3	2.4
ΔK_{th} [MPa√m]	9.5	5.6	4.3	2.6

Tab. 4.15: Fatigue crack growth parameters for pancake solution treated

Equiaxed microstructure

The comparison of the long crack growth behavior of pancake recrystallization-annealed and the feedstock billet in as-received condition shows distinct differences in the near-threshold region, but almost identical behavior in the Paris-regime. These differences may be caused by variations in the microstructure; the α-grain size is the same for both materials but the connectivity is completely different (cf. Tab. 3.5). The macrozones in the microstructure of the feedstock billet are believed to cause a roughening of the fracture surface, increased roughness-induced crack closure and higher long crack growth thresholds.

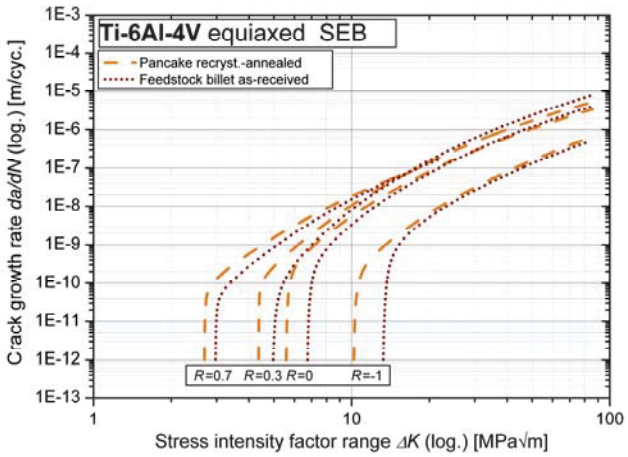

Fig. 4.33: Long crack growth behavior of equiaxed Ti-6Al-4V

Pancake RA	*R*=-1	*R*=0	*R*=0.3	*R*=0.7
C [m/(Cyc. MPa√m)]	1.74E-10	1.44E-10	1.03E-10	1.83E-11
m [-]	1.8	2.2	2.4	3.1
ΔK_{th} [MPa√m]	10.2	5.8	4.6	2.8

Tab. 4.16: Fatigue crack growth parameters for pancake recryst.-annealed

Feedstock billet	*R*=-1	*R*=0	*R*=0.3	*R*=0.7
C [m/(Cyc. MPa√m)]	7.64E-11	1.25E-10	2.07E-10	2.05E-11
m [-]	1.9	2.3	2.3	3.1
ΔK_{th} [MPa√m]	12.9	7.0	5.0	3.0

Tab. 4.17: Fatigue crack growth parameters for feedstock billet

Lamellar microstructure

The lamellar microstructure of the beta-annealed pancake results in relatively slow crack propagation rates and stress intensity factor thresholds for all tested stress ratios, Fig. 4.34.

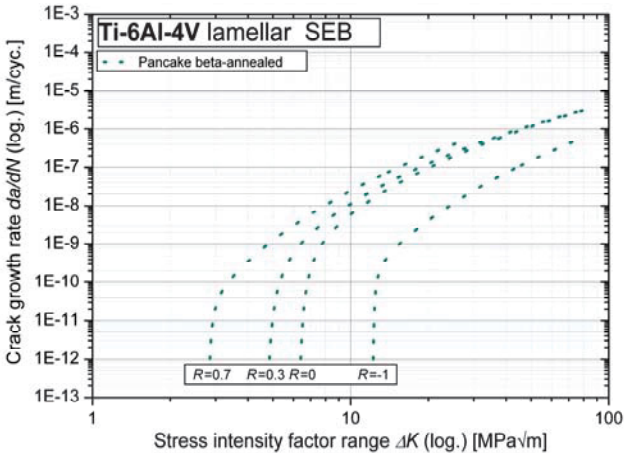

Fig. 4.34: Long crack growth behavior of lamellar Ti-6Al-4V

Pancake BA	*R*=-1	*R*=0	*R*=0.3	*R*=0.7
C [m/(Cyc. MPa√m)]	6.87E-12	1.38E-10	1.05E-09	3.88E-10
m [-]	2.6	2.2	1.7	2.1
ΔK_{th} [MPa√m]	11.5	6.5	4.8	2.9

Tab. 4.18: Fatigue crack growth parameters for pancake beta-annealed

Comparison of different microstructures

Fig. 4.35 shows the long crack growth behavior of all tested microstructures. Thereby, the equiaxed microstructure of the feedstock billet results in the slowest crack propagation rate, whereas the mill-annealed microstructure of the pancake causes relatively fast long crack growth.

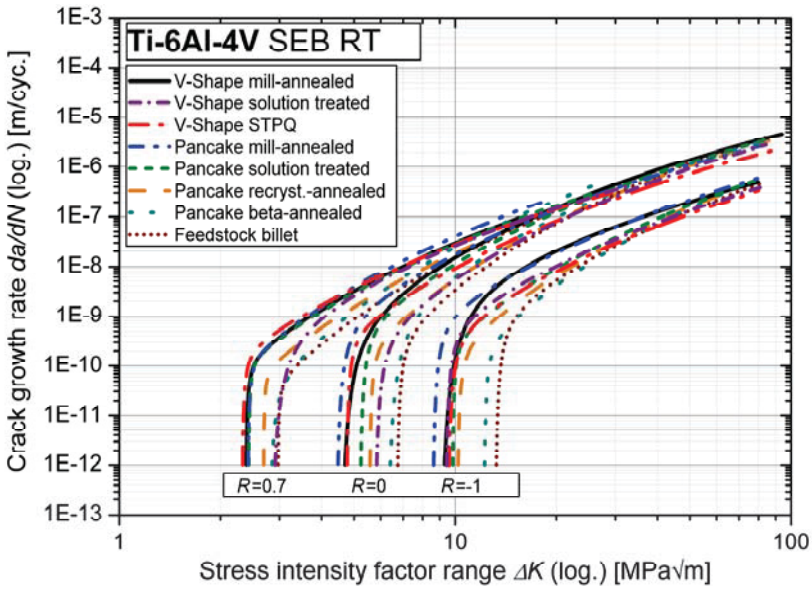

Fig. 4.35: Comparison of long crack growth in Ti-6Al-4V with different microstructures

Crack growth was found down to propagation rates of 10^{-12} m/cycle which was also reported by Stanzl-Tschegg [161]. Above crack growth rates of approximately 10^{-7} m/cycle, all investigated microstructures show almost the same crack propagation behavior. Distinct differences were found in the near-threshold region in respect of the stress ratio owing to crack closure effects, cf. [73]. Both mill-annealed microstructures lead to an anomalous high crack growth rate in the region between 10^{-9} m/cycle and 10^{-7} m/cycle. The ranking of the different microstructures regarding crack propagation is not affected by the stress ratio.

The influence of roughness induced crack closure on the near-threshold region is qualitatively observable in a comparison of the different fracture surfaces for a certain stress ratio, cf. Fig. 4.36 ($R = 0$, crack propagation direction from left to right). It was observed that the highest fracture surface roughness (darker regions of the fracture surfaces in Fig. 4.36) arise from crack propagation in the near-threshold region. The same behavior was found at flat specimens used for physically short crack propagation tests, what will be discussed later.

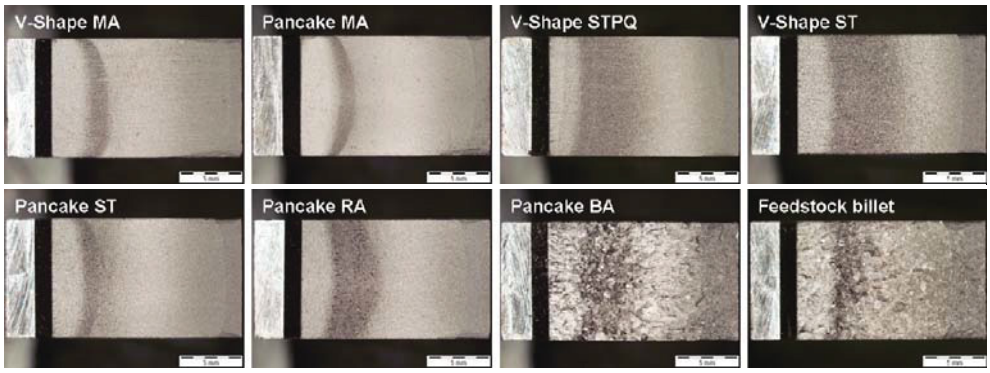

Fig. 4.36: Fracture surfaces of SEB specimens tested with a stress ratio of zero

Roughness measurements were performed with a confocal laser-scanning microscope (LEXT) in the region of near-threshold crack propagation of the fracture surfaces. It was observed that the center-line average roughness R_a correlates with the primary α-grain size of equiaxed and bimodal microstructures, respectively (Fig. 4.37).

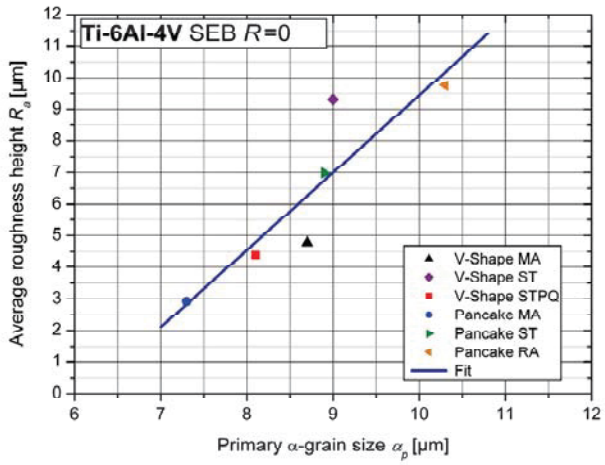

Fig. 4.37: Correlation between primary α-grain size and center-line average roughness

The microstructure of the mill-annealed V-shape led to a lower average roughness than predicted by the linear correlation. In contrast, the solution treated V-shape exhibited a higher fracture surface roughness, what can be ascribed to the contribution of the large (α+β)-colonies to the fracture surface roughness. This was confirmed with scanning electron microscopy of the SEB fracture surfaces and will be discussed below.
The average roughness height of the fracture surface can also be linked to the stress intensity factor threshold (Fig. 4.38). This linear correlation is especially in accordance with the data points for the (important) forged equiaxed and bimodal microstructures; the maximum deviation is 4%. A higher scatter (10%) is observable for feedstock billet and pancake beta-annealed. It can be assumed that the observed macrozones are the reason for the uncommon high stress intensity factor threshold of the equiaxed microstructure of the feedstock billet.

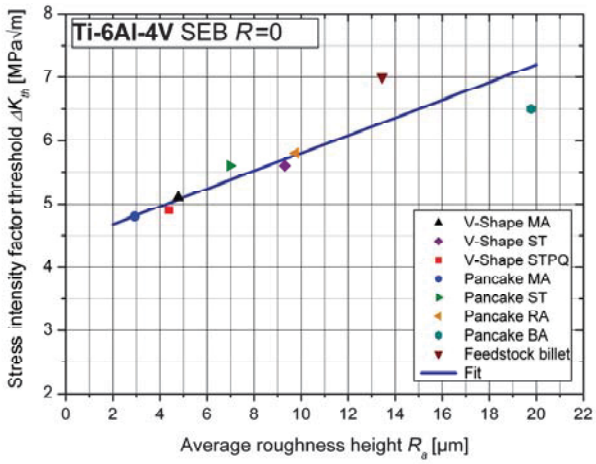

Fig. 4.38: Correlation between stress intensity factor threshold and center-line average roughness

Finally, it can be concluded that the stress intensity factor threshold is primarily influenced by roughness-induced crack closure. From the correlation between fracture surface roughness and primary α-grain size arises therefore a link between stress intensity factor threshold and primary α-grain size. This behavior will be discussed in detail in the chapter "Phenomenological models".

The fracture surfaces were also analyzed with a scanning electron microscope (SEM). The long crack propagation direction relating to these pictures was from the left to the right. They were taken from the middle of SEB specimens (plane strain state); loaded in the lower Paris-region with a stress ratio of zero. Distinct differences are observable owing to the varying microstructures. Fig. 4.39 shows the comparison of the equiaxed microstructures of recrystallization-annealed pancake and feedstock billet.

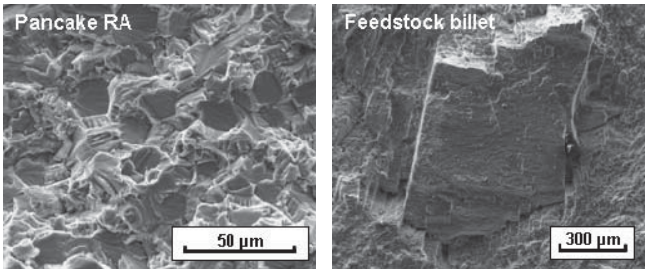

Fig. 4.39: Fracture surface of pancake RA (l) and feedstock billet (r); $R = 0$

Transcrystalline fracture of primary α-grains was determined for the recrystallization-annealed material, what explains the correlation of α-grain size and fracture surface roughness. The anomalous high long crack growth threshold of the feedstock material was ascribed to the observed macrozones, which cause large features at the fracture surface as shown in Fig. 4.39 (r). These features are that large that they were not measured as fracture surface roughness, they belong to waviness. However, they contribute to the roughness-induced crack closure and increase the long crack growth threshold of the feedstock material, cf. Fig. 4.38.
Three transcrystalline fracture planes of the recrystallization-annealed microstructure are shown in Fig. 4.40. The crack propagation direction is again from the left to the right. At first view, the transcrystalline planes seem to exhibit a "river pattern", typically for cleavage fracture, cf. [29].

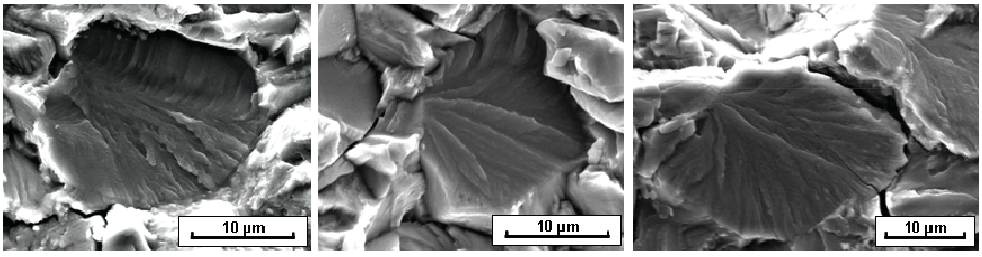

Fig. 4.40: Transcrystalline fracture planes observed in the fracture surface of pancake RA; near-threshold, $R = 0.3$

However, the observed fracture plane patterns show their split-up in the contrary direction with respect to the crack propagation direction as usually observed for cleavage fracture. Following again the analogon of a river, the determined fracture characteristic in Ti-6Al-4V is named "delta pattern", much like a river open out into the ocean.

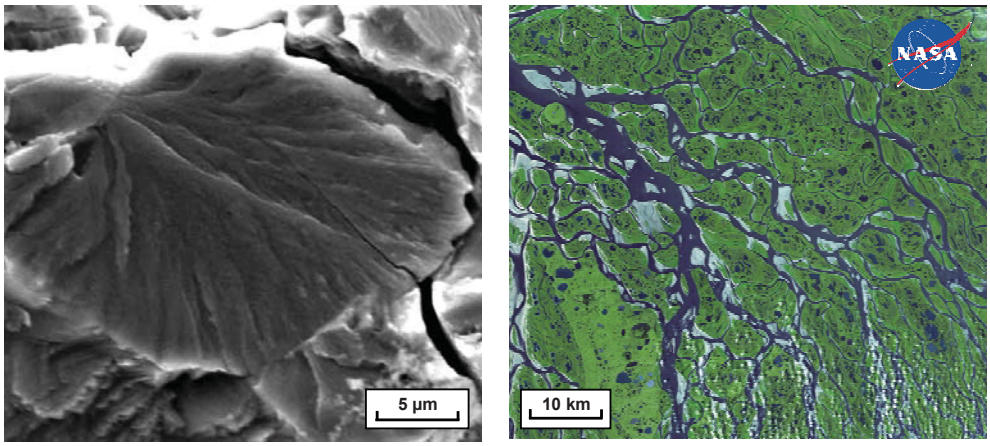

Fig. 4.41: Comparison of "delta pattern" of fractured α-grain (l) and Lena River Delta, Russia [118] (r)

Fig. 4.41 shows the comparison of a "delta pattern" of a transcrystalline fractured primary α-grain (l) and a part of the Lena River Delta in Russia (captured by the Advanced Spaceborne Thermal Emission and Reflection Radiometer (ASTER) on NASA's Terra satellite on July 16, 2005) during the area's short summer. After a 4,400 km journey north from the mountains of south-central Russia, the Lena River fractures into myriad streams that fan out across the tundra and empty into the Arctic Ocean via the Laptev Sea. Its far northern location keeps the Lena River Delta frozen for as long as seven months of the year, but during the short summer, it thaws into a wetland of tremendous ecological importance. Vegetation-covered areas are green, while bright white areas are probably places that were scoured by the annual spring floods. Mudflats and other areas covered by shallow water appear light blue. [118]

Regarding delta pattern, it was assumed that a crack initiates by prismatic slip (owing to the more easily activation, cf. [43]) near a grain boundary (stress raiser), forming the "river" of the delta pattern. Then the crack propagates along a transcrystalline fracture plane, generating the delta pattern by a sort of striation formation. Striations are clearly observable in the left picture of Fig. 4.40, in the upper half of the fracture plane. With reference to Bridier et al. [43], which concluded that crack formation in the finite life region requires a combination of a high Schmid factor in addition to high elastic stiffness, inducing a high tensile stress normal to a basal plane, it was assumed that the observed fracture planes are basal planes.

The striation dimensions of the delta pattern in Fig. 4.40 (l) were measured for determination of the local crack growth rate. The crack growth rate within an α-grain, $6 \cdot 10^{-7}$ m/cyc, was determined to be more than a decade higher than the global crack growth rate of $1 \cdot 10^{-8}$ m/cyc (loading conditions: $R = 0.3$, $\Delta K = 9.5$ MPa√m).

The differences in fracture surface roughness with respect to the stress intensity factor observed with the light optical microscope were also determinable with the SEM, Fig. 4.42. Pictures of the fracture surfaces were taken in the near-threshold crack propagation region and at the beginning of the Paris-regime. The near-threshold crack growth leads to higher surface roughness for both, equiaxed- and bimodal-type microstructures, Fig. 4.42.

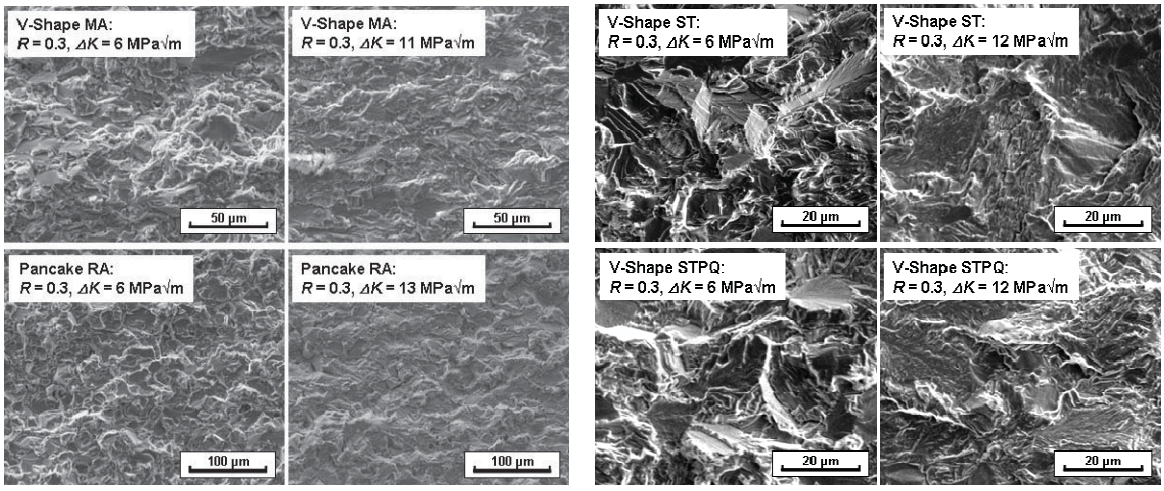

Fig. 4.42: Differences in fracture surface roughness: equiaxed-type (l) and bimodal-type (r) microstructures

Delta patterns were observed in all analyzed microstructures at regions of near-threshold crack propagation, whereby the quantity of delta patterns decreases with increasing (α+β)-content. However, fracture surface analysis of the solution treated pancake revealed that delta pattern formation could also occur in α-lamellae of (α+β)-phase, if their thickness is large enough. In this case, these large transcrystalline fracture planes contribute to crack closure and increase both, fracture surface roughness and long crack propagation threshold, cf. Fig. 4.37.

With respect to the change of fracture surface roughness from near-threshold to Paris-region crack propagation it can be assumed that the lower crack-driving force in the near-threshold region results in crack growth especially in preferable-oriented grains, Fig. 4.43 (l). Starting from an existing crack (1) the stress field in front of the crack tip causes slip and crack formation in a preferable-oriented grain (2). If the stress is high enough, the non-preferable-oriented grain in-between fails (3). This mechanism continues (4), (5).

Therefore, many transcrystalline (supposably basal) fracture planes (delta patterns) can be identified in these fracture surfaces. These fracture planes are located at different heights (with respect to the fracture surface) and are twisted or tilted against each other, and lead hence to a high fracture surface roughness.
In the near-threshold region, the primary α-grain size plays a major role with respect to roughness-induced crack closure. Larger primary α-grains lead to more crack deflection, higher fracture surface roughness and slower crack growth. Therefore, the crack propagation behavior of microstructures with different primary α-grain sizes varies in the near-threshold region.

Crack propagation in the Paris-regime, Fig. 4.43 (r), involves a higher crack-driving force and higher crack growth rates. Therefore, crack growth also occurs in non-preferable oriented grains (2), (4). The near-threshold propagation mechanism discussed before is too slow and is outran by conventional crack growth. This leads to a decreased fracture surface roughness. This mechanism was confirmed by physically short crack growth observations and will be discussed in the next chapter. It can be supposed that this behavior is the reason for the congruent crack growth curves in the Paris regime for different isotropic equiaxed and bimodal microstructures.

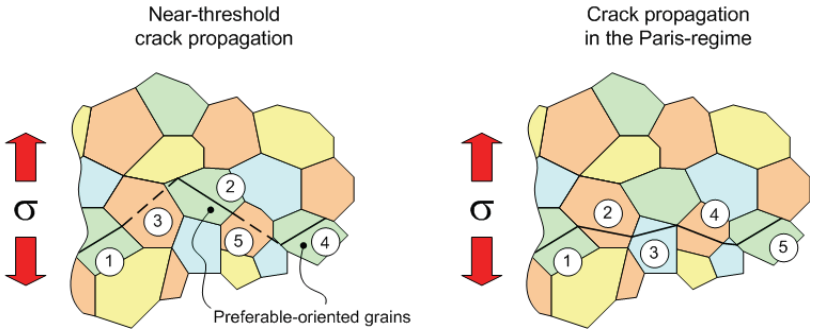

Fig. 4.43: Crack propagation in the near-threshold region (l) and in the Paris-region (r)

4.1.2.3. Short crack growth

Crack initiation and short crack propagation are the determining factors of fatigue in the finite life region. With respect to fatigue of specimens, long crack propagation is negligible, due to the small dimensions of the fatigue tests specimens. Even for forgings, the fraction of long crack growth phase relating to total lifetime is usually small. It is hence important to characterize the short crack growth with respect to microstructure. Physically short crack growth tests were done to determine the influence of initial crack length on the fatigue behavior. Microstructurally short crack propagation tests were performed on Ti-6Al-4V with three different microstructures, to analyze the crack initiation and propagation behavior with respect to microstructural features.

Physically short crack propagation tests on mill-annealed Ti-6Al-4V

If a crack is short (possibly microstructurally short) in crack propagation direction and long perpendicular to the crack propagation direction, it can be classified as physically short. An influence of microstructure on the global crack propagation behavior can be excluded.

Tension/compression fatigue tests were performed with three different stress ratios R (-1, 0 and 0.3) on a servo-hydraulic test stand (Fig. 4.45) at room temperature and ambient air with a testing frequency of 30 Hz.

Plane short crack growth (SCG) specimens (cf. Fig. 3.41) were used, provided with wire eroded initial cracks with a width of 0.04 mm and an initial crack length a_0 of 0.2 or 0.4 mm, respectively (Fig. 4.44).

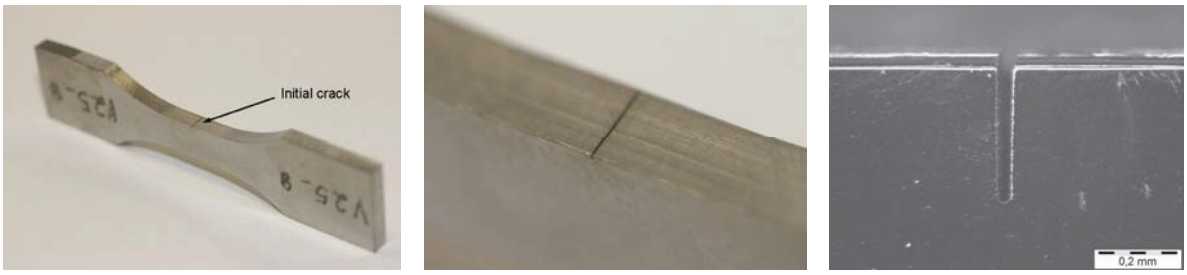

Fig. 4.44: Position of the initial crack on the flat specimen (l, c) and LOM picture of an initial crack (r)

The measurement of the short crack propagation was done with a purpose developed camera device. A compact, digital progressive charge-coupled device (CCD) monochrome area scan camera (JAI CM-140 GE) with 1380 x 1040 pixel resolution and eight-fold magnification (Linos macro CCD lens) was used in combination with dark field illumination (Fig. 4.45). This illumination technique capitalizes on oblique illumination to enhance contrast of surface defects. The crack appears hence bright with dark background (Fig. 4.46). The specimens were polished and ultrasonic cleaned to avoid light scatter due to surface roughness or impurities. The fatigue tests were interrupted after certain load cycles to take a picture of the crack with the camera system; then the fatigue tests were continued. This procedure was repeated until fracture.

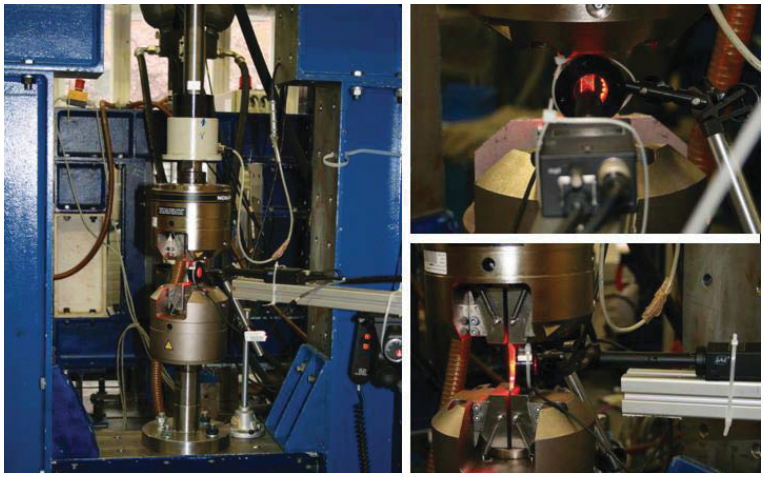

Fig. 4.45: Hydraulic test stand (l) and camera system with dark field illumination (r)

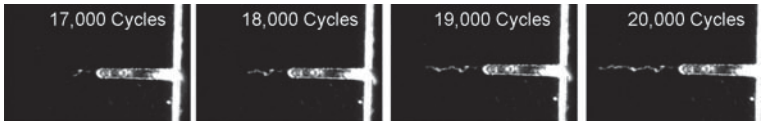

Fig. 4.46: Crack propagation at R = -1 for a_0 = 0.4 mm

The crack initiation phase was determined for all stress ratios. Thereby, the cycles until first crack propagation detection in the notch root (crack elongation $\Delta a \approx 0.02$ mm) were related to the cycles to failure. It was observed that the average crack initiation phase was 25% of the total life. This indicates that the wire eroded initial cracks can be classified as severe crack-like notches.

The plastic zone near the crack tip is small in Ti-6Al-4V, cf. Fig. 4.30. The application of linear elastic fracture mechanics is hence possible. For the determination of the short crack growth curves, the stress intensity factor was chosen according to Murakami [114], Equ. (4.10). The crack length was measured with the camera system explained before.

$$\Delta K_I = \Delta\sigma\sqrt{\pi a}\cdot\left(1.12-0.231\left(\frac{a}{W}\right)+10.55\left(\frac{a}{W}\right)^2-21.72\left(\frac{a}{W}\right)^3+30.39\left(\frac{a}{W}\right)^4\right) \qquad \text{Equ. (4.10)}$$

The physically short crack propagation results were compared with the long crack growth curves (cf. Fig. 4.31) obtained from single edge bending tests, Fig. 4.47. It was observed that the physically short crack growth data and long crack growth curves match for all three tested stress ratios. The physically short cracks do not grow faster than the long cracks, and no crack propagation was observed beneath the long crack growth threshold. A higher scatter of crack growth data was determined for the short cracks. This can be attributed to the type of crack length measurement. The crack length was measured with the camera system on the surface of the specimens. The influence of the local microstructure in the surface region hence affects the measured crack growth rate especially in the near-threshold region, where stress intensity factor and crack driving force are small. Additionally, it can be assumed that the transition of crack propagation mode (from Paris-region to near-threshold as explained in the chapter before) causes local variability of crack growth rate.

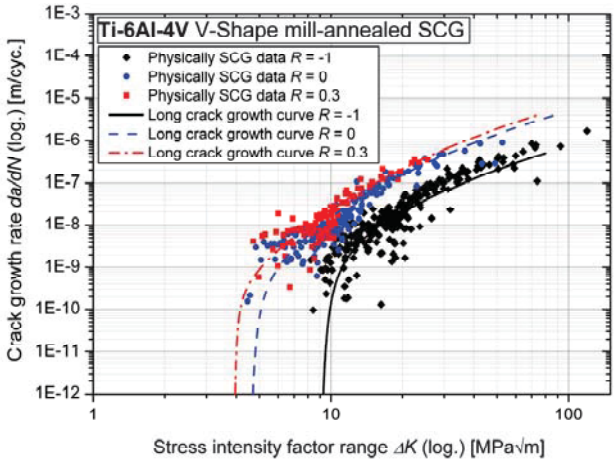

Fig. 4.47: Comparison of physically short crack growth data and long crack growth curves

The cycles to failure of the flat specimens used for the measurement of the short crack growth were also utilized for S/N-curve determination, Fig. 4.48 to Fig. 4.53 (l). The evaluation of the S/N-curves in the finite life region was based on the logarithmic normal distribution. The high cycle fatigue strengths at 10^7 load cycles were determined according to the *arcsin√P*-method [55]. Due to the limited specimen lot sizes, the fatigue limit and especially the scatter are not statistically firm. The fracture surfaces were analyzed with a stereo light optical microscope (Olympus SZX12). One exemplary picture (11.2x magnification) of an according fracture surface is shown for each stress ratio and initial crack length, Fig. 4.48 to Fig. 4.53 (r). The initial crack site is located at twelve o'clock position in all pictures.

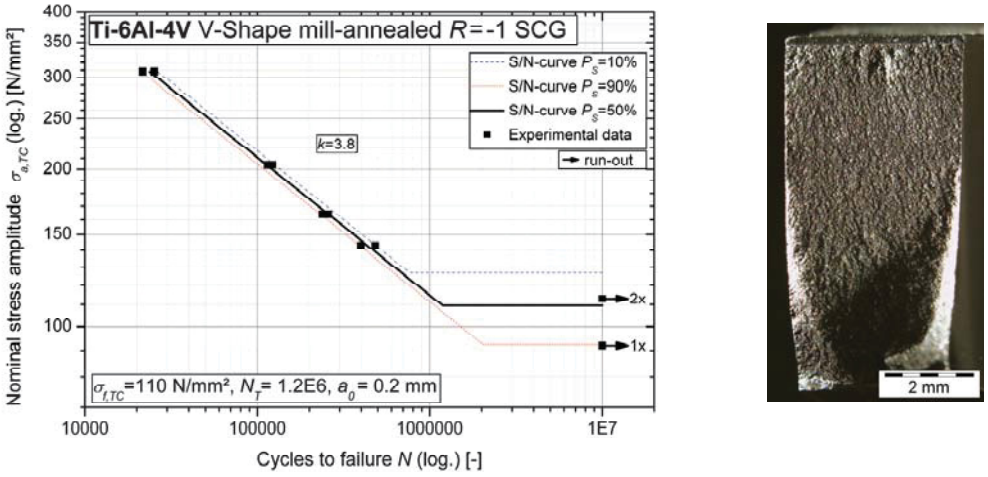

Fig. 4.48: TC S/N-curve (l) and fracture surface (r) for plane SCG specimens, R = -1 and a_0 = 0.2 mm

Symbol	Description	Unit	Value
σ_f	Fatigue strength at N=10^8	MPa	110
N_T	Cycles at transition	-	1.2E6
k	Slope	-	3.8
T_N	Scatter at finite life	-	1:1.2
T_S	Scatter at N=10^8	-	1:1.4

Tab. 4.19: Parameters of TC S/N-curve for SCG specimens, R = -1 and a_0 = 0.2 mm

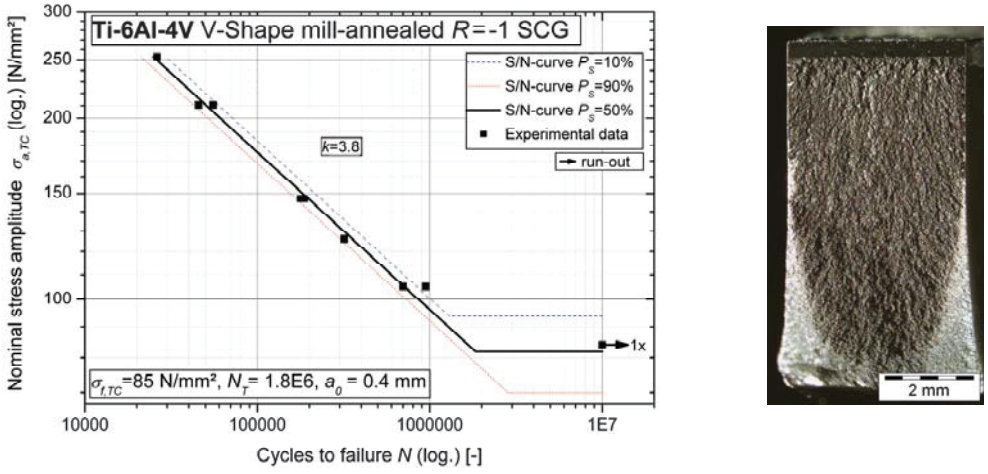

Fig. 4.49: TC S/N-curve (l) and fracture surface (r) for plane SCG specimens, R = -1 and a_0 = 0.4 mm

Symbol	Description	Unit	Value
σ_f	Fatigue strength at N=10^8	MPa	85
N_T	Cycles at transition	-	1.8E6
k	Slope	-	3.8
T_N	Scatter at finite life	-	1:1.4
T_S	Scatter at N=10^8	-	1:1.3

Tab. 4.20: Parameters of TC S/N-curve for SCG specimens, R = -1 and a_0 = 0.4 mm

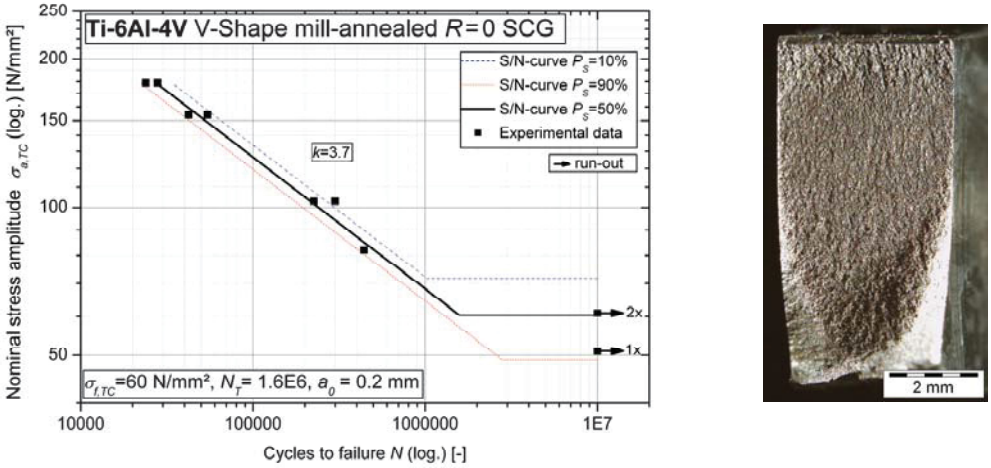

Fig. 4.50: TC S/N-curve (l) and fracture surface (r) for plane SCG specimens, $R = 0$ and $a_0 = 0.2$ mm

Symbol	Description	Unit	Value
σ_f	Fatigue strength at N=10^8	MPa	60
N_T	Cycles at transition	-	1.6E6
k	Slope	-	3.7
T_N	Scatter at finite life	-	1:1.5
T_S	Scatter at N=10^8	-	1:1.5

Tab. 4.21: Parameters of TC S/N-curve for SCG specimens, $R = 0$ and $a_0 = 0.2$ mm

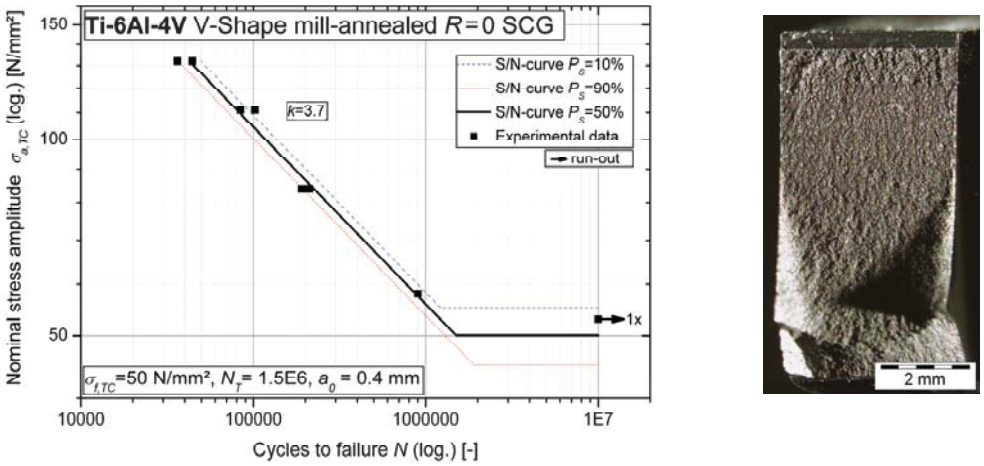

Fig. 4.51: TC S/N-curve (l) and fracture surface (r) for plane SCG specimens, $R = 0$ and $a_0 = 0.4$ mm

Symbol	Description	Unit	Value
σ_f	Fatigue strength at N=10^8	MPa	50
N_T	Cycles at transition	-	1.5E6
k	Slope	-	3.7
T_N	Scatter at finite life	-	1:1.4
T_S	Scatter at N=10^8	-	1:1.2

Tab. 4.22: Parameters of TC S/N-curve for SCG specimens, $R = 0$ and $a_0 = 0.4$ mm

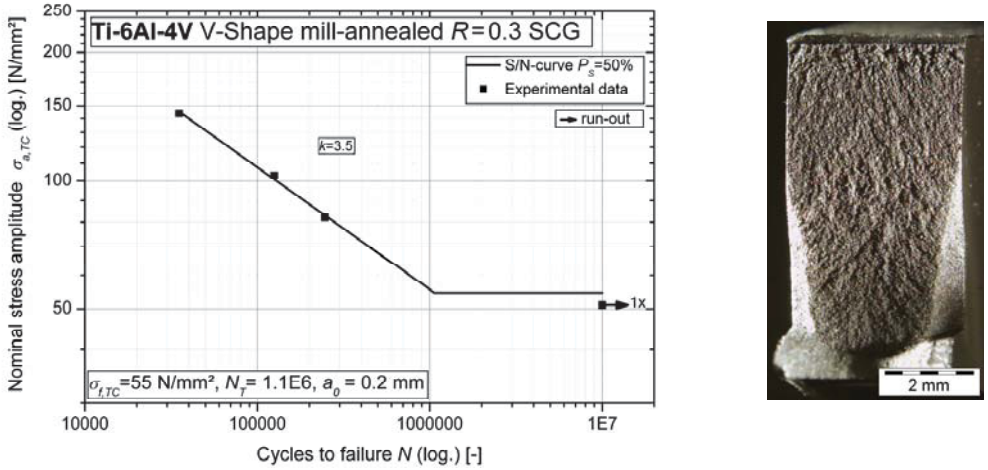

Fig. 4.52: TC S/N-curve (l) and fracture surface (r) for plane SCG specimens, R = 0.3 and a_0 = 0.2 mm

Symbol	Description	Unit	Value
σ_f	Fatigue strength at N=10^8	MPa	55
N_T	Cycles at transition	-	1.1E6
k	Slope	-	3.5
T_N	Scatter at finite life	-	-
T_S	Scatter at N=10^8	-	-

Tab. 4.23: Parameters of TC S/N-curve for SCG specimens, R = 0 and a_0 = 0.2 mm

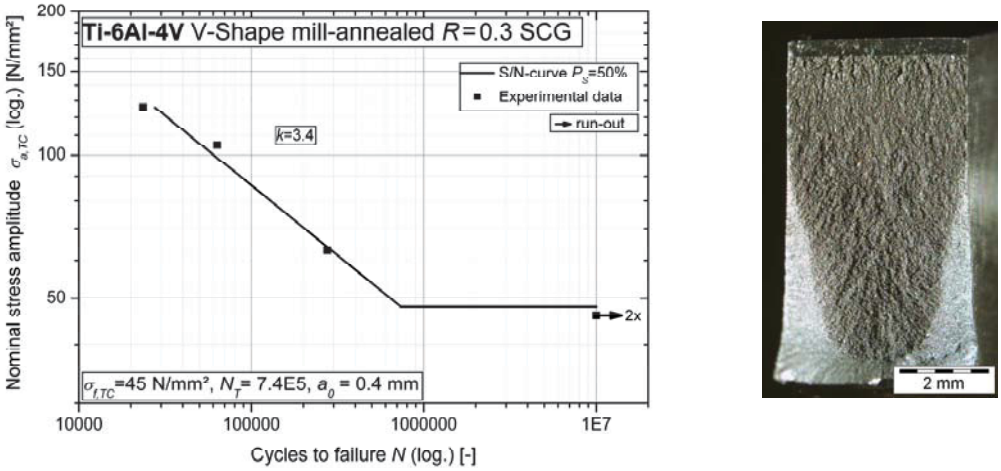

Fig. 4.53: TC S/N-curve (l) and fracture surface (r) for plane SCG specimens, R = 0.3 and a_0 = 0.4 mm

Symbol	Description	Unit	Value
σ_f	Fatigue strength at N=10^8	MPa	45
N_T	Cycles at transition	-	7.4E5
k	Slope	-	3.4
T_N	Scatter at finite life	-	-
T_S	Scatter at N=10^8	-	-

Tab. 4.24: Parameters of TC S/N-curve for SCG specimens, R = 0.3 and a_0 = 0.4 mm

The tension/compression S/N-curves for different stress ratios and initial crack lengths are compared in Fig. 4.54. It was observed that the slope of the S/N-curves in the finite life region is very high (typical for severe notches, $k \approx 3.7$) and almost identical for all stress ratios and initial crack lengths. Both, the ratio of the fatigue strengths at 10^5 load cycles and the ratio of the fatigue limits for initial crack length 0.2 mm to initial crack length 0.4 mm approximate 1.2 for the three investigated stress ratios.

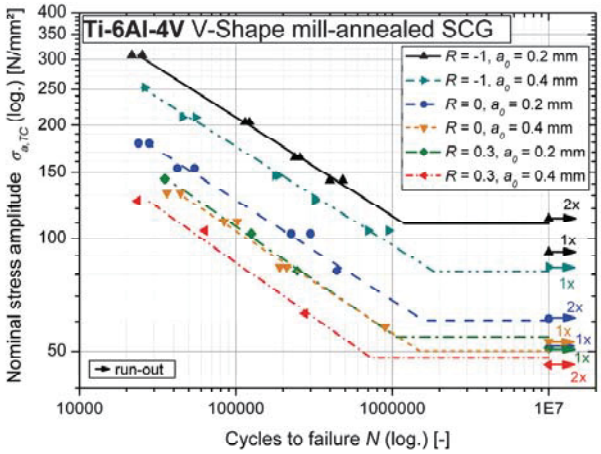

Fig. 4.54: Comparison of S/N-curves at different stress ratios with two different initial crack lengths

The fracture surfaces' roughness of the flat specimens showed the behavior known from the single-edge bending specimens. The first millimeter of the fracture surface exhibits a higher fracture surface roughness owing to near-threshold crack propagation, Fig. 4.55. The explanation for this transition of crack growth mode was already discussed in the previous chapter.

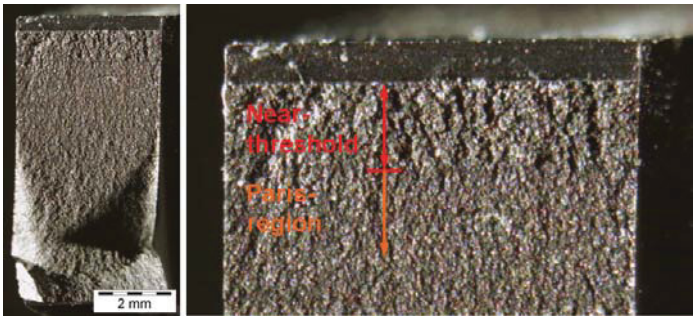

Fig. 4.55: Change in fracture surface roughness of a mill-annealed flat specimen, $R = 0$, $a_0 = 0.4$ mm

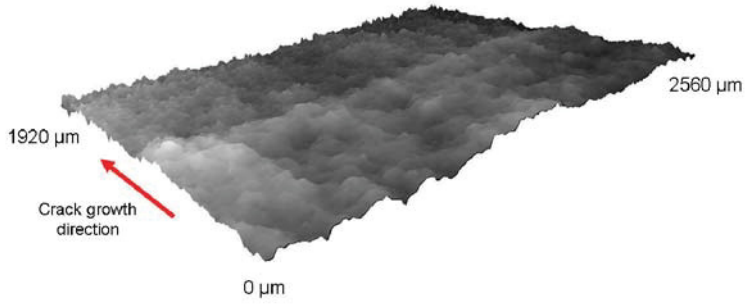

Fig. 4.56: Change in fracture surface topography of a mill-annealed flat specimen, $R = 0$, $a_0 = 0.4$ mm

The topography of this transition region was also analyzed with a confocal laser-scanning microscope, Fig. 4.56 (the crack propagation direction is marked with an arrow). It was determined that the center-line average roughness R_a decreases abruptly from 4.5 µm to 3.4 µm.

This transition is sharp for the mill-annealed microstructure, which was also determined at the fracture surfaces of the single edge bending specimens. This can be attributed to the high primary α-content of the mill-annealed microstructure, because the near-threshold fracture surface roughness is controlled by the primary α-grain size. For microstructures with less primary α-grains this transition is fuzzy, which is confirmed by the fracture surfaces of the single edge bending specimens for different microstructures, cf. Fig. 4.36. The transition from rough (dark) surface to smoother (bright) surface is thereby, for example, sharp for the mill-annealed pancake ($C_{\alpha+\beta}$ = 31%) and fuzzy for the solution treated and polymer-quenched V-shape ($C_{\alpha+\beta}$ = 61%). This may also be one reason for the influence of the (α+β)-content on the finite life fatigue strength of bimodal microstructures, what will be discussed in the chapter "Phenomenological models".

The fracture surface roughness of the physically short crack growth specimens was significantly reduced at a certain transition crack length; depending on the stress ratio and independent from the initial crack length. It was determined that these transition crack lengths correspond to a certain crack growth rate, namely $7 \cdot 10^{-8}$ m/cyc. This finding confirms the approach of crack growth mode transition discussed above. Furthermore, it was observed that the physically short crack growth curves for different stress ratios, cf. Fig. 4.47, exhibit a knee at this transition crack growth rate, owing to a stronger decrease of crack growth rate with decreasing stress intensity factor in the near-threshold crack propagation mode. The scatter of the physically short crack growth data increase also abruptly at this transition crack growth rate.

Microstructurally short crack growth in Ti-6Al-4V

A crack is called microstructurally short if the crack length is in the range of a characteristic microstructural dimension (micro-crack limiting obstruction distance d_o). Microstructurally short cracks have to be short in all dimensions (maximum crack length ~ 5-10 d_o) and their propagation behavior is significantly influenced by microstructure.

The crack initiation and short crack growth in Ti-6Al-4V with three different microstructures were characterized according to the method presented by Wagner and Lütjering [181]. Thereby, hourglass specimens were electrolytically polished to get a smooth surface and to remove residual stresses from machining. For crack initiation, the polished specimens ($d \approx 5.85$ mm) were loaded under rotating bending (R = -1, ambient air and room temperature) with a stress amplitude of 750 MPa for 4,000 load cycles. After this crack initiation phase, the specimens were etched (composition of the used etchant see Tab. 3.3) for visualization of the microstructure and for accentuation of the initiated cracks.
For evaluation of the crack length with a confocal laser-scanning microscope (LEXT), crack opening was necessary. Therefore, a pretensioning device was designed for static loading of the round specimens during the microscopy, cf. Fig. 4.57. The initiated cracks were searched on eight positions (every 45°) on the specimens. Over 50 initiated cracks were found on each position on a specimen. Therefore, several cracks were selected randomly to get a sum of approximately 80 cracks per specimen for the observation of the short crack growth. Then the fatigue tests were continued at the same stress level and interrupted after a given number of cycles (ΔN = 1,000) for measurement of the crack propagation.

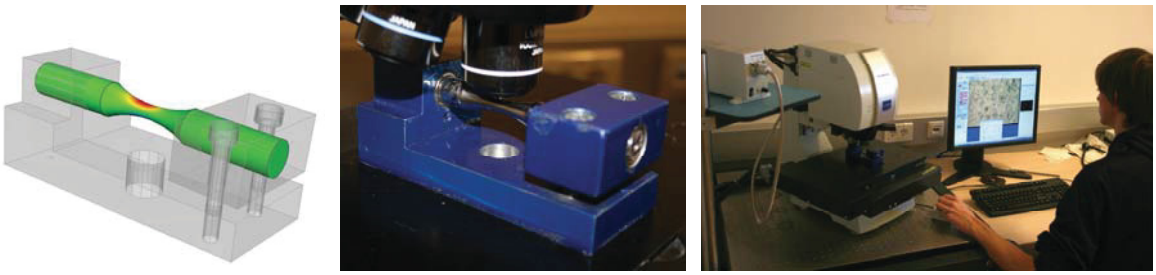

Fig. 4.57: FE-model (l), real pretensioning device (c) and the confocal laser-scanning microscope (r)

The comparison of the initial crack lengths after 4,000 load cycles (stress amplitude 750 MPa) is shown in Fig. 4.58 (l). It was assumed that the crack length distribution follows a Weibull curve. The peak value of the initial crack length distribution correlates with the microstructural parameters primary α-grain size and colony length. The crack initiation in the equiaxed-type microstructures ($C_{\alpha+\beta} \leq 20\%$, this definition will be discussed in the next chapter) of the recrystallization annealed pancakes and mill-annealed V-shapes is dominated by the primary α-grain size. The ratio of initial crack length (peak value of the Weibull distribution) and the primary α-grain size is 1.7 for both equiaxed-type microstructures. In bimodal-type microstructures ($C_{\alpha+\beta} > 25\%$), in this case in those of the solution treated pancakes, crack initiation occurs primarily in (α+β)-phase. The initial crack length can hence be linked with the colony length. The ratio of this microstructural size and initial crack length is again 1.7; analogical to the findings for the equiaxed-type microstructures. This value of 1.7 indicates that the observed "initial cracks" were already propagated into adjacent grains. This causes a shift of the Weibull-distributions to longer crack lengths. It is remarkable that the recrystallization-annealed microstructure exhibits a relatively large portion (12%) of noticeably longer cracks. It is unclear, whether they belong to the initial crack distribution, or if their initiation phase was completed and considerably exceeded after 4,000 load cycles.

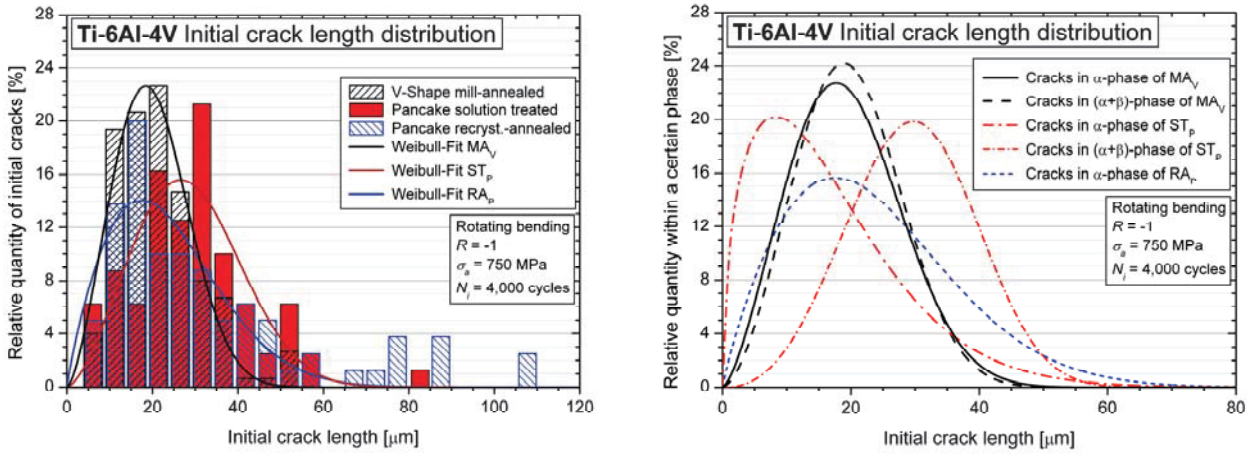

Fig. 4.58: Initial crack length distribution: total (l) and separated for α- and (α+β)-phase (r)

In the mill-annealed microstructure ($C_{\alpha+\beta} = 20.3\%$), 60% of the cracks initiated in (α+β)-phase. The higher (α+β)-content of the solution treated microstructure ($C_{\alpha+\beta} = 50.9\%$) increases the percentage of initial cracks in (α+β)-phase to 80%.
The crack length distributions were separated for α- and (α+β)-phase, Fig. 4.58 (r). It was observed that the crack length distributions in both phases are very similar for the mill-annealed microstructure.

In contrast, the distributions for the solution treated pancake are significantly different. Thereby, the distribution of the initial cracks in the α-phase exhibits a maximum at a crack length approximating the primary α-grain size. This means that they were not significantly propagated after 4,000 load cycles. However, those cracks which initiated in (α+β)-phase were considerably longer owing to two facts: the colony length is larger than the primary α-grain size and the initial cracks were already propagated.

The orientation of the initial cracks with regard to the load direction is presented in Fig. 4.59 (r). It was determined that the separation in α- and (α+β)-phase does not affect these distributions. It has to be mentioned that the crack orientation can only be measured at the surface (2D information). Therefore, the unknown third (radial) dimension has to be included theoretically in these advisements regarding crack initiation, considering the texture-free material with a huge amount of grains in the highest loaded region.
Schmid's law (cf. e.g. [71]) is given in Equ. (4.11); the according delineation is shown in Fig. 4.59 (l). Thereby, φ is the angle between the normal vector $\underline{n}$ of a cutting plane (slip plane) and the load direction, λ the angle between slip direction $\underline{d}$ and load direction, F the applied force, and m the so-called Schmid factor. The vectors $\underline{n}$ and $\underline{d}$ have to be perpendicular. This leads to the following inequation for the Schmid factor: $0 \leq |m| \leq 0.5$. The maximum possible shear stress τ_{max} is hence half the applied normal stress σ.

$$\tau = \sigma \cdot \cos\lambda \cdot \cos\varphi = \sigma \cdot m \qquad \text{Equ. (4.11)}$$

The maximum shear stress plane (φ = 45°) is drawn in Fig. 4.59 (l). It can be observed that surface cracks which lay on the maximum shear stress plane featuring several possible orientations regarding load direction; from 45° up to 90°. From a continuum mechanical point of view, it can be assumed that every orientation between 45° and 90° has the same probability to occur. If the crack initiation is solely shear stress controlled, the distribution of the crack orientation should approximate a value as plotted in Fig. 4.59 (r). Thereby the percentage of cracks with orientations ≤ 45° was subtracted for each material; the residual percentages should then be uniformly distributed on the orientations 46°-90°.

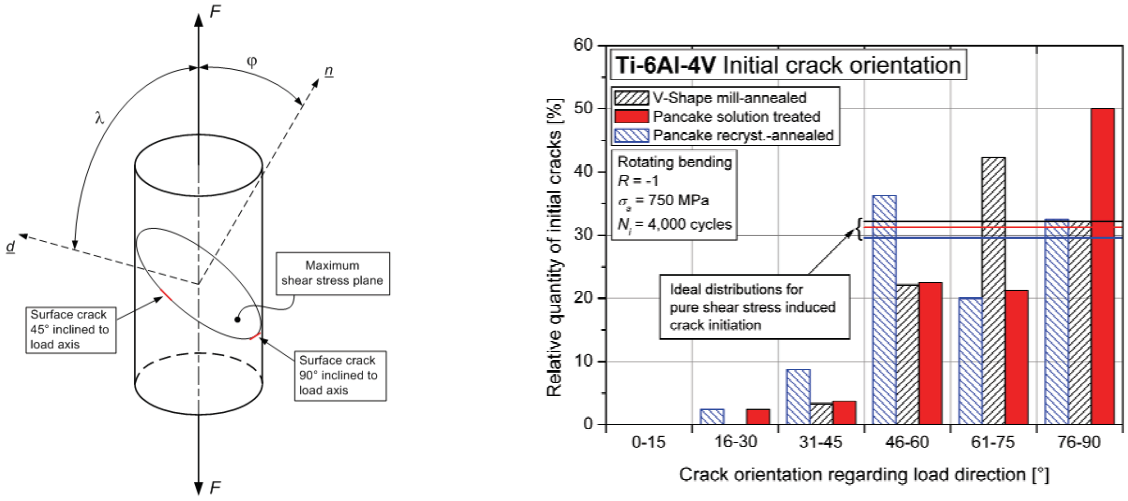

Fig. 4.59: Possible surface crack orientations for maximum shear stress (l), measured initial crack orientations (r)

It was observed that both equiaxed-type materials (V-shape MA and pancake RA) follow their ideal distributions for pure shear stress induced crack initiation (maximum deviation 10%). In contrast, the solution-treated pancake shows a maximum at orientations between 76° and 90°. This reveals that some fatigue cracks (~ 20%) also initiate under maximum normal stress, which is just possible at orientations close to 90°.
Linear elastic fracture mechanics, cf. Equ. (4.7), were used for determination of the applied stress intensity factor range. The thereby used geometry factor $Y = 0.75$ was an average of the proposed values of De Freitas and François [53] and Murakami [115]. This approach was also used (for purpose of comparison) in the region where linear elastic fracture mechanics might loose its validity (crack length $a < 150$ µm, cf. [170]). The crack growth behavior of the microstructurally short cracks was compared with those of long cracks for each microstructure (Fig. 4.60 to Fig. 4.62). Thereby, cracks, which did not grow during the last 1,000 load cycles, were marked as non-propagating cracks. It can be assumed, that those non-propagating cracks, which stopped at stress intensity factors higher than the long crack growth threshold, would continue to grow after certain load cycles. This behavior can be attributed to the analysis method; the growth of larger cracks occurs increasingly beneath the surface, but the crack size can only be measured at the surface. Intermittent crack stopping was determined for several microstructurally short cracks at and beneath the threshold. This behavior is caused by microstructurally barriers, e.g. grain boundaries.

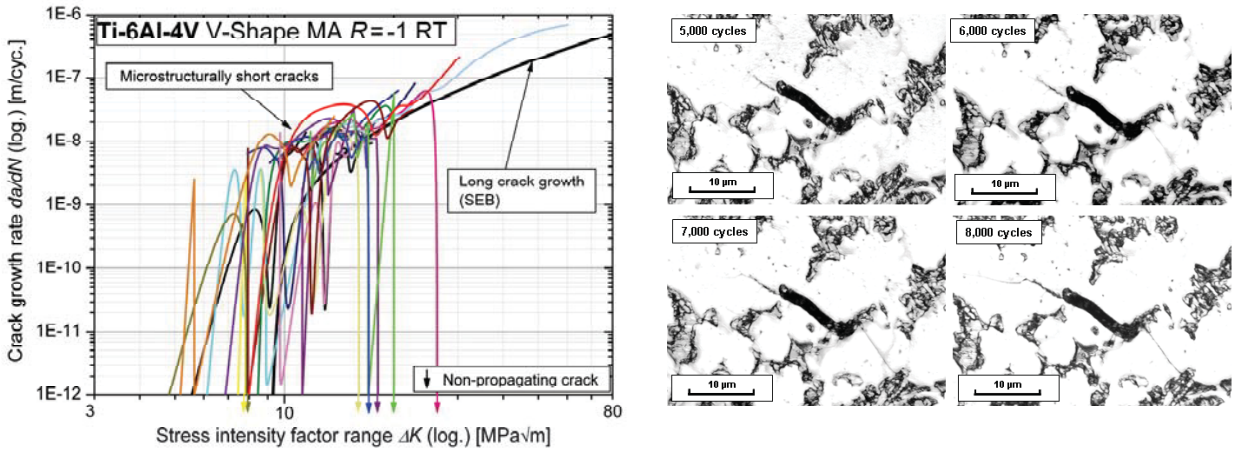

Fig. 4.60: Microstructurally short crack growth in mill-annealed Ti-6Al-4V

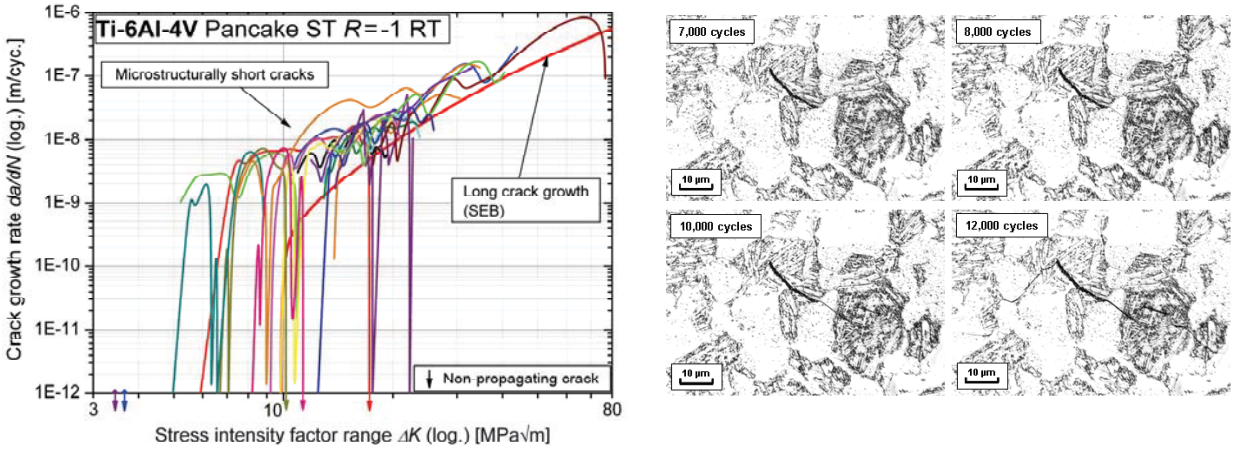

Fig. 4.61: Microstructurally short crack growth in solution treated Ti-6Al-4V

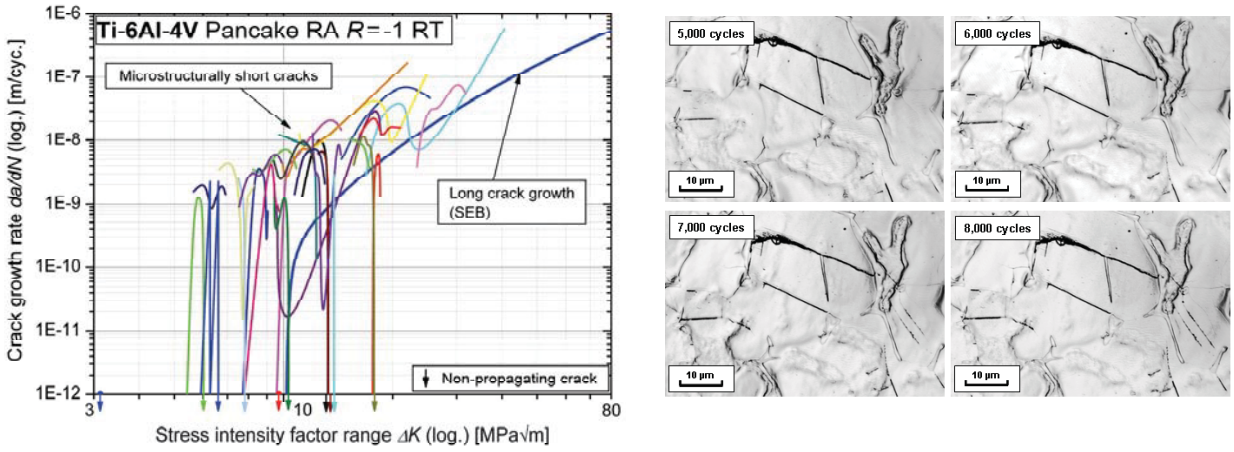

Fig. 4.62: Microstructurally short crack growth in recryst.-annealed Ti-6Al-4V

The comparison of the experimental data points for the three analyzed materials is shown in Fig. 4.63 (l). A relatively large scatter was determined independent from material, owing to the significant influence of local microstructure on the crack propagation of microstructurally short cracks. It is hence important to analyze an adequate amount of microstructurally short cracks to get a meaningful average crack growth behavior. The experimental short crack growth data was fitted with a power law (consistent with the Paris-law for long cracks, Equ. (4.9)) and compared with the long crack growth behavior, Fig. 4.63 (r) and Tab. 4.25. It was observed that the threshold of the short cracks lays in the region 4-5 MPa√m. Beneath 4 MPa√m just non-propagating cracks were determined, above 5 MPa√m each analyzed crack grew at least for a while.

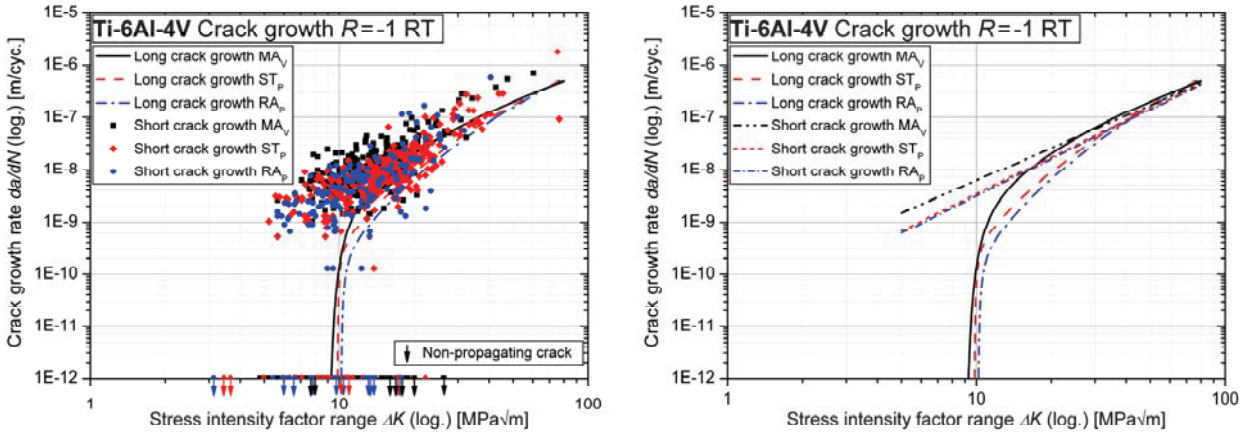

Fig. 4.63: Comparison of short and long crack growth for diff. microstructures, experimental data (l) and fits (r)

Short crack growth	V-Shape MA	Pancake ST	Pancake RA
C [m/(Cyc. MPa√m)]	5.34E-11	1.57E-11	1.36E-11
m [-]	2.06	2.34	2.36

Tab. 4.25: Fitting parameters of the mean short crack growth behavior

The comparison of short and long crack growth curves for the three different microstructures reveals that the analyzed microstructurally short cracks are already influenced by roughness-induced crack closure. The higher average crack growth rates of mill-annealed microstructures, which were observed in single edge bending tests (cf. Fig. 4.35), were confirmed with the microstructurally short crack growth tests. It can be assumed that this behavior is caused by the elongated primary α-grains of the mill-annealed microstructure. The striation measurements of delta patterns revealed that the local crack propagation rate within a primary α-grain is more than a decade higher than the average global one in the near-threshold region. This means that the crack formation within an α-grain consumes approximately 98% of the time for crack propagation on the scale of the average grain size. However, it can be assumed that elongated and interconnected α-grains lead for the same time of crack formation to an approximately two times higher crack propagation distance and hence crack growth rate.

The cycles to failure N_f consist of the cycles spent for crack initiation N_i and the cycles of crack growth N_g, Equ. (4.12). The combination and integration (from initial crack length a_0 to failure-causing crack length a_f) of Paris law, Equ. (4.9), and basic equation of the linear elastic fracture mechanics, Equ. (4.7), provides an estimation of the cycles consumed for crack growth N_g, Equ. (4.13). The average Paris-parameters determined for short crack growth (Tab. 4.25) were calibrated using the measured cycles consumed for crack growth (cycles to failure minus 4,000 cycles for crack initiation) and the initial crack length after 4,000 load cycles. A slight increase (10%) of the Paris-coefficient was necessary for good approximation.

$$N_f = N_i + N_g \qquad \text{Equ. (4.12)}$$

$$N_g = \int_{a_0}^{a_f} \frac{1}{C \cdot Y^m \cdot \Delta\sigma^m \cdot (\pi a)^{0.5m}} da \qquad \text{Equ. (4.13)}$$

These corrected Paris-parameters were consequently used for the estimation of the "real" crack initiation cycles. Thereby, the mean primary α-grain size (for MA_V) or mean colony length (for ST_P) plus the according standard deviation were used as initial crack length a_0. The calculated crack growth cycles were thus subtracted from the cycles to failure to get the crack initiation cycles. The measured cycles to failure N_f, the calculated crack growth cycles N_g, and the crack initiation cycles N_i for solution treated pancakes and mill-annealed V-shapes are summarized in Tab. 4.26. The electrolytically polished specimen with the recrystallization-annealed microstructure exhibited an anomalous low finite life fatigue strength (N_f = 10,700 for σ_a = 750 MPa) compared to the fatigue tests of machined specimens, cf. Fig. 4.28. The microstructural crack growth data showed no irregularity. An initial crack length on the scale of the grain size leads to a calculated lifetime slightly higher than those of the solution treated microstructure, Tab. 4.26, what corresponds to the fatigue tests on machined specimens. It can be concluded that the crack initiation phase is responsible for the low fatigue strength of the recrystallization-annealed material, what is confirmed by the anomalous initial crack length distribution, cf. Fig. 4.58. It is currently unclear, whether this anomalous crack initiation is solely caused by the residual stress free surface of the electrolytically polished specimens, or if the electrolytic polishing by itself causes this behavior.

Material	Calibrated Paris-Coeff. C [m/(Cyc. MPa√m)]	Paris-Exp. m [-]	Initial crack length a_0 [µm]	N_f [-]	N_g [-]	N_i [-]
V-Shape MA	6.1E-11	2.06	16	16,800	14,200	2,600 (15%)
Pancake ST	1.7E-11	2.34	22	21,400	19,400	2,000 (9%)
Pancake RA	1.6E-11	2.36	15	24,600*	22,200	2,400* (10%)

*Assumption

Tab. 4.26: Fatigue crack initiation and propagation calculations

The electrolytic polishing of the recrystallization-annealed specimen led to a relatively bad surface quality compared with the other analyzed specimens. However, this seems not to be the reason for the anomalous crack initiation. In spite of the just slightly lower microhardness of the primary α-grains of pancake recrystallization-annealed compared to V-shape mill-annealed (cf. Fig. 3.27), crack initiation was significantly easier in the recrystallization-annealed material, Fig. 4.64. Not only the length of the initial cracks was thereby anomalous large, also the quantity of initial cracks was higher, what may be attributed to the unknown effect (possibly notch effect) of the interstice phase between the primary α-grains of the recrystallization-annealed material. This interstice is not present in other microstructures. The notch effect of the interstice may be exceeded and hence annulled by that of the surface roughness of the machined specimens.

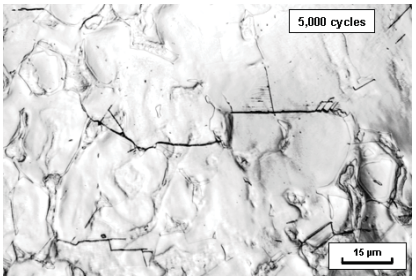

Fig. 4.64: Initial crack in recryst.-annealed Ti-6Al-4V

4.1.3. Phenomenological models

The experimental results clearly show that fatigue of Ti-6Al-4V is highly influenced by microstructure. To use this knowledge for optimization of Ti-6Al-4V forgings, the microstructure has to be linked with fatigue strength. Therefore, several models are presented to link microstructural parameters with finite life fatigue strength, high cycle fatigue strength and long crack growth behavior. They are based on and thus valid for equiaxed and bimodal forged Ti-6Al-4V without any precipitations or crystallographic texture.

4.1.3.1. High cycle fatigue strength

As mentioned before, both, the presented test results and the literature ([94], [113]) raise the suspicion that Ti-6Al-4V has a distinct fatigue limit. Therefore the wording “fatigue limit” is generally used. It was observed that the analyzed microstructures can be separated in two categories with regard to (α+β)-content: equiaxed- ($C_{\alpha+\beta} \leq 20\%$) and bimodal-type ($C_{\alpha+\beta} > 25\%$). The microstructural based findings discussed before showed that the limiting microstructural parameter with respect to the fatigue limit is different for these two categories. The primary α-grain size α_p is significant for the equiaxed-type microstructures and the (α+β)-colony length *Col* determines the fatigue limit (survival probability 50%) of the bimodal-type microstructures, Fig. 4.65.

Two different fatigue limits are plotted in Fig. 4.65 for the mill-annealed V-shape. They were observed in tension/compression and rotating bending fatigue tests on unnotched and notched round specimens, cf. chapter "Influence of relative stress gradient on the fatigue behavior". It can be assumed that the (α+β)-content of the microstructure of the mill-annealed V-shape is directly at the transition between equiaxed- and bimodal-type microstructure, which is confirmed by the finding that the fraction of initial cracks in α- and (α+β)-phase is almost identical in this microstructure. Slight variations in the microstructure turn the balance for equiaxed- or bimodal-type fatigue behavior.
The reasons for the transition from equiaxed- to bimodal-type fatigue behavior at a relatively low (α+β)-content are not clarified. However, it is believed that the almost identical microhardness of the primary α-grains of pancake RA and V-shape mill-annealed, and the elevated microhardness of bimodal-type microstructures is an indication for this transition. One possible reason could be the local alloying element concentrations (the aluminum is an α-stabilizer, vanadium a β-stabilizer) and their influence on the lattice parameters, especially the aspect ratio of the hdp lattice and the according effect on the slip activation, cf. [71].

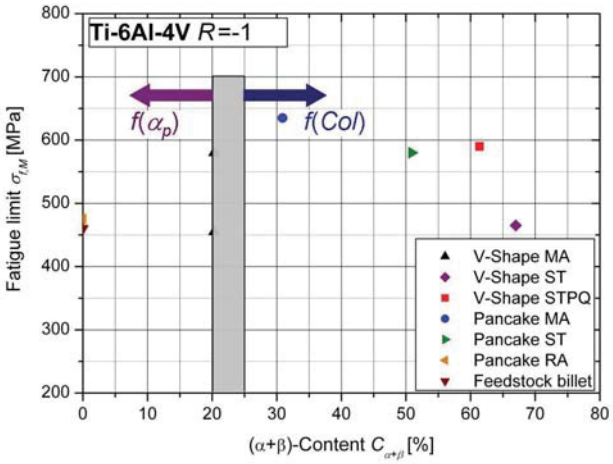

Fig. 4.65: Fatigue limits in respect of (α+β)-content

Two different models were developed for the link between primary α-grain size α_p [m] or (α+β)-colony length *Col* [µm] with the fatigue limit (stress amplitude, *R*=-1) $\sigma_{f,M}$ [MPa] in respect of microstructure, cf. Equ. (4.14) and Equ. (4.15). These relationships are plotted in Fig. 4.66.

$$If\ C_{\alpha+\beta} \le 20\%: \quad \sigma_{f,M} = 0.36 \frac{1}{\sqrt{\alpha_p}} + 350 \qquad \text{Equ. (4.14)}$$

$$If\ C_{\alpha+\beta} > 25\%: \quad \sigma_{f,M} = 685 - 6.8\, Col \qquad \text{Equ. (4.15)}$$

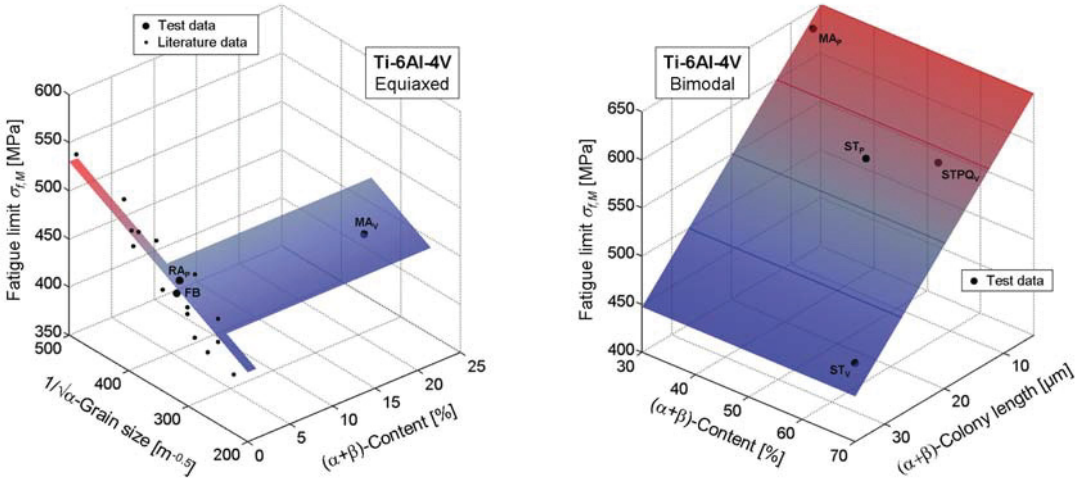

Fig. 4.66: Fatigue limit in respect of microstructure

In the transition regime between 20% and 25% (α+β)-content, to be conservative, both possible fatigue limits should be calculated and the lower one should be used for lifetime estimation. Literature data from Calles [45], Lucas and Konieczny [102] (absolute value corrected), Ivanova et al. [87] (absolute value corrected) and Lütjering and Williams [105] (absolute value corrected) was added in Fig. 4.66 (l) to confirm the used Hall-Petch-relationship.

In statistics, the coefficient of determination R^2 defines how well a model approximates real data points. R^2 is defined as the regression sum of squares divided by the total sum of squares, Equ. (4.16), whereby y_i are the data set values, f_i the modeled values and y_m and f_m are the means of the observed data and modeled values respectively. A R^2 of 1.0 indicates a perfect fit, a R^2 of smaller 0.7 a moderate correlation. The R^2 of the model for equiaxed microstructures is 0.98 and the R^2 of the model for bimodal microstructures is 0.99. The correlation between models and experimental data is hence good.

$$R^2 = \frac{\sum_i (f_i - f_m)^2}{\sum_i (y_i - y_m)^2} \qquad \text{Equ. (4.16)}$$

4.1.3.2. Finite life fatigue strength

The finite life fatigue strength was characterized by the cycles to failure N_{700MPa} (survival probability 50%) at a stress amplitude (R = -1) of 700 MPa. The same classification of microstructures (with respect to the (α+β)-content) as for the fatigue limit model was used for the link of fatigue strength in the finite life region with several microstructural parameters. The primary α-grain size α_p [m] is the crucial factor for the fatigue strength in the finite life regime of equiaxed-type microstructures, Equ. (4.17). The colony length Col [µm] and the (α+β)-content $C_{\alpha+\beta}$ [%] determine the fatigue strength of bimodal-type microstructures, Equ. (4.18). The slope k of the S/N-curve in the finite life region was determined to be constant eight.

$$If\ C_{\alpha+\beta} \le 20\%: \quad N_{700MPa} = 930\frac{1}{\sqrt{\alpha_p}} - 245000 \qquad \text{Equ. (4.17)}$$

$$If\ C_{\alpha+\beta} > 25\%: \quad N_{700MPa} = 1100\,C_{\alpha+\beta} - 800\,Col + 4900 \qquad \text{Equ. (4.18)}$$

An anomalous fatigue behavior in the finite life region was found for both, mill-annealed pancake and mill-annealed V-shape. Fatigue tests on mild-notched round specimens under tension/compression loading with the same stress gradient as unnotched specimens under rotating bending loading (cf. chapter "Influence of relative stress gradient") revealed that this anomaly is not caused by relative stress gradient. Therefore, the "normal" (and conservative) finite life fatigue strength of the mill-annealed materials was used for the model and for visualization in Fig. 4.67. The use of literature data was not expedient for the finite life fatigue strength due to the significant influence of the (unknown) surface state (residual stresses, surface roughness) of the fatigue test specimens used in literature, considering the comparatively small difference in respect of microstructure.

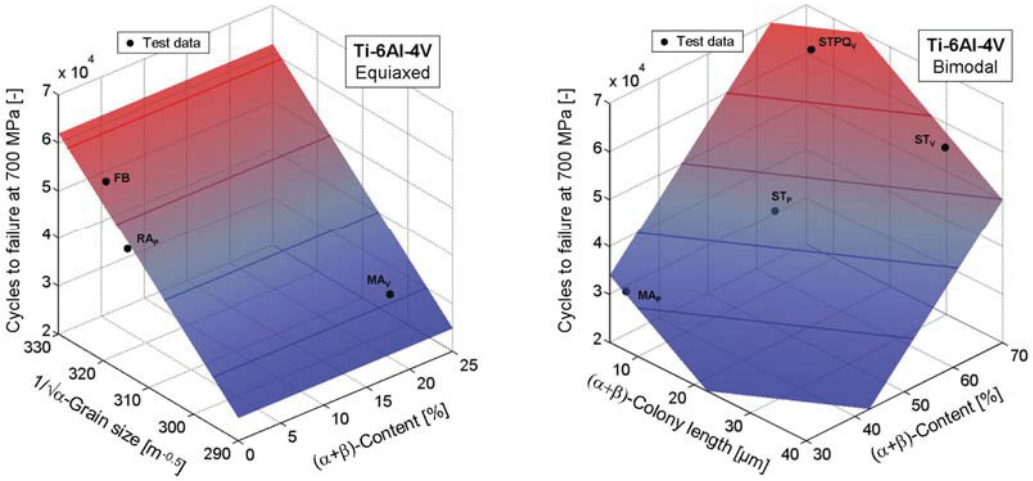

Fig. 4.67: Finite life fatigue strength in respect of microstructure

4.1.3.3. Estimation of tensile strength

The literature shows that the correlation between fatigue strength and tensile strength is not well defined for Ti-6Al-4V. Boyer et al. [42] mention that the effects of microstructure and strength can be offsetting factors so that no change in fatigue performance might be observed even when strength is increased. Excluding again lamellar microstructures, a rough model was developed based on literature data according to Bartlo [36] and Sparks and Long [160]. Furthermore, the results for the mill-annealed V-shape were used, cf. chapter "Appendix". The used data and the model are shown in Fig. 4.68.

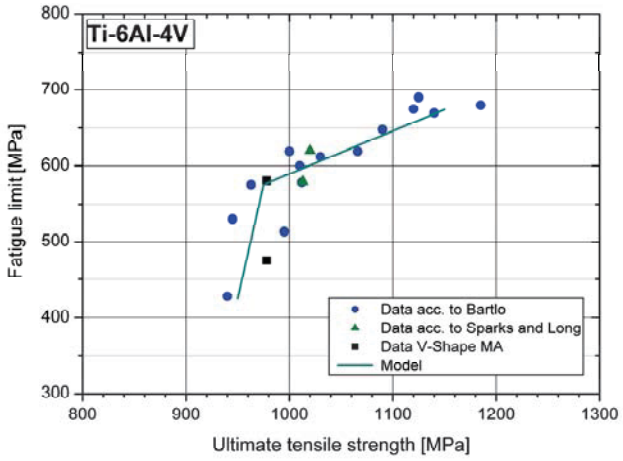

Fig. 4.68: Linking fatigue limit and tensile strength

The ultimate tensile strength R_m [MPa] can be linked with the high cycle fatigue strength of unnotched specimens $\sigma_{f,M}$ [MPa] with the following approach, Equ. (4.19) and Equ. (4.20).

$$\text{For } \sigma_{f,M} \leq 575 \text{ MPa: } R_m = \frac{\sigma_{f,M} + 5275}{6} \qquad \text{Equ. (4.19)}$$

$$\text{For } \sigma_{f,M} > 575 \text{ MPa: } R_m = \frac{\sigma_{f,M} - 19}{0.57} \qquad \text{Equ. (4.20)}$$

Furthermore, a link between 0.2%-yield strength $R_{p0.2}$ [MPa] and ultimate tensile strength R_m [MPa] was found, Equ. (4.21).

$$R_m = 1.08\, R_{p0.2} \qquad \text{Equ. (4.21)}$$

Literature data [42] was also used to link the compressive yield strength $R_{p,c}$ and the tensile yield strength $R_{p,t}$, Equ. (4.22).

$$R_{p,c} = 1.04\, R_{p,t} \qquad \text{Equ. (4.22)}$$

4.1.3.4. Fatigue crack growth threshold

The microstructure also plays a major role regarding long crack growth. The feedstock material exhibited anomalous high long crack growth thresholds due to macrozones in the microstructure, and was therefore excluded from the model. The long crack propagation of all analyzed forged equiaxed- or bimodal-type microstructures exhibited interdependencies with the primary α-grain size owing to roughness-induced crack closure. Such a grain size effect on the fatigue crack propagation (owing to differences of the crack front profiles) is reported in [105] and was confirmed with fracture surface roughness measurements (cf. Fig. 4.37 and Fig. 4.38).

For a quantitative link between microstructure and crack growth, the experimental stress intensity factor range thresholds were plotted in respect of the stress ratio R (Fig. 4.69). A linear relationship was chosen to fit the data points. Thereby, a fixed point was found at a stress ratio of 0.87 and a stress intensity factor range threshold of 1.75 MPa√m. Carboni et al. [46] found a similar linear correlation of stress ratio and stress intensity factor thresholds for steel. They reported, that the stress intensity factor threshold for a stress ratio $R = -2$ matches this relation too. Therefore it can be assumed that the observed linear relation is valid in the region $-2 \leq R \leq 0.87$.

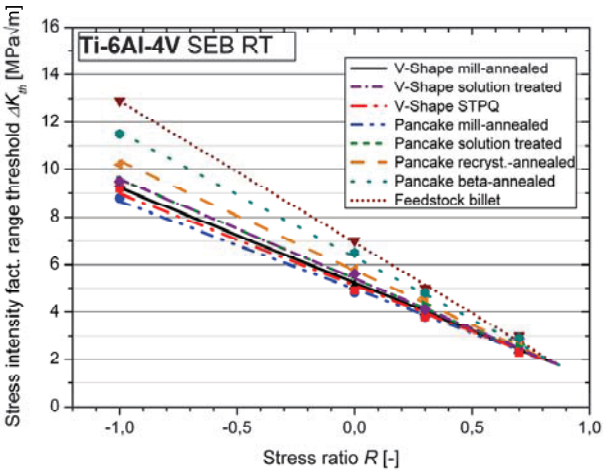

Fig. 4.69: Linking crack growth threshold and stress ratio

The slope k_{th} [-] of the fitting lines was linked with the microstructural parameter primary α-grain size α_p [µm], cf. Equ. (4.23) and Fig. 4.70. This model leads for the forged materials to a coefficient of determination R^2 of 0.97.

$$k_{th} = -0.31\,\alpha_p - 1.4 \qquad \text{Equ. (4.23)}$$

This equation yields in combination with the fixed point mentioned before to a model for the estimation of the stress intensity factor threshold in respect of microstructure and stress ratio. The equation for the stress intensity factor threshold ΔK_{th} [MPa√m] for stress ratios R between -2 and 0.87 is given in Equ. (4.24).

$$\Delta K_{th}\left(-2 \leq R \leq 0.87\right) = k_{th}\,(R - 0.87) + 1.75 \qquad \text{Equ. (4.24)}$$

For $R \geq 0.87$ it is assumed:

$$\Delta K_{th}\left(0.87 \leq R < 1\right) = 1.75 \qquad \text{Equ. (4.25)}$$

And for $R < -2$ it is suggested that the threshold remains on the same level as for $R = -2$:

$$\Delta K_{th}\left(R < -2\right) = -2.87\,k_{th} + 1.75 \qquad \text{Equ. (4.26)}$$

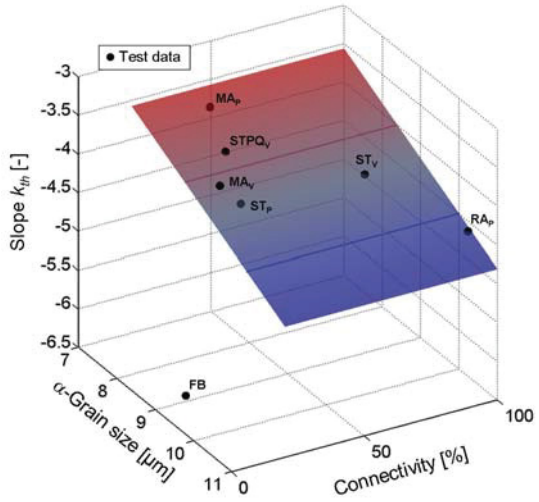

Fig. 4.70: Linking slope of fitting lines and microstructure

As mentioned above, a link between the roughness of the single edge bending fracture surfaces, primary α-grain sizes and stress intensity factor thresholds was found. This ties in well with the presented model. It can be concluded that the stress intensity factor threshold is primarily influenced by roughness-induced crack closure. Owing to the correlation between fracture surface roughness and primary α-grain size, a link between α-grain size and stress intensity factor thresholds was determined and implemented in this model.

4.1.3.5. Fatigue crack growth in the near-threshold region

The fatigue crack growth behavior in the near-threshold region was described with the stress intensity factor range, which is necessary to achieve crack growth rates of 1E-9, 1E-8 and 1E-7 m/cycle. It was determined that this stress intensity factor range at a certain crack growth rate correlates with the stress intensity factor threshold, independent from the stress ratio, Fig. 4.71. A discrepancy was only found for R = 0.7 for the crack growth rates of 1E-8 and 1E-7 m/cycle, because these crack growth rates are already located in the Paris-region of the crack growth curves.

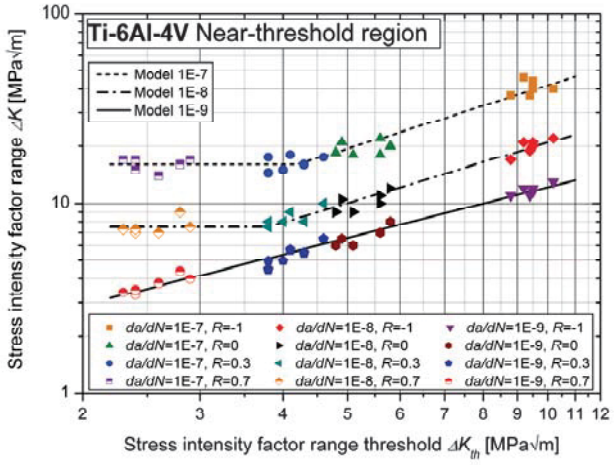

Fig. 4.71: Correlation of stress intensity at certain growth rates [m/cyc] and stress intensity factor threshold

The correlations of stress intensity factor threshold ΔK_{th} [MPa√m] and stress intensity factor range ΔK [MPa√m] at crack growth rates of 1E-9, 1E-8 and 1E-7 m/cyc are given in Equ. (4.27) to Equ. (4.29).

$$\Delta K_{1E-9} = 1.57\,\Delta K_{th}^{0.89} \qquad \text{Equ. (4.27)}$$

$$\Delta K_{1E-8}\left(\Delta K_{th} \geq 3.8\right) = 1.82\,\Delta K_{th}^{1.06} \qquad \text{Equ. (4.28)}$$

$$\Delta K_{1E-7}\left(\Delta K_{th} \geq 4.2\right) = 3.40\,\Delta K_{th}^{1.09} \qquad \text{Equ. (4.29)}$$

Equ. (4.28) is valid down to stress intensity factor thresholds of 3.8 MPa√m. For lower thresholds Equ. (4.30) applies.

$$\Delta K_{1E-8}\left(\Delta K_{th} < 3.8\right) = 7.5 \qquad \text{Equ. (4.30)}$$

Equ. (4.29) is applicable for stress intensity factor thresholds $\Delta K_{th} \geq 4.2$ MPa√m. For lower stress intensity factor thresholds Equ. (4.31) applies.

$$\Delta K_{1E-7}\left(\Delta K_{th} < 4.2\right) = 16 \qquad \text{Equ. (4.31)}$$

4.1.3.6. Fatigue crack growth in the Paris-regime

The stress ratio plays a major role in respect of fatigue crack propagation. However, as mentioned before, the crack growth in the Paris-regime is not considerably influenced by microstructure (cf. Fig. 4.35). Only for a stress ratio R = 0.7, an effect of microstructure was determinable.
Therefore, a rough model was developed for approximation. The parameters C and m of the Paris-Erdogan-equation, Equ. (4.9), were averaged for low stress ratios (Tab. 4.27).

R [-]	***C*** [m/(Cyc. MPa√m)]	***m*** [-]
-1	4.70E-11	2.00
0	1.23E-10	2.26
0.3	2.17E-10	2.28

Tab. 4.27: Paris-parameters for low stress ratios

A polynomial equation was used for determination of the Paris-exponent m in respect of the stress ratio R, Equ. (4.32). With the knowledge of the stress intensity factor belonging to the crack growth rate da/dN = 1E-7 m/cyc which results from the near-threshold model described before, it is possible to predict the Paris-region of the crack growth curve for $-1 \leq R \leq 0.3$.

$$m = 2.26 + 0.11\,R - 0.15\,R^2 \qquad \text{Equ. (4.32)}$$

For $R > 0.3$ the near-threshold model already provides enough information for approximation of the Paris-region, because a part of the modeling results already belongs to the Paris-region.

For $R = 0.7$ a complementary correlation was found, which can be used for calculation of the Paris-exponent m and Paris-coefficient C. A potential correlation between stress intensity factor range threshold ΔK_{th} [MPa√m] and m was thereby used for the forged microstructures, cf. Equ. (4.33) and Fig. 4.72.

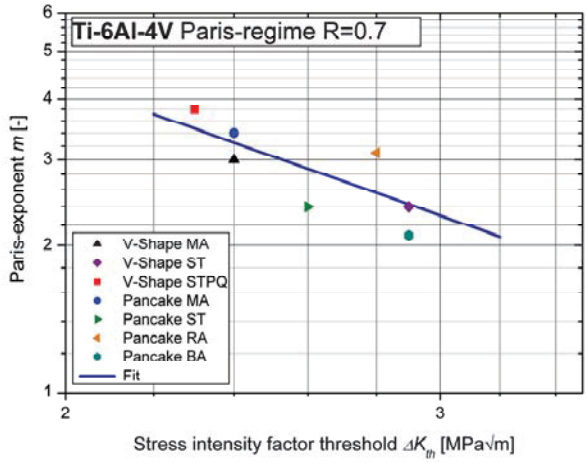

Fig. 4.72: Correlation of stress intensity factor threshold and Paris-exponent for R=0.7

Furthermore, it was shown that C and m can be linked for Ti-6Al-4V with an exponential correlation (Fig. 4.73); also known from other structural alloys, cf. [40] and [167]. Therefore, the Equ. (4.34) of the fitting line for a stress ratio of 0.7 was used to correlate the calculated Paris-exponent m of Equ. (4.33) with the Paris-coefficient C.

$$m_{R=0.7} = 12.52\,\Delta K_{th}^{(-1.54)} \qquad \text{Equ. (4.33)}$$

$$C_{R=0.7} = 1.21 \cdot 10^{-7} \cdot e^{(-2.82\,m_{R=0.7})} \qquad \text{Equ. (4.34)}$$

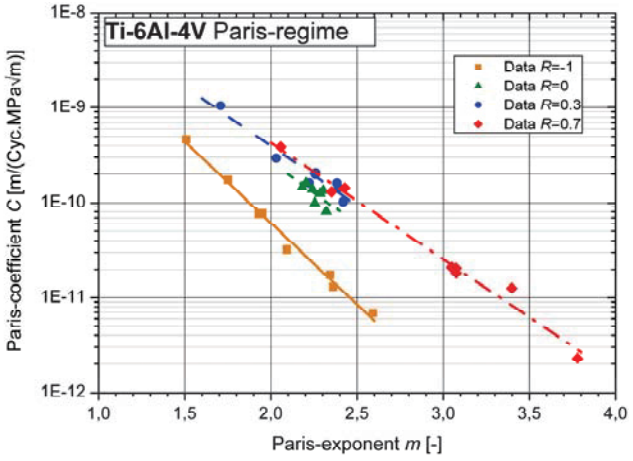

Fig. 4.73: Correlation of Paris-coefficient and Paris-exponent

4.1.4. Application of the new developed models

The presented models were randomly applied for one equiaxed (pancake recryst.-annealed) and one bimodal (V-shape STPQ) microstructure. The microstructural parameters summarized in Tab. 3.5 were thereby used as input for the models explained above.

The results of the S/N-curve models are shown in Fig. 4.74. A good accordance was determined for both, finite life and high cycle fatigue region.

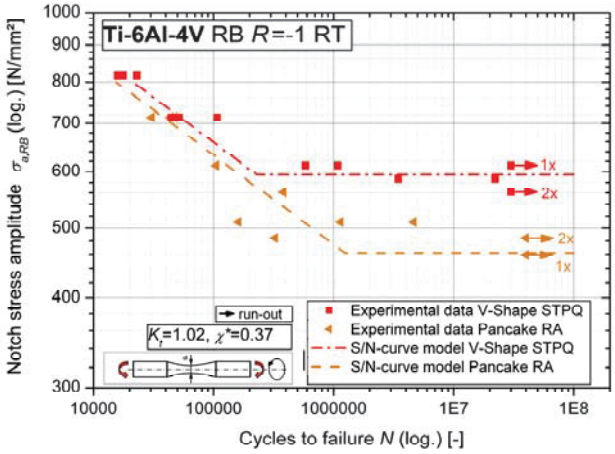

Fig. 4.74: Comparison of experimental data and S/N-curve model

Furthermore, the crack growth models were used for determination of the long crack growth curves of both microstructures for two different stress ratios, Fig. 4.75. Again, a good accordance of experimental data and model prediction was observed.

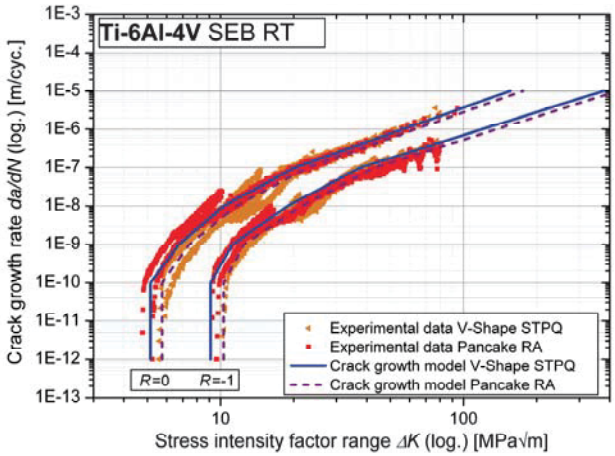

Fig. 4.75: Comparison of experimental data and crack growth model

The developed microstructural models are hence applicable for the determination of rotating bending S/N-curves and single edge bending long crack growth curves. The verification of these models was done with experimental results of Böhler Schmiedetechnik and will be discussed in the according chapter.

4.1.5. Conclusion

- Both, the finite life fatigue strength and the fatigue limit of Ti-6Al-4V are considerably influenced by microstructure. Furthermore, the long crack growth behavior shows a correlation with the microstructure.

- It was determined that the analyzed microstructures can be classified with respect to their (α+β)-content into equiaxed- and bimodal-type. Separate finite life fatigue strength and fatigue limit models were developed for both microstructure-types, which link basic microstructural parameters (primary α-grain size, (α+β)-colony length, (α+β)-content) with the according fatigue strength.

- It was observed that the long crack growth thresholds can be linked with the primary α-grain size. The reason for this correlation is the link of grain size and fracture surface roughness. The long crack growth threshold again is primarily controlled by roughness-induced crack-closure.

- Higher fracture surface roughness was determined in the near-threshold region. This behavior was explained by crack initiation and propagation in α-grains causing “delta patterns” in the fracture surface. These delta patterns are the reason for the correlation of fracture surface roughness and primary α-grain size. The near-threshold crack propagation mode occurs solely underneath a certain crack growth rate limit.

- Microstructurally short crack growth tests were performed. It was observed that the average microstructurally short crack growth rate is in accordance with the extension of the Paris-region of long crack growth data. Physically short crack growth tests matched the single edge bending long crack growth test results. It can be concluded that the crack growth behavior is primarily controlled by fracture surface roughness.

4.2. Influence of relative stress gradient on the fatigue behavior

In the lifetime estimation concept based on local stresses, the so-called supporting effect of materials is considered with the relative stress gradient. Therefore, several fatigue tests were performed on unnotched and notched specimens under rotating bending and tension/compression loading, respectively, to determine the notch sensitivity and to characterize the supporting effect of Ti-6Al-4V in respect of the relative stress gradient.

4.2.1. State-of-the-art

Complex components usually feature geometry transitions, discontinuities and notches. Such notches lead to a stress concentration in the notch root, cf. Fig. 4.76.

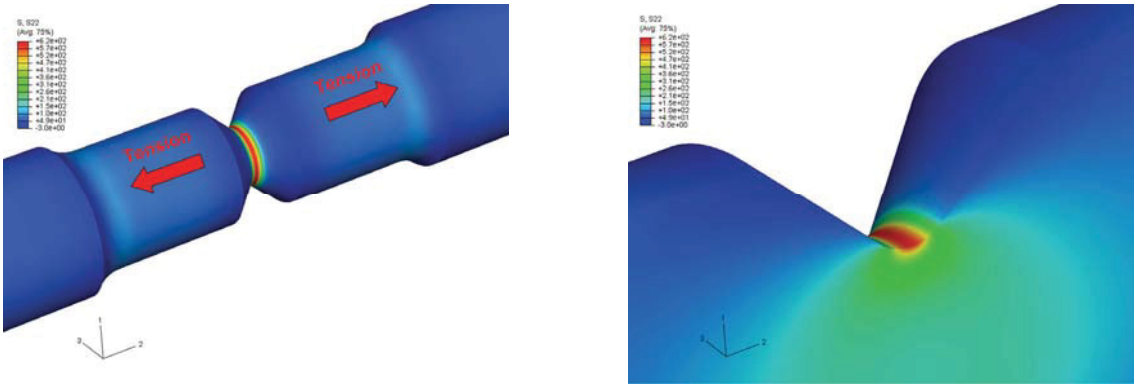

Fig. 4.76: Stress concentration at a circumferential notch of a round specimen under tension load

In addition to the stress concentration, a multiaxial stress state occurs; even under uniaxial loading. Fig. 4.77 shows exemplarily the stresses in longitudinal, tangential and circumferential direction, the nominal and the Mises equivalent stresses for the specimen shown in Fig. 4.76.

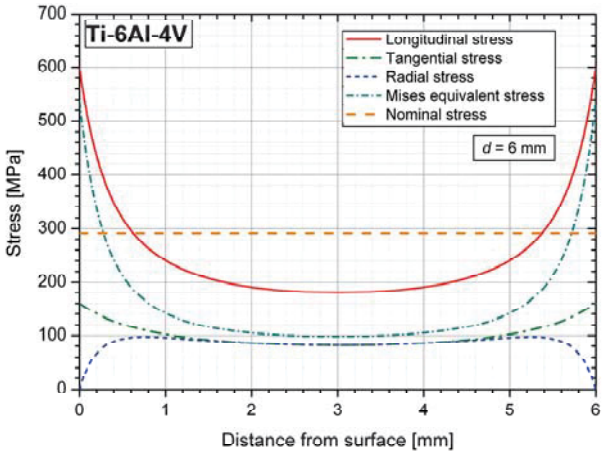

Fig. 4.77: Stress distributions in a sharp notched round specimen

In the concept based on nominal stresses, the theoretical geometric stress concentration factor K_t is defined as the maximum stress σ_{max} in the notch root divided by the nominal stress σ_{nom}, Equ. (4.35). K_t is independent from stress level and material and depends solely on geometry.

$$K_t = \frac{\sigma_{max}}{\sigma_{nom}} \qquad \text{Equ. (4.35)}$$

In the nominal stress concept, the notch effect with respect to fatigue is considered with the so-called fatigue notch factor K_f. The fatigue notch factor, Equ. (4.36), is defined as the fatigue limit of unnotched specimens σ_f divided by the fatigue limit of notched specimens $\sigma_{f,n}$; both fatigue limits are thereby based on nominal stress amplitudes. K_f is an empirical factor and has to be determined experimentally.

$$K_f = \frac{\sigma_f}{\sigma_{f,n}} \qquad \text{Equ. (4.36)}$$

The supporting effect of a material means that the local fatigue strength at a stress concentration site (high relative stress gradient) is usually higher than the fatigue strength of a material loaded with relative stress gradient of zero, despite identical local stresses. This leads to the following inequation, Equ. (4.37).

$$1 \leq K_f \leq K_t \qquad \text{Equ. (4.37)}$$

The relation of K_t and K_f can be described with the supporting factor n, Equ. (4.38).

$$n = \frac{K_t}{K_f} \qquad \text{Equ. (4.38)}$$

A material exhibits a full notch sensitivity if n = 1. If the supporting factor equals the stress concentration factor, it means full notch insensitivity.

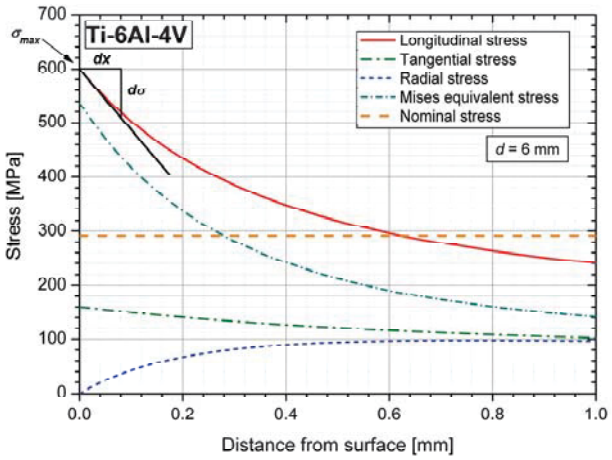

Fig. 4.78: Definition of stress gradient and maximum stress of a stress distribution

In the lifetime estimation concept based on local stresses, the relative stress is used for characterization of the supporting effect of a material. The relative stress gradient χ^* [mm^{-1}] is defined as the slope of the stress distribution at the point of maximum stress and is related to the maximum stress, Equ. (4.39) and Fig. 4.78.

$$\chi^* = \frac{1}{\sigma_{max}} \left(\frac{d\sigma}{dx} \right) \qquad \text{Equ. (4.39)}$$

One approach for consideration of the supporting effect in a lifetime estimation based on local stresses for aluminum alloys and steels was presented by Eichlseder [60]. The model is based on the fatigue limit $\sigma_{f,TC}$ under tension/compression loading of unnotched specimens ($\chi^* = 0$) and the fatigue limit $\sigma_{f,B}$ under bending loading of unnotched specimens with gauge diameter d ($\chi^* = 2/d$). Eichlseder used an exponential relation, Equ. (4.40), for interpolation between these two experimentally determined fatigue limits, characterized with the material-specific exponent K_D.

$$\sigma_f = \sigma_{f,TC} \cdot \left(1 + \left(\frac{\sigma_{f,B}}{\sigma_{f,TC}} - 1 \right) \cdot \left(\frac{\chi^*}{2/d} \right)^{K_D} \right) \qquad \text{Equ. (4.40)}$$

Many interpretations of the supporting effect have been given in literature. Verreman and Limodin [174] listed the following ones: small stressed volume, effect of notch machining, biaxial stresses, reversed yielding, etc. One of the most popular explanations of the supporting effect is based on the concept of critical distance [122], [123], [134] or process zone volume [168]. These approaches state that the material is not sensitive to the peak stress, but rather to an average stress over some finite volume of material that would be involved for the fatigue damage process to develop. Many expressions for the fatigue notch factor have hence been developed, cf. [182]. The Peterson approach [134] is the easiest: it uses the local stress at a particular point, located at a material-constant distance from the notch root. Neuber, Kuhn and Hardraht (reported in [182]) suggested a similar approach, cf. Equ. (4.41). ρ is thereby the radius of the notch root and a_n a material-specific constant assumed to be proportional to the grain size by Neuber.

$$K_f = 1 + \frac{K_t - 1}{1 + \sqrt{\frac{a_n}{\rho}}} \qquad \text{Equ. (4.41)}$$

Frost et al. [67] discussed the notched fatigue strength of ductile homogeneous materials, in which surface microcracks are initiated by continuing cyclic slip. They introduce a diagram that plots the fatigue limit over the stress concentration factor, Fig. 4.79. Curve 1 on this diagram represents the plain fatigue limit of the material divided by K_t, curve 2, the experimentally determined notched fatigue limits based on the alternating stress required to initiate a crack at the notch root, and curve 3, the conventional notched fatigue limit, that is the maximum alternating stress that will just not propagate a crack formed at the notch root. The position of this line above the abscissa varies with notch depth.

Frost et al. attributed the differences between curves 1 and 2 to the supporting effect interpretations listed before (small stressed volume, biaxial stress, etc.). For sharp notches, they suggested a fracture mechanical point of view. For notches of a given depth having values of K_t less than $K_{t,critical}$, the nominal alternating stress required to initiate a crack at the notch root is higher than the minimum propagation stress and all cracks which form will grow to cause complete failure of the specimen. For notches having K_t values greater than $K_{t,critical}$, the minimum cyclic propagation stress (and hence the conventional notched fatigue limit) remains constant and is independent of the stress concentration factor. Non-propagating cracks will be present in all specimens having notches sufficiently sharp to initiate a crack at the notch root tested at all nominal stresses less than that represented by curve 3. Verreman and Limodin [174] introduced a nomenclature for the notches with respect to the Frost diagram. If the stress concentration factor of a notch is smaller than $K_{t,critical}$ the notch is a blunt notch and K_t approximates K_f (classical fatigue approaches are valid), otherwise the notch is called severe (fracture mechanical approaches are valid) and K_f is smaller than K_t.

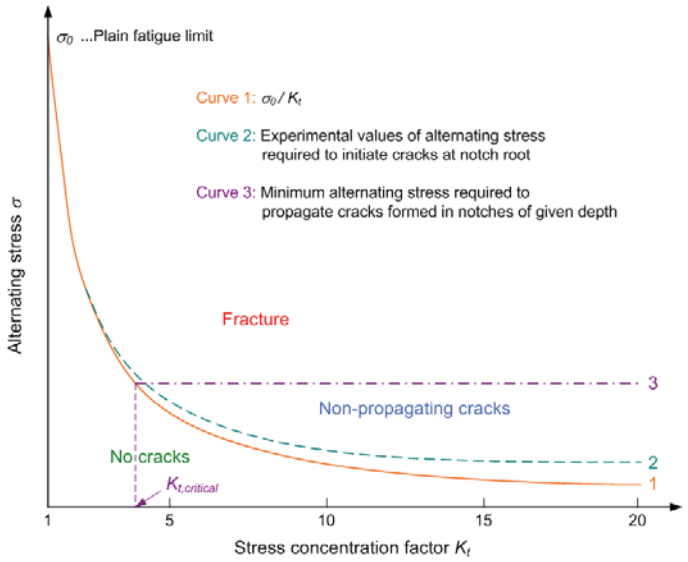

Fig. 4.79: Schematical Frost diagram [67]

Rösler et al. [145] reported that the crack propagation in stage I is crucial for the explanation of the supporting effect in a ductile material. Since fatigue cracks usually start at the surface of the specimen at the notch root, a growing crack enters a region with smaller stress and can thus be partially unloaded. Fig. 4.80 shows the Kitagawa diagram (assuming Y = constant) for this case.

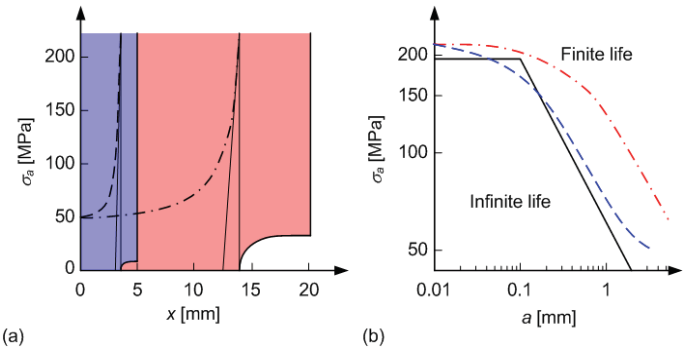

Fig. 4.80: Illustration of the notch supporting effect using a Kitagawa diagram [145]

Subfigure (a) shows two geometries with $K_t = 3$. The stress fields of the geometries differ in the stress gradient at the notch root. If a crack starts there, it is in the upper (finite life) part of the Kitagawa diagram, subfigure (b). If the gradient is large, the crack is unloaded and stops; if the gradient is small, the crack continues to grow.

The notch effect of Ti-6Al-4V is reported in [81] and [99], but the fatigue test results of these publications are based on step tests and therefore loose. They found no notch size effect for an untextured material (plate forging). The textured material (bar) showed a notch size effect, whereby it is not stated if there also exists a crystallographic texture.

4.2.2. Experimental procedure

Unnotched and notched round specimens (cf. chapter "Sampling") were used for high cycle fatigue tests for the determination of the notch supporting effect. The according residual stresses of the samples are shown in Fig. 3.47. The determination of relative stress gradients and stress concentration factors was done with the aid of finite element (FE) analysis. K_t and χ^* of samples are usually based on normal stresses but in a computational lifetime estimation based on local stresses, equivalent stresses of critical cutting planes are used (cf. chapter "Influence of multiaxial loading on the fatigue behavior"). Therefore, the relative stress gradients and stress concentration factors were determined for both, normal stresses and Mises equivalent stresses.
The element size has a significant influence on the results of a finite element analysis, especially on the stress gradient; the coarser the mesh, the lower the stress gradient. To achieve the "true" stress gradient, an element size of approximately 3 µm was used at the notch root. The stress gradient was defined as the slope of a linear fit of the first few nodes, whereby the depth of the measurement path beneath the surface approximated the material's grain size (~ 10 µm). The influence of the element size on the relative stress gradient model will be discussed in more detail below. The results of the FE analysis of K_t and χ^* based on normal stresses and Mises equivalent stresses for all relevant specimens are summarized in Tab. 4.28.

Type of load	Type of notch	Notch radius [mm]	K_t [-]	χ^* [mm^{-1}]	$K_{t,Mises}$ [-]	χ^*_{Mises} [mm^{-1}]
Tension/Compression	Unnotched	50	1.03	0.04	1.02	0.05
Tension/Compression	Mild notched	5	1.25	0.41	1.17	0.56
Tension/Compression	Sharp notched	1	2.05	2.54	1.84	3.60
Rotating Bending	Unnotched	50	1.02	0.37	1.01	0.38
Rotating Bending	Notched	1.5	1.50	1.58	1.36	2.05
Rotating Bending	Sharp notched	1	1.69	2.11	1.52	2.73

Tab. 4.28: Relative stress gradients and stress concentration factors for round specimens

Rotating bending and tension/compression fatigue tests were performed on unnotched and notched samples from three different materials (mill-annealed V-shape, mill-annealed pancake and V-shape STPQ) at ambient air and room temperature with a stress ratio $R = -1$. The frequency varied between 70 and 110 Hz.
It was measured that the surface roughness of the specimens increases with decreasing notch radius (cf. Tab. 3.6). It can be assumed that these variations lead to slightly lower fatigue limits. Lower compressive residual stresses were determined for smaller notch radii, which may result in a lower finite life fatigue strength. It can hence be concluded that the supporting effect is possibly underrated. However, it has to be mentioned that the machining was consistent for all different types of notches and these variations will also occur in real components.

The evaluation of the S/N-curves in the finite life region was based on the logarithmic normal distribution. The high cycle fatigue strengths at 10^8 load cycles were determined according to the *arcsin√P*-method [55]. Due to the limited specimen lot sizes, the high cycle fatigue strength and especially the scatter are not statistically firm.

The fracture surfaces were analyzed with a stereo light optical microscope (Olympus SZX12). Two exemplary pictures of a fracture surface are shown for each microstructure and notch type; one overview (16x magnification) and one detailed view of the crack initiation site (64x magnification). The crack initiation site is located at twelve o'clock position in all pictures. The fracture surface analyses revealed that the fatigue cracks initiate at the surface. One or more crack initiation sites were thereby observed, whereby the number of crack initiation sites increase by trend with increasing stress amplitude.

4.2.2.1. V-Shape mill-annealed

The rotating bending fatigue tests on unnotched hourglass specimens sampled from mill-annealed V-shape were already discussed (cf. Fig. 4.20), the tension/compression tests will be discussed in the next chapter (cf. Fig. 4.105). The results of tension/compression and rotating bending fatigue tests performed on varying notched specimens are summarized in Fig. 4.81 to Fig. 4.84 and Tab. 4.29 to Tab. 4.32.

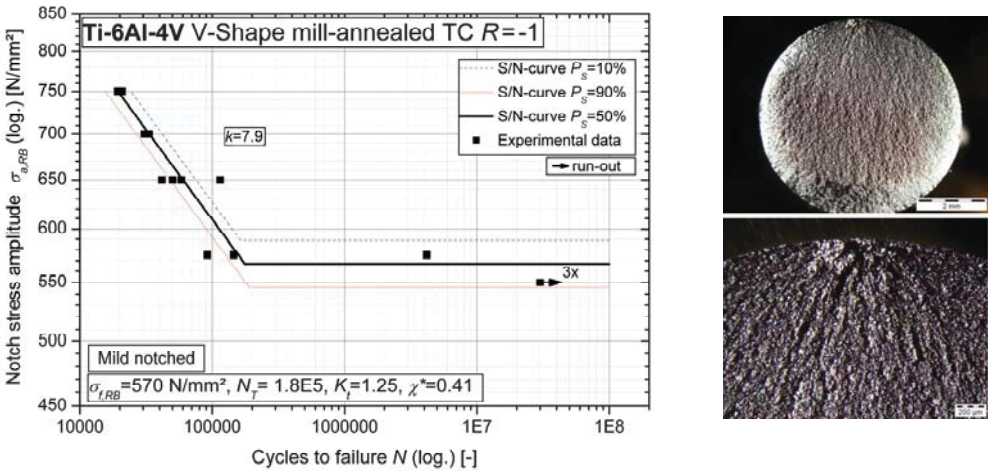

Fig. 4.81: TC S/N-curve (l) and fracture surface (r) for V-shape MA mild notched

Symbol	Description	Unit	Value
σ_f	Fatigue strength at N=10^8	MPa	570
N_T	Cycles at transition	-	1.8E5
k	Slope	-	7.9
T_N	Scatter at finite life	-	1:1.7
T_S	Scatter at N=10^8	-	1:1.1

Tab. 4.29: Parameters for TC S/N-curve V-shape MA mild notched

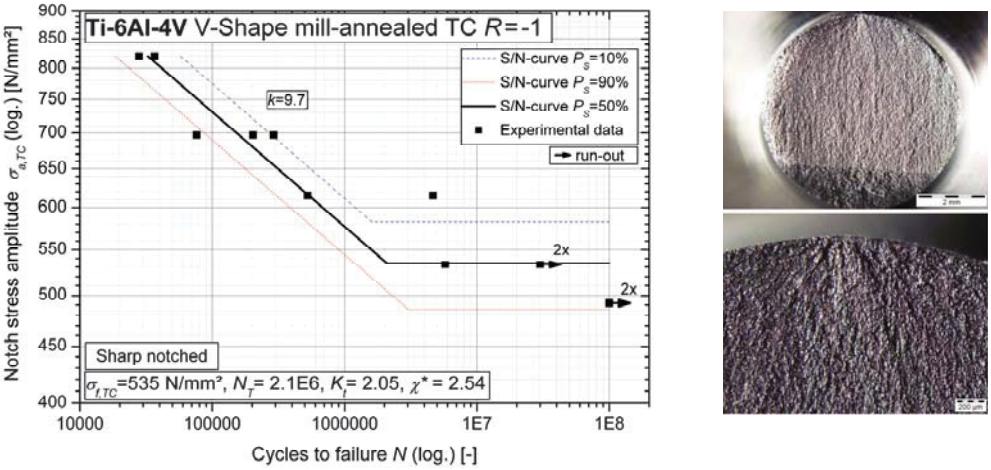

Fig. 4.82: TC S/N-curve (l) and fracture surface (r) for V-shape MA sharp notched

Symbol	Description	Unit	Value
σ_f	Fatigue strength at N=10^8	MPa	535
N_T	Cycles at transition	-	2.1E6
k	Slope	-	9.7
T_N	Scatter at finite life	-	1:3.1
T_S	Scatter at N=10^8	-	1:1.2

Tab. 4.30: Parameters for TC S/N-curve V-shape MA sharp notched

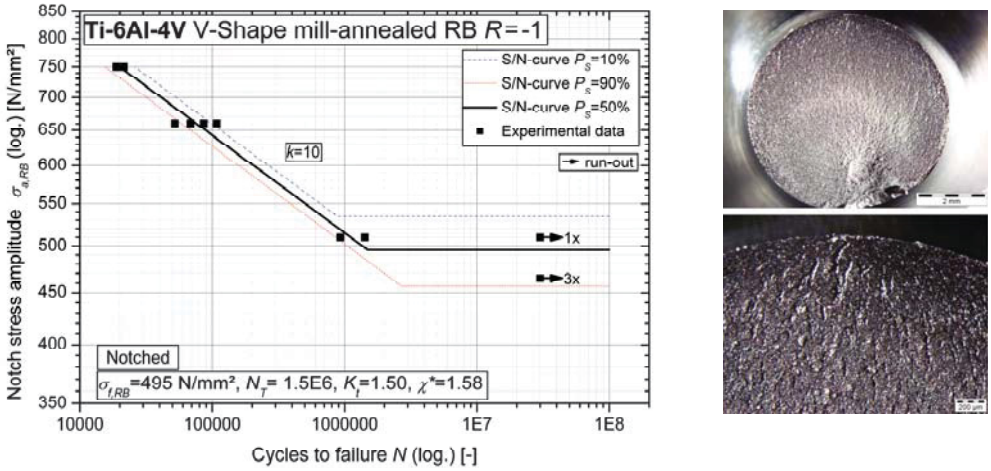

Fig. 4.83: Rotating bending S/N-curve (l) and fracture surface (r) for V-shape MA notched

Symbol	Description	Unit	Value
σ_f	Fatigue strength at N=10^8	MPa	495
N_T	Cycles at transition	-	1.5E6
k	Slope	-	10
T_N	Scatter at finite life	-	1:1.7
T_S	Scatter at N=10^8	-	1:1.2

Tab. 4.31: Parameters for RB S/N-curve V-shape MA notched

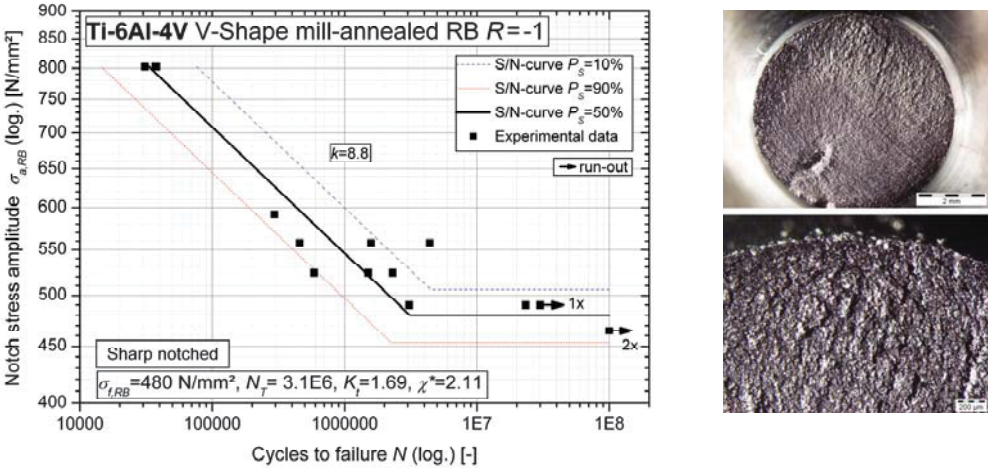

Fig. 4.84: Rotating bending S/N-curve (l) and fracture surface (r) for V-shape MA sharp notched

Symbol	Description	Unit	Value
σ_f	Fatigue strength at N=10^8	MPa	480
N_T	Cycles at transition	-	3.1E6
k	Slope	-	8.8
T_N	Scatter at finite life	-	1:5.3
T_S	Scatter at N=10^8	-	1:1.1

Tab. 4.32: Parameters for RB S/N-curve V-shape MA sharp notched

The comparison of S/N-curves for varying notched specimens and load types is shown in Fig. 4.85. A supporting effect was determined for both, finite life region and fatigue limit. Anomalous high fatigue limits were determined for smooth stress gradients ($\chi^* \approx 0.4$ mm^{-1}) under rotating bending and tension/compression load. This can be explained by the transition from equiaxed- to bimodal-type fatigue strength (cf. chapter "Influence of microstructure on the fatigue behavior"). The finite life fatigue strength for the same relative stress gradient exhibits an (conservative) anomalous behavior too, which is limited on rotating bending loading. This behavior cannot be explained by microstructural features and is currently unclear.

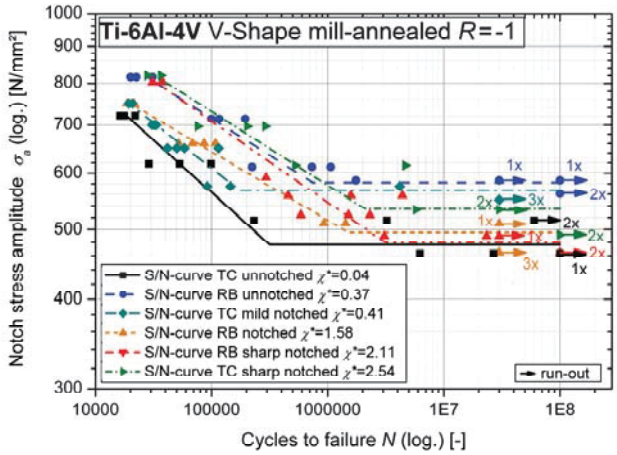

Fig. 4.85: Influence of notches on the HCF strength of V-shape mill-annealed

4.2.2.2. Pancake mill-annealed

Due to the limited testing lot size, the S/N-curve for sharp notched specimens under tension/compression loading was determined in accordance to the rotating bending results (cf. Fig. 4.21), Fig. 4.86. It was assumed that the (conservative) variance between slope of the S/N-curve and the experimental results originates from the high scatter of mill-annealed microstructures in the finite life region. The S/N-curve for notched specimens under rotating bending loading is presented in Fig. 4.87.

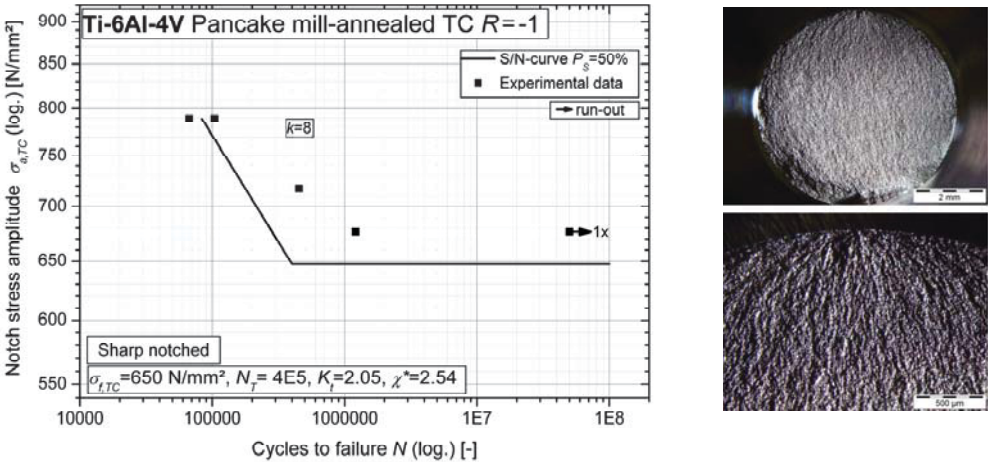

Fig. 4.86: TC S/N-curve (l) and fracture surface (r) for pancake MA sharp notched

Symbol	Description	Unit	Value
σ_f	Fatigue strength at N=10^8	MPa	650
N_T	Cycles at transition	-	4E5
k	(Estimated) Slope	-	8
T_N	Scatter at finite life	-	-
T_S	Scatter at N=10^8	-	-

Tab. 4.33: Parameters for TC S/N-curve pancake MA sharp notched

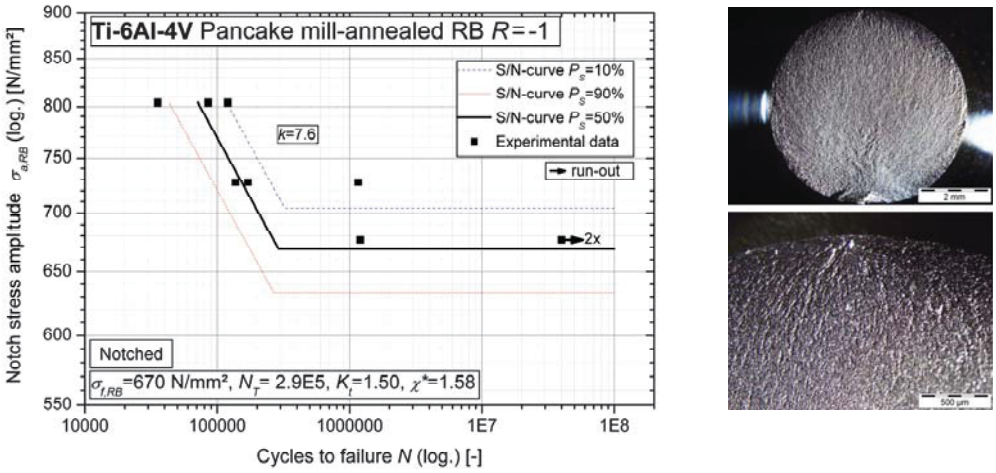

Fig. 4.87: RB S/N-curve (l) and fracture surface (r) pancake MA notched

Symbol	Description	Unit	Value
σ_f	Fatigue strength at N=10^8	MPa	670
N_T	Cycles at transition	-	2.9E5
k	Slope	-	7.6
T_N	Scatter at finite life	-	-
T_S	Scatter at N=10^8	-	-

Tab. 4.34: Parameters for RB S/N-curve pancake MA notched

Fatigue tests were performed on varying notched specimens sampled from mill-annealed pancake. In addition, few fatigue tests (too less for statistical analysis) were done under tension/compression loading on unnotched and mild notched specimens. The experimental data and the according S/N-curves are summarized in Fig. 4.88. Significant statements with respect to the supporting effect at the fatigue limit were not possible due to the limited specimen lot sizes in combination with material scatter and no major differences. Nevertheless, a notch supporting effect was observed for the finite life region. The finite life fatigue strength of unnotched round specimens under rotating bending loading exhibited thereby the same anomalous behavior as the mill-annealed V-shape material. This conservative anomaly is limited on mill-annealed microstructures and can not be explained currently.

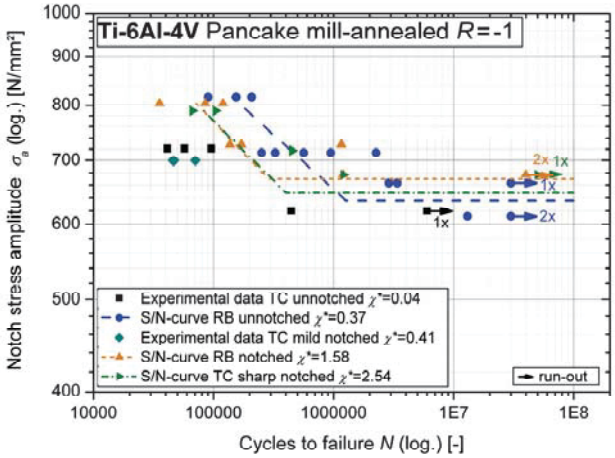

Fig. 4.88: Influence of notches on S/N-curves for pancake mill-annealed

4.2.2.3. V-Shape STPQ

Fatigue tests were performed under rotating bending loading on unnotched (cf. Fig. 4.23) and notched specimens (Fig. 4.89), respectively. Supplementary tension/compression fatigue tests were done on unnotched samples, cf. Fig. 4.116, and also on mild notched specimens at one stress level (notch stress amplitude $\sigma_{a,TC}$ = 700 MPa). The comparison of these test results is shown in Fig. 4.90. A notch supporting effect was determined for both, finite life fatigue strength and fatigue limit.

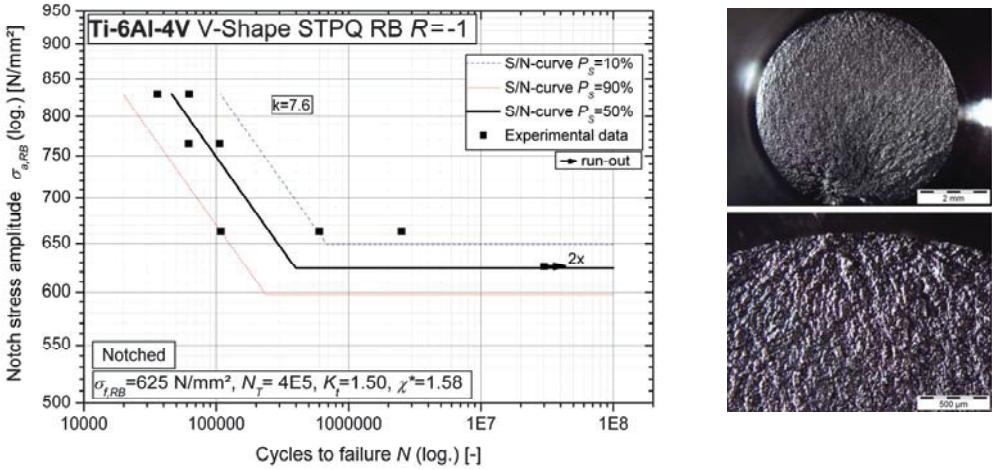

Fig. 4.89: RB S/N-curve (l) and fracture surface (r) for V-shape STPQ notched

Symbol	Description	Unit	Value
σ_f	Fatigue strength at N=10^8	MPa	625
N_T	Cycles at transition	-	4E5
k	Slope	-	7.6
T_N	Scatter at finite life	-	1:5.4
T_S	Scatter at N=10^8	-	1:1.1

Tab. 4.35: Parameters for RB S/N-curve V-shape STPQ notched

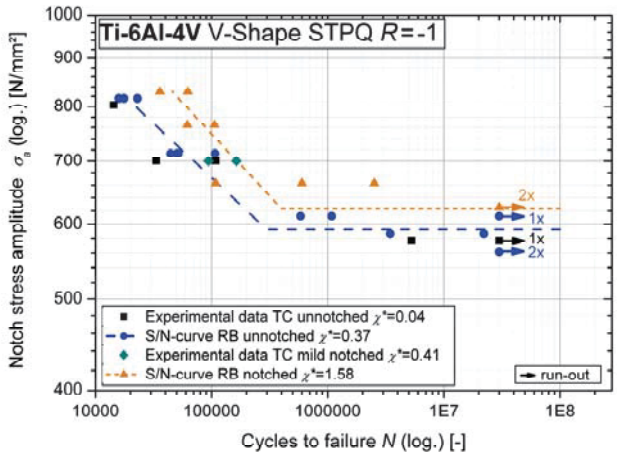

Fig. 4.90: Influence of notches on S/N-curves for V-shape STPQ

4.2.3. Discussion

For both, equiaxed and bimodal microstructures it was observed that the notch sensitivity is very high, especially in the high cycle fatigue region. This means that the maximum stress in the notch root determines the fatigue limit. A supporting effect based on normal stresses was observed but it was anomalous low compared to e.g. aluminum alloys.

The relation of fatigue strength and relative stress gradient is linear for both, finite life and fatigue limit. If Mises equivalent stresses (and their according stress concentration factors and relative stress gradients, cf. Tab. 4.28) are used, no supporting effect was determined for the fatigue limit and just a very low one for the finite life region. The current available models are hence not applicable and new models were developed (cf. chapter "Phenomenological models") to account for these anomalies.

A Frost diagram was plotted for the experimental results of V-shape mill-annealed to determine the stress concentration factor for the transition of classical fatigue approaches and fracture mechanical approaches. The test results for the round specimens shown before are supplemented by the S/N-curves derived from the physically short crack growth measurements (Fig. 4.48 and Fig. 4.49). Therefore, a linear elastic FE simulation was done to determine the stress distribution in the notch root of the flat short crack growth specimens (cf. Fig. 3.41 and Fig. 3.42). A distinct descent of stress was determined in the first hundredths of a millimeter beneath the surface, Fig. 4.91. Due to the microstructural scale of this stress descent, an averaging with respect to the mean primary α-grain size (11 µm) was performed. The maximum averaged stress was used for the determination of the stress concentration factors (5.3 and 7.4) of these severe notches.

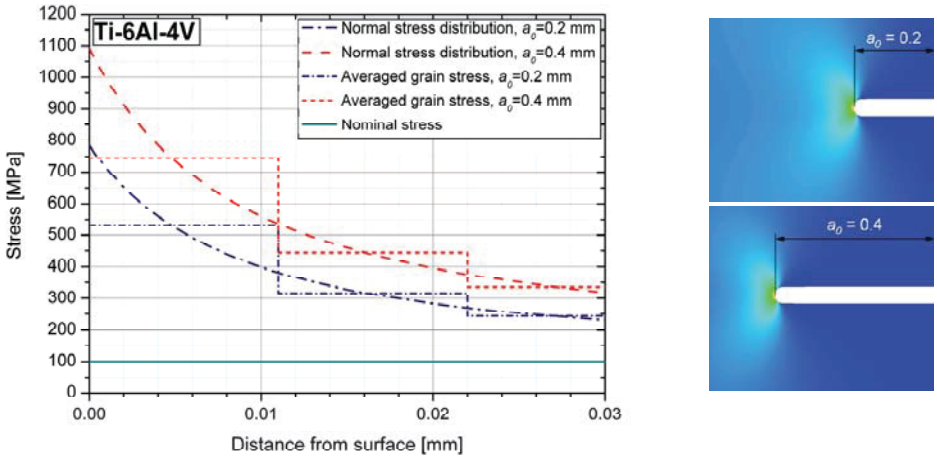

Fig. 4.91: Stress distribution in the flat severe notched specimens

The Frost diagram for the high cycle fatigue region is shown in Fig. 4.92 (l). Thereby, just the experimental data of the round specimens ($1 \leq K_t \leq 2$) were fitted with a potential relation. According to Frost et al. [67], this curve represents the experimental values of nominal alternating stress required to initiate a crack at the notch root. However, it was observed that this curve and the experimental data of the flat specimens with the severe notches are congruent. This reveals that the reason for the supporting effect can be the same for both, blunt notches of round specimens and severe notches of flat short crack growth specimens.

The Frost diagram was also plotted for finite life fatigue strength ($N = 10^5$), Fig. 4.92 (r). It was observed that the principle of this diagram is also applicable for the finite life region. Furthermore, it can be shown that the potential fitting curve of the experimental data of the blunt notched round specimens approximates the fatigue test results of the severe notched flat specimens. A comparison of both diagrams in Fig. 4.92 exhibits, that the supporting effect is more distinct in the finite life region.

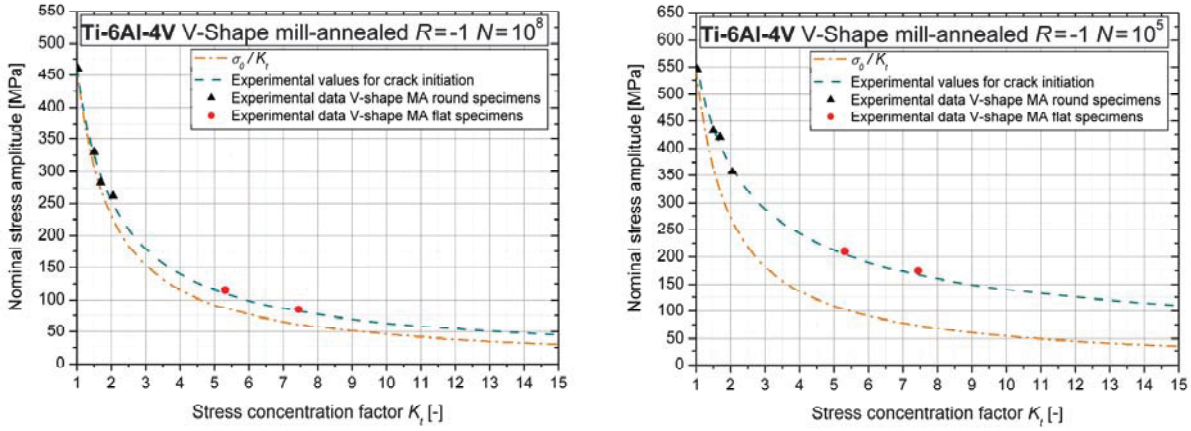

Fig. 4.92: Frost diagram for fatigue limit (l) and finite life region (r)

A reason for the low supporting effect of Ti-6Al-4V can be given with the aid of the Kitagawa diagram [145]. The stress distributions at the according fatigue limits (by using the normal stress supporting effect model) were plotted for several types of notched round specimens, Fig. 4.93 (l). An initial crack is thereby affected by a stress range at the left hand side of the stress distribution. With increasing crack length the applied stress range decreases according to the stress distribution. It was observed that all stress distributions intersect in one point. This reveals that the shape of the classical Kitagawa-curve (cf. Fig. 4.12) or the one proposed by Chapetti (cf. Fig. 4.13) with their severe knees are valid for Ti-6Al-4V. The Kitagawa-curve was plotted, using the fatigue limit of the microstructural model. The geometry factor was determined in accordance to Murakami [115]; $Y \approx 0.75$.
The stress intensity factor threshold was adapted (to 7.5 MPa$\sqrt{m}$) to meet the intersection point of the stress distributions. It can be concluded that this threshold value is valid for short cracks under the given conditions. In this case, the low supporting effect can be explained with non-propagating cracks. The notch stress distribution will intersect the Kitagawa-curve if the applied stress range is lower than the determined fatigue limit for notched specimens. This means that a crack initiates (if the stress range is higher than the fatigue limit of the unnotched specimens) in the finite life region of the Kitagawa diagram but (owing to the decreasing stress range with increasing crack length) the crack reaches the infinite life region of the diagram and stops. At higher applied stress ranges, the crack load will always lie in the finite life region of the Kitagawa diagram. It can be assumed that the crack initiation in the notch root is solely maximum stress controlled (independent from the relative stress gradient) and the slight supporting effect results from the higher stress gradients of notched specimens which lead to increased unloading of growing initial cracks.

The Chapetti-curve [47] for the threshold in respect of crack length was plotted in Fig. 4.93 (r), whereby the microstructural barrier parameter d was assumed to approximate the primary α-grain size, $Y \approx 0.75$. The notch stress distributions of the different specimens were adapted to meet the knee of the Chapetti-curve, resulting in a very low supporting effect. The reason for the supporting effect are the same as explained before, namely increased unloading of growing cracks. It is believed that this is the explanation for the non-existence of a supporting effect if the experimental data is based on Mises equivalent stresses. It can be assumed that the measured supporting effect in the finite life and high cycle fatigue region is lower as predicted by this Kitagawa-diagram due to the increasing roughness and decreasing residual compressive stresses with decreasing notch radius, cf. chapter “Specimen characterization”.

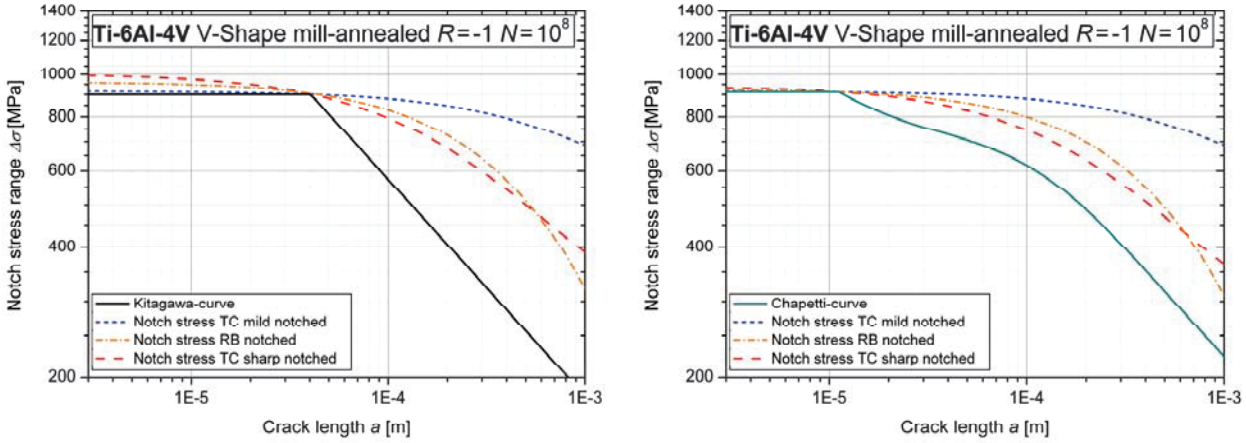

Fig. 4.93: Kitagawa-curve (l) and Chapetti-curve (r) with according notch stress distributions

The notch root surface of a sharp notched tension/compression fatigue test run-out specimen (V-shape MA) was analyzed with respect to non-propagating cracks with a confocal laser scanning microscope. Cracks were hard to indentify due to the surface roughness of the precision-turned specimens in combination with the small crack length (< 0.04 mm). One possible non-propagating crack is shown in Fig. 4.94. Fatigue tests on polished specimens would be necessary for confirmation of these findings.

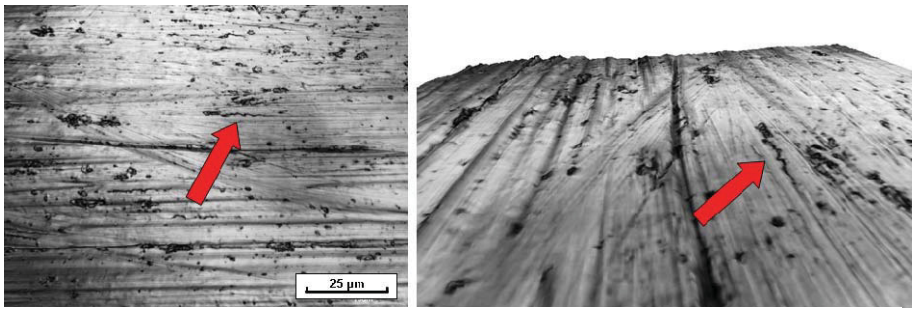

Fig. 4.94: Non-propagating crack in the notch root of sharp notched run-out specimen

However, a non-propagating crack was determined at the root of a small forging lap of an as-forged plane specimens after four point bending loading (cf. chapter “Influence of surface arrangement on the fatigue behavior”). This corroborates that non-propagating cracks play a role with respect to the fatigue behavior.

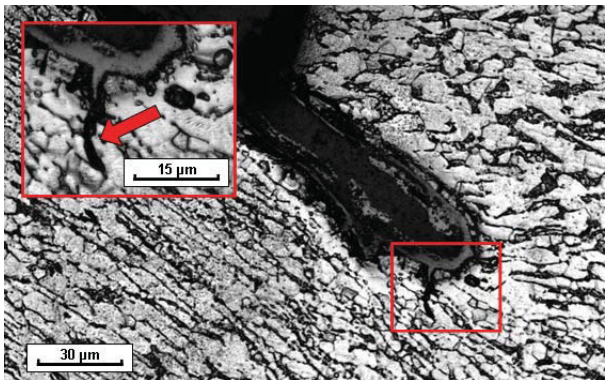

Fig. 4.95: Non-propagating crack at the root of a forging lap

The low supporting effect of Ti-6Al-4V compared to other metals, e.g. aluminum alloys, may arise from the shape of the Kitagawa diagram. The initial crack length a_{th} at the knee of the Kitagawa-curve for identical geometry factors is ~ 0.04 mm for Ti-6Al-4V and ~ 0.4 mm for an aluminum cast alloy (cf. [125]); a difference of factor 10. This shift could be responsible for the higher supporting effect (for a relative stress gradient of 2.5 mm^{-1} approximately two times higher) of aluminum alloys compared to Ti-6Al-4V. A comparison on the basis of the Chapetti-curve is more complicated, because the supporting effect depends on the microstructural characteristic dimension.
The Chapetti-curve was used for the explanation of the supporting effect of the severe notched flat SCG specimens too. Fig. 4.96 shows the Kitagawa diagram for the stress ratios -1 and zero. The geometry factor ($Y \approx 0.75$) was chosen according to Murakami [115] and the findings of Nakajima [116]. It was observed, that the stress gradient is almost identical for both initial crack lengths and does not play a major role for the supporting effect of these severe notches. The Chapetti-curves were again based on a microstructural barrier size equal to the primary α-grain size. The knee of the Chapetti-curve shows a good accordance with the notch stress distributions, which is an explanation for the observed supporting effect.

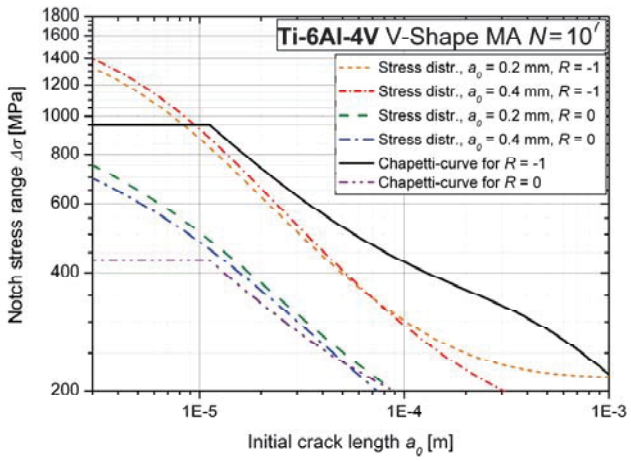

Fig. 4.96: Kitagawa diagram for the severe notched SCG specimens at $N = 10^7$

The material parameter k, which defines the development of the extrinsic threshold component, was (conservatively) modified, Equ. (4.42), to shift the steady state level of the extrinsic threshold component to larger crack lengths. Thereby, d is the microstructural barrier length, ΔK_{thR} the fatigue crack propagation threshold for long cracks, and ΔK_{dR} the microstructural intrinsic threshold, cf. [47]. A Chapetti-curve for the original k is shown in Fig. 4.93 (r), two modified curves are presented in Fig. 4.96.

$$k_{Ti64} = \frac{1}{20\,d} \cdot \frac{\Delta K_{dR}}{\Delta K_{thR} - \Delta K_{dR}} \qquad \text{Equ. (4.42)}$$

Finally, it can be concluded that the supporting effect of Ti-6Al-4V depends not solely on the relative stress gradient, but also on the fatigue limit and possibly on the microstructural barrier length d proposed by Chapetti [47]. For "common" notch geometries and relative stress gradients (as observed for the notched round specimens), these influencing variables play a minor part with respect to the supporting effect. The similarity of the determined supporting effects for different microstructures confirms this assumption.

4.2.4. Phenomenological models

It raises the question, whether to use fatigue test data based on normal stresses or based on equivalent stresses for the determination of the supporting effect. Usually, normal stress based data is used in literature for relative stress gradient models. However, a computational lifetime estimation is based on equivalent stresses. Therefore, the equivalent stress used in the computational lifetime estimation should also be the basis for the supporting effect models.

Phenomenological models were hence developed based on both normal and equivalent stresses. Their application depends on the result of the lifetime prediction. If the lifetime of fatigue test specimens is predicted (these results are usually normal stress based), the normal stress supporting effect model has to be chosen. If the lifetime of a component is predicted based on finite element analysis, the equivalent stress based supporting effect model is the right choice.
It was observed that Ti-6Al-4V has generally a high notch sensitivity, especially in the high cycle fatigue region. The fatigue strength for both, finite life region and fatigue limit shows a linear correlation with the relative stress gradient, independent from the stress type.

The chosen element size of the finite element (FE) mesh is another important point with respect to the stress gradient for both, specimen and component analysis. The conservative approach is to determine the stress gradients of specimens as good as possible with a fine mesh. The mesh of a component FE analysis will be coarser, leading to lower stress gradients and an underestimation of the supporting effect. Non-conservative would be the determination of the relative stress gradient of specimens with a coarse FE mesh, what results in an underestimation of the real stress gradients and a seemingly higher supporting effect. If the FE mesh of a component is consequently finer than those used for the specimens, the seemingly higher notch supporting effect leads to a non-conservative lifetime estimation.
Therefore, the relative stress gradients of the specimens used for this research were determined with finite element analysis using a very fine mesh (element size in the notch root approximated 3 µm). The stress distribution of the first 10 microns (~ grain size) beneath the surface was used for a linear fit for determination of the stress gradient. It can be concluded that the determined stress gradient models are conservative for coarse meshed FE models of components.

The last question with respect to the stress gradient model is the influence of a possible plastification at the notch root. However, the utilization of linear elastic FE analysis for both, material characterization (specimens) and component analyses leads to a compensation of possible influences of local plastifications. The influence of plastification on the mean stress rearrangement can be included in a lifetime estimation with the aid of the Neuber-approach [122], [123].

4.2.4.1. High cycle fatigue strength

Due to the limited specimen lot sizes for fatigue tests, the high cycle fatigue strength is not statistically firm. However, two models were developed to account for the low supporting effect of Ti-6Al-4V.
A linear approach, Equ. (4.43), was used to link the relative stress gradient χ^* [mm^{-1}] and the fatigue limit $\sigma_{f,MG}$ [MPa] based on normal stresses. The input for this model, the fatigue limit $\sigma_{f,M}$ [MPa] at a relative stress gradient of 0.37 mm^{-1}, derives from the microstructural based model explained in the previous chapter.

$$\sigma_{f,MG} = 20\chi^* + \sigma_{f,M} - 7.5 \qquad \text{Equ. (4.43)}$$

No supporting effect was determined for the Mises equivalent stress based test results. This can be explained by the insignificant supporting effect resulting from non-propagating cracks, cf. Fig. 4.93 (r) in combination with the increasing surface roughness and decreasing compressive residual stresses (cf. chapter "Specimen characterization") with increasing stress gradient. The fatigue limit $\sigma_{f,MG,Mises}$ can hence be calculated, Equ. (4.44), whereby the input is again the result of the microstructural model, $\sigma_{f,M}$. The coefficient of 0.99 results from the fact, that the microstructural model is based on normal stresses (K_t = 1.02) and has to be converted into Mises equivalent stresses (K_t = 1.01), owing to the different stress concentration factors.
The relation of fatigue limit and relative stress gradient was calculated based on the microstructural model output for V-shape mill-annealed, pancake mill-annealed and V-shape STPQ. These results, compared with experimental data, are shown in Fig. 4.97. It was observed that the combination of microstructural and relative stress gradient model accurately fits the experimental data.

$$\sigma_{f,MG,Mises} = 0.99 \cdot \sigma_{f,M} \qquad \text{Equ. (4.44)}$$

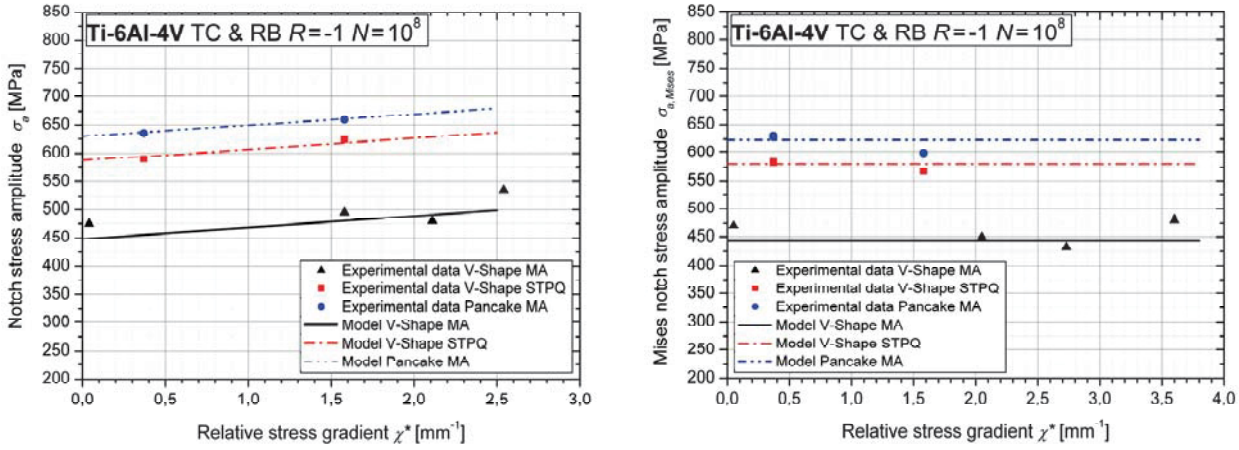

Fig. 4.97: Relative stress gradient models for the high cycle fatigue region, based on different stress types

4.2.4.2. Finite life fatigue strength

The finite life fatigue strength at 10^5 load cycles $\sigma_{N=10^5,MG}$ [MPa] was also linked with the relative stress gradient χ^* [mm^{-1}] via linear relations. Thereby, the fatigue strength at 10^5 load cycles $\sigma_{N=10^5,M}$ is calculated with the information derived from the microstructural model. Again, two different relations were determined for normal stresses, Equ. (4.45), and Mises equivalent stresses, Equ. (4.46). The slope of the S/N-curve in the finite life region remains constant with increasing relative stress gradient, Equ. (4.47).

$$\sigma_{N=10^5,MG} = 58\chi^* + \sigma_{N=10^5,M} - 21.5 \qquad \text{Equ. (4.45)}$$

$$\sigma_{N=10^5,MG,Mises} = 25\chi^* + 0.99\sigma_{N=10^5,M} - 9.5 \qquad \text{Equ. (4.46)}$$

$$k_{MG} = k_M = 8 \qquad \text{Equ. (4.47)}$$

The relation of finite life fatigue strength and relative stress gradient was calculated based on the microstructural model output for V-shape mill-annealed, pancake mill-annealed and V-shape STPQ. These results were compared with experimental data, Fig. 4.98. A good approximation was observed, especially for the equivalent stresses.

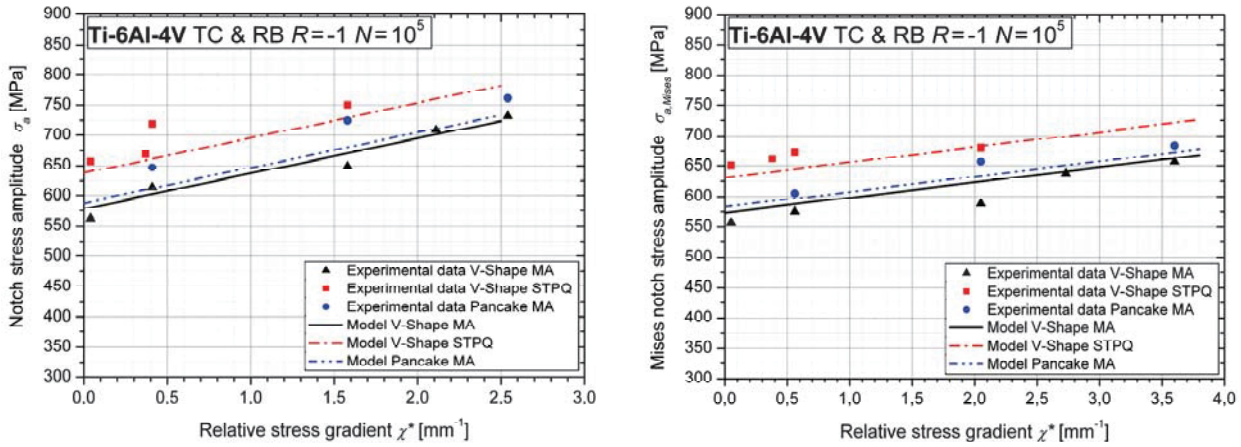

Fig. 4.98: Relative stress gradient models for the finite life region, based on different stresses

The equivalent stress based results are believed to be more meaningful than the normal stress based ones. Especially for the well-defined STPQ microstructure, no significant difference should be observable between the fatigue strengths for tension/compression mild notched and rotating bending unnotched owing to the similar stress gradient (~ 0.4 mm^{-1}). This behavior was indeed observed for the equivalent stress based results (Fig. 4.98, right diagram), but a difference of 100 MPa was determined for the normal stress based ones (Fig. 4.98, left diagram). These findings confirm the equivalent stress based approach and call other models into question.

4.2.5. Conclusion

- An anomalous high notch sensitivity (and therefore low notch supporting effect) was determined for equiaxed- and bimodal-type microstructures, especially in the high cycle fatigue region. This means that the maximum stress in a notch root determines the fatigue limit, almost independent from the relative stress gradient.

- The low supporting effect can be explained with the Kitagawa diagram. It can be supposed that the crack initiation in the notch root is maximum stress controlled (cleavage-type crack initiation) and independent from the relative stress gradient. An initiated crack emanating from a notch root grows – owing to the stress descent – into lower stressed regions and possibly stops. This behavior results in slightly increased fatigue limits with increasing relative stress gradient. Non-propagating cracks play hence a role with respect to the supporting effect of Ti-6Al-4V.

- The supporting effect was analyzed based on normal stress and equivalent stress based fatigue test results. Normal stress based results are commonly used for conventional stress gradient models. This approach does not make sense, if the supporting effect model serves in a computational lifetime estimation based on equivalent stresses. Therefore, it is suggested to use the same equivalent stress for the determination of supporting effect and for lifetime estimation.

- The influence of the element size of a finite element (FE) mesh was discussed with respect to the relative stress gradient. The determination of relative stress gradients of specimens based on a coarse FE mesh leads to a non-conservative notch supporting effect model, if the element size in the FE analysis of a component is smaller. Conservative models can be guaranteed in this research owing to sufficiently fine meshed FE models of the used specimen geometries.

- Models were developed to link finite life fatigue strength and fatigue limit with the relative stress gradient based on normal and equivalent stresses, respectively. In all cases, a linear approach was used. The lower notch supporting effect was thereby determined for the equivalent stress based fatigue test results.

- The equivalent stress based results are believed to be more meaningful than the normal stress based ones. Therefore, the supporting effect was discussed based on equivalent stresses. No supporting effect was ascertained for the fatigue limits. This can be explained by the insignificant supporting effect resulting from non-propagating cracks (as shown in the Kitagawa diagram with Chapetti-curves), combined with the fact of increasing surface roughness and decreasing compressive residual stresses with increasing stress gradient (decreasing notch radius) of the used fatigue test specimens.

- The comparison of Chapetti-curves for two different stress ratios and notch stress distributions of severe notched specimens at the according fatigue limits revealed the applicability of the Chapetti-approach for the determination of the crack growth threshold in respect of crack length for Ti-6Al-4V. The material parameter k, which defines the development of the extrinsic threshold component, was (conservatively) modified to shift the steady state level of the extrinsic threshold component to larger crack lengths.

4.3. Influence of impressed mean stress on the fatigue behavior

The influence of impressed mean stress plays an important role regarding fatigue behavior. Results in literature showed that Ti-6Al-4V exhibits an abnormally high mean stress sensitivity, but the basic mechanisms are not clarified until yet. The focus of this research work is on mill-annealed microstructure without any texture. Solution treated polymer-quenched and hence bimodal Ti-6Al-4V is used for verification.

4.3.1. State-of-the-art

The basic parameters of a periodical fatigue load are summarized in Fig. 4.99. Important are the stress amplitude σ_a, the mean stress σ_m, the maximum stress σ_{max}, the minimum stress σ_{min} and the periodic time T.

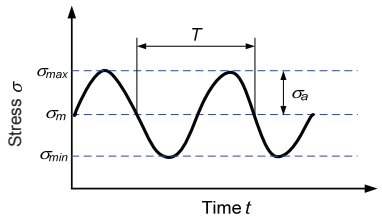

Fig. 4.99: Parameters of a fatigue load

The stress ratio R is used to describe the fraction of mean stress in a fatigue load and is defined as the minimum stress divided by the maximum stress, Equ. (4.48).

$$R = \frac{\sigma_{min}}{\sigma_{max}} \qquad \text{Equ. (4.48)}$$

The influence of mean stress on the bearable stress amplitude at certain load cycles is presented in a Smith or, recently more common, in a Haigh (also known as Goodman) diagram, cf. [78]. A Haigh diagram plots the bearable stress amplitude over the appropriate mean stress for certain load cycles, Fig. 4.100 (l). A Haigh diagram for Ti-6Al-4V (without any additional information) is reported in [153], Fig. 4.100 (r).

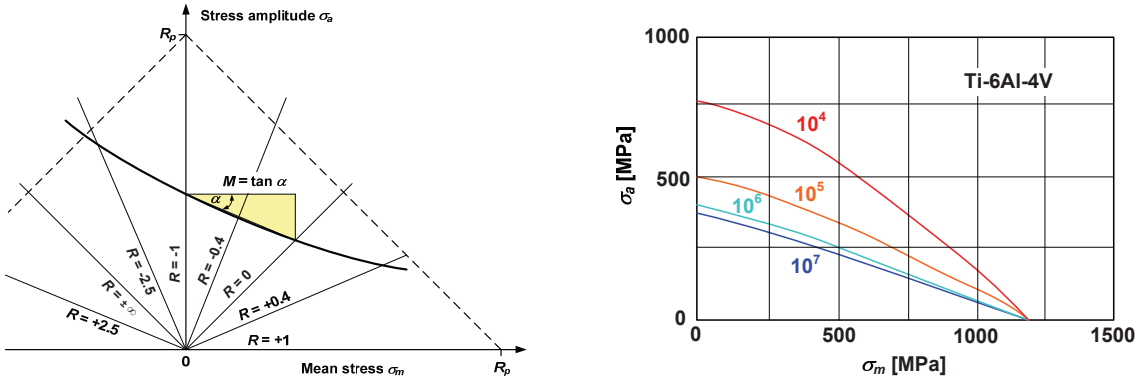

Fig. 4.100: Schematical Haigh diagram (l) [78], and Haigh diagram for Ti-6Al-4V acc. to Schijve [153]

Schütz [154] analyzed various materials with respect to mean stress dependence. He used the bearable stress amplitude at high load cycle values at stress ratios of zero and -1, and defined the mean stress sensitivity *M* as the slope of a constant-life line linking these two values, Equ. (4.49) and Fig. 4.100 (l).

$$M = \tan\alpha = \frac{\sigma_a(R=-1) - \sigma_a(R=0)}{\sigma_m(R=0)} \qquad \text{Equ. (4.49)}$$

Sonsino (reported in [78]) presented a compilation of mean stress sensitivities for different materials in respect of the tensile strength, with the problem that there is no information regarding cycles to failure. It can be assumed that the reported values are valid for (the typical run-out level) 10^7 load cycles. Sonsino stated mean stress sensitivities of 0.25 to 0.35 for titanium alloys. However, these values are not correct for Ti-6Al-4V.

The rare literature regarding influence of mean stress on the fatigue behavior of Ti-6Al-4V indicates anomalous mean stress dependence. Wagner and Gregory [177] summarized the current knowledge, and reported that the anomalous mean stress dependence is crack initiation controlled and it occurs both, in air and in vacuum. Lamellar (β-annealed) microstructures do not show this effect. In (α+β)-annealed – equiaxed or bimodal – microstructures, the influence of mean stress depends on the crystallographic texture and on the loading direction.

This behavior was originally reported by Adachi et al. [26], cf. Fig. 4.101. They analyzed three bimodal and one fine lamellar microstructure and found an anomalous mean stress effect depending on microstructure, texture and loading direction. Pronounced mean stress sensitivity was found for the bimodal microstructures (basal/transverse texture) tested under transverse direction (TD) loading (basal planes perpendicular to the loading direction) but not so under rolling direction (RD) loading (basal planes parallel to the loading direction). Furthermore, they found that the fatigue strengths at 10^7 load cycles at higher stress ratios are the same in vacuum and in air. The fracture surfaces of microstructures exhibiting the anomalous mean stress dependence revealed in the regions of crack nucleation large portions of fracture planes (transcrystalline) of the primary α-phase with the same orientation to the stress axis. This effect was not observed for those microstructures having a "normal" mean stress dependence.

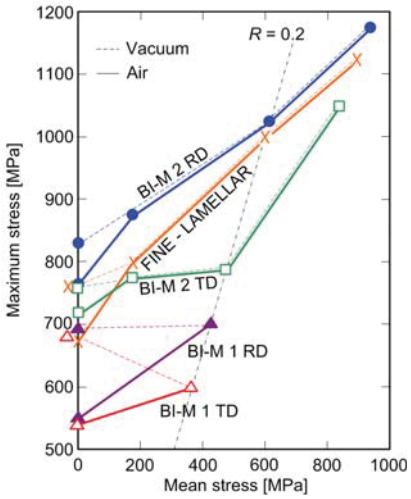

Fig. 4.101: Smith diagram for fatigue strength at 10^7 load cycles for different microstructures [26]

Ivanova et al. [87] analyzed uni-rolled, cross-rolled, and forged Ti-6Al-4V with varying microstructures with respect to mean stress dependence, Fig. 4.102. They found anomalous mean stress dependence at 10^7 load cycles for both, bimodal and equiaxed microstructures with basal/transversal texture. In contrast, they reported "normal" mean stress behavior for textured (uni-rolled) bimodal Ti-6Al-4V and material with lamellar microstructure. However, this "normal" behavior was limited on stress-controlled fatigue tests and not determined under strain-controlled loading. Furthermore, they observed cleavage-like facets at the crack initiation sites for both, bimodal microstructures with or without anomalous mean stress dependence.

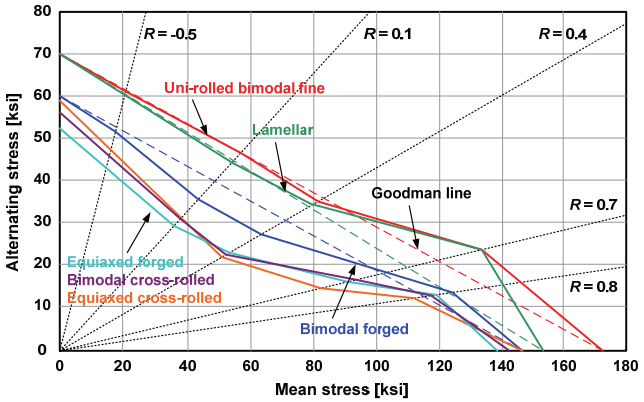

Fig. 4.102: Haigh diagram for Ti-6Al-4V at 10^7 load cycles acc. to Ivanova et al. [87]

Research work of Morrissey et al. ([111], [112]) showed, that equiaxed Ti-6Al-4V (with uneconomical heat treatment) exhibits pronounced stress ratio effects under high cycle fatigue loading (cf. Fig. 4.103). They reported that at high stress ratios ($R > 0.7$), a transition of failure mode occurs from traditional surface fatigue crack initiation and growth to bulk-dominated damage initiation and coalescence of multiple microcracks consistent with a ductile tensile test. At these high stress ratios, with peak stress at or near the macroscopic yield strength, cyclic strain ratcheting is observed, leading to progressive plastic strain accumulation until final failure. Furthermore, their results indicate that there is a significant frequency effect in equiaxed Ti-6Al-4V, especially at low stress ratios (cf. Fig. 4.103). The higher the frequency, the higher is the stress that will cause failure at 10^7 cycles. Morrisey et al. explained the frequency dependence with the interaction of several mechanisms, such as strain rate effects on dislocation motion, diminished active primary slip systems at high frequencies in hcp and bcc materials, and therefore their composites as Ti-6Al-4V, and environmental damage. This stands in contrast to a newer publication of the same authors [113], cf. Fig. 4.10, what calls their results into question.

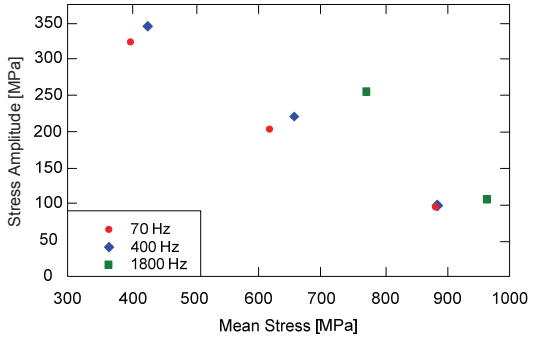

Fig. 4.103: Fatigue strengths at frequencies of 70, 400 and 1800 Hz [111]

Several models exist for the consideration of the mean stress dependence of materials in a lifetime estimation [140]. Three common models are the Goodman approach, Equ. (4.50), the Soderberg approach, Equ. (4.51), and the Gerber parable, Equ. (4.52).

$$\sigma_a = \sigma_a\Big|^{R=-1} \cdot \left(1 - \frac{\sigma_m}{R_m}\right) \qquad \text{Equ. (4.50)}$$

$$\sigma_a = \sigma_a\Big|^{R=-1} \cdot \left(1 - \frac{\sigma_m}{R_{p,t}}\right) \qquad \text{Equ. (4.51)}$$

$$\sigma_a = \sigma_a\Big|^{R=-1} \cdot \left(1 - \left(\frac{\sigma_m}{R_m}\right)^2\right) \qquad \text{Equ. (4.52)}$$

The Goodman approach is often used for Ti-6Al-4V (for lack of alternatives); with the problem that the anomalous mean stress dependence is neglected. This leads to a non-conservative lifetime estimation.

4.3.2. Experimental procedure

The test program for the determination of the influence of impressed mean stress on the fatigue behavior of Ti-6Al-4V consisted of uniaxial tension/compression fatigue tests at six different stress ratios R. All tests were performed at room temperature and ambient air up to 10^8 load cycles.

Unnotched hourglass specimens (Fig. 3.34) were sampled from mill-annealed V-shapes and tested on a SincoTec Power Swing MAG 150 kN resonant testing machine (Fig. 4.104). The testing frequency was approximately 96 Hz. The fatigue tests were performed with stress ratios R of -1, 0, 0.3 and 0.7; some specimens were complementary tested with stress ratios of $-\infty$ and -0.5. The evaluation of the S/N-curves in the finite life region was based on the logarithmic normal distribution. The fatigue strengths at 10^8 load cycles were determined according to the *arcsin*$\sqrt{P}$-method [55].

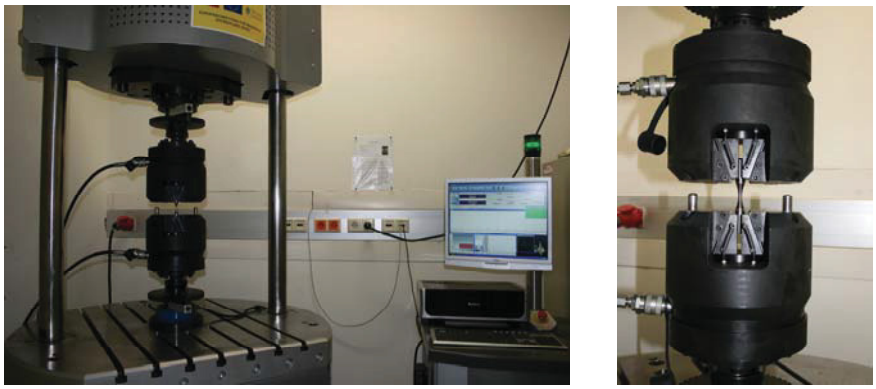

Fig. 4.104: SincoTec Power Swing MAG resonant testing machine

The fracture surfaces were analyzed with a stereo light optical microscope (Olympus SZX12). Two exemplary pictures of a fracture surface are shown for each stress ratio; one overview (16x magnification) and one detailed view of the crack initiation site (64x magnification). The crack initiation site is located at twelve o'clock position in all pictures.

The S/N-curves for stress ratios of -1, 0 and 0.3 are shown in Fig. 4.105 to Fig. 4.107. The corresponding S/N-curve parameters can be found in Tab. 4.36 to Tab. 4.38.

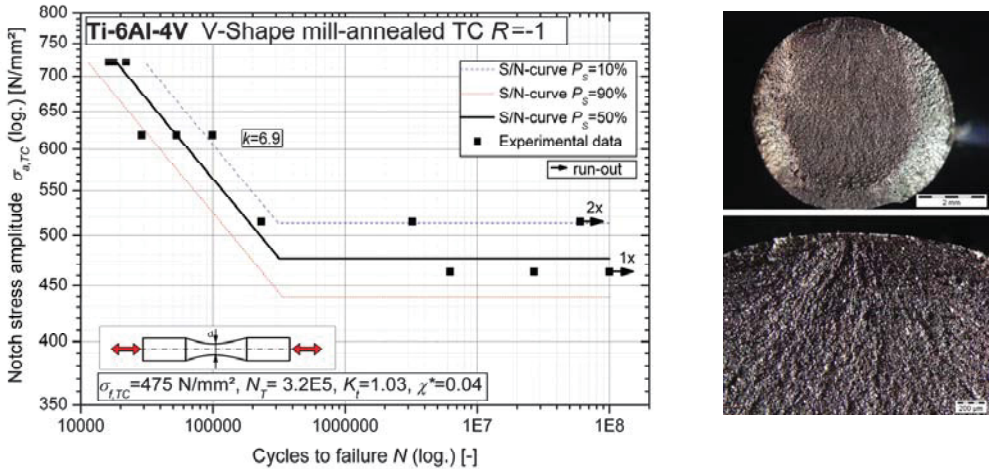

Fig. 4.105: TC S/N-curve (l) and fracture surface (r) for V-shape mill-annealed unnotched, R=-1

Symbol	Description	Unit	Value
σ_f	Fatigue strength at N=10^8	MPa	475
N_T	Cycles at transition	-	3.2E5
k	Slope	-	6.9
T_N	Scatter at finite life	-	1:2.7
T_S	Scatter at N=10^8	-	1:1.2

Tab. 4.36: Parameters for TC S/N-curve V-shape mill-annealed unnotched, R=-1

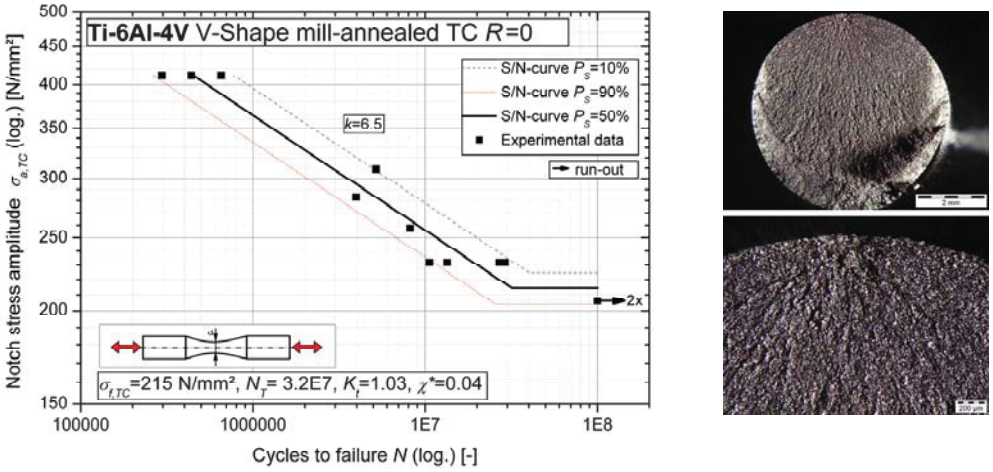

Fig. 4.106: TC S/N-curve (l) and fracture surface (r) for V-shape mill-annealed unnotched, R=0

Symbol	Description	Unit	Value
σ_f	Fatigue strength at N=10^8	MPa	215
N_T	Cycles at transition	-	3.2E7
k	Slope	-	6.5
T_N	Scatter at finite life	-	1:2.9
T_S	Scatter at N=10^8	-	1:1.1

Tab. 4.37: Parameters for TC S/N-curve V-shape mill-annealed unnotched, R=0

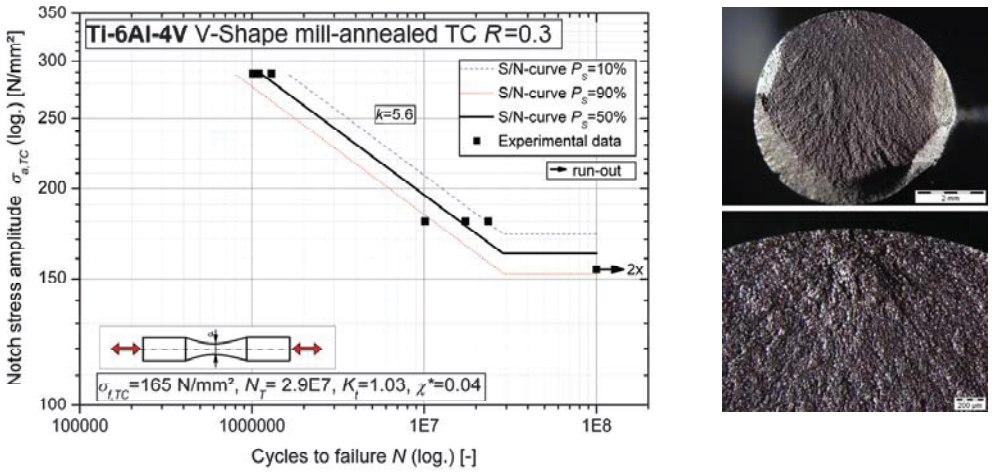

Fig. 4.107: TC S/N-curve (l) and fracture surface (r) for V-shape mill-annealed unnotched, R=0.3

Symbol	Description	Unit	Value
σ_f	Fatigue strength at N=10^8	MPa	165
N_T	Cycles at transition	-	2.9E7
k	Slope	-	5.6
T_N	Scatter at finite life	-	1:2.0
T_S	Scatter at N=10^8	-	1:1.1

Tab. 4.38: Parameters for TC S/N-curve V-shape mill-annealed unnotched, R=0.3

Fatigue tests at stress ratios of 0.7, -0.5 and -∞ were also performed, but there was too less experimental data for determination of S/N-curves. The data point are plotted in Fig. 4.110. The fracture surfaces of specimens tested with stress ratio 0.7 and -0.5 are shown in Fig. 4.108. It was observed that crack initiation occurred independent from stress ratio at or directly underneath the surface.

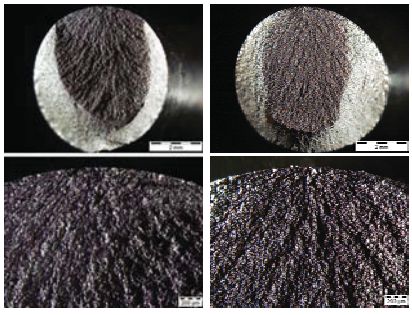

Fig. 4.108: Fracture surface of V-shape mill-annealed unnotched, R=0.7 (l) and R=-0.5 (r)

As mentioned before in the chapter "State-of-the-art", Adachi et al. [26] and also Ivanova et al. [87] reported that the fracture surfaces of microstructures exhibiting the anomalous mean stress dependence revealed in the regions of crack nucleation large portions of (transcrystalline) fracture planes of the primary α-phase with the same orientation to the stress axis. Scanning electron microscopy (SEM) of fracture surfaces of fatigue specimens tested with stress ratios of zero and 0.3 was performed, Fig. 4.109. It was observed that the mill-annealed microstructure without crystallographic texture leads to transcrystalline fracture planes at the crack initiation sites.

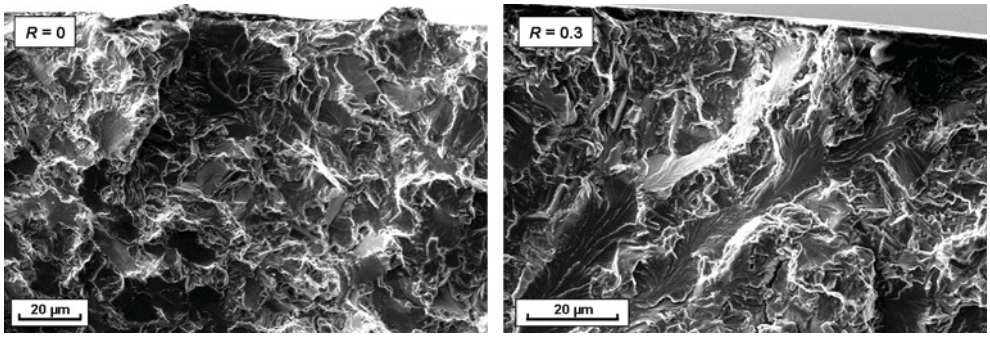

Fig. 4.109: SEM pictures of the crack initiation sites of specimens tested with $R = 0$ (l) and $R = 0.3$ (r)

4.3.3. Discussion

The comparison of all tension/compression fatigue tests on unnotched specimens performed with different stress ratios are shown in Fig. 4.110. It was observed that the bearable stress amplitude is considerably decreased with increasing mean stress. Furthermore, it is important that the cycles at transition between finite life and fatigue limit lies beyond 10^7 load cycles for stress ratios $R \geq 0$. The fatigue test results in literature (e.g. [26] or [87]) are usually related to run-out levels of 10^7 load cycles. This leads to an overestimation of the "fatigue limits" at stress ratios $R \geq 0$. Therefore, the anomalous mean stress dependence is more pronounced for the fatigue limit as supposed in literature.

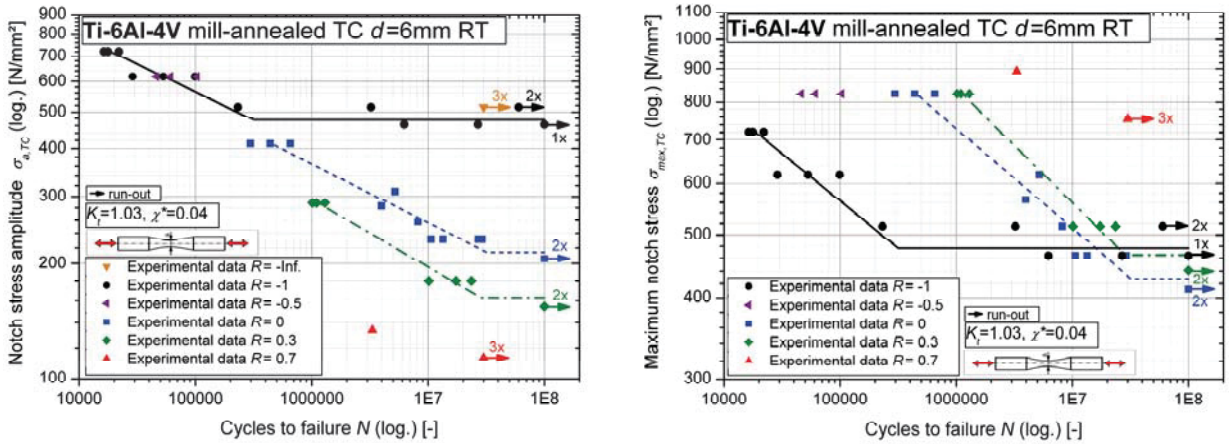

Fig. 4.110: Comparison of TC S/N results at different stress ratios

The mean stress sensitivity M can be calculated according to Equ. (4.49), and varies with the load cycles. The evaluation of the presented fatigue test results is stated in Tab. 4.39.

N [-]	M [-]
10^6	0.3
10^7	0.8
10^8	1.2

Tab. 4.39: Mean stress sensitivity M in respect of the cycles to failure N

Until now, the conventional wisdom has been that the maximum possible mean stress sensitivity is 1, and that the typical mean stress sensitivity for aluminum alloys, titanium alloys and steels ranges from 0.1 to 0.8. However, there is no distinct explanation in literature for such mean stress dependencies.
On the contrary, the results presented for mill-annealed Ti-6Al-4V can be explained by basic fatigue and fracture mechanisms. The fatigue limit of Ti-6Al-4V follows the maximum stress due to cleavage-type crack initiation, independent from the stress ratio. The stress level that has to be reached for cleavage-type fracture of a grain or phase boundary will always be the same in an isotropic material. In addition, impressed mean stress decreases the stress intensity threshold, which may be the reason for the slight decrease of the fatigue limit based on maximum stress for stress ratios $R \geq 0$, cf. Fig. 4.110 (r). Machining induced residual stresses are another possibility for mean stress sensitivities > 1.
The fatigue strength in the finite life region depends on stress amplitude and stress ratio. It can be assumed that the (maximum stress controlled) crack initiation phase does not play a major role. However, the fatigue strength is considerably influenced by crack growth. If the basic Equ. (4.7) of the linear elastic fracture mechanics is used as a basis, it is well known that a decrease of the stress range leads to a one-to-one decrease of the stress intensity factor. At a stress ratio $R = 0$, a fatigue crack already initiates at lower stress amplitudes (stress ranges) due to the achievement of the maximum stress limit as mentioned above. An initiated crack grows at a lower stress amplitude (lower stress range and therefore also lower stress intensity factor). Assuming almost the same crack growth behavior for applied stress ratios of $R = 0$ and $R = -1$, the finite life S/N-curve based on stress amplitude for $R = 0$ has to be the extension of the finite life S/N-curve for $R = -1$, cf. Fig. 4.110. One possible reason for the similar crack growth rates is, that the local effective stress ratio and effective stress intensity factor range of a short crack is influenced by the residual stresses. With increasing mean stress ($R = 0.3$) the fatigue limit still follows the maximum stress. In the finite life region it can be assumed that the crack growth is accelerated owing to decreased crack closure, which leads to a lower finite life fatigue strength.
Fig. 4.111 depicts schematically the mean stress dependence of Ti-6Al-4V including the basic findings explained before.

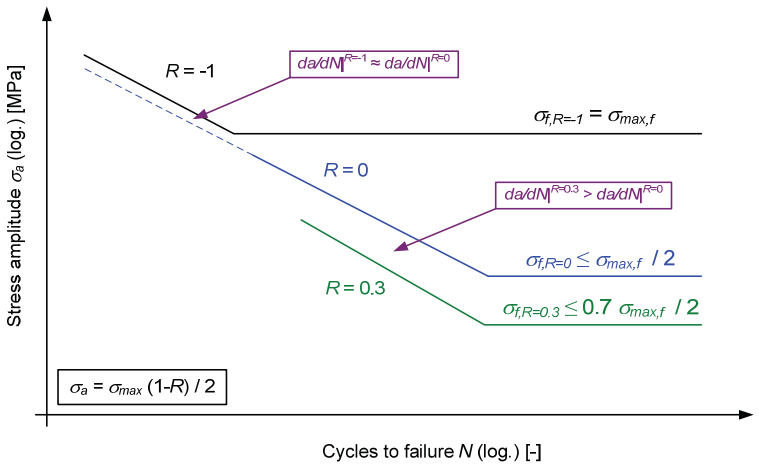

Fig. 4.111: Influence of impressed mean stress on S/N-curves based on stress amplitudes

4.3.4. Phenomenological models

It was observed that the analyzed Ti-6Al-4V exhibits anomalous mean stress dependence. This high mean stress sensitivity is associated with α-phase and their transcrystalline fracture. Phenomenological models for the finite life and high cycle fatigue region were developed based on the fatigue test results shown before. They are valid for forged Ti-6Al-4V without any precipitations or crystallographic texture.

4.3.4.1. High cycle fatigue strength

Fig. 4.112 shows the bearable notch stress amplitudes at 10^8 load cycles for stress ratios of -1, 0, 0.3 and 0.7. It was observed that (using a logarithmical scaling of the stress axis) the data points represent a line.

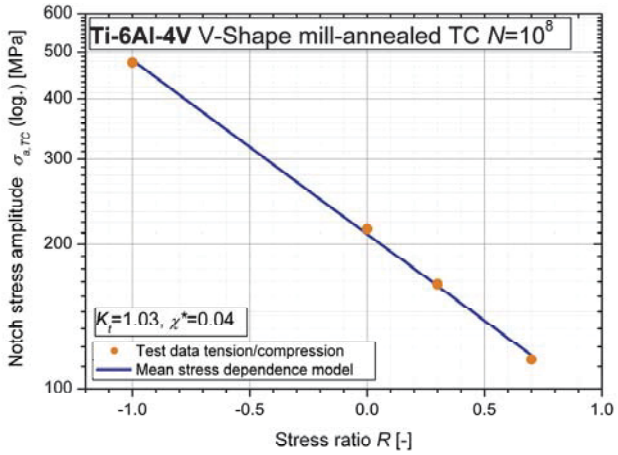

Fig. 4.112: Influence of mean stress on the fatigue limit

Therefore, the high cycle fatigue strengths at 10^8 load cycles (fatigue limits) were exponentially linked with the stress ratio R for the region $-1 \leq R \leq 0.7$, Equ. (4.53). Thereby, $\sigma_{f,MGM}$ [MPa] is the fatigue limit amplitude considering the mean stress dependence of Ti-6Al-4V, $\sigma_{f,MG}$ [MPa] is the fatigue limit amplitude resulting from the microstructural model supplemented by the stress gradient model and R [-] is the stress ratio.

$$-1 \leq R \leq 0.7: \quad \sigma_{f,MGM} = \sigma_{f,MG} \cdot e^{-0.83(1+R)} \qquad \text{Equ. (4.53)}$$

The according mean stress $\sigma_{fm,MGM}$ to the fatigue limit is defined in Equ. (4.54).

$$-1 \leq R \leq 0.7: \quad \sigma_{fm,MGM} = \sigma_{f,MGM} \frac{1+R}{1-R} \qquad \text{Equ. (4.54)}$$

For stress ratios $1 > R > 0.7$, a linear connection, Equ. (4.55), between the fatigue limit for stress ratio 0.7 and the 0.2%-yield strength $R_{p0.2}$ was chosen in accordance to the approach of Soderberg [140]. This approach was used to be conservative with respect to the high mean stress sensitivity. Goodman [140] chose the ultimate tensile strength as upper limit for the mean stress.

However, it has to be mentioned at this point that, owing to the small difference between yield strength and ultimate tensile strength (caused by the almost ideal-elastic ideal-plastic behavior of Ti-6Al-4V), there will not be a significant variance between this two approaches. For the determination of the 0.2%-yield strength, the correlations explained in the chapter "Estimation of tensile strength" were used, cf. Equ. (4.19) to Equ. (4.22).

$$\sigma_{f,MGM} = \frac{\sigma_{f,MGM}\Big|^{R=0.7} \cdot R_{p0.2} \cdot (1-R)}{R_{p0.2} + \sigma_{f,MGM}\Big|^{R=0.7} - \sigma_{fm,MGM}\Big|^{R=0.7} + R \cdot \left(\sigma_{f,MGM}\Big|^{R=0.7} + \sigma_{fm,MGM}\Big|^{R=0.7} - R_{p0.2}\right)} \qquad \text{Equ. (4.55)}$$

For stress ratios between -∞ and -1, a linear relation was chosen to link fatigue limit and mean stress, Equ. (4.56).

$$-\infty \le R \le -1: \quad \sigma_{f,MGM} = \frac{\sigma_{f,MG}}{1 + 0.08\dfrac{1+R}{1-R}} \qquad \text{Equ. (4.56)}$$

For the region $1 < R \le \infty$, the fatigue limit at R = -∞ was linear connected with the compressive yield strength $R_{p,c}$. The mathematic description can be found in Equ. (4.57). The compressive yield strength $R_{p,c}$ was achieved according to Equ. (4.22), cf. chapter "Estimation of tensile strength".

$$1 < R \le \infty: \quad \sigma_{f,MGM} = \frac{\sigma_{f,MGM}\Big|^{R=-\infty} \cdot R_{p,c} \cdot (R-1)}{2\sigma_{f,MGM}\Big|^{R=-\infty} - R_{p,c} + R \cdot R_{p,c}} \qquad \text{Equ. (4.57)}$$

A Haigh diagram plots the bearable stress amplitude at certain load cycles over the corresponding mean stress [78]. Fig. 4.113 shows the Haigh diagram (experimental data and the results of the presented models) at 10^8 load cycles for the mill-annealed V-Shape based on notch stresses.

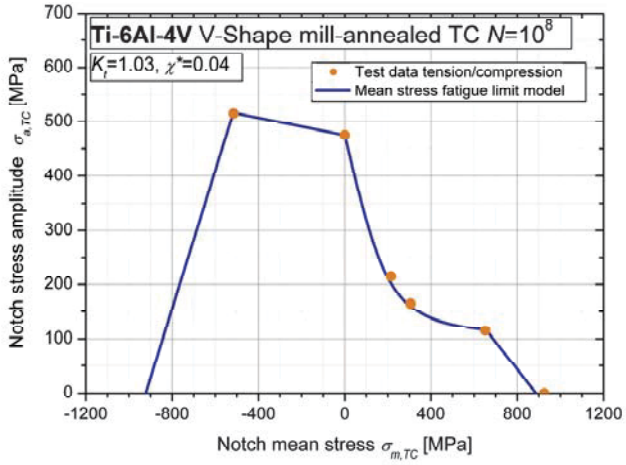

Fig. 4.113: Haigh diagram of mill-annealed Ti-6Al-4V

4.3.4.2. Finite life fatigue strength

The mean stress dependence of the finite life region was described with two models, which link the number of cycles at transition and the slope of the S/N-curve in the finite life region with the stress ratio. The combination of these two models leads to a description of the finite life region in respect of mean stress.

The dependence of the number of cycles at transition under consideration of the mean stress $N_{T,MGM}$ and stress ratio R in the region $-1 \leq R \leq 0$ is given in the exponential Equ. (4.58). Thereby, $N_{T,MG}$ is the number of cycles at transition of the stress gradient corrected microstructural-based S/N-curve.

$$-1 \leq R \leq 0: \quad N_{T,MGM} = N_{T,MG} \cdot e^{4.5(1+R)} \qquad \text{Equ. (4.58)}$$

For $-\infty \leq R \leq -1$ and $1 < R \leq \infty$ applies:

$$-\infty \leq R \leq -1 \quad and \quad 1 < R \leq \infty: \quad N_{T,MGM} = N_{T,MGM}\Big|^{R=-1} \qquad \text{Equ. (4.59)}$$

Equ. (4.60) is used for stress ratios between zero and one.

$$0 \leq R < 1: \quad N_{T,MGM} = N_{T,MGM} \cdot e^{4.5} \qquad \text{Equ. (4.60)}$$

The application of these models for the mill-annealed V-shape is shown in Fig. 4.114 (l). The chosen models fit the test data of the mill-annealed V-shape very well.

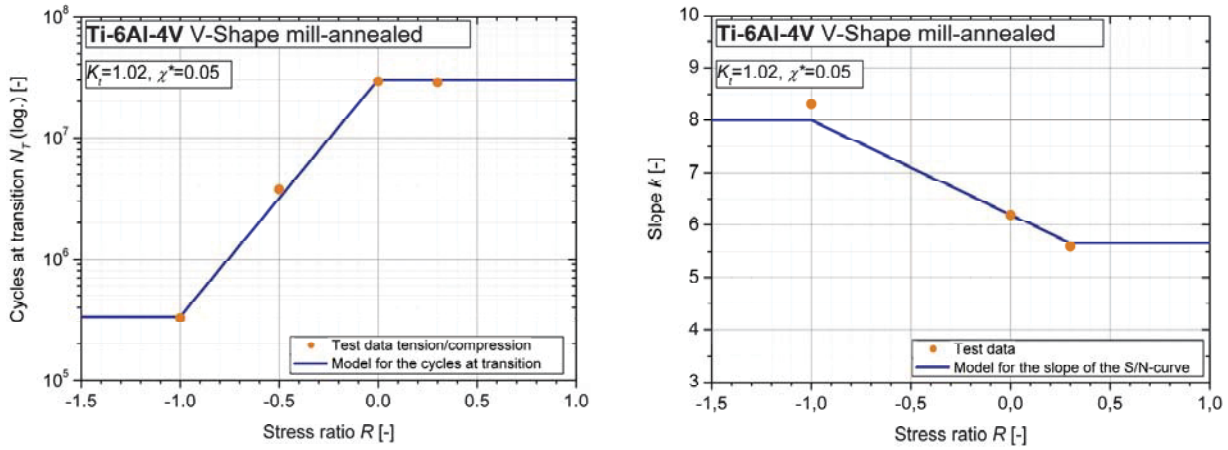

Fig. 4.114: Influence of stress ratio on the number of cycles at transition (l) and slope (r) of the S/N-curve

The slope k_{MGM} of the mean stress corrected S/N-curve is given in Equ. (4.61) in respect of the stress ratio R; valid for $-1 \leq R \leq 0.3$.

$$-1 \leq R \leq 0.3: \quad k_{MGM} = k_{MG} - 1.8 \cdot (1 + R) \qquad \text{Equ. (4.61)}$$

It was assumed that the slope remains constant for $-\infty \leq R \leq -1$ and $1 < R \leq \infty$, Equ. (4.62).

$$-\infty \leq R \leq -1 \quad and \quad 1 < R \leq \infty: \quad k_{MGM} = k_{MGM}\Big|^{R=-1} \qquad \text{Equ. (4.62)}$$

Furthermore, it was supposed that the slope remains constant at stress ratios between 0.3 and 1, Equ. (4.63).

$$0.3 \leq R < 1: \quad k_{MGM} = k_{MGM}\Big|^{R=0.3} \qquad \text{Equ. (4.63)}$$

Fig. 4.114 (r) compares the model for the slope of the S/N-curve with the experimental data for the mill-annealed V-shape. A good accordance was observed.

4.3.4.3. Visualization

The derived models for high cycle and finite life region were used for generation of a new developed S/N/R-surface. The S/N/R-surface shows the influence of the stress ratio R on the fatigue strength for any number of cycles to failure. The modeled S/N/R-surface for the mill-annealed V-shape is shown in Fig. 4.115. It is based on the measured microstructural parameters (cf. Tab. 3.5) and application of the microstructural, relative stress gradient, and mean stress models discussed before. Additionally, the experimental data of the tension/compression fatigue tests on unnotched specimens are plotted.

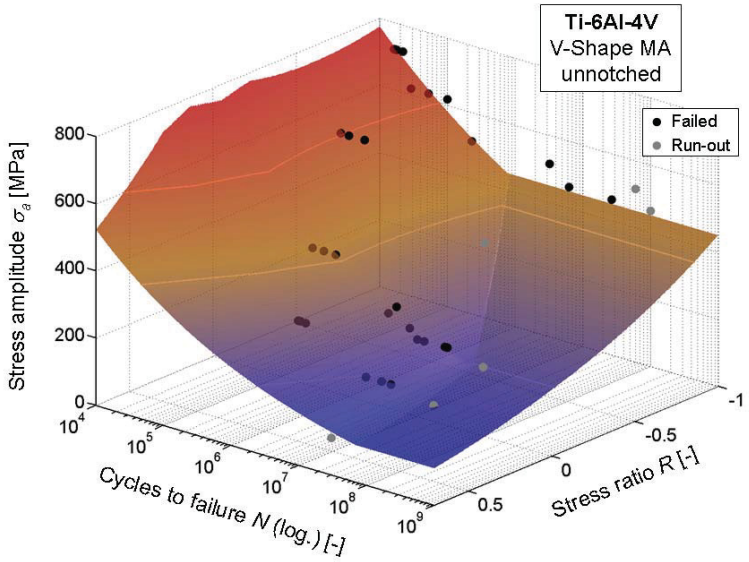

Fig. 4.115: S/N/R-surface for V-shape mill-annealed

A good accordance of modeled S/N/R-surface and experimental results was observed. This is a first confirmation of the chosen approaches.

4.3.5. Verification

The verification of the developed models was done on solution treated polymer-quenched (STPQ) V-shape. Unnotched specimens were tested under tension/compression loading with stress ratios of -1 and 0.3.
The S/N-curves were determined according to the models (microstructure, stress gradient, mean stress) described before, using the microstructural parameters of the V-shape STPQ as a basis. Fig. 4.116 shows the comparison of experimental data and modeled S/N-curves. It was observed that the used models lead to an accurate estimation of all analyzed S/N-curves for the solution treated polymer-quenched V-shape.

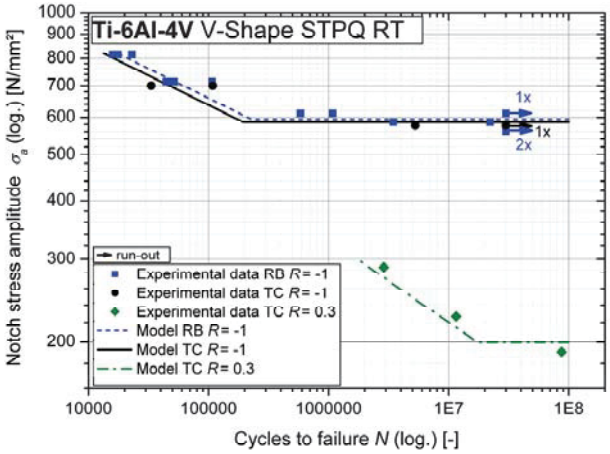

Fig. 4.116: Comparison of experimental data and modeled S/N-curves

4.3.6. Conclusion

- Both, isotropic Ti-6Al-4V with equiaxed- and bimodal-type microstructures exhibit anomalous mean stress dependence. A higher mean stress sensitivity ($M \geq 1$, full mean stress sensitivity) was found for the fatigue limit (fatigue strength at 10^8 load cycles) than reported in literature. This behavior is caused by the shift of the cycles at transition between finite life and fatigue limit beyond 10^7 load cycles for stress ratios $R \geq 0$.

- Scanning electron microscopy analyses of fracture surfaces at the crack initiation site revealed that transcrystalline fracture planes play a major role regarding mean stress dependence. It can be concluded that there are enough favorable-oriented cleavage planes with respect to crack initiation in an isotropic material to cause anomalous mean stress dependence.

- A mean stress sensitivity $M = 1$ implies that the maximum stress determines the fatigue limit of isotropic equiaxed- and bimodal-type Ti-6Al-4V (for $-1 \leq R \leq 0.3$). New phenomenological models were hence developed, which consider this anomalous mean stress sensitivity and describe the mean stress dependence of both, finite life region and fatigue limit. Currently used mean stress models for the fatigue limit, e.g. the Goodman or Soderberg approach, are non-conservative (cf. Fig. 4.117) and should not be used for Ti-6Al-4V with bimodal or equiaxed microstructures.

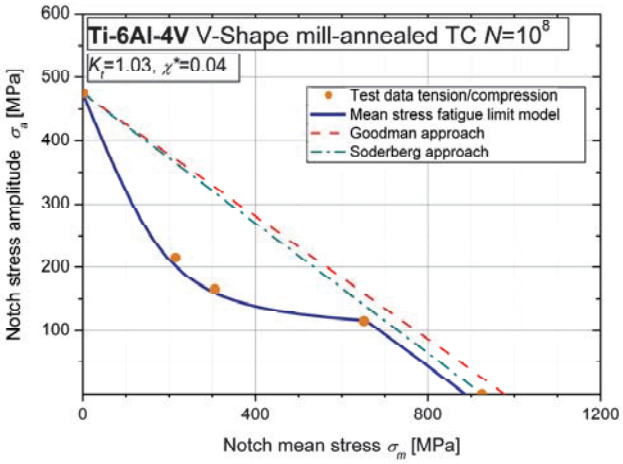

Fig. 4.117: Comparison of the developed mean stress dependence model and currently used approaches for the fatigue limit

- The anomalous mean stress sensitivity of Ti-6Al-4V was discussed by means of basic fatigue and fracture mechanisms. The finding that the maximum stress determines the high cycle fatigue strength (full mean stress sensitivity) is consistent with the high notch sensitivity, cf. chapter “Influence of relative stress gradient on the fatigue behavior”, and also with the crack initiation mechanism discussed in the chapter “Influence of microstructure on the fatigue behavior”. It means, that a fatigue crack initiates, if a certain maximum stress is reached to cause cleavage fracture; almost independent from stress ratio or stress gradient.

4.4. Influence of multiaxial loading on the fatigue behavior

The influence of multiaxial loading is important for a lifetime estimation based on local stresses. No nominal stresses can be calculated in components with complex geometries; finite element (FE) analysis has to be used. A FE analysis determines the stress tensor in every element of a FE mesh. Different methods exist for conversion of this stress tensor in a useful input for damage accumulation, e.g. critical plane criteria. Thereby, the normal stress and shear stress in every plane have to be summarized to an equivalent stress. The choice of the right type of equivalent stress criterion (e.g. Mises, Tresca, etc.) is therefore crucial for a lifetime estimation based on local stresses.

4.4.1. State-of-the-art

The information in literature regarding influence of multiaxial loading on the fatigue behavior of Ti-6Al-4V is very limited. Delahay [54] reported fatigue limits for different types of loading (tension/compression, rotating bending, torsion, plane bending, combined plane bending and torsion). Data is also available from prior research [1], done on lamellar Ti-6Al-4V.

Type of load	τ_f [MPa]	σ_f [MPa]	Source
Tension/compression	-	583	Delahay
Rotating bending	-	602	Delahay
Torsion	411	-	Delahay
Plane bending	-	652	Delahay
Plane bending + torsion	255	442	Delahay
Tension/compression	-	320	Oberwinkler
Rotating bending	-	320	Oberwinkler
Torsion	210	-	Oberwinkler
Rotating bending + torsion	115	230	Oberwinkler

Tab. 4.40: Summary of literature data ([1], [54]) regarding influence of type of load on the fatigue limit

Kallmeyer et al. [89] reported several fatigue test results for proportional and non-proportional multiaxial loading on bimodal Ti-6Al-4V. They determined, that the finite life fatigue strength for a 90° out-of-phase load (90° sinusoidal lag between the shear and axial stress), a load path that is often considered to be critical with regard to deformation and fatigue damage [159], is higher (factor 1.6 in lifetime) than for proportional loading. Furthermore, they mentioned, that when the maximum shear stress exceeds about 80% of the torsional yield strength, the allowable stress amplitude in bending or torsion is reduced relative to the fully reversed case. For levels of maximum stress less than 80% of the torsional yield strength, a static or mean shear stress has little effect on the fatigue strength of metals, cf. [157].

4.4.2. Experimental procedure

The test program for the determination of the influence of multiaxial loading on the fatigue behavior of Ti-6Al-4V consisted of uniaxial tension/compression, rotating bending, alternating torsion, and combined rotating bending / alternating torsion fatigue tests (stress ratio R = -1) up to maximum 10^8 load cycles. All tests were performed at room temperature and ambient air.

Unnotched hourglass specimens (Fig. 3.34) were sampled from mill-annealed V-shapes and tested on several test stands. The rotating bending and tension/compression tests were already discussed. The torsional (T) and multiaxial (MAX) fatigue tests were performed on a test rig designed at the Chair of Mechanical Engineering (Fig. 4.118). The testing frequency for torsion and multiaxial testing was 30 Hz. The fatigue tests were performed with a stress ratio R of -1 and in particular -0.5. The multiaxial loading was a proportional and synchronal combination of alternating torsion and rotating bending, Fig. 4.119. The ratio of shear stress to normal stress for multiaxial loading was chosen to be 0.5. For the purpose of comparison, other microstructures ($STPQ_V$, ST_V) and sharp notched specimens were additionally tested under alternating torsion.

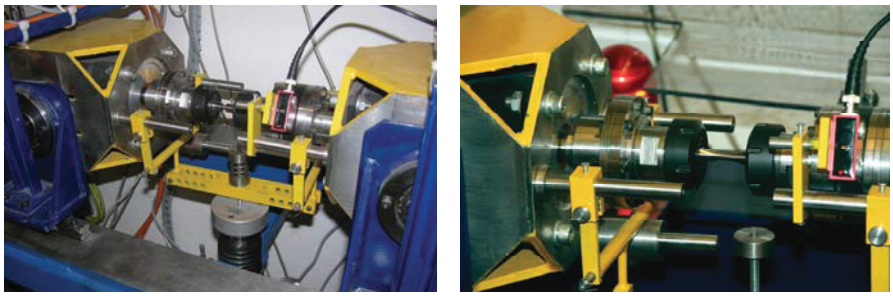

Fig. 4.118: Test rig for torsion and multiaxial loading

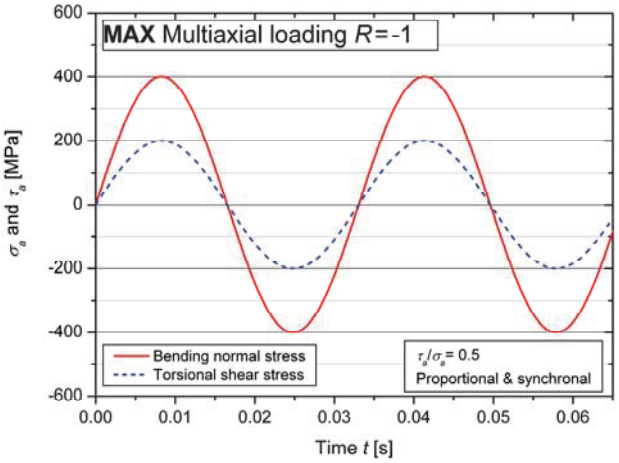

Fig. 4.119: Example for proportional synchronal multiaxial loading

The evaluation of the S/N-curves in the finite life region was based on the logarithmic normal distribution. The fatigue limits were determined according to the *arcsin√P*-method [55]. The fatigue strengths and especially the scatter are not statistically firm due to the limited specimen lot sizes.

The tension/compression S/N-curve for mild-notched specimens (relative stress gradient comparable to unnotched torsion and multiaxial loading) was already presented, cf. Fig. 4.81. The S/N-curves for torsional and multiaxial loading (Fig. 4.120 and Fig. 4.121) and their according parameters (Tab. 4.41 and Tab. 4.42) are reported below.

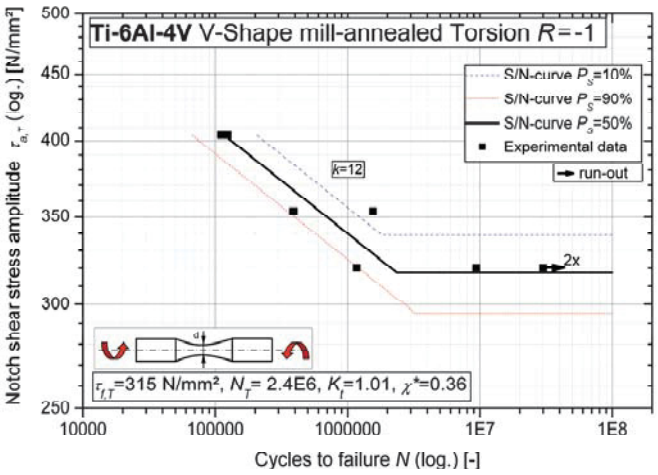

Fig. 4.120: Alternating torsion S/N-curve for V-shape mill-annealed unnotched, *R*=-1

Symbol	Description	Unit	Value
τ_f	Fatigue strength at N=10^8	MPa	315
N_T	Cycles at transition	-	2.4E6
k	Slope	-	12
T_N	Scatter at finite life	-	1:3.1
T_S	Scatter at N=10^8	-	1:1.2

Tab. 4.41: Parameters for alternating torsion S/N-curve V-shape mill-annealed unnotched, *R*=-1

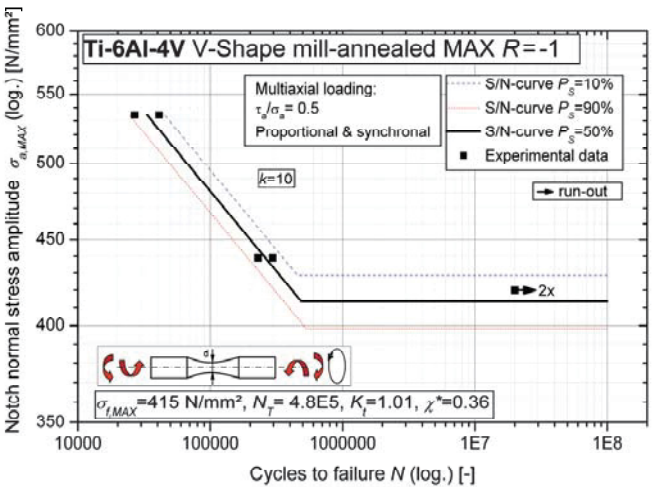

Fig. 4.121: Combined torsion and rotating bending S/N-curve for V-shape mill-annealed unnotched, *R*=-1

Symbol	Description	Unit	Value
σ_f	Fatigue strength at N=10^8	MPa	415
N_T	Cycles at transition	-	4.8E5
k	Slope	-	10
T_N	Scatter at finite life	-	1:1.9
T_S	Scatter at N=10^8	-	1:1.1

Tab. 4.42: Parameters for multiaxial S/N-curve V-shape mill-annealed unnotched, *R*=-1

4.4.3. Discussion

The fracture surfaces were analyzed with a stereo light optical microscope (Olympus SZX12). It has to be mentioned at this point that the interpretation of fracture surfaces of torsional and multiaxial loaded samples is difficult due to the smearing of the fracture surfaces owing to the shear stresses.

It was observed that the characteristic of the fatigue crack initiation site of torsional loaded specimens depends on the stress amplitude. At high stress levels the crack initiation was clearly caused by shear stresses (crack direction perpendicular to the specimen axis), Fig. 4.122. The crack propagation mode switched at a certain crack length from shear stress controlled to normal stress controlled.

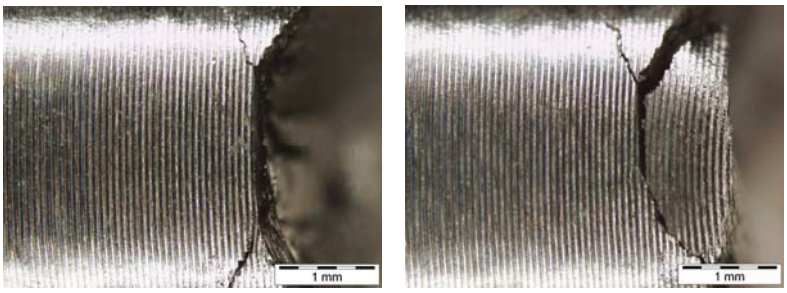

Fig. 4.122: Crack initiation site at torsional loaded specimens, high stress amplitude

At lower stress levels, the crack initiation mechanism is significantly harder to identify, cf. Fig. 4.123. The left picture shows a macroscopic depiction of the crack initiation site (marked with a red ellipse). The crack direction was determined to meet the specimen axis at an angle of approximately 60°; neither the direction of the maximum normal stress (45°) nor those with the maximum shear stress (90°).

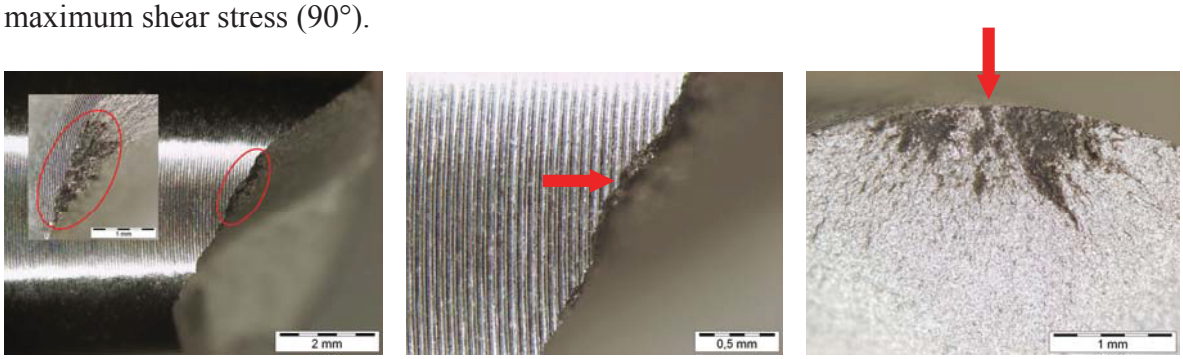

Fig. 4.123: Crack initiation site at a torsional loaded specimen

The microscopic analysis of the crack initiation site revealed that the macroscopic angle results from combination of shear stress (perpendicular to stress axis) and normal stress (under 45° to stress axis) dominated crack fractions. It can be assumed that the crack initiates shear stress controlled (Fig. 4.123, center and right picture, marked with red arrow), propagates alternating shear and normal stress controlled and switches finally to pure normal stress controlled (Fig. 4.123, left picture). It has to be mentioned that crack initiation from a microstructural point of view can be different to these findings, which was already discussed in the chapter “Influence of microstructure on the fatigue behavior”.
The transition from shear stress or combined shear and normal stress controlled crack propagation to pure normal stress controlled crack propagation occurs (independent from the stress level) at a crack length of approximately 1 mm.

A schematical illustration of the applied multiaxial loading and the according Mohr's circle of stress are shown in Fig. 4.124.

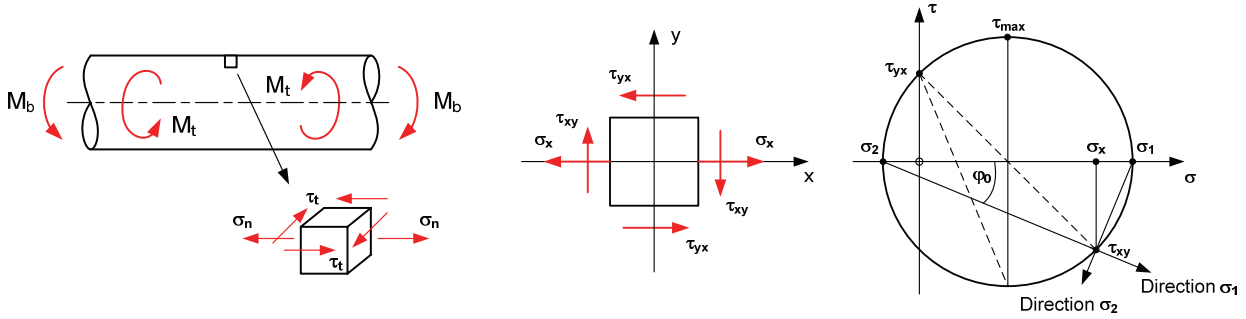

Fig. 4.124: Schematical illustration of the applied multiaxial loading and the according Mohr's circle

The direction of the principal normal stress meets the specimen axis at an angle φ_0. For the present load case $\tau_a/\sigma_a = 0.5$, $\varphi_0 = \pm 22.5°$. The maximum shear stress applies hence at ±22.5° and ±67.5°, respectively. The direction of the principal stresses is continuously constant. These relations are valid for two points of the round specimen, namely when maximum bending stress (tension or compression) and maximum torsional stress occur at the same time. All other regions of the perimeter of a cross section have a phase shift between maximum torsion and maximum bending stress, which leads to smaller maximum normal and shear stresses and differences in the direction of the maximum principal stresses.

The analysis of the fracture surfaces of the multiaxial loaded samples led to an ambiguous result. Crack initiation either due to shear stresses or due to normal stresses is possible with respect to the fracture characteristics, cf. Fig. 4.125.

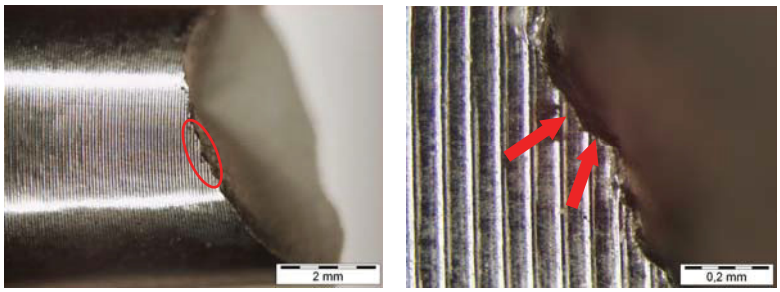

Fig. 4.125: Crack initiation site at a multiaxial loaded specimen

The ratio of the fatigue limit in torsion and tension/compression is a measurement for the shear stress sensitivity. A fatigue limit ratio τ_f/σ_f of 0.6 was observed for the mill-annealed V-shape. Prior research [1] and results of Delahay [54] showed a similar ratio, namely 0.7.

In a lifetime estimation based on local stresses, an equivalent stress is used to combine normal and shear stresses for damage accumulation. A typical approach for ductile metals is thereby the von Mises equivalent stress, Equ. (4.64).

$$\sigma_{Mises} = \sqrt{\sigma_x^2 + \sigma_y^2 + \sigma_z^2 - \sigma_x \sigma_y - \sigma_x \sigma_z - \sigma_y \sigma_z + 3\left(\tau_{xy}^2 + \tau_{xz}^2 + \tau_{yz}^2\right)} \qquad \text{Equ. (4.64)}$$

A more material-specific equivalent stress, which has to be used in combination with the critical plane approach, is reported in [106]. Thereby, the weighting of the normal and shear stresses depends on the ratio of the fatigue limits under tension/compression and alternating torsion c_{equ}, Equ. (4.65). For $c_{equ} > 1.4$ applies Equ. (4.66).

$$c_{equ} = \frac{\sigma_{f,TC,R=-1}}{\tau_{f,T,R=-1}} \qquad \text{Equ. (4.65)}$$

$$\sigma_{equ} = \sqrt{c_{equ}^2 \left(1 - \frac{c_{equ}^2}{4}\right)\sigma_n^2 + c_{equ}^2 \cdot \tau^2} \qquad \text{Equ. (4.66)}$$

Based on the experimental results and in accordance to the equivalent stress presented above, a modified equivalent stress $\sigma_{equ,Ti64}$ for the critical plane approach was achieved for Ti-6Al-4V, Equ. (4.67).

$$\sigma_{equ,Ti64} = \sqrt{0.75\sigma_n^2 + 3\tau^2} \qquad \text{Equ. (4.67)}$$

The comparison of the equivalent stress criterion proposed for Ti-6Al-4V and the von Mises equivalent stress reveals identically shear stress weighting. The reason for the need of a normal stress coefficient in the critical plane equivalent stress is stated in [106].

The experimental S/N-curves were compared based on equivalent stresses (Fig. 4.126). It was observed that the used equivalent stress, Equ. (4.67), leads in combination with the critical plane approach to a good accordance of the fatigue limits for all types of loading. In the finite life region, the multiaxial and pure torsional loading led to higher finite life fatigue strengths. This can be ascribed to slower crack growth owing to shear mode or combined shear mode and crack opening mode propagation. The influence of the (α+β)-content with respect to this behavior will be discussed below.

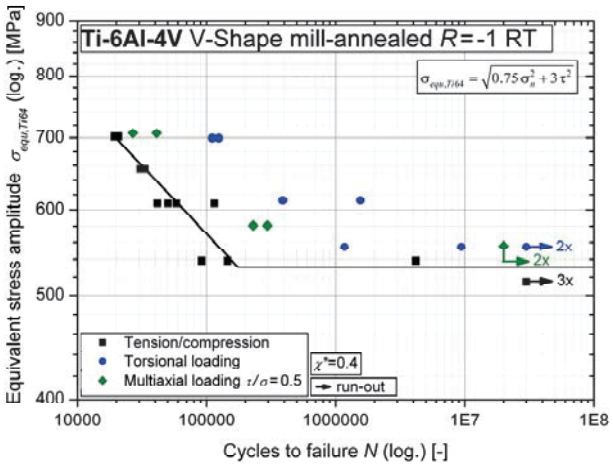

Fig. 4.126: Comparison of S/N-curves under different types of loading

Another empirical model for consideration of multiaxial loading is the Gough-Pollard equation [72], Equ. (4.68). σ_f and τ_f are thereby the fatigue limits under bending and torsional loading, respectively. This equation represents an ellipse and contains a material-specific weighting of shear and normal stresses. Gough et al. found that this relation describes the fatigue behavior of multiaxial loaded steel samples.

$$\left(\frac{\sigma_{n,a}}{\sigma_f}\right)^2 + \left(\frac{\tau_a}{\tau_f}\right)^2 = 1 \qquad \text{Equ. (4.68)}$$

For other materials, a modified Gough-Pollard relation was introduced; using an exponent z, Equ. (4.69).

$$\left(\frac{\sigma_{n,a}}{\sigma_f}\right)^z + \left(\frac{\tau_a}{\tau_f}\right)^z = 1 \qquad \text{Equ. (4.69)}$$

For the analyzed mill-annealed microstructure, the original value $z = 2$ leads to a good accordance with the experimental data, Fig. 4.127. The comparison of Gough-Pollard relation and equivalent stress model exhibits that they are almost identical. The reason for this small difference is, that the shear stress fatigue limit is used as input in the Gough-Pollard approach, whereas the equivalent stress model estimates the shear stress fatigue limit based on the results for normal stresses. The Gough-Pollard approach is descriptive for simple multiaxial load cases. However, the disadvantage of the Gough-Pollard relation is that the applicability is limited to the fatigue limit, and the shear stress fatigue limit has to be known. Therefore, the equivalent stress $\sigma_{equ,Ti64}$ was used in combination with the critical plane approach for lifetime estimation.

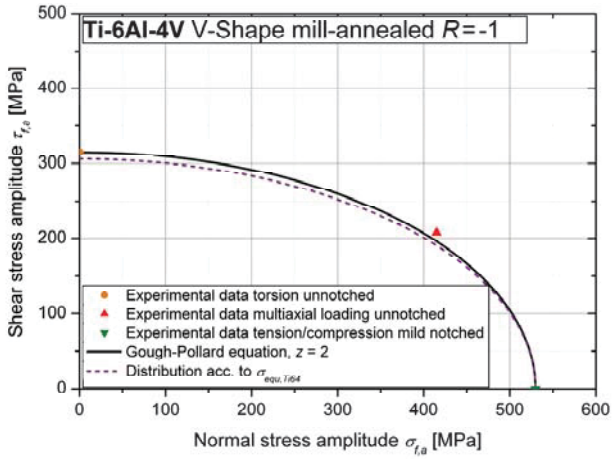

Fig. 4.127: Comparison of Gough-Pollard relation, equivalent stress model and experimental data

With respect to crack propagation, the presented equivalent stress should not be used for calculation of stress intensity factors. Normal stresses (crack opening mode I) are considerably more unfavorable with respect to crack growth than shear stresses (propagation mode II and mode III). Therefore, it is suggested that the maximum principal stress should be used for the determination of stress intensity factors.

This leads still to conservative stress intensity factors, because it implies the worst case of crack-to-load arrangement (maximum principal stress perpendicular to crack ➝ pure opening mode I).

The influence of mean shear stress and the influence of a relative stress gradient on the torsional fatigue strength were additionally determined for the mill-annealed V-shape, to verify the findings of Sines and Ohgi [157] regarding mean stress effect, and the developed relative stress gradient models (which are based on pure normal stress loading) for pure shear stress.

The comparison of test results for two different stress ratios, namely R = -1 and R = -0.5, are shown in Fig. 4.128. It was observed that the influence of mean shear stress is insignificant in the high cycle fatigue region, but the finite life fatigue strength is decreased at high stress amplitudes. Fröschl [66] found for quenched and tempered steel, that yielding occurs under pure torsion at a von Mises equivalent stress level, which is 19% higher than the yield point under pure tension. Assuming a similar behavior for Ti-6Al-4V, the torsion yield strength should approximate 1100 MPa Mises equivalent stress. The tested equivalent stress amplitude levels (R = -0.5) of 700 MPa and 610 MPa yield in maximum stress levels of 930 MPa and 815 MPa. These maximum stress levels are higher (mean shear stress effect observable) and lower (no mean shear stress effect) than 80% of the torsional yield strength (880 MPa), respectively. It can hence be assumed, that the findings of Sines and Ohgi [157] (little mean shear stress effect if maximum shear stress is lower than 80% of torsional yield strength) are valid for Ti-6Al-4V.

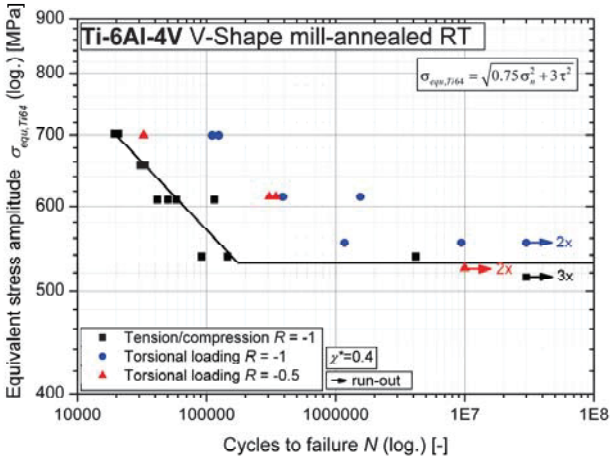

Fig. 4.128: Influence of impressed mean shear stress on the fatigue behavior

The S/N-curve for sharp notched specimens under torsional loading was determined based on the unnotched test results using the relative stress gradient model, Fig. 4.129 (l). The comparison of modeled S/N-curve and experimental data exhibits that the supporting effect in the finite life region is higher under pure torsion than predicted by the relative stress gradient models (which are based on tension/compression tests). This may be explained by the different crack propagation modes. A good accordance was determined for the fatigue limit.

The fracture characterization with a stereo light optical microscope (Olympus SZX12) exhibited several crack initiation sites. Fig. 4.129 (r) shows the fracture-causing crack initiation site (marked with red arrows) and a secondary crack initiation site on the fragment (orange arrow). Shear stress induced crack initiation (crack perpendicular to specimen axis) was observed, comparable to the findings for unnotched specimens under torsional loading.

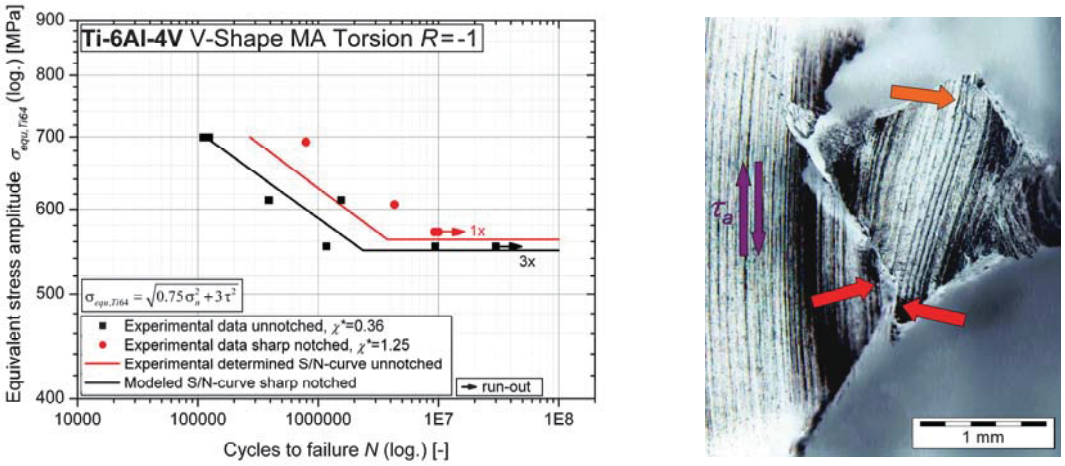

Fig. 4.129: Influence of relative stress gradient on the torsional fatigue strength (l), fracture analysis (r)

4.4.4. Verification

The verification of the chosen equivalent stress criterion was done on unnotched specimens sampled from V-shape ST and V-shape STPQ. Fatigue tests were performed under alternating torsional loading at room temperature. The experimental results were compared with modeled S/N-curves based on the microstructural models presented before, using the according microstructural parameters as input. The shear stress amplitudes of the torsional loading were converted into equivalent stresses. The good accordance of experimental data and modeled S/N-curves for both bimodal microstructures reveals that the chosen equivalent stress is suitable for Ti-6Al-4V. The finite life fatigue strength is approximately 10% underestimated. It is believed that the lesser difference of modeled S/N-curves and experimental data in the finite life region for these microstructures compared to the mill-annealed one are based on the (α+β)-content. The (short) crack growth behavior in equiaxed-type microstructures is dominated by primary α-phase. It can be assumed that the crack growth rate in primary α-phase is significantly lower under shear propagation mode, whereas in (α+β)-phase shear mode propagation leads to similar crack growth rates compared to pure crack opening mode.

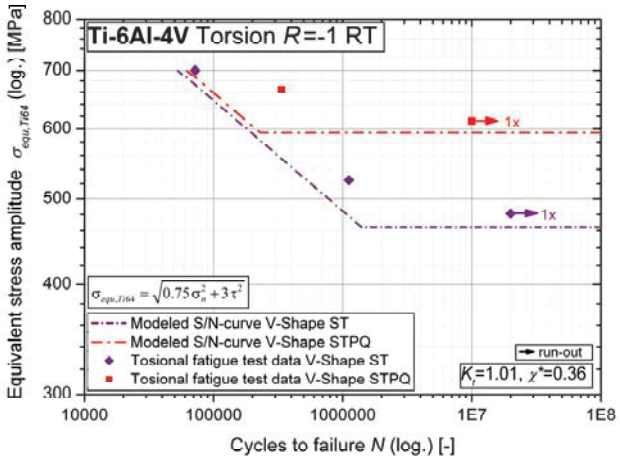

Fig. 4.130: Comparison of modeled S/N-curves and experimental data for different microstructures

4.4.5. Conclusion

- Several fatigue tests were performed under tension/compression, torsional and multiaxial loading, respectively. Based on these experimental results, a modified equivalent stress criterion was proposed for Ti-6Al-4V.

- For torsional loading, it was observed that fatigue cracks initiate under maximum shear stress. The long crack propagation is pure normal stress controlled if the crack reaches a length of approximately 1 mm.

- It was shown that the proposed equivalent stress criterion is valid for the high cycle fatigue strength (fatigue limit) of Ti-6Al-4V under torsional and under proportional multiaxial loading.

- The usage of the modified equivalent stress for finite life fatigue strength of equiaxed-type microstructures under alternating torsion leads to a (conservative) overestimation of shear stresses owing to the disregard of decelerated crack propagation in shear mode. An overestimation was also determined for bimodal-type microstructures, but the (conservative) difference between model and experimental data was just 10%.

- The proposed equivalent stress should not be used for determination of stress intensity factors. A conservative approach is to use the maximum principal stress.

- The influence of mean shear stress on the fatigue strength of Ti-6Al-4V is insignificant as long as the maximum shear stress does not exceed about 80% of the torsional yield strength, cf. [157].

- The proposed notch supporting effect models lead to a conservative prediction of the finite life fatigue strength under alternating torsion load. A good accordance was determined for the fatigue limit.

- It can be assumed that the crack growth rate in primary α-phase is significantly lower under shear propagation mode, whereas in (α+β)-phase shear mode propagation leads to similar crack growth rates compared to pure crack opening mode.

4.5. Influence of flaws on the fatigue behavior

The requirement for tolerance of components to flaws and damages, especially for aerospace applications, necessitates the utilization of damage tolerant (DT) component design. The influence of two different types of flaws on the fatigue behavior of Ti-6Al-4V is analyzed in this research, namely crack-like flaws and indentations.

4.5.1. State-of-the-art

Lazzeri and Mariani [100] summarized, that "Damage Tolerance" (the regulation uses the term "fail-safe (residual strength after flaw growth) evaluation") requires that the structure can retain, after a partial failure, the capability to withstand the limit load. It is based on the use of redundant solutions (fail-safe) or on the slow crack propagation approach (or, preferably, on the no-growth approach). The use of redundant solutions is often possible in stiffened shell structures, and sometimes multiple load paths can be easily introduced. Nevertheless, most cyclic loaded components cannot be other than single load path design. In this case, the slow crack growth (or the no-growth) option is the recommended one. Inspection intervals must be determined, in order to ensure that, if a defect is present, this is timely detected and consequent repair actions taken.

In literature, the influence of flaws resulting from foreign-object damage (FOD) is often discussed, especially with respect to turbine gas engines. Oakley and Nowell [124] reported that FOD is usually taken to refer to hard objects such as stones, hardware and pavement fragments, in contrast to soft-body damage, which refers to objects such as ice, birds and animals. FOD is typically caused when the rotating blade strikes the object, and the velocity of the blade is often more significant than the axial velocity of the object. The result of the impact is localized damage in the form of a notch or dent (typically on or close to the leading edge), together with microstructural damage and a surrounding residual stress field. The damage will significantly reduce the fatigue strength of the blade and may lead to premature failure under typical operating loads. During operation, the blades are subjected to significant tensile stresses due to centrifugal loading and during the flight cycle may experience aerodynamically induced vibrations, leading to additional stresses. The amplitude of the vibrational loading is typically much smaller than that due to centrifugal loading and hence vibration is generally thought to give rise to high cycle fatigue (HCF). In contrast, the effect of centrifugal loading is frequently considered to be low cycle fatigue (LCF), although it does not always fit the classical definition of LCF since there may not be macroscopic plasticity in the blade. Under the overall combined HCF/LCF loading, investigations ([52], [82], [144]) have shown a two-phase crack growth process whereby a crack may initiate and grow under LCF until the crack is sufficiently long for the stress intensity factor range caused by HCF loading to exceed the threshold. From this point of onset, HCF dominates the crack growth process and essentially marks the end of the component's useful life ([136], [137]). Following a FOD event, however, the situation is more complex. The damaged blade may initially experience HCF crack growth due to the high stress concentration at the notch, coupled with a reduced short crack threshold. This growth will continue until the stress intensity range drops below the HCF threshold. The crack may then continue growing under LCF until it reaches a length where HCF growth can recommence [82].

Oakley and Nowell [124] analyzed ballistic impact damaged, blade-like specimens and introduced an elastic short crack arrest approach to estimate the fatigue life of blades under combined high- and low cycle fatigue following FOD.

They reported, that for high applied stress ratios, residual compressive stresses will merely modify the local stress ratio of a propagating crack and will have relatively little effect on the crack driving force, whereas for low applied stress ratios, the stress intensity factor range experienced by the crack will be reduced because of a compressive residual stress field. However, their proposed approach includes the Goodman approach for consideration of the mean stress sensitivity and a simple model for the prediction of crack growth thresholds in respect of the stress ratio, and can hence be classified as weak. They produced non-conservative prediction for $R = 0.3$ and conservative ones for $R = 0.8$, which may be attributed to the negligence of the anomalous mean stress dependence of Ti-6Al-4V.

Peters et al. [129] analyzed solution treated and overaged Ti-6Al-4V with a primary α-grain size of 20 µm and an (α+β)-content of 40%. They reported that FOD reduces the fatigue strength primarily due to four factors: stress concentration, microcrack formation, impact-induced plasticity and tensile residual stresses associated with the impact damage. Although all of these factors play an important role under certain conditions, in the case of high impact velocities (300 m/s), the formation of damage-induced microcracks appears to be the primary contributor to lifetime reduction. During subsequent cycling after impact, these microcracks, which are formed in the pile-up of material around the rim, can act as preferred sites for propagating fatigue cracks. When applied stresses are large compared to the impact-induced tensile residual stresses, and in the presence of relatively large (~30-50 µm) impact-induced microcracks, HCF failures (after 10^5-10^6 cycles) initiate directly at the impact site and lead to short fatigue lives. In contrast, at low applied stresses relative to the residual stresses, HCF failures (after 10^7-10^8 cycles) initiate in locations away from the impact site at regions of peak tensile residual stresses, and the necessity for crack nucleation leads to longer fatigue lives. Peters et al. proposed a Kitagawa-Takahashi approach, where the limiting threshold conditions are defined by the stress-concentration corrected smooth-bar fatigue limit (at microstructurally small crack sizes) and a "worst case" stress intensity factor threshold (at larger crack sizes). This approach must be additionally corrected for the presence of tensile residual stresses to account for FOD failures initiated away from the impact site.

Ruschau et al. [150] studied the influence of high-speed, glass bead FOD impacts on the fatigue strength of simulated airfoil samples. They reported that fatigue strength losses could not be correlated to FOD depth alone. Irregular features such as small tears, notches, etc., caused by the FOD impacts appear to influence fatigue strength more than the depth of the FOD.

Mall et al. [108] investigated the high cycle fatigue behavior at 10^7 load cycles of Ti-6Al-4V, after being subjected to simulated FOD. They found, that the effective stress ratio or mean stress near FOD was different from that applied to the specimen, due to residual stresses introduced from the impact. They concluded that these modified stress states provided the explanation for reduction in the fatigue strength of the material with FOD.

Vaughan and Chang [173] took a critical look at the application of damage tolerance methods to rotorcraft components. They found that NASGROW 3, NASGROW 4, and AFGROW, three commonly used fatigue crack growth programs, have shown large scatter in crack growth life prediction. Analytical and experimental approaches for determination of crack growth rates and thresholds are not well established, and they remain an active research topic. In addition, the material test data for the threshold region is limited and exhibits significant scatter. How this data is treated will significantly affect structural integrity assessment.

Prevey et al. [139] reported that low plasticity burnishing provides an order of magnitude improvement in the damage tolerance of a Ti-6Al-4V fan blade, owing to introduced compressive residual stresses extending through the thickness of the leading edge.

It can be concluded that it is possible to predict the lifetime of foreign-object damaged components, if all conditions are known. This includes the type, shape and material of the object, the relative impact velocity, and the impact angle. If all these parameters are available, a simulation of the residual stress distribution at the impact site is possible. Extensive microscopy of the damaged part is additionally necessary to define, whether microcrack formation occured during the impact or not. Usually, it is not the case that all necessary information is available for the lifetime estimation of a component after FOD.

Other damaging mechanisms, e.g. fretting, are also hard to include in a computational lifetime estimation. Lindley [101] summarized, that fretting is the oscillatory sliding motion of small slip amplitude between two contacting surfaces. It is promoted by high frequency, low amplitude vibratory motion and commonly occurs in clamped joints and “shrunk-on” components found, for example, in keyways, splines and dovetail joints. The surface damage produced by fretting can take the form of fretting wear (with or without environmental assistance) or fretting fatigue where the material fatigue properties can be seriously degraded. Fretting fatigue involves a highly complex interplay between mechanical, metallurgical and environmental factors and their individual contributions can be quite different from those operative in plain fatigue. Cadario [44] concluded that the fretting fatigue phenomenon could be characterized by the following main features: stick-slip conditions with highly concentrated surface damage, relatively low wear and debris formation, non-proportional and multiaxial contact stress state, high stress gradients, and contained plastic deformations and material transfer at the contacting surfaces.

Lindley [101] critically examined analytical procedures for fretting fatigue based on either crack initiation (S/N-approach) or crack growth (fracture mechanics approach). They concluded that fretting fatigue problems should be eliminated or minimized by good design involving reduction of local stresses and avoidance of contacting interfaces wherever possible. In situations where fretting fatigue remains a threat, palliatives can be considered. The widespread S/N-methodology (using fretting fatigue strength reduction factors) can be used to assess the performance of various palliative treatments (friction reduction at the fretting interface for decrease of stresses available to promote fatigue crack initiation and early crack growth, or improvement of the near surface fatigue properties by introducing compressive residual stresses). The fretting fatigue damage parameter (the product of tangential stress σ_t along the line contact, interface shear stress τ, and relative slip amplitude between surfaces δ) of Ruiz et al., [147] to [149], can be used to rationalize palliative action in combating fretting. It should be noted that a lubricant, which lowers the coefficient of friction, would have opposite effects on τ and δ, and hence the combined effect must be carefully considered.

The fretting wear (e.g. [77]) and fretting fatigue behavior (e.g. [51]) of Ti-6Al-4V has widely been reported in literature, but the influencing variables are extensive and further research is necessary to include these damaging mechanisms in a computational lifetime estimation.

It can be concluded that both, foreign object damage and fretting damage are highly complex and cannot be generally modeled and considered in computational lifetime estimation. However, it is necessary to provide a simple model for design engineers to estimate the damage tolerance of a component for any flaw or damage, using an estimated maximum flaw size as input. Such a model will be discussed below.

4.5.2. Experimental procedure

Fatigue tests were performed on specimens provided with two different types of initial flaws, namely crack-like flaws, and indentations. The physically short crack specimens (which were already discussed in the chapter "Influence of microstructure on the fatigue behavior") were used for determination of the influence of crack-like flaws on the fatigue behavior. Additionally, round specimens were provided with hardness indentations at the gauge to characterize the influence of indentations on the fatigue behavior.

4.5.2.1. Physically short crack specimens

Tension/compression fatigue tests were performed with three different stress ratios R (-1, 0 and 0.3) on a servo-hydraulic test stand at room temperature and ambient air with a testing frequency of 30 Hz. Plane short crack growth (SCG) specimens (cf. Fig. 3.41) were used, provided with wire eroded initial cracks with a width of 0.04 mm and a length a_0 of 0.2 or 0.4 mm, respectively. These fatigue tests were already discussed in the chapter "Influence of microstructure on the fatigue behavior"; the results are shown in Fig. 4.48 to Fig. 4.54.

The practical relevance of these types of specimens can be explained by the comparison of a typical forging lap and the wire-eroded initial crack. Both, the shape and the dimensions of the forging lap and the wire-eroded initial crack are similar. It can be concluded that the SCG specimens with the wire-eroded initial cracks are suitable for the determination of the influence of crack-like flaws, e.g. forging laps, on the fatigue strength.

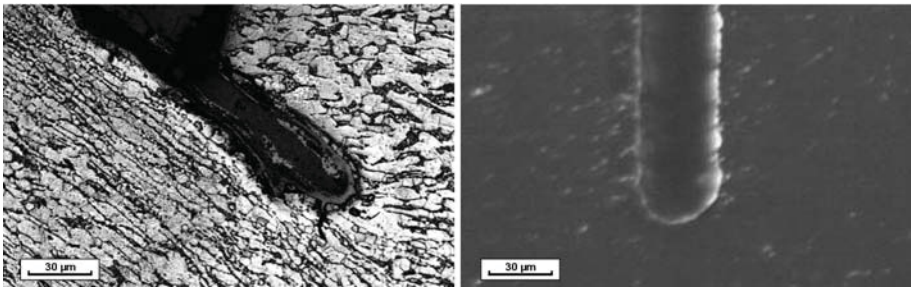

Fig. 4.131: Comparison of forging lap (l) and wire-eroded initial crack (r)

4.5.2.2. Flawed round specimens

High cycle fatigue tests were performed on flawed hourglass specimens under rotating bending loading ($R = -1$) or tension/compression loading ($R = -1$ and $R = 0$) at room temperature and ambient air with a testing frequency of 65 - 95 Hz. The specimens were provided with a cone-shaped Rockwell (HRC) indentation at the gauge to simulate a flaw. The fatigue test results are shown in Fig. 4.132 to Fig. 4.134; the according parameters can be found in Tab. 4.43 to Tab. 4.45. The fracture surfaces were analyzed with a stereo light optical microscope (Olympus SZX12). Two exemplary pictures of a fracture surface are shown for each S/N-curve; one overview (16x magnification) and one detailed view of the crack initiation site (64x magnification). The crack initiation site is located at twelve o'clock position in all pictures. It was observed that the fatigue crack usually initiates at the indentation. This will be discussed more in detail below.

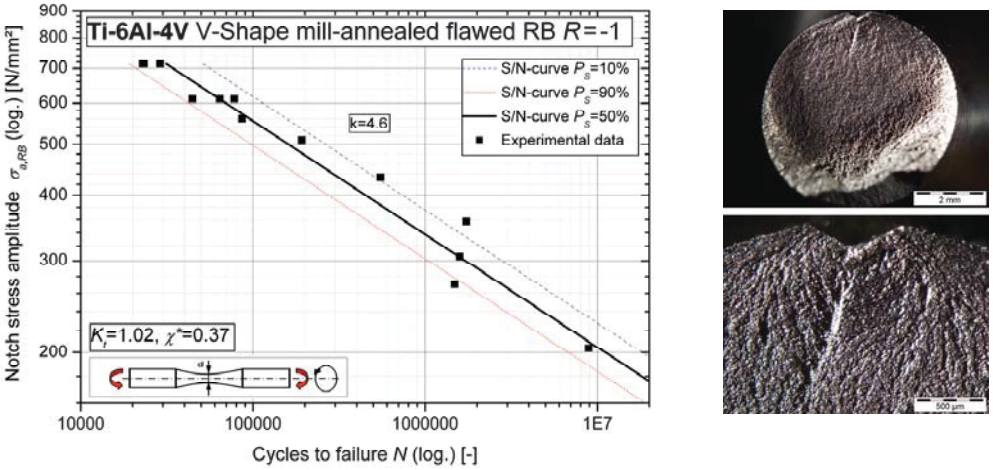

Fig. 4.132: Rotating bending S/N-curve (l) and fracture surface (r) for V-shape mill-annealed flawed

Symbol	Description	Unit	Value
σ_a	Fatigue strength at N=10^7	MPa	205
N_T	Cycles at transition	-	-
k	Slope	-	4.6
T_N	Scatter at finite life	-	1:2.7
T_S	Scatter at N=10^8	-	-

Tab. 4.43: Parameters for RB S/N-curve V-shape mill-annealed flawed

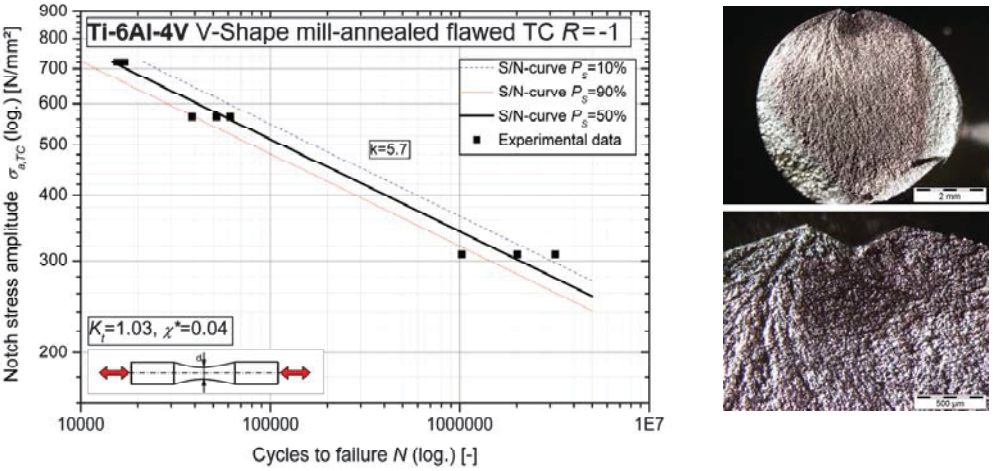

Fig. 4.133: TC S/N-curve (l) and fracture surface (r) for V-shape mill-annealed flawed, R=-1

Symbol	Description	Unit	Value
σ_a	Fatigue strength at N=10^6	MPa	340
N_T	Cycles at transition	-	-
k	Slope	-	5.7
T_N	Scatter at finite life	-	1:2.1
T_S	Scatter at N=10^8	-	-

Tab. 4.44: Parameters for TC S/N-curve V-shape mill-annealed flawed, R=-1

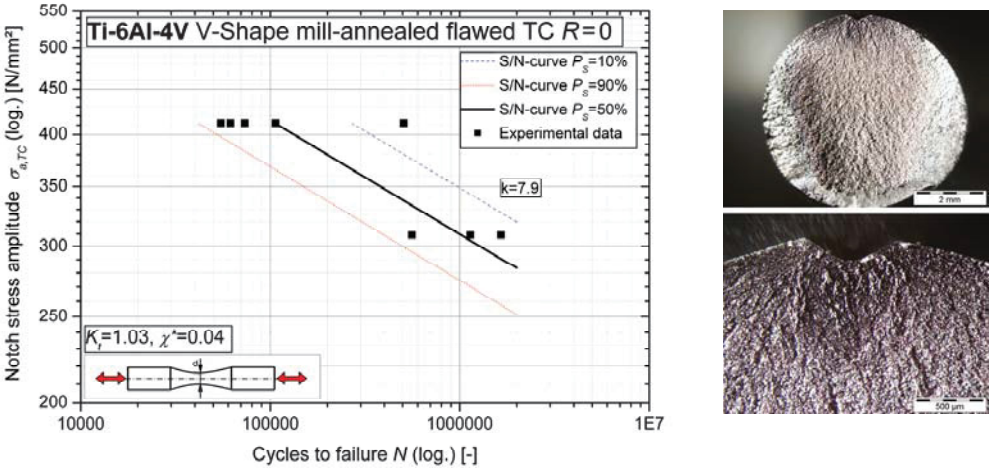

Fig. 4.134: TC S/N-curve (l) and fracture surface (r) for V-shape mill-annealed flawed, R=0

Symbol	Description	Unit	Value
σ_a	Fatigue strength at N=10^6	MPa	310
N_T	Cycles at transition	-	-
k	Slope	-	7.9
T_N	Scatter at finite life	-	1:6.5
T_S	Scatter at N=10^8	-	-

Tab. 4.45: Parameters for TC S/N-curve V-shape mill-annealed flawed, R=0

The comparison of the fatigue test results of unflawed and flawed specimens is shown in Fig. 4.135. It was observed that the indentation has a significant influence on the fatigue limit and, depending on the stress ratio, also on the finite life fatigue strength. The similarity of the finite life regions of the unflawed specimens for R = 0 and those of the flawed specimens for R = -1 already indicates that the residual stresses at the indentation and the resulting local modification of the stress ratio plays an important role regarding fatigue strength of the flawed specimens.

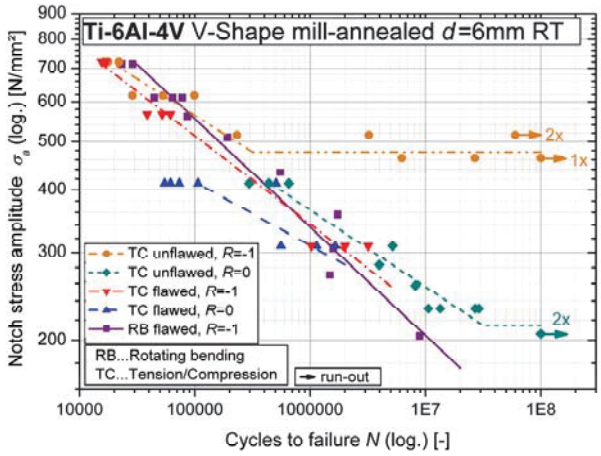

Fig. 4.135: Comparison of S/N-curves of unflawed and flawed round specimens

4.5.3. Discussion

4.5.3.1. Physically short crack specimens

The applicability of the Chapetti-curve for Ti-6Al-4V was already discussed (cf. chapter "Influence of relative stress gradient on the fatigue behavior", Fig. 4.96), and the material constant for the development of the extrinsic threshold component with increasing crack length was adapted, Equ. (4.42). The determined correlation of stress intensity factor threshold and crack length was consequently used in this chapter.

The principle of the Kitagawa diagram was also used for the finite life region. The Kitagawa-curve ($Y = 1.12$, according to [114]) was determined for defined cycles to failure. The finite life fatigue strength of the unnotched tension/compression tests were used as upper limit of the Kitagawa-curve. The "finite life threshold" was adapted, so that the knee of the Kitagawa-curve is tangent to the stress distributions. The supporting effect in the finite life region can therefore be explained in a similar manner as already discussed for the fatigue limit. The stress descent in the notch root leads to a decrease of the crack tip loading. If the stress distribution intersects the Kitagawa-curve for e.g. 10^5 load cycles, the lifetime will be $> 10^5$ load cycles. If the stress distribution proceeds continuously above the Kitagawa curve, the according lifetime is $< 10^5$ load cycles.

The Kitagawa-curve for $R = 0$ and 10^5 load cycles, supplemented by the notch stress distributions of the physically short crack growth specimens at the same number of cycles to failure, is exemplarily shown in Fig. 4.136 (l). This procedure was done for the three analyzed stress ratios, and the determined finite life thresholds were plotted in respect of the according long crack growth thresholds, Fig. 4.136 (r). A linear correlation was found between long crack growth threshold and finite life short crack growth threshold, whereby the slope of the fitting lines varies with the cycles to failure.

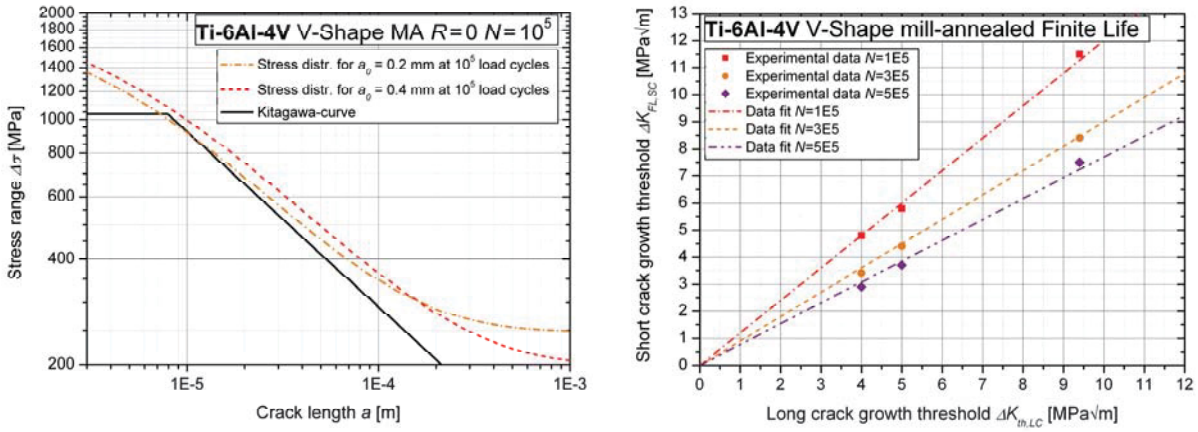

Fig. 4.136: Kitagawa diagram for the SCG specimens (l), correlation of short and long crack growth thresholds (r)

The slopes of the fitting lines in Fig. 4.136 (r) were therefore potentially linked with the cycles to failure, Fig. 4.137. This leads to the following Equ. (4.70) for the finite life thresholds $\Delta K_{FL,SC}$ of short cracks in respect of the cycles to failure N and the long crack growth thresholds $\Delta K_{th,LC}$ (derived from the microstructural model).

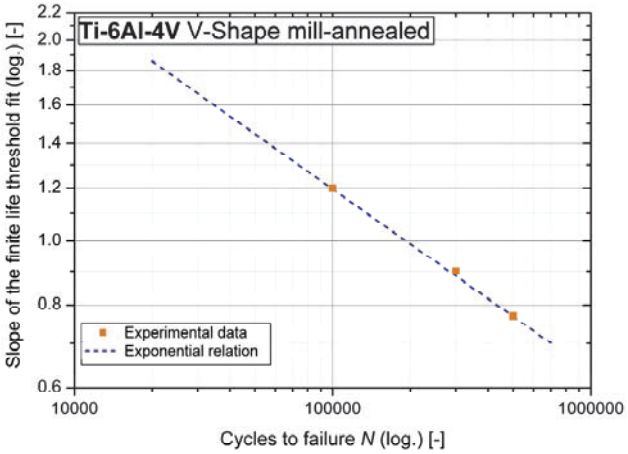

Fig. 4.137: Correlation of the slope of the finite life threshold fit and the cycles to failure

$$\Delta K_{FL,SC} = 28\,\Delta K_{th,LC} \cdot N^{-0.274} \qquad \text{Equ. (4.70)}$$

The lifetime of the short crack growth specimens in the finite life region is dominated by crack growth, and, due to the small specimen dimensions, especially by short crack growth. It can be concluded that a lifetime estimation based on the determined threshold values is conservative for forged components, because their dimensions are larger and the additional contribution of the long crack growth phase extend the cycles to failure.

The smallest detectable flaw size of non-destructive testing methods is approximately 0.5 mm, cf. [119], and therefore physically short. It can be assumed that roughness-induced crack closure plays already a role for the value of the crack growth threshold of such physically short cracks. Therefore, the influence of microstructure on the short crack growth of such physically short cracks is comparable to that on the long crack growth threshold (as already shown on the basis of the matching crack growth curves for physically short and long cracks, cf. Fig. 4.47). Equ. (4.70) is hence applicable for different microstructures.

Both, the Chapetti-curve [47], that describes the crack growth threshold in respect of the crack length, and the finite life threshold model discussed above, were used in combination with the microstructural models and the mean stress models to define a new developed damage tolerance method, the S/N/a-surface. The S/N/a-surface is a combination of S/N-curve and Kitagawa-diagram, and valid for a specific geometry factor ($Y = 0.86$ can be an approximation for initiated fatigue cracks). It can be used in different ways. If the initial crack length (e.g. the smallest detectable flaw size of non-destructive testing methods) and the applied stress range are known, it is possible to predict the according lifetime. The allowable crack size can be calculated if the lifetime and the applied stress range are given. The Matlab-code and principle for calculation of a S/N/a-surface can be found in the Appendix.

S/N/a-surfaces were exemplarily plotted for two stress ratios, namely -1 (Fig. 4.138) and zero (Fig. 4.139). A geometry factor $Y = 1.12$ was applied. Additionally, the fatigue test data of the tension/compression tests on unnotched round specimens and on flat short crack growth specimens with two different initial crack lengths were plotted.

The determination of the S/N/a-surfaces started from the microstructural parameters and used the microstructural models, the mean stress models and the threshold models. The left diagrams show the S/N/a-surface by using the Chapetti-curve. This leads to an overestimation of the fatigue limit of the SCG specimens, because they have a crack length of 0.2 and 0.4 mm but exhibit no extrinsic threshold contribution (no roughness-induced crack closure due to their shape) as assumed by the Chapetti-approach. Therefore, the right diagrams show the S/N/a-surface in "short crack version" for constant infinite life threshold. The threshold was thereby, independent from the crack length, the microstructural short crack threshold based on the Chapetti-approach ($a = d$). In this case, a good accordance of experimental data and S/N/a-surface was determined. In the finite life region, a slight underestimation (< 20%) of the fatigue strengths of the short crack growth specimens were observed due to the disregard of the supporting effect of the wire-eroded initial crack.

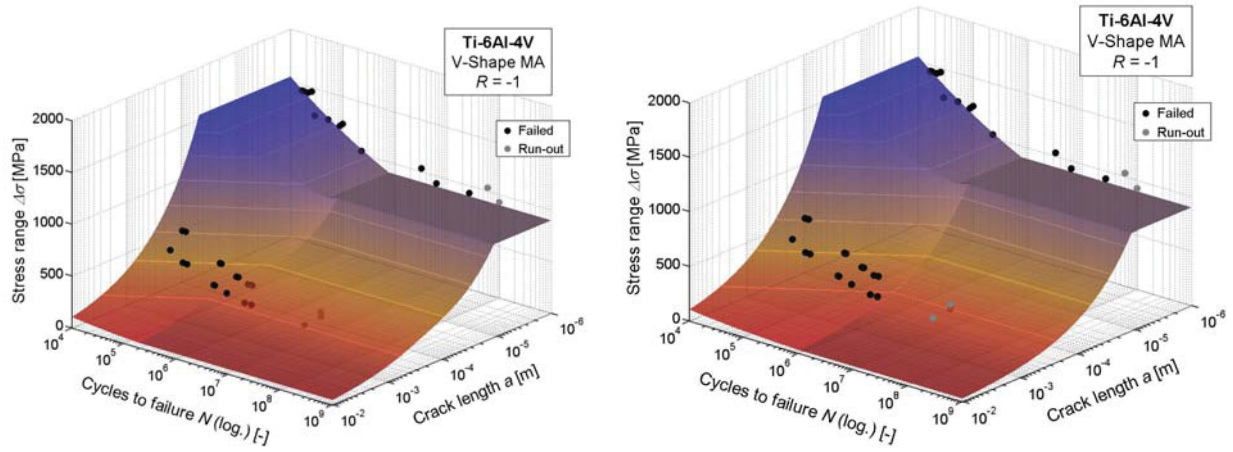

Fig. 4.138: S/N/a-surface ($R = -1$) for V-shape mill-annealed, general (l) and short crack version (r)

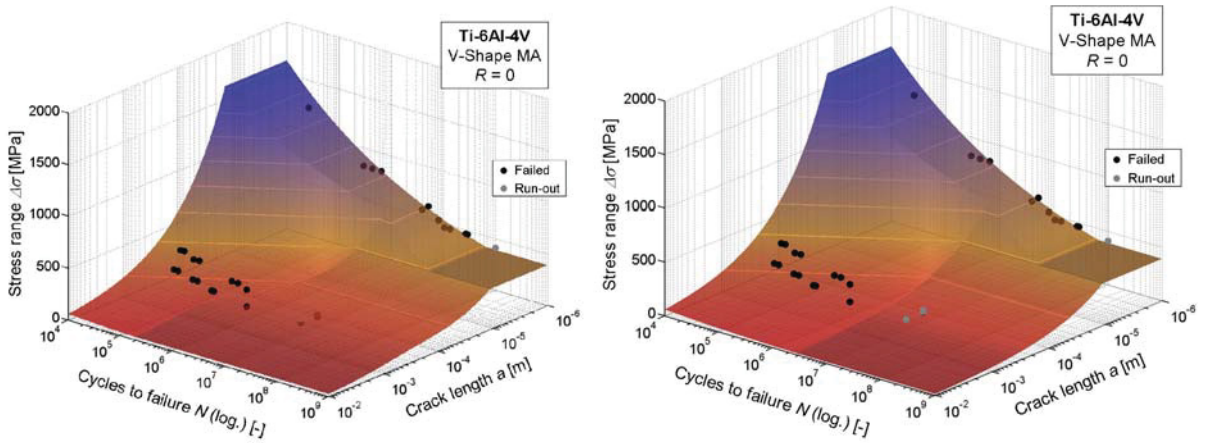

Fig. 4.139: S/N/a-surface ($R = 0$) for V-shape mill-annealed, general (l) and short crack version (r)

The S/N/a-surface in the short crack version is therefore valid for initial cracks (flaws), which have no extrinsic threshold contribution (no crack-closure). Such a type of flaw is for example a forging lap, cf. Fig. 4.131. In contrast, the threshold of a "naturally" initiated fatigue crack follows the Chapetti-curve and the general S/N/a-surface is the right choice for lifetime estimation.

4.5.3.2. Flawed round specimens

It has already been discussed, that flaws, that are not real cracks, behave like notches in Ti-6Al-4V. Therefore, the stress concentration factor and the relative stress gradient at the HRC indentation were determined using FE-analysis (Abaqus™). The results are summarized in Tab. 4.46. The normal stress distribution for pure tension is plotted aside (blue means 0 MPa, green 100 MPa and red 220 MPa).

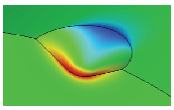

Type of load	Type of notch	K_t [-]	χ^* [mm^{-1}]
Tension/Compression	HRC indentation	2.21	10.5
Rotating Bending	HRC indentation	2.07	10.5

Tab. 4.46: Stress distribution (l), stress concentration factors and relative stress gradients of flawed specimens (r)

The residual stress distribution at the HRC indentation owing to the deformation process was simulated with the aid of FE-analysis in the software tool Abaqus™. The deformation involves a maximum principal residual stress distribution as shown in Fig. 4.140 (l). The maximum tensile stresses occur at the indentation tip. They are caused by high shear stresses, cf. Fig. 4.141 (c). Underneath the tip, distinct compressive residual stresses are observable. It has to be mentioned that this FE-analysis has primarily a qualitative utility. The mesh-quality near the indentation tip is bad due to the high deformation resulting in uncertain absolute stress values.

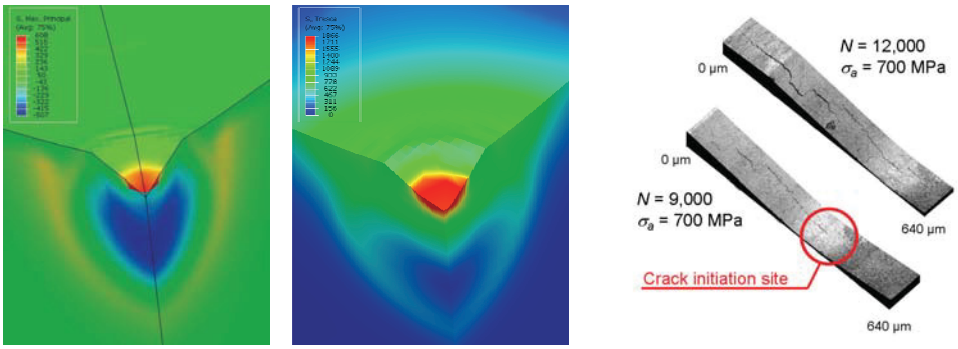

Fig. 4.140: Max. prin. (l) and Tresca equivalent residual stress distribution (c); crack growth observations (r)

The crack initiation and crack growth was investigated on a rotating bending specimen (σ_a = 700 MPa, N_f = 23,300) with a confocal laser scanning microscope, using the pretensioning device developed for the microstructurally short crack observations (cf. Fig. 4.57). Crack initiation occurred at the indentation tip, Fig. 4.140 (r). Then the crack propagates over the shoulder of the indentation and leads to failure.

The detailed analysis of a fracture surface of a tension/compression specimen (R = -1) reveals the same crack growth behavior explained before. After crack initiation at the indentation tip the crack grows over the shoulder to evade the compressive residual stresses beneath the indentation, cf. Fig. 4.141. The region of the compressive residual stresses can be identified in the fracture surface owing to darker fracture surface characteristics.

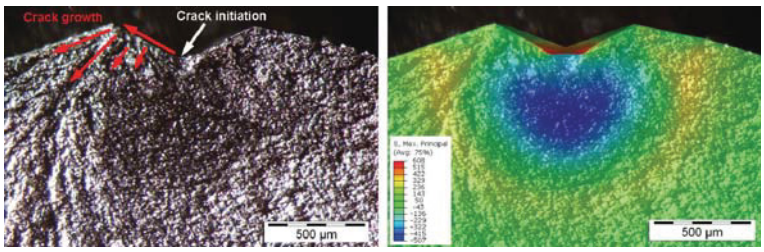

Fig. 4.141: Fracture surface (l) and maximum principal residual stress distribution mapped on fracture surface (r)

An initiated crack at the indentation tip grew typically on both sides of the indentation (cf. Fig. 4.134 (r)), but partly at different levels. Consequently, they coalesce after certain load cycles (cf. Fig. 4.132 (r)) or they grow separately and the more critical crack leads to fracture (cf. Fig. 4.133 (r)). These three types of fracture occurred independent from stress ratio or type of loading.

It can be concluded that the fatigue behavior of these flawed specimens is dominated by two influencing factors, namely impressed mean stress (owing to residual stresses) and relative stress gradient. S/N-curves were hence calculated, based on the microstructural, the relative stress gradient and the mean stress model. The machining factor was approximated based on the results of the residual stress free chemically milled specimens, because the existent residual stresses were included as impressed mean stress. The absolute value of the residual stress, which serves as contribution to the mean stress, was thereby adapted to meet the experimental data points. A very high residual stress of 1000 MPa was determined based on these considerations. The according S/N-curves are plotted in Fig. 4.142, using the local stress amplitude at the indentation tip. The stated stress ratios are thereby based on the applied load. The effective stress ratios vary from -0.2 to 0.4 (for R = -1) and from 0.3 to 0.5 (for R = 0) at the according stress levels, owing to the residual stresses. It has to be mentioned that both, the influence of the deformation on the material behavior (increase of dislocation density, grain shape deformation) and the unusual crack growth were neglected. This might result in lower fatigue strength and hence lower residual tensile stresses to meet the experimental data.

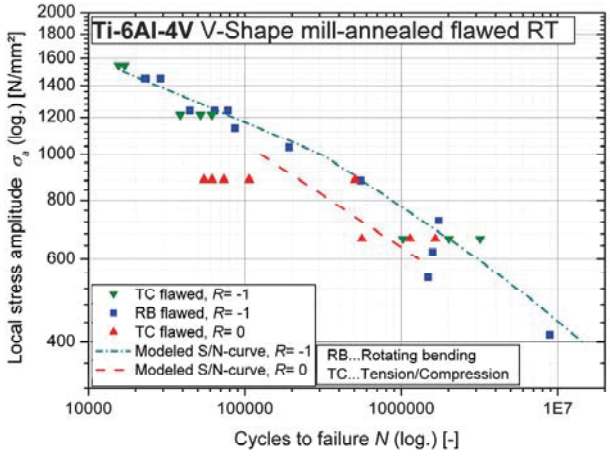

Fig. 4.142: Estimation of the fatigue strength of flawed specimens based on local stresses

A lifetime estimation based on local stresses is able to predict the behavior of such flawed specimens, if all important influencing parameters (stress concentration factor, relative stress gradient, residual stresses) are known. However, this is in practice not the case.

Therefore, the lifetime was also estimated based on the S/N/a-surface introduced before. The geometry factor (Y = 0.64) was thereby estimated according to Murakami [115] for a semi-elliptical surface crack under uniform tension. It was observed that the utilization of the S/N/a-surface leads to a conservative estimation of the fatigue strength. This is caused by two facts: the indentation is not a crack-type flaw and load cycles are additionally consumed for crack initiation, and crack propagation is decelerated by the compressive residual stresses beneath the indentation.

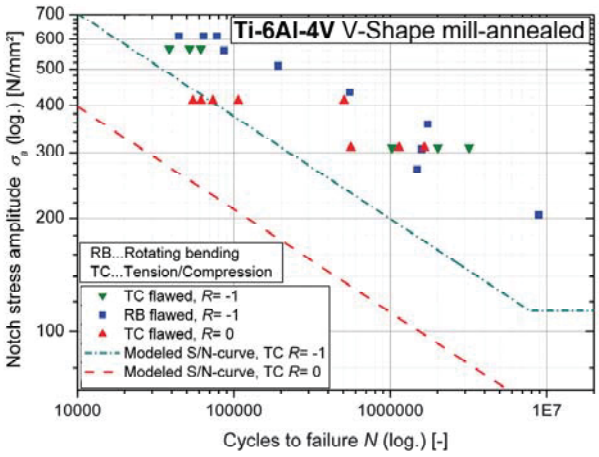

Fig. 4.143: Estimation of the fatigue strength of flawed specimens based on fracture mechanics

4.5.4. Conclusion

- The literature and presented research results show that it is possible to estimate the fatigue strength of flawed specimens based on fracture mechanical or S/N-based approaches. However, this is just possible if all important influencing variables and conditions are known. In practice, this is not the case and such methods are hence not generally applicable.

- A new approach was introduced, combining the Kitagawa-Takahashi-diagram and the S/N-approach to an S/N/a-surface. The (flaw-less) plain fatigue limit is thereby determined according to the microstructural, stress gradient, and mean stress models. For the infinite life region, the Chapetti-curve is used for estimation of the crack growth threshold in respect of the crack length. The finite life region of the S/N/a-surface is based on the flaw-less modeled S/N-curves and finite life thresholds, which are a function of the load cycles. This approach provides a simple model for design engineers to estimate the damage tolerance of a component for any flaw or damage.

- A good estimation of the fatigue behavior of specimens provided with crack-like initial flaws (simulating forging-laps) was achieved by modeled S/N/a-surfaces. An underestimation of < 20% of the finite life fatigue strength was determined due to the disregard of the notch supporting effect of the initial flaws.

- The detrimental effect of indentations was also estimated with S/N/a-surfaces. A conservative estimation of the fatigue strength (30-50% lower) was thereby achieved.

4.6. Influence of surface state on the fatigue behavior

The goal of this research was to generate fatigue data that is neither conservative nor non-conservative with respect to service conditions. Therefore, precision turned specimens were used for the characterization of the fatigue behavior of Ti-6Al-4V. However, mechanical testing laboratories often use different types of polished specimens. Such specimens lead, owing to the residual stress free surface layer, to lower fatigue data scatter but also to lower fatigue strengths, especially in the finite life region, compared with the material in service condition. In contrast, subsequent surface treatments (e.g., shot peening) serve to increase the fatigue strength of components. Therefore, unnotched specimens with three different types of surface states are analyzed: precision turned specimens without any surface treatment (used for determination of several influences on the fatigue behavior of Ti-6Al-4V in this research), chemically milled specimens, and shot peened specimens.

4.6.1. State-of-the-art

Lütjering and Williams [105] reported that the preparation of titanium and titanium alloy fatigue specimens for fatigue testing must be done very carefully. They mentioned that laboratory fatigue specimens are often electrolytically polished to provide a maximum consistency in surface quality and minimize the scatter due to this factor. This could be a useful approach for research purposes. For generation of fatigue data, mechanical polishing is a better approximation to the surface of titanium components that would be used in manufactured products. Fig. 4.144 (l) shows the variation in fatigue life that can be obtained due to different specimen preparation methods, such as rough mechanical polishing, electrolytic polishing, fine mechanical polishing, and shot peening.

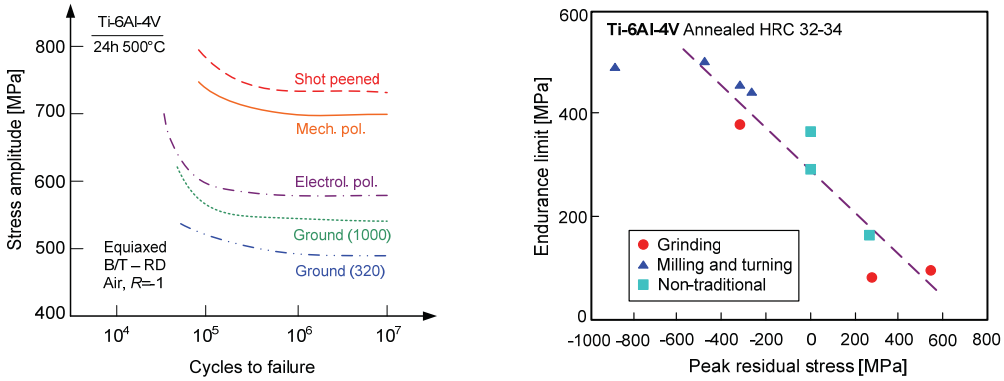

Fig. 4.144: S/N-curves for Ti-6Al-4V showing the effect of specimen preparation (l) [105] and correlation between endurance limit and peak residual stress (r) [95]

Wagner and Bigoney [175] reported that the surface state could be described by the three following surface properties: surface roughness, degree of cold work or dislocation density, and residual stresses. Since the fatigue life is simply the sum of the numbers of cycles to crack initiation and those of crack propagation, modifying surface properties may well have contradictory effects on fatigue life. The surface roughness determines whether fatigue strength is primarily crack initiation (smooth surface) or crack propagation controlled (rough surface). For smooth surfaces, a hardened surface layer leads to a retardation of crack initiation owing to the increase in strength. For rough surfaces, there may even be no crack initiation phase at all and the hardened surface layer is a disadvantage for crack propagation owing to the low residual ductility. Compressive residual stresses in the surface layer are very favorable since they strongly retard microcrack propagation if cracks are present, Tab. 4.47.

Surface properties	Crack initiation	Microcrack propagation
Roughness	Accelerated	-
Cold working	Retarded	Accelerated
Compr. residual stresses	Small influence	Retarded

Tab. 4.47: Influence of surface properties on the fatigue behavior [175]

Boyer et al. [42] reported that the surface residual stress is a predominant factor influencing fatigue, and the residual stress effect is most pronounced in the infinite-life stress range of the endurance limit regime (10^7 cycles or more). Residual stress is even a more potent indicator than surface roughness in this regime, although residual stress and surface roughness are closely related in many instances. Surface residual stress is important, but the effect is not simple because of the combined influences of residual stress, cold working and surface roughness. These findings stand in contrast to those of Wagner and Bigoney [175] mentioned above, cf. Tab. 4.47. These differences may arise from the fact that Boyer et al. [42] discussed an endurance limit regime (10^7 cycles or more) which is in fact still the finite life region. Koster [95] presented a rough correlation between fatigue limit and peak residual stress, Fig. 4.144 (r), but it has to be mentioned at this point that general rules of thumb regarding residual stresses must be exercised with care.

Surface treatments and especially shot peening are often performed to increase the fatigue strength of components. A shot peening treatment is a cold working process (increase of dislocation density) and it induces compressive residual stresses in the surface layer. Concurrently, shot peening increases the roughness, what is a problem with respect to crack initiation and hence fatigue limit; especially for Ti-6Al-4V with its high notch sensitivity.
Extensive fatigue test results are reported in literature for the influence of shot peening on the fatigue behavior of Ti-6Al-4V. It was already mentioned that the fatigue behavior is considerably influenced by the versatile microstructure (resulting from the high diversity of possible thermomechanical treatments); for shot peening, this diversity is additionally multiplied by the parameters of the shot peening treatment. The S/N-curves of the shot peened state are usually compared with an unpeened surface condition, which leads to another influencing variable.

Fig. 4.145 shows the rotating bending fatigue test results (performed on unnotched hourglass specimens at room temperature and 500°C) of Gray et al. [74]. The shot peening was done with an Almen intensity of 0.28 A(mm).
At room temperature, shot peening leads to an increase of 25% of the fatigue strength at 10^7 load cycles compared to the electrolytically polished specimens. A reduced roughness by electrolytic polishing after the shot peening has no effect on the fatigue strength, unless stress relieving was performed. At 500°C the stress relieving has no effect because the testing temperature leads in any case to stress relieve. Shot peening with its increased surface roughness reduces the fatigue strength because the roughness predominates the cold working effect. The reduced roughness of the shot peening plus electrolytic polishing leads to an increase owing to the increased dislocation density. These results show hence the separate and combined effects of the three important surface properties roughness, residual stresses and cold working.

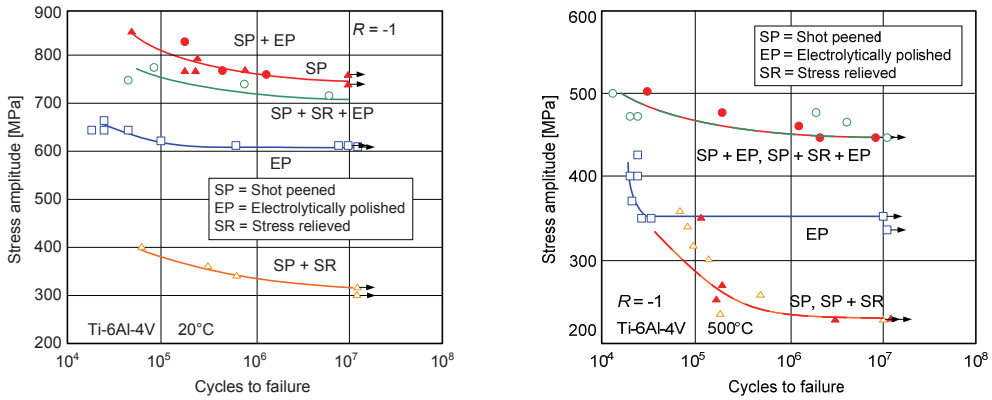

Fig. 4.145: Effect of surface treatments on the fatigue strength at room temperature (l) and at 500°C (r) [74]

Wagner et al. [176] achieved at rotating bending fatigue tests on fine equiaxed Ti-6Al-4V an increase of 17% of the fatigue strength at 10^7 load cycles owing to shot peening with an intensity of 0.15 A(mm) compared to the electrolytically polished surface state, Fig. 4.146 (l). Franz and Olbricht [63] reported a similar increase of the high cycle fatigue strength under four-point-bending loading owing to a shot peening treatment with an intensity of 0.15 A(mm), Fig. 4.146. Similar findings are also documented by Koster et al. [96].

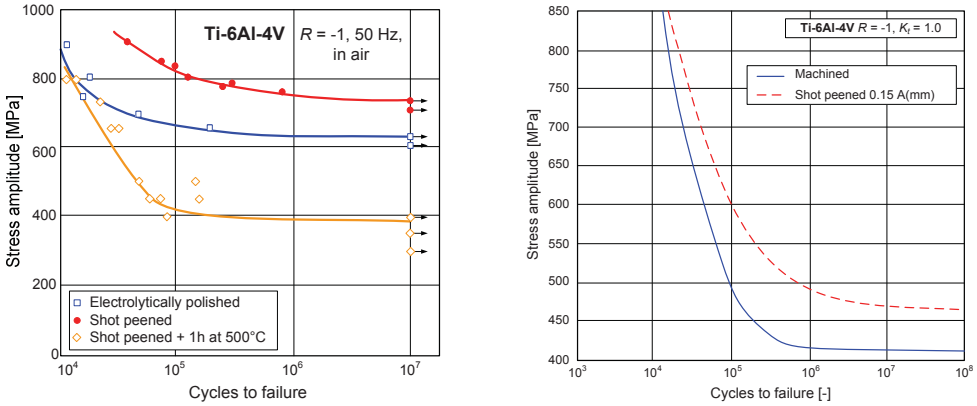

Fig. 4.146: Influence of shot peening acc. to Wagner et al. [176] (l) and Franz et al. [63] (r)

Wohlfahrt [184] performed alternating bending fatigue tests on milled and shot peened specimens, Fig. 4.147 (l). He reported an increase of finite life fatigue strength owing to shot peening with an intensity of 0.25 A(mm), but also a concomitant decrease of high cycle fatigue strength. A higher peening intensity of 0.40 A(mm) led to almost the same finite life strength but the high cycle fatigue strength was more decreased. It can be assumed that this behavior is caused by the increased roughness with increasing peening intensity. Additional glass bead peening for surface roughness reduction increased both, the finite life and high cycle fatigue strength significantly.

Wagner and Lütjering [179] performed rotating bending fatigue tests on one stress level for determination of the influence of several shot peening parameters on the finite life fatigue strength and surface properties of coarse lamellar Ti-6Al-4V, Fig. 4.147 (r). They found that the peak residual stress and the depth of the compressive residual stresses increase with increasing peening pressure. The surface roughness reaches saturation with respect to the peening duration but the saturation plateau increases with increasing peening pressure.

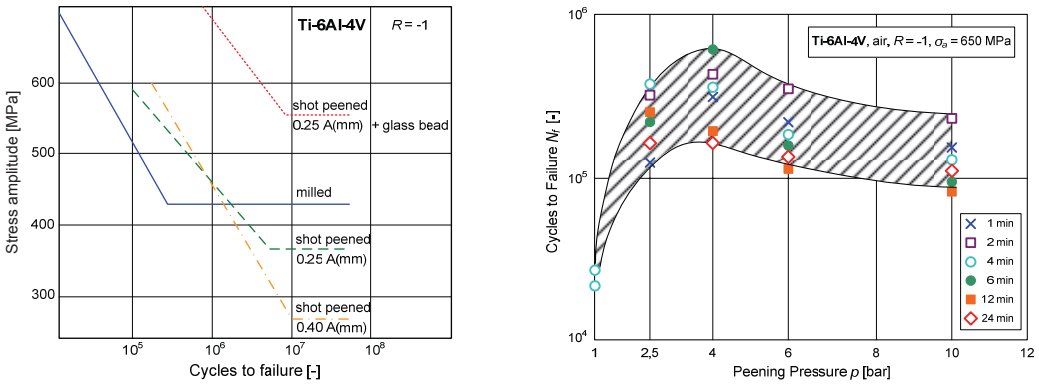

Fig. 4.147: Influence of shot peening acc. to Wohlfahrt [184] (l) and Wagner et al. [179] (r)

Prior research [1] showed the influence of shot peening intensity and type of loading on the fatigue behavior of lamellar (as-received) Ti-6Al-4V bar stock, Fig. 4.148. It was observed that the finite life fatigue strength is increased by shot peening. A peening intensity of 0.25 A(mm) led to an overpeening and reduced fatigue strength. The high cycle fatigue strength at 10^8 load cycles was considerably decreased due to overpeening compared to the machined surface state. Under torsional loading, it was determined that shot peening increase the finite life fatigue strength. The high cycle fatigue strength was not increased by shot peening; neither under rotating bending nor under torsional loading.

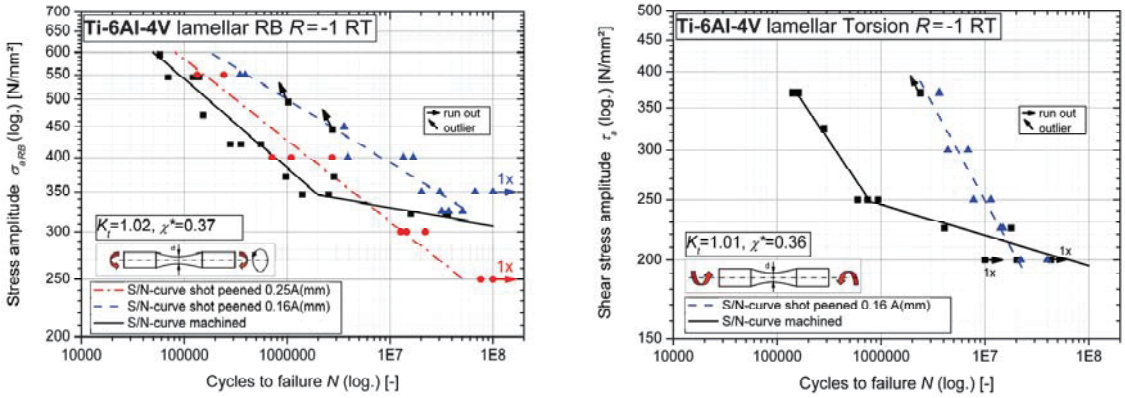

Fig. 4.148: Influence of shot peening on rotating bending (l) and alternating torsion fatigue (r) [1]

The residual stresses of the specimens used in [1] were measured with XRD. It was observed that the axial residual stresses induced by shot peening are higher than the tangential ones, Fig. 4.149 (l). However, cyclic loading in the high cycle fatigue region leads to stress redistribution and both, the axial and the tangential residual stresses converge to the average initial residual stress distribution. Therefore, it can be concluded that it is valid to average the measured axial and tangential residual stresses of shot peened surface states. Loading in the finite life region also unifies the stress distributions in axial and tangential direction. Additionally, a stress relaxation was observed, reducing the peak residual stress and the depth of the compressive residual stresses. An increase of shot peening intensity from 0.16 A(mm) to 0.25 A(mm) does not lead to significant variations of the residual stresses, Fig. 4.149 (r). Nevertheless, the surface roughness increases with increasing peening intensity and leads to lower fatigue strength in the finite life region, cf. Fig. 4.148 (l).

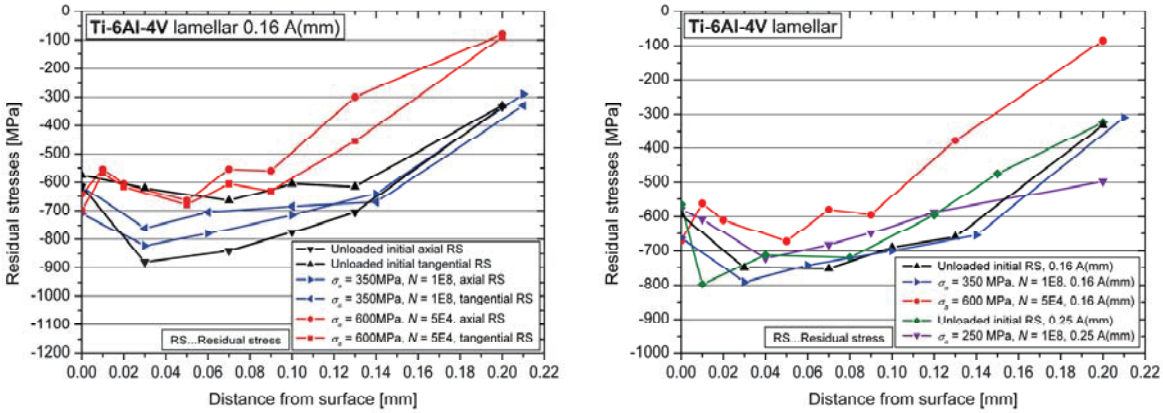

Fig. 4.149: Residual stress distributions of shot peened surface states [1]

4.6.2. Experimental procedure

Fatigue tests were performed on specimens with chemically milled (residual stress free) or shot peened (compressive residual stress afflicted) surface states. Experimental data from machined specimens was used as a reference, cf. Fig. 4.20, Fig. 4.21, and Fig. 4.81.

Chemical milling was performed on machined specimens sampled from mill-annealed pancakes, cf. Fig. 3.39; a surface layer of approximately 0.36 mm was thereby removed. The composition of the bath used for chemical milling can be found in Tab. 3.1.
The shot peening was performed on precision turned specimens sampled from mill-annealed V-shapes. The peening intensities of 0.16, 0.20 and 0.25 A(mm) were chosen in accordance with the military specifications MIL-S-13165C [171] and MIL-P-81985 [172]. A coverage of 200% was used for all experiments. A steel ball shot was used, StD-G3-0.35-HV640, with size classification 0.35 mm and hardness HV640.The appropriate saturation curves are shown in Fig. 4.150.

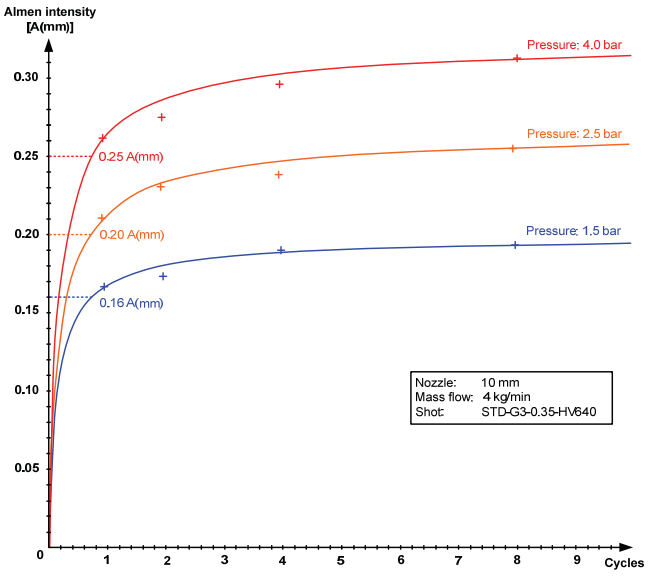

Fig. 4.150: Saturation curves of the shot peened round specimens

4.6.2.1. Specimen characterization

The roughness of all analyzed surface states was measured with a confocal laser scanning microscope (Olympus LEXT OLS3000). The topographies of the different surface states are shown in Fig. 4.151; the according roughness values can be found in Tab. 4.48.

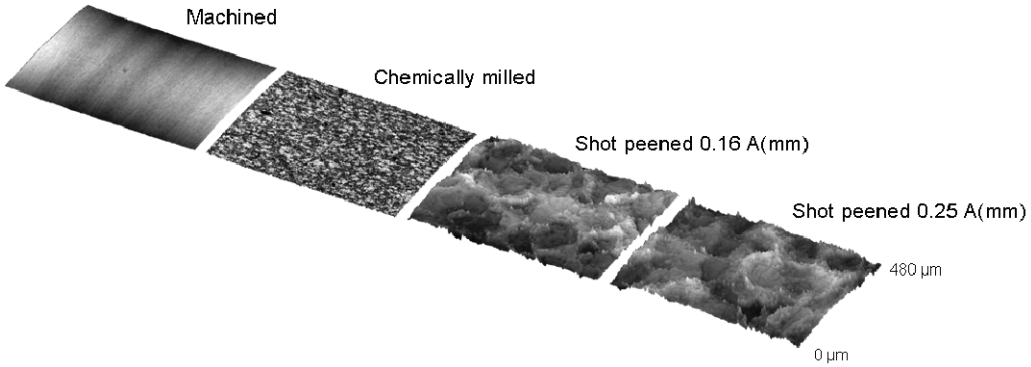

Fig. 4.151: Topographies of different surface states

Type of specimen	R_a [µm]	R_z [µm]
Machined	0.6	1.4
Chemically milled	0.9	2.4
Shot peened 0.16 A(mm)	4.0	9.3
Shot peened 0.20 A(mm)	4.5	9.9
Shot peened 0.25 A(mm)	4.9	11.2

Tab. 4.48: Influence of surface treatment on the surface roughness

It was observed that the machined surface state exhibits a certain waviness owing to the precision turning, but the roughness is low, R_a = 0.6 µm. Chemical milling leads to a decrease of waviness due to the removal of a surface layer of approximately 0.36 mm. However, the roughness is increased compared to the machined surface state. This is caused by the fact, that chemical milling is a rough kind of etching, which is confirmed by the comparison of the chemical composition of the chemical milling bath (Tab. 3.1) and the used etchant for the micrographs (Tab. 3.3). The microstructure is hence visible in the surface topography of the chemically milled surface state in Fig. 4.151. The roughness is significantly increased by shot peening. An increase of shot peening intensity leads thereby to an increase of surface roughness.

Residual stress measurements were performed using X-ray diffraction (XRD) in combination with the $sin^2\psi$ method. Fig. 4.152 shows the residual stress distributions for five different surface states. Graphs of residual stresses are comprised of measured data points (calculated by the average of data in the longitudinal and transversal direction, assuming a homogenous plane stress state), with no smoothing. Machining leads to residual compressive stresses in the first hundredths of a millimeter beneath the surface. In contrast, the chemically milled surface state exhibits a residual stress free surface layer. Shot peening of the machined initial surface leads to a marked increase in the residual compressive stresses. The peak value of the residual compressive stresses increases from -400 MPa for an unpeened machined surface to -650 MPa for a shot peened surface; a difference of over 50%. The increase of peening intensity leads to an insignificant increase of the peak residual stress.

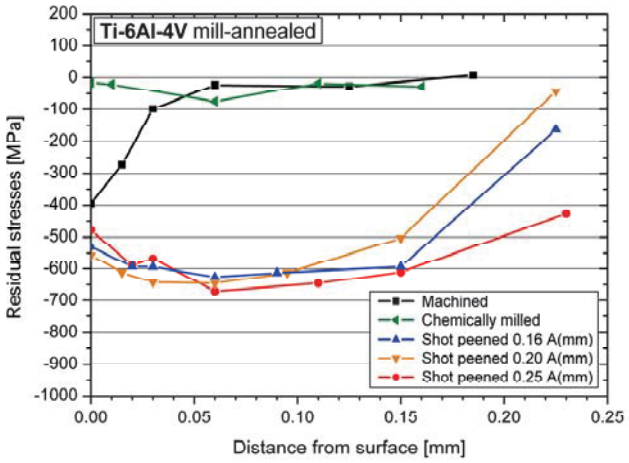

Fig. 4.152: Influence of surface treatment on the residual stress distribution

4.6.2.2. Chemically milled specimens

Fatigue tests were performed on chemically milled round hourglass specimens (Fig. 3.39) under rotating bending loading (stress ratio R = -1) with a frequency of 70 Hz. Fig. 4.153 shows the experimental data and the corresponding S/N-curve. The evaluation of the S/N-curve in the finite life region was based on the logarithmic normal distribution. The high cycle fatigue strength at 10^8 load cycles was determined according to the *arcsin*$\sqrt{P}$-method [55]. Due to the limited specimen lot sizes the high cycle fatigue strength and especially the scatter are not statistically firm.

The fracture surfaces were analyzed with a stereo light optical microscope (Olympus SZX12). Two exemplary pictures of a fracture surface are shown in Fig. 4.153 (r); one overview (16x magnification) and one detailed view (64x magnification). It was observed that the fatigue crack initiates directly at the surface (twelve o'clock position). Lower stress amplitudes resulted in one or two crack initiation sites, higher stress amplitudes in several ones. It can be assumed that this behavior is caused by the residual stress free surface layer.

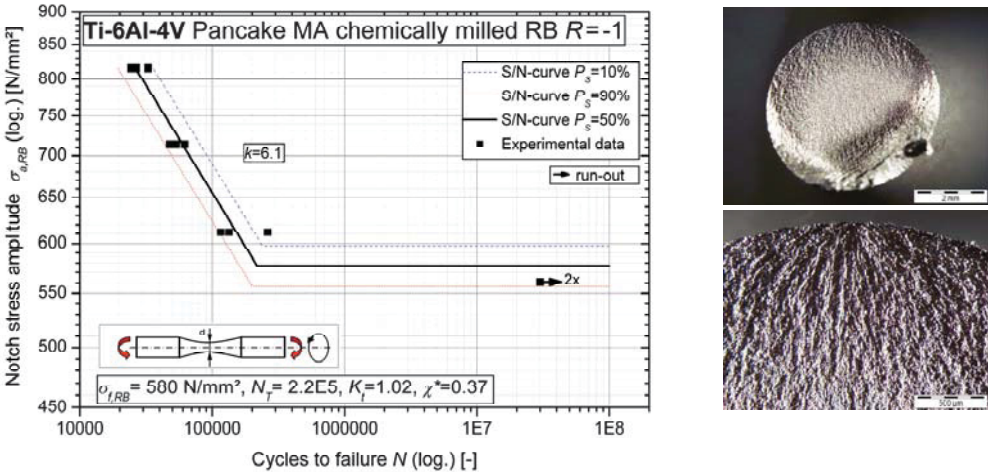

Fig. 4.153: Rotating bending S/N-curve (l) and fracture surface (r) for pancake mill-annealed, chemically milled

Symbol	Description	Unit	Value
σ_f	Fatigue strength at N=10^8	MPa	580
N_T	Cycles at transition	-	2.2E5
k	Slope	-	6.1
T_N	Scatter at finite life	-	1:1.8
T_S	Scatter at N=10^8	-	1:1.1

Tab. 4.49: Parameters for RB S/N-curve pancake mill-annealed, chemically milled

The comparison of the S/N-curves for machined and chemically milled specimens is shown in Fig. 4.154. It was observed that chemical milling leads to a lower fatigue strength, especially in the finite life region. The scatter at finite life was significantly reduced from 1:3.7 to 1:1.8 owing to the chemical milling.

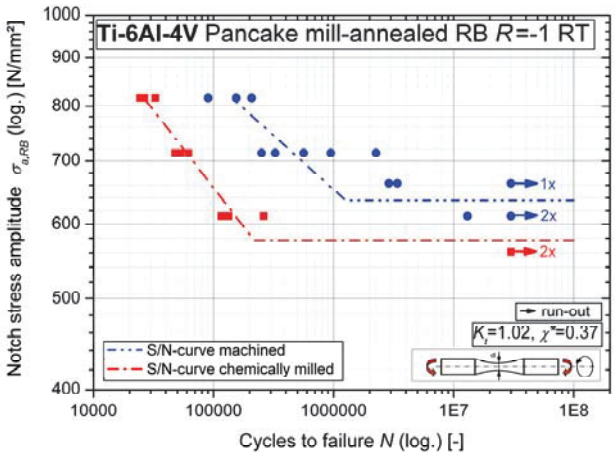

Fig. 4.154: Comparison of S/N-curves for machined and chemically milled fatigue specimens

Chemical milling leads to a residual stress free surface state (cf. Fig. 4.152) owing to the removal of a surface layer with a thickness of approximately 0.36 mm. In contrast, the machined specimens exhibit compressive residual stresses reaching a depth of 0.05 mm beneath the surface. The surface roughness of the specimens was increased by a factor of 1.5 by chemical milling (cf. Tab. 4.48). It can be concluded that the 6% lower fatigue limit of the chemically milled specimens results from the higher surface roughness in combination with a lower dislocation density. A higher roughness promotes crack initiation and leads therefore to a decrease of the high cycle fatigue strength, cf. Tab. 4.47. Machining leads to a higher dislocation density in the surface layer and retards crack initiation. The non-existent compressive residual stresses of the chemically milled surface have just a small (negative) influence on crack initiation and hence fatigue limit. However, the finite life fatigue strength is considerably influenced by residual stresses. The compressive residual stresses of the machined specimens lead to deceleration of microcrack propagation and consequently to a higher finite life fatigue strength.

4.6.2.3. Shot peened specimens

Fatigue tests were performed on (unnotched and notched) shot peened round specimens under several loading conditions. The evaluation of the S/N-curves in the finite life region was carried out using a logarithmic normal distribution. Due to the limited specimen lot sizes the scatter is not statistically firm.

A determination of the fatigue limit was not possible, due to the shift of the transition from finite life to infinite life region to $>10^8$ load cycles. The fracture surfaces were analyzed with a stereo light optical microscope (Olympus SZX12). The findings are discussed below.

The experimental results of the rotating bending fatigue tests on unnotched shot peened specimens (peening intensity 0.16 A(mm)) are shown in Fig. 4.155. As mentioned before, no fatigue limit was determined for $N < 10^8$ load cycles. The slope of the S/N-curve in the finite life region is lower than those of the machined specimens. The scatter T_N increases from 1:2.8 for the machined surface state (cf. Tab. 4.10) to 1:4.2 in shot peened condition; a factor of 1.5.

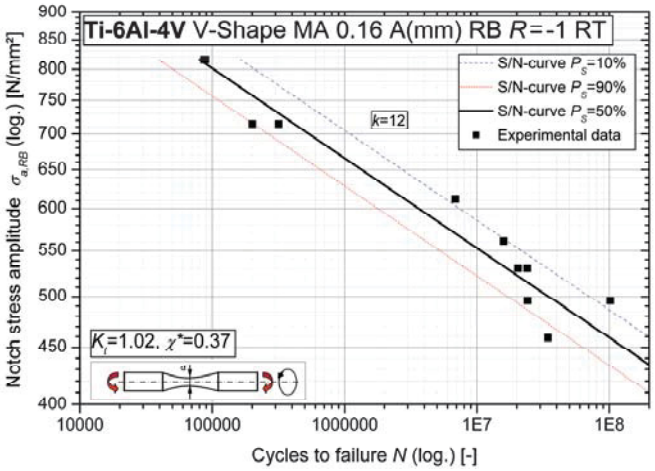

Fig. 4.155: Rotating bending S/N-curve for V-shape mill-annealed, shot peened 0.16 A(mm)

Symbol	Description	Unit	Value
σ_a	Fatigue strength at N=10^8	MPa	460
N_T	Cycles at transition	-	-
k	Slope	-	12
T_N	Scatter at finite life	-	1:4.2
T_S	Scatter at N=10^8	-	-

Tab. 4.50: Parameters for RB S/N-curve V-shape mill-annealed, shot peened 0.16 A(mm)

The comparison of the S/N-curve of the shot peened specimens with those of the machined surface state is shown in Fig. 4.156. Experimental data for higher shot peening intensities is additionally plotted in this diagram. It was observed that the shot peening treatment leads to an increase of the fatigue strength in the finite life region. However, the fatigue limit is definitely not increased, possibly decreased. An increase of peening intensity does not lead to a higher finite life fatigue strength due to the almost identical residual stress distributions, cf. Fig. 4.152.

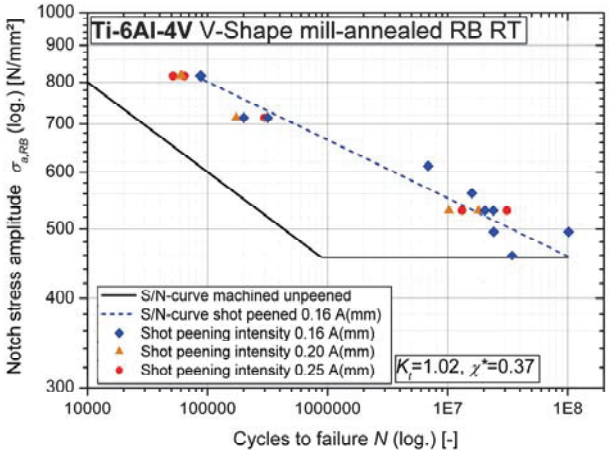

Fig. 4.156: Influence of shot peening intensity on the rotating bending fatigue strength

It can be concluded that the increase of the finite life fatigue strength is caused by deceleration of the microcrack propagation owing to the compressive residual stresses induced by shot peening. Especially the sub-surface crack initiation and microcrack growth without contact to ambient air (similar to vacuum crack growth, cf. Fig. 4.16) are believed to cause the increase of the finite life fatigue strength. Due to the insignificant variation of the residual stress state with increasing peening intensity (cf. Fig. 4.152), the finite life fatigue strength is not increased with increasing peening intensity.

The fatigue limit is dominated by crack initiation. It can be concluded that the fatigue limit is decreased due to shot peening treatment, because both, the equilibrium tensile residual stresses and the increased roughness could promote crack initiation. The fracture surface analysis revealed sub-surface crack initiation, cf. Fig. 4.159. It can hence be concluded that the tensile residual stresses act as impressed mean stress and increase the local stress ratio. Due to the anomalous high mean stress sensitivity of Ti-6Al-4V, the fatigue limit is lowered by a shot peening treatment.

The influence of a relative stress gradient was determined on notched shot peened specimens. It was observed that the finite life fatigue strength is not increased compared to the unnotched shot peened samples, Fig. 4.157 (l). This behavior may be explained by the resulting stress distributions of load stress (notch stress amplitude 600 MPa) and residual stress (shot peening intensity 0.16 A(mm)) for unnotched and notched specimens, Fig. 4.157 (r). The maximum stress is higher for unnotched specimens. However, the finite life fatigue strength is dominated by microcrack propagation. Therefore, it can be assumed that the identical stress range (and also stress intensity factor range) leads in combination with the similar stress ratios to the same crack growth rate and hence finite life fatigue strength.

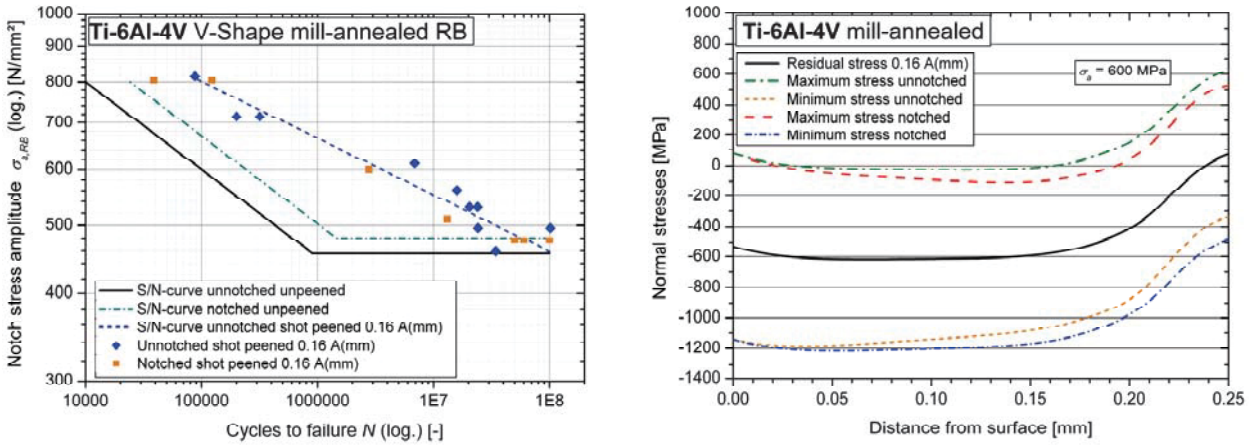

Fig. 4.157: Influence of the relative stress gradient on the effectiveness of shot peening (l), stress distributions (r)

The influence of impressed mean stress on the effectiveness of the shot peening treatment was determined under tension/compression loading. The comparison of shot peened and machined surface state are presented in Fig. 4.158. It was observed that the shot peening treatment leads to an increase of the finite life fatigue strength for a stress ratio $R = -1$, similar to findings under rotating bending loading discussed before. The finite life fatigue strength for impressed mean stress ($R = 0$, $R = 0.3$) is not increased. This behavior may be caused by the residual stresses induced by the shot peening treatment.

The compressive residual stresses shift the crack initiation beneath the surface and lead to slower microcrack propagation. However, the local stress ratio is increased due to equilibrium tensile stresses. It was observed that an increase from $R = -1$ to $R = 0$ has no effect on the finite life fatigue strength (cf. chapter "Influence of impressed mean stress on the fatigue behavior"), which could be the reason for the effectiveness of the shot peening treatment for a global $R = -1$. Global stress ratios > 0 lead to a decrease of finite life fatigue strength for identical stress ranges. It can hence be assumed that the residual stresses increase the local stress ratio (for example, for global $R = 0$) to values > 0, which abrogates the positive effect of subsurface crack initiation and results in similar finite life fatigue strengths of machined and shot peened specimens.

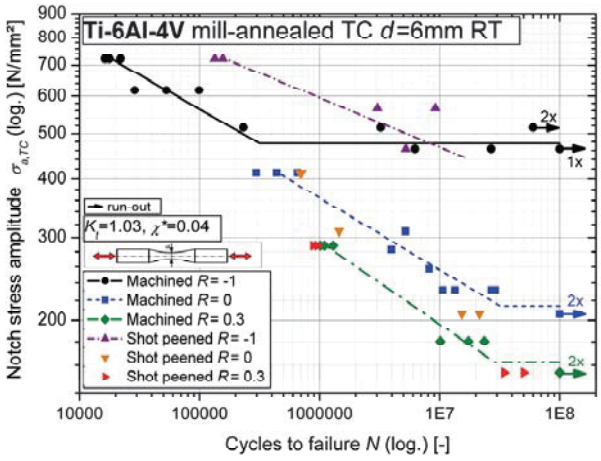

Fig. 4.158: Influence of impressed mean stress on the effectiveness of shot peening

The fracture surface analyses of the shot peened tension/compression fatigue test specimens revealed sub-surface crack initiation for both, R = -1 and R = 0, cf. Fig. 4.159. The center picture shows a detailed view of a fracture surface; the crack initiation site is marked with an arrow. The distance of surface and crack initiation site (~ 0.25 mm) is in accordance to the residual stress distributions (Fig. 4.152, compressive residual stresses reaching into a depth of ~ 0.25 mm beneath the surface). Furthermore, a zone of finer fracture characteristics was observable (marked with a dotted line) with a radius of approximately 0.38 mm. This zone corresponds to the crack growth without contact to ambient air.

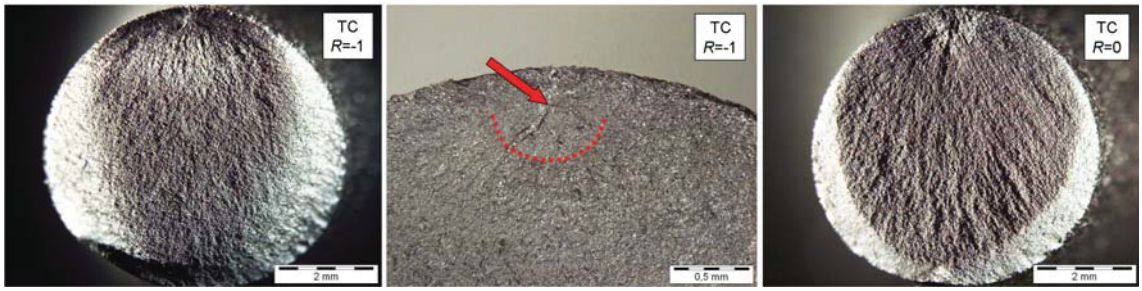

Fig. 4.159: Fracture surfaces of shot peened specimens, intensity 0.16 A(mm); loaded under tension/compression

Some shot peened specimens were also tested under alternating torsion and multiaxial loading. The comparison with the test results of the machined specimens, Fig. 4.160, exhibited that the shot peening treatment leads to an increase of the finite life fatigue strength, independent from the type of loading for a stress ratio R = -1.

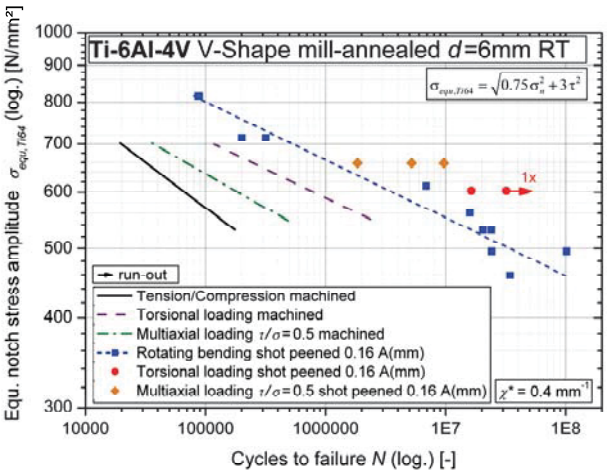

Fig. 4.160: Influence of the type of loading on the effectiveness of shot peening

4.6.3. Phenomenological models

Including the surface state in the lifetime estimation is difficult due to the complex interaction of several influencing variables, especially residual stresses and surface roughness, with other fatigue influences, for example, stress ratio and relative stress gradient. Therefore, it is currently not possible to predict the fatigue strength of an arbitrary surface state. A simple model was hence implemented, using three coefficients for the description of the S/N-curve shift relative to the machined surface state.

Starting from the output of the mean stress model, the S/N-curve parameters are adapted for the representation of the surface state. The coefficient $c_{S,k}$ describes thereby the variation of the S/N-curve slope, Equ. (4.71). The shift of the fatigue limit is given by $c_{S,f}$, Equ. (4.72). The number of cycles at transition can be determined according to Equ. (4.73), utilizing the finite life coefficient $c_{S,FL}$ which describes the change of the finite life fatigue strength at 10^5 cycles to failure. The coefficients for the analyzed surface states, stress ratio R = -1, are summarized in Tab. 4.51.

$$k_{MGMS} = c_{S,k} \cdot k_{MGM} \qquad \text{Equ. (4.71)}$$

$$\sigma_{f,MGMS} = c_{S,f} \cdot \sigma_{f,MGM} \qquad \text{Equ. (4.72)}$$

$$N_{T,MGMS} = 10^5 \left(\frac{c_{S,f}}{c_{S,FL}} \cdot \sqrt[k_{MGM}]{\frac{10^5}{N_{T,MGM}}} \right)^{-k_{MGMS}} \qquad \text{Equ. (4.73)}$$

Surface state	$c_{S,FL}$ [-]	$c_{S,k}$ [-]	$c_{S,f}$ [-]
Chemically milled	0.77	0.70	0.91
Shot peened 0.16 A(mm)	1.34	1.50	≤ 1

Tab. 4.51: Summarized surface state coefficients for R=-1

4.6.4. Conclusion

- The influence of the surface state on the fatigue behavior is hard to define due to the combined influences of residual stresses, cold working and surface roughness. Concerning Ti-6Al-4V it can be concluded that the finite life region is dominated by residual stresses and the fatigue limit is mainly influenced by surface roughness.

- The scatter in the finite life region is significantly affected by the variance of existing residual stresses. A residual stress free surface layer leads to the lowest scatter (T_N = 1:1.8), which corresponds to the material scatter. Machining (T_N = 1:2.8) and shot peening (T_N = 1:4.2) significantly increase the finite life scatter.

- It was determined that shot peening does not compulsorily lead to an increase of finite life fatigue strength, especially for cyclic loading with impressed mean stress.

- Including the surface state in the lifetime estimation is difficult due to the complex interaction of several influencing variables, especially residual stresses and surface roughness, with other fatigue influences, for example, stress ratio and relative stress gradient. A simple model was hence implemented, using three coefficients for the description of the S/N-curve shift relative to the machined surface state.

4.7. Influence of surface arrangement on the fatigue behavior

Manufacturing parts according to customer specifications by using forming techniques has both cost and quality advantages, compared to cutting and machining parts out of feedstock plates or bars. Because of this, components are increasingly manufactured by forging. Forging results in better utilization of material through near net shape manufacturing, and also reduces manufacturing costs and provides better mechanical properties, such as high fatigue strengths. Some surfaces of forged components remain in the as-forged condition, whereas functional surfaces are subjected to additional machining (Fig. 4.161). Subsequent surface treatments (e.g., shot peening) serve to increase the fatigue strength.

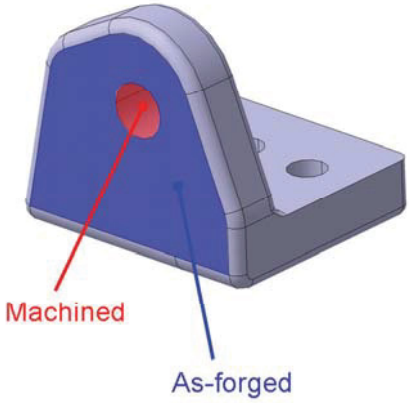

Fig. 4.161: Arrangement of different types of surface states at a forged component

4.7.1. State-of-the-art

The fatigue behavior in respect of as-forged surface condition has very rarely been reported. Gessinger and Corti [69] showed that the fatigue strength of isothermally forged Ti-6Al-4V specimens is much lower when the surface is in the as-forged condition, as opposed to the machined condition. They suggested that this is not due to a forging skin effect, but rather an effect of mechanically working the surface during milling, which causes an improvement in the fatigue strength. Surface treatments and especially shot peening are often performed to increase the fatigue strength of components. A shot peening treatment is a cold working process (increase of dislocation density) and induces compressive residual stresses in the surface layer. Concurrently the roughness is increased by shot peening. These competing effects on the fatigue process were already discussed in the chapter “Influence of surface state on the fatigue behavior”, cf. Tab. 4.47. However, the influence of the arrangement of surfaces with different surface states has not been discussed in literature.

4.7.2. Experimental procedure

As mentioned above, some of the surfaces of forged components will remain in the as-forged condition, whereas functional surfaces are subject to additional machining (e.g., drilling holes, Fig. 4.161). To analyze the fatigue behavior of such components, plane specimens were designed such that an as-forged surface borders a machined one (Fig. 4.162). For the purpose of comparison, plane specimens with a machined surface bordering another machined surface were also tested. Additional shot peening was performed on as-forged and machined specimens.

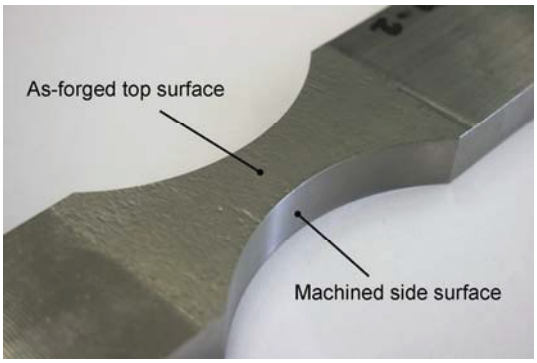

Fig. 4.162: As-forged four point bending fatigue test specimen

4.7.2.1. Specimen characterization

Two planar four-point bending test specimens, 200 mm long, were extracted from each pancake in the longitudinal direction (Fig. 3.43). Regarding the quality of the top surface, two different types of specimens were produced: as-forged (from pancakes with a thickness of 13.5 mm, after chemical milling) and machined (from pancakes with a thickness of 15 mm), Fig. 3.31 and Fig. 3.32. All square edges were consistently deburred. According to finite element simulation, the stress concentration factor K_t of the specimen geometry is 1.07. Four-point bending loading of the plane fatigue test specimens results in a relative stress gradient of 0.15 mm^{-1}.

The shot peening was performed on both as-forged and machined specimens. The specimens were rotated during the shot peening treatment. The peening intensity of 0.18 A(mm) was chosen in accordance with MIL-S-13165C [171] and MIL-P-81985 [172]. A coverage of 200% was used for all experiments. A steel ball shot was used, StD-G3-0.35-HV640, with size classification 0.35 mm and hardness HV640. The appropriate saturation curve is shown in Fig. 4.163.

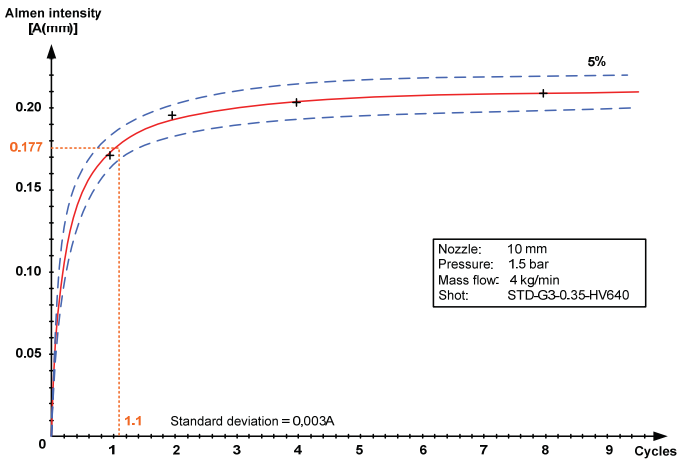

Fig. 4.163: Saturation curve for a shot peening intensity of 0.18 A(mm)

Crack initiation typically takes place at the surface or close to the surface. For a better understanding of the initiation mechanism, the roughness, hardness, residual stresses and microstructure of the surface layer were analyzed.

The roughness was measured with a confocal laser scanning microscope, Fig. 4.164. Analysis revealed that the as-forged surfaces have a slightly higher center-line average roughness R_a compared to the machined surfaces. The shot peening treatment significantly increases the roughness in both the as-forged and machined cases, with the final as-forged surfaces still rougher than the machined and shot peened surfaces.

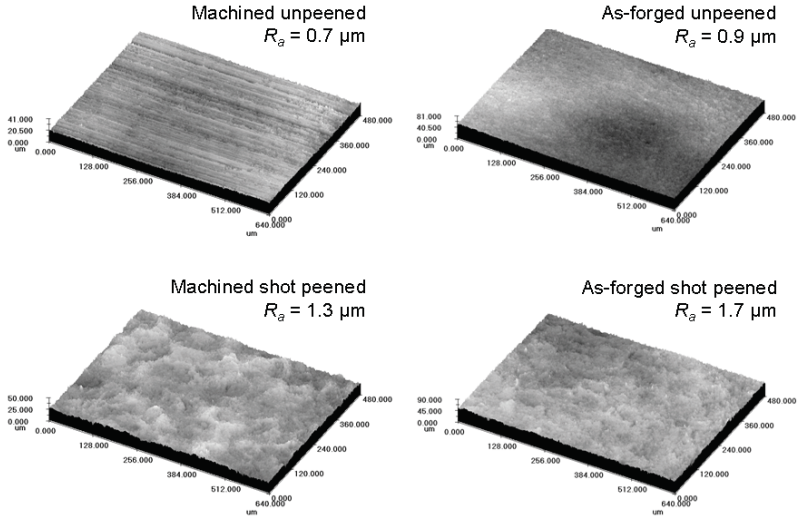

Fig. 4.164: Roughness analyses of machined and as-forged surfaces in the unpeened and shot peened condition respectively (Note: different height scales)

Vickers hardness (load ~ 10 N) and Rockwell hardness (load 1500 N) measurements were performed for the as-forged and the machined surface state. The as-forged surface leads to an average hardness of 361HV1 and 38HRC. In contrast, the hardness of the machined surface is 343HV1 and 37HRC. This slight difference in Vickers hardness of approximately 5% suggests differences in the residual stress states.

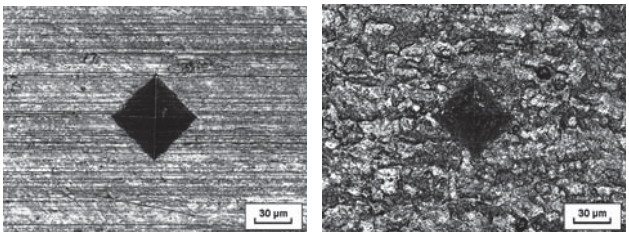

Fig. 4.165: Vickers hardness indentation in machined (l) and as-forged (r) surface layer

All residual stress measurements were performed using X-ray diffraction (XRD) in combination with the $sin^2\psi$ method. Fig. 4.166 shows the residual stress distributions for four different surface states. Graphs of residual stresses are comprised of measured data points (calculated by the average of data in the longitudinal and transversal direction, assuming a homogenous plane stress state), with no smoothing. Machining leads to residual compressive stresses in the first hundredths of a millimeter beneath the surface. In contrast, the as-forged surface exhibits distinct residual compressive stresses, reaching a depth of 0.25 mm beneath the surface. The peak value of the residual stress distribution for machined and as-forged surface state differs by a factor of 1.5.

Shot peening of the machined initial surface leads to a marked increase in the residual compressive stresses in the surface layer. The peak value of the residual compressive stresses increases from -400 MPa for an unpeened machined surface to -850 MPa for a shot peened machined surface, a difference of over 100%. The shot peening treatment of the as-forged initial surface leads to the same peak value as the peening of the machined surface. However, the extent of the residual compressive stresses at depths greater than 0.13 mm is different and the residual stress profile for the as-forged shot peened sample merges with the as-forged unpeened profile.

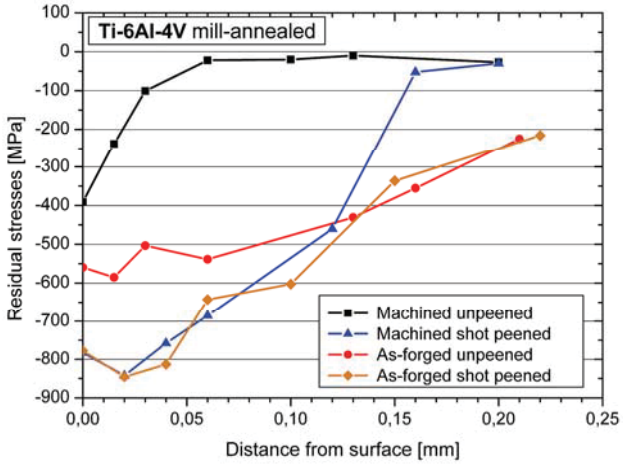

Fig. 4.166: Residual stress distribution for different surface states

Differences in the stress distributions of shot peened flat specimens (Fig. 4.166) and round specimens (cf. Fig. 4.152) were observed, in spite of identical shot peening parameters. This can be attributed to the different geometries and indicates the problem of the definition of the shot peening treatment by Almen intensity. Shot peening with the same Almen intensity can result in different residual stress distributions and also surface roughness, leading to variations of the fatigue strength.

4.7.2.2. Four point bending fatigue tests

For testing Ti-6Al-4V hour glass shaped plane specimens with a Rumul Mikrotron resonant testing machine, an existing four-point-bending (FPB) test rig was redesigned in cooperation with Russenberger Prüfmaschinen AG, Switzerland. In that way the tension/compression load on the rods of the test rig was converted with bending springs into a bending load for the specimen. The bending mode was considered to be the most feasible since the highest stresses occur in the surface layer.

A finite element analysis was done with the Abaqus™ software tool to determine the maximum load and the eigenfrequency of the four-point-bending test rig. Therefore, a quarter-model (due to symmetry) of the test rig was meshed with 8-node linear bricks. With an applied force of 10 kN a bending stress of approximately 1000 MPa can be achieved in the specimen (cf. Fig. 4.167 left). Thereby, the maximum equivalent stress in the bending springs reaches 320 MPa, which is under the endurance limit of the used steel. An eigenfrequency of 99 Hz was calculated for the four-point-bending test rig with the Lanczos-eigensolver. The buckle analysis showed, that there is a safety factor of 38 against buckling of the bending springs for an applied load of 10 kN (Fig. 4.167 (r)).

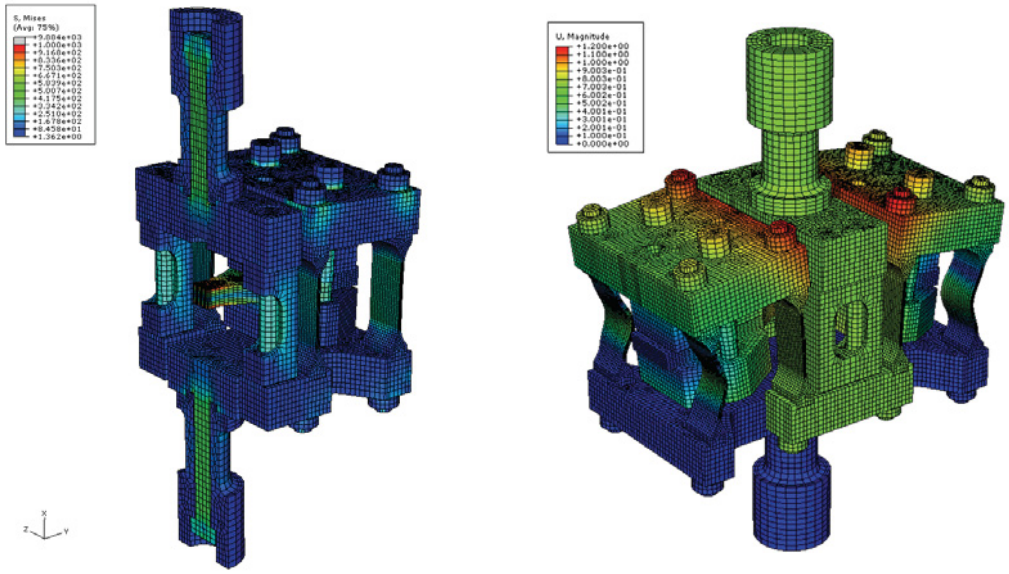

Fig. 4.167: Stress distribution in test rig for an applied load of 10 kN (l) and buckle analysis (r)

All fatigue tests were carried out at room temperature and ambient air up to 10^7 load cycles with a stress ratio R = -1 and a frequency of 66 Hz. It is well known that Ti-6Al-4V is sensitive to fretting fatigue. Therefore, brass sheets were used to avoid fretting damage at the point of restraint of the specimens (see Fig. 4.168).

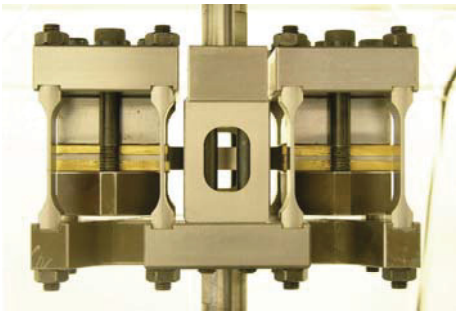

Fig. 4.168: Four-point-bending test rig with applied plane specimen

Fig. 4.169 shows the results of the four-point-bending fatigue tests. All S/N-curves correspond to a survival probability of 50%. It can be seen from the data points that the as-forged surface condition leads to a significantly higher scatter (range of scatter T_N = 1/6.6) than the machined condition (T_N = 1/2.8). The determined scatter for the machined condition shows a good accordance with the suggested range of scatter for mill-annealed Ti-6Al-4V, cf. Tab. 4.10. It has to be mentioned that the fatigue limit for the as-forged surface state is an approximation and not statistically confirmed. In the finite life region, the as-forged specimens exhibit a lower fatigue strength compared to the machined specimens, resulting in a difference in lifetime of a factor of ten.

The shot peening treatment of the machined specimens leads to a decrease in fatigue strength within the finite life region. The range of scatter of the shot peened surfaces (T_N = 1/2.5) is only slightly lower than that of the unpeened surfaces (T_N = 1/2.8). The shot peening of the as-forged specimens results in a significant increase in the fatigue strength within the finite life region, comparable with the fatigue strength of the machined shot peened specimens. The high scatter of the as-forged specimens (T_N = 1/6.6) is significantly reduced by the shot peening treatment (T_N = 1/2.9).

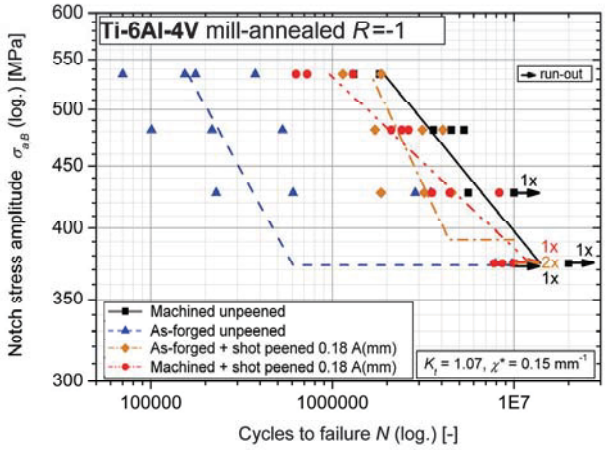

Fig. 4.169: Four-point-bending fatigue test results

The analysis of the fracture surfaces showed that for the machined surface condition, the crack emanated from the edge of the four-point-bending test specimen (Fig. 4.170, left). In contrast, the crack initiation for the specimens with the as-forged top surface (Fig. 4.170, right) occurred near the machined side surface, approximately 340 µm beneath the as-forged surface. However, there is no observable region of different fracture characteristics near the crack initiation site. This means that the fraction of subsurface fatigue crack growth without contact to the ambient air is insignificant. The crack grows beneath the as-forged top surface, within the compressive residual stresses. If the fatigue crack is of a certain length, the edge region fails due to forced rupture at 45°.

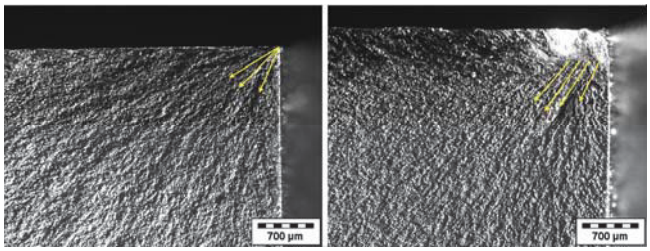

Fig. 4.170: Fracture surface of machined (l) and as-forged (r) plane specimens

For the shot peened surfaces, subsurface crack initiation beneath the edge was present (Fig. 4.171). Furthermore, a region of subsurface fatigue crack growth without contact to the ambient air (and therefore in vacuum) can be identified in the fracture surfaces, resulting in finer fracture characteristics, see Fig. 4.172 left. The transition between crack growth in vacuum and crack growth in air is marked with a dashed line. If the fatigue crack is of a certain length, the edge region fails due to forced rupture at 45°.

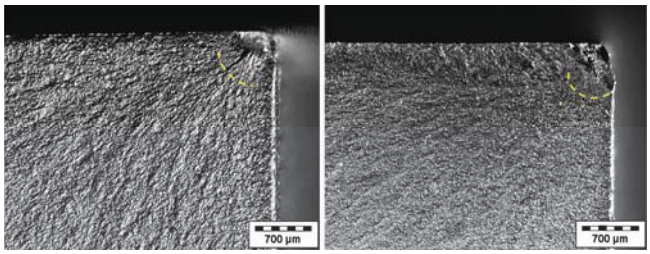

Fig. 4.171: Fracture surface of machined shot peened (l) and as-forged shot peened (r) plane specimens

A finite element simulation was done to determine the equilibrium residual stress distribution for the edge region of the machined shot peened surface state. The measured residual stresses were thereby applied as initial conditions. The result of the finite element analysis, mapped on the fracture surface, is shown in Fig. 4.172, right. The coloring indicates the maximum principal stresses; red represents 400 MPa and blue -25 MPa. It was observed that the fatigue crack initiates at the region with conjoint positive maximum principal and high Mises residual stress.

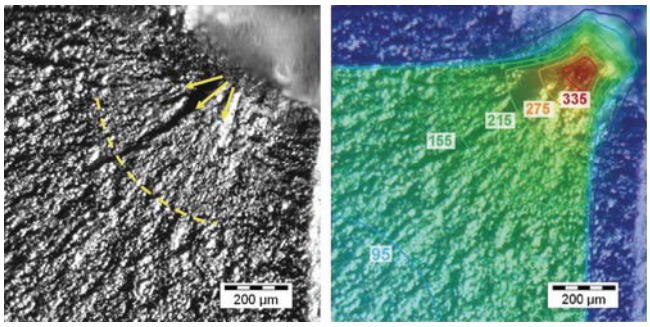

Fig. 4.172: The crack initiation site at the edge of a machined shot peened plane specimen

4.7.3. Discussion

The measured fatigue strength for mill-annealed Ti-6Al-4V in the high cycle fatigue region is very low compared to results of the fatigue tests done on round specimens under a rotating bending loading (cf. Fig. 4.28). Therefore, the microstructure at the edge region of the four-point-bending specimens was characterized. The determined parameters served as input for the microstructural fatigue models. The comparison of the modeled S/N-curve for the given relative stress gradient and the four-point-bending test results is shown in Fig. 4.173.

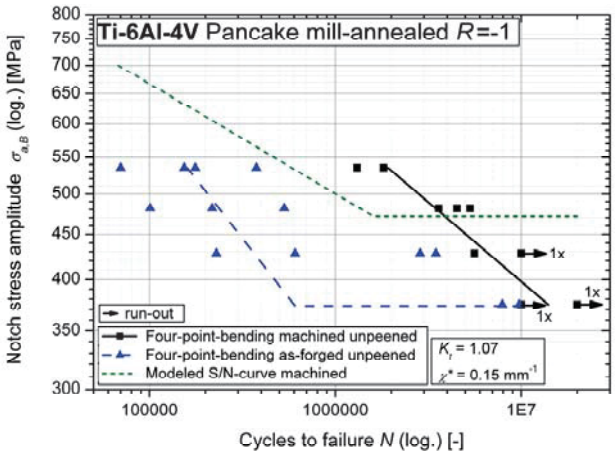

Fig. 4.173: Comparison of four-point-bending fatigue tests and modeled S/N-curve

One possible reason for the low values is the rectangular shape of the cross section with the deburred edges. The influence of edges on fatigue behavior has rarely been reported in literature. Cohen et al. [50] analyzed the effects of specimen geometry on the fatigue behavior of carburized steel. They used cantilever bend specimens with square or round edges. They suggested that the 13% lower fatigue limit of the specimens with the square edges was due to the presence of a higher volume fraction of retained austenite in the sample corners and lower residual surface compressive stress.

It is believed that the residual stress state at the edge region is responsible for the significant differences between modeled S/N-curve and four-point-bending fatigue tests data. This assumption is confirmed by the results of the fracture surface analysis discussed below. However, this comparison shows the importance of the influence of surface state arrangement on the fatigue behavior. Furthermore, it can be concluded that the consideration of the surface state in the fatigue model solely based on coefficients can be insufficient, if residual stresses can interact at an edge region.

For the machined plane specimens, crack initiation took place at the edge. This can be explained by the condition introduced by the four-point bending load, where the highest stresses occur in the top surface and the presence of the stress concentration due sample edges.

The samples where the as-forged top surface bordered the machined side surface had significantly lower fatigue strengths, especially within the finite life region. Furthermore, the cracks did not initiate from the edge, at the location of maximum nominal stresses, but beneath the as-forged top surface, near the machined side surface. This can be attributed to the residual stress state in the as-forged surface layer, illustrated in Fig. 4.174. The residual compressive stresses in the as-forged surface layer involved a maximum principal stress distribution as shown, mapped on the fracture surface, in Fig. 4.174, right. The coloring indicates the maximum principal stresses: red represents 230 MPa and blue -20 MPa. This stress distribution ties in well with the crack initiation mechanism suggested with respect to the fracture surface. However, there is a slight deviation between the depth of the maximum stress and the real crack initiation site. At this point, it has to be mentioned that the residual stresses in the as-forged surface layer are believed to vary with the position on the pancake. The residual stress distribution shown in Fig. 4.166 was measured in the middle of the specimen. Therefore, it can be assumed that the deviation between fracture surface and finite element simulation may be caused by variations of the residual stresses in the as-forged surface. Furthermore, the high scatter of the as-forged specimens compared with the machined ones can contribute to such variations.

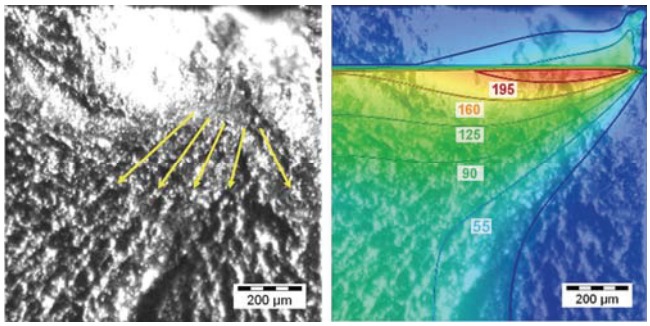

Fig. 4.174: Crack initiation site at the edge of an as-forged plane specimen

The shot peening of the as-forged surface leads to a significantly higher roughness, but the residual stress state is slightly modified. From a design point of view, to be conservative, it can be assumed that shot peening treatment of an as-forged surface (without any machining in safety critical regions) results in higher manufacturing costs and a lower fatigue strength, due to the increased roughness.

Shot peening of square edges leads to high residual tensile stresses beneath the surface, which promotes early crack initiation. The fatigue strength in the finite life region of machined specimens is slightly decreased.

This means that the negative effect of premature subsurface crack initiation caused by the residual tensile stresses prevails the positive effect of decelerated crack growth in vacuum.

The shot peening of the as-forged specimens leads to a significant increase in the fatigue strength in the finite life region; comparable with the fatigue strength of the machined shot peened specimens. This can be explained by the shift of the residual tensile stresses near the machined side surface into deeper regions, resulting in subsurface crack initiation and propagation. The difference in the fatigue strengths of machined shot peened and as-forged shot peened surface states arises from variations in the residual stress distributions; the failure mechanism is the same for both.

4.7.4. Conclusion

- Machined square edges result in decreased fatigue strengths, as compared to round specimens. This may arise due to the residual stress state in the edge regions (lower compressive or multiaxial residual tensile stresses). For this reason, chamfered edges are recommended.

- Shot peening of square edges leads to a decrease in fatigue strength if both adjacent surfaces have been machined. If just one of the adjacent surfaces is shot peened, the sample will behave as the as-forged specimens, due to residual tensile stresses at or near a surface, resulting in a significant decrease in fatigue strength. Therefore, shot peening is not recommended for square edges.

- The as-forged surface of mill-annealed Ti-6Al-4V exhibits high residual compressive stresses in the surface layer. A shot peening treatment leads to a significantly higher roughness and a slight modification in the residual stress distribution. For safety critical regions of shot peened, as-forged surfaces, when no machining is performed, in order to be conservative it can be assumed that the fatigue strength is lowered at concomitant higher manufacturing costs.

- If an as-forged surface borders a machined surface, tensile residual stresses are exposed. This leads to significantly lower fatigue strength. Such transition regions should be shot peened, causing the residual tensile stresses to shift beneath the surface, allowing for increased fatigue strength.

- Residual stresses should be considered as impressed mean stress in computational lifetime estimation, if a residual stress afflicted surface layer is present at an edge region of a component. Especially, if the residual stresses are distinct, such as as-forged or shot peened surfaces, the detrimental effect on the fatigue strength can be enormous, even for chamfered edges.

4.8. Influence of operating temperature

The maximum operating temperature of Ti-6Al-4V is usually 350°C. Nevertheless, the influence of elevated temperature on the tensile properties and fatigue behavior has rarely been reported. Existing tensile and fatigue test results from Böhler Schmiedetechnik GmbH & Co KG were used in addition to literature data for the evaluation of the influence of elevated temperature on tensile and fatigue properties of Ti-6Al-4V.

4.8.1. Influence of elevated temperature on the tensile properties

Krishnamohanrao et al. [97] presented a fracture mechanism map for the tensile properties of Ti-6Al-4V over the whole temperature range, Fig. 4.175 (l). A typical operating temperature range, from -50°C to 300°C, was complementary drawn. It was observed that this temperature interval is affected by ductile fracture; transgranular creep fracture may also occur at higher temperatures of 200°C to 300°C.

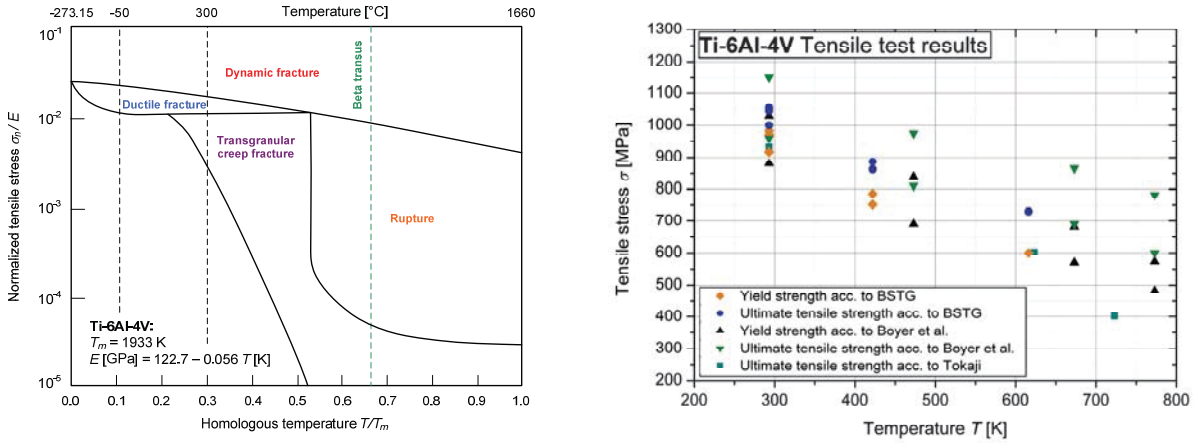

Fig. 4.175: Fracture mechanism map for Ti-6Al-4V according to [97] (l), Tensile properties at different testing temperatures (r)

Boyer et al. [42] and Tokaji [169] reported tensile properties of Ti-6Al-4V at room temperature and at elevated temperatures. They found that both, ultimate tensile strength and yield strength are significantly decreased with increasing temperature. Tensile test results of Böhler Schmiedetechnik (BSTG) were used to confirm these literature trends and to achieve models for the link of temperature and tensile strength, Fig. 4.175 (r). An exponential relationship between tensile strength and testing temperature was observed for 20°C < T < 350°C and new models for the estimation of the tensile properties were hence developed, Equ. (4.74) and Equ. (4.75). The tensile properties [MPa] at room temperature (RT) are used as input for the models in combination with the operating temperature T [K]. The results are the ultimate tensile strength $R_{m,OT}$ [MPa] and the yield strength $R_{p0.2,OT}$ [MPa] at operating temperatures (OT).

$$R_{m,OT} = R_{m,RT} \cdot e^{0.0011(293-T)} \qquad \text{Equ. (4.74)}$$

$$R_{p0.2,OT} = R_{p0.2,RT} \cdot e^{0.0015(293-T)} \qquad \text{Equ. (4.75)}$$

4.8.2. Influence of elevated temperature on the fatigue behavior

Wagner and Gregory [177] reported a significant decrease of the fatigue limit (stress ratio $R = -1$) of electrolytically polished specimens at high temperatures; from 600 MPa at room temperature to 350 MPa at 500°C.

Tokaji [169] showed for crystallographic textured Ti-6Al-4V that the high cycle fatigue behavior is considerably influenced by temperature. Both, the fatigue limit (-50%) and the finite life fatigue strength decreased significantly at a testing temperature of 350°C. Crack initiation occurred much earlier at elevated temperature, thus most of fatigue life was dominated by short crack growth. The short crack growth rates at elevated temperature were faster than those at room temperature; increasing with an increase in temperature. Since fracture surfaces were brittle with increasing temperature and applied stress, crack growth occurred in a brittle manner at elevated temperatures. This may be attributed to oxygen penetration into the crack tip region.

Results of Kato and Takafuji [91] reveal that the influence of elevated temperature on the fatigue limit is not significant for Ti-6Al-4V, Fig. 4.176. A decrease (20%) of fatigue limit was only reported for the high temperature of 450°C.

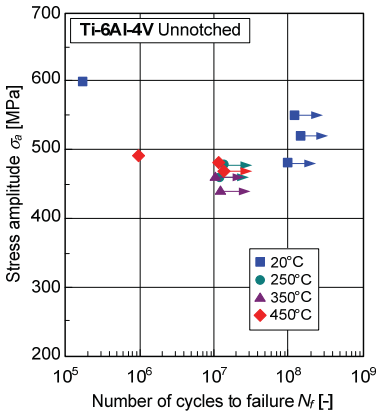

Fig. 4.176: Influence of elevated temperature on the fatigue strength, test results according to [91]

Majidi [107] analyzed the finite life fatigue strength of Ti-6Al-4V at 25°C and 300°C (induction heating system) with a stress ratio of 0.1. He determined a significant decrease of fatigue strength, namely a factor of seven in lifetime. However, it has to be mentioned that his S/N-curve analysis is disputable. He used plastic replicas for crack length measurement. The replica was taken every 500 cycles after cracks were detected. The influence of this interruption regarding lifetime, especially for the elevated testing temperature, was not discussed.

Takafuji et al. [166] observed that the effectiveness of a shot peening treatment decreases with increasing operating temperature. They determined an increase of fatigue strength owing to shot peening treatment of ~25% at room temperature and 0% at 350°C. Similar findings are reported by Gray et al. [74], cf. Fig. 4.145. This fact has to be considered in a lifetime estimation. It can be assumed that the reason for this decrease is the relaxation of the compressive residual stresses, which was reported by Prevey et al. [138]. They found a decrease of the peak residual stress from -750 MPa to -600 MPa at 325°C and from -750 MPa to -300 MPa at 475°C within an hour.

Goswami [70] reported the crack propagation behavior of STOA Ti-6Al-4V at elevated temperatures. He found similar crack growth rates for temperatures varied from 175°C to 345°C.

Sarrazin-Baudoux et al. [151] analyzed the fatigue crack growth in solution treated Ti-6Al-4V and found little influence of temperature for rates higher than 10^{-8} m/cyc where room temperature propagation is slightly faster than at 300°C. The more significant difference is a plateau phenomenon observed at 300°C at about 10^{-8} m/cyc, which appears to be a critical rate. Below this critical rate, temperature has a greater influence. In this rate range, increasing temperature induces crack growth rates of one order of magnitude higher than at room temperature at the same stress intensity factor range. The nominal threshold at both temperatures is almost identical.

Fatigue test results of Böhler Schmiedetechnik GmbH & Co KG reveal that temperatures up to 350°C do not significantly affect the fatigue strength, neither in the finite life region nor at the fatigue limit. However, the low cycle fatigue strength is considerably decreased due to the decrease of the tensile strength. Therefore, it is important to determine the decrease of the flow stress at elevated temperatures, Equ. (4.83), and calculate the transition from finite life to low cycle fatigue, Equ. (4.84) and Equ. (4.85). This will be discussed in the next chapter. It has to be mentioned that an estimated room temperature ultimate tensile strength (cf. Fig. 4.68) is not sufficient for these calculations.

In the current model, the influence of elevated temperature on the fatigue strength is represented by coefficients for slope ($c_{T,k}$), finite life fatigue strength at 10^5 load cycles ($c_{T,FL}$) and fatigue limit ($c_{T,f}$), which are applied to the results of the surface state models, Equ. (4.76) to Equ. (4.78). As things are now, the temperature coefficients can be set equal one, for temperatures between 20°C and 350°C for the analyzed surface state. Further research is necessary for determination or verification of the influence of elevated (and eventually also lowered) operating temperature on the fatigue behavior of Ti-6Al-4V. Furthermore, the influence of thermomechanical fatigue of Ti-6Al-4V would be interesting with respect to gas engine applications.

$$k_{MGMST} = c_{T,k} \cdot k_{MGMS} \qquad \text{Equ. (4.76)}$$

$$\sigma_{f,MGMST} = c_{T,f} \cdot \sigma_{f,MGMS} \qquad \text{Equ. (4.77)}$$

$$N_{T,MGMST} = 10^5 \left(\frac{c_{T,f}}{c_{T,FL}} \cdot \sqrt[k_{MGMS}]{\frac{10^5}{N_{T,MGMS}}} \right)^{-k_{MGMST}} \qquad \text{Equ. (4.78)}$$

Shot peening for elevated operating temperatures is just limited recommended. It can be assumed, that the slope coefficient and the finite life coefficient are < 1 for temperatures over 300°C, due to the temperature-caused residual stress relaxation reported by Prevey et al. [138].

4.9. Comparison of stress- and strain-controlled fatigue data

The low cycle fatigue (LCF) behavior of materials (which is considerably affected by plastic strain) is usually characterized with strain-controlled fatigue tests. Some customers of Böhler Schmiedetechnik GmbH & Co KG also prefer strain-controlled fatigue tests for the characterization of the finite life fatigue strength where the plastic strains are lower. The presented lifetime models were developed on the basis of stress-controlled fatigue data. Therefore, LCF tests were performed on the mill-annealed V-shape for comparison of stress- and strain-controlled data in the S/N-field and to find a method for estimation of the LCF strength.

4.9.1. Experimental procedure

LCF tests were performed on a servo-hydraulic test rig (250 kN Schenck Hydropuls PSB, Fig. 4.177) at two different mean strain levels (strain ratios R_ε = -1 and R_ε = 0) on round specimens (Fig. 3.30) sampled from mill-annealed V-shapes. The strain was measured with a dynamic axial clip-on extensometer (Instron). The LCF tests were done with triangular strain waveform in ambient air and at room temperature with a strain rate of 0.01 s^{-1}.

Fig. 4.177: LCF testing of round specimens on a servo-hydraulic test rig

The stress evolution with increasing load cycles and the plastic strain amplitude ($\varepsilon_{a,p}$) history for different total strain amplitudes $\varepsilon_{a,t}$ are shown in Fig. 4.178 for R_ε = -1 and in Fig. 4.179 for R_ε = 0.

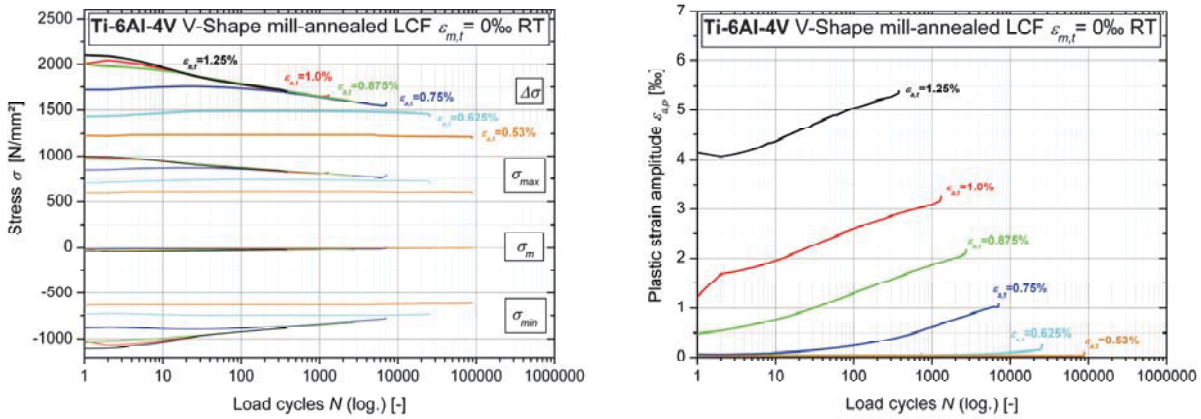

Fig. 4.178: Stress evolution (l) and plastic strain amplitude history (r) for different total strain amplitudes, R_ε = -1

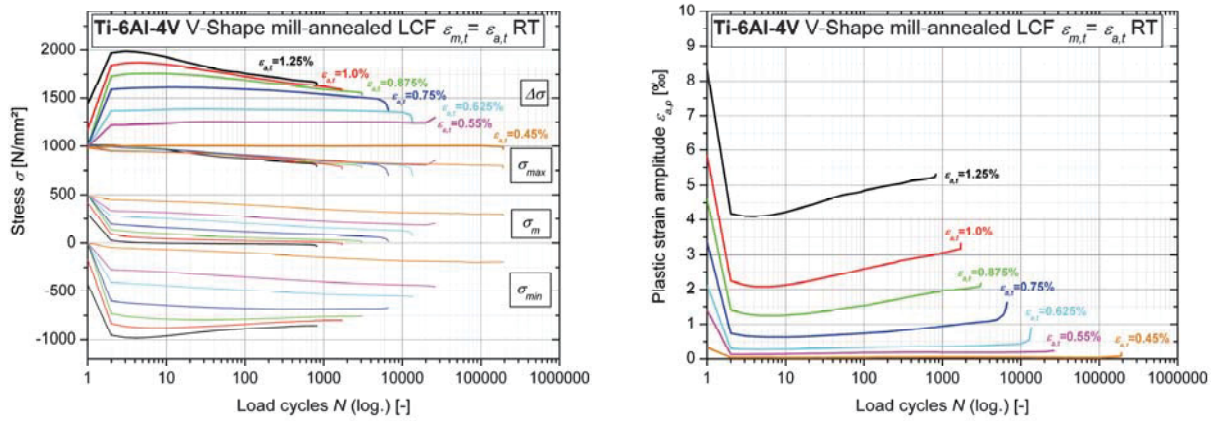

Fig. 4.179: Stress evolution (l) and plastic strain amplitude history (r) for different total strain amplitudes, $R_\varepsilon = 0$

The stress-strain-hysteresis evolution for a total strain amplitude of 1.25% for two different strain ratios are presented in Fig. 4.180.

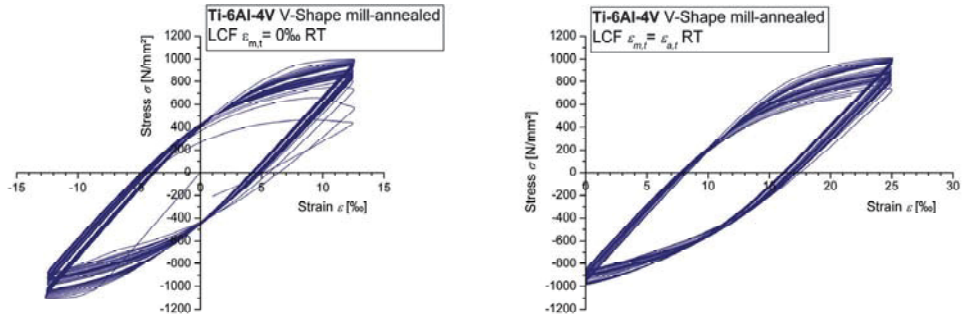

Fig. 4.180: Hysteresis evolution for the same total strain amplitude but different total mean strain levels

The strain-life-curves were determined according to the Manson-Coffin-Basquin-model. Thereby, the Manson-Coffin-curve describes the plastic fraction and the Basquin-curve the elastic fraction of the four-parametric total strain-life-curve, Equ. (4.79).

$$\varepsilon_{a,t} = \varepsilon_{a,e} + \varepsilon_{a,p} = \left(\frac{\sigma'_f}{E}\right) \cdot N_f{}^b + \varepsilon'_f \cdot N_f{}^c \qquad \text{Equ. (4.79)}$$

The elastic and plastic fraction of the strain amplitude varies with the load cycles. The strain amplitudes at half cycles to failure $N_{f/2}$ were therefore used for the analysis of the strain-life behavior. [143]

The cyclic stress-strain-curve is stated according to Ramberg-Osgood [141], Equ. (4.80).

$$\varepsilon_{a,t} = \varepsilon_{a,e} + \varepsilon_{a,p} = \frac{\sigma_a}{E} + \left(\frac{\sigma_a}{K'}\right)^{\frac{1}{n'}} \qquad \text{Equ. (4.80)}$$

A direct link exists between strain-life-curve and cyclic stress-strain-curve. A vertical section in the strain-life-plot is consistent with a horizontal section in the cyclic stress-strain-curve. This compatibility is used for the calculation of the stabilized parameters of the cyclic stress-strain-curve. The compatibility conditions are:

$$n' = \frac{b}{c} \qquad \text{Equ. (4.81)}$$

$$K' = \frac{\sigma_f'}{(\varepsilon_f')^{n'}} \qquad \text{Equ. (4.82)}$$

Impressed mean strain ($\varepsilon_{m,t} = \varepsilon_{a,t}$, $R_\varepsilon = 0$) leads to a slight increase in lifetime for higher strain levels and a slight decrease in lifetime for lower strain levels, see Manson-Coffin-Basquin plot (Fig. 4.181). The lifetime decreasing effect for $R_\varepsilon = 0$ for cycles above 10,000 results from the first few cycles, where the higher plastic strains cause higher damage rates. The lifetime increasing effect for $R_\varepsilon = 0$ at higher strain levels follows from lower stress amplitudes visible at the hysteresis characteristics (cf. Fig. 4.180) and the Ramberg-Osgood plot (cf. Fig. 4.182).

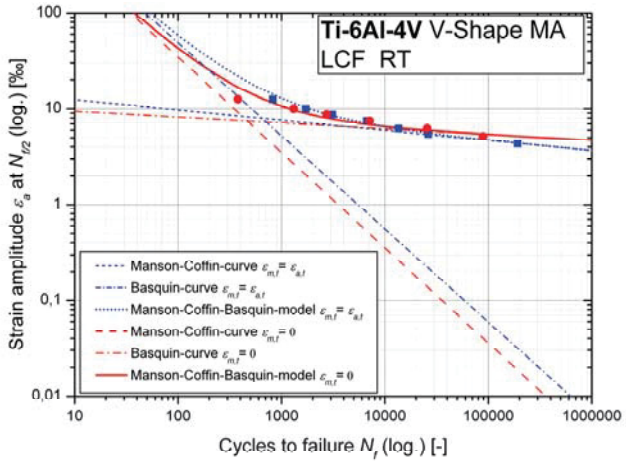

Fig. 4.181: Strain-life-curves

The comparison of the cyclic stress strain curves with the monotonic stress strain curve resulting from tensile tests exhibits cyclic softening (Fig. 4.182). The parameters of the strain-life-curves and the cyclic stress-strain-curve are summarized in Tab. 4.52.

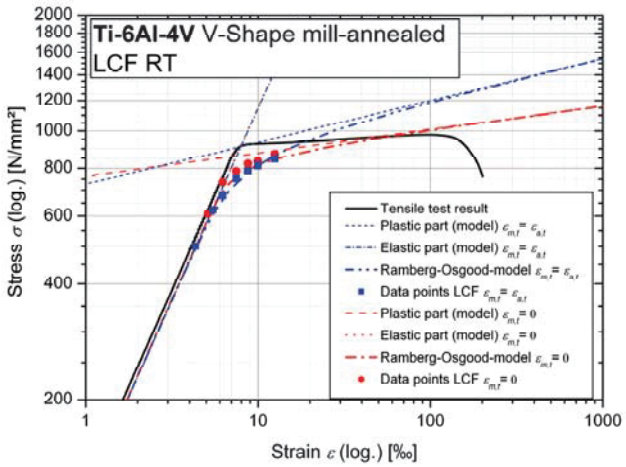

Fig. 4.182: Monotonic and cyclic stress-strain-curve (r)

Para-meter	$R = 0$ $\varepsilon_{m,t} = \varepsilon_{a,t}$	$R = -1$ $\varepsilon_{m,t} = 0$	Unit	Description
K'	1542	1162	[N/mm²]	Cyclic strain hardening coefficient
n'	0.1088	0.0611	[-]	Cyclic strain hardening exponent
E	114,5	115,4	[GPa]	Young's modulus
σ_f'	1807	1252	[N/mm²]	Fatigue strength coefficient
b	-0.1057	-0.0608	[-]	Fatigue strength exponent
ε_f'	4.281	3.375	[-]	Fatigue ductility coefficient
c	-0.9715	-0.9950	[-]	Fatigue ductility exponent

Tab. 4.52: Low cycle fatigue parameters for V-shape mill-annealed

4.9.2. Discussion

The cyclic stabilized strain-controlled fatigue data was compared with stress-controlled tension/compression test results, Fig. 4.183. Therefore, the strain-based fatigue data was converted into stress-based data by utilizing the cyclic stabilized stress values at the half number of cycles to failure. A good accordance of the finite life fatigue strength was found for both stress ratios.

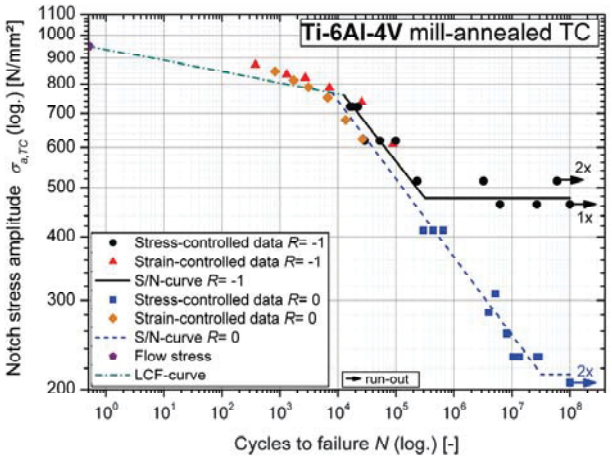

Fig. 4.183: Comparison of stress- and strain-controlled fatigue data

The low cycle fatigue (LCF) strength was estimated with a S/N-curve starting from the flow stress at operating temperature $R_{f,OT}$ (the average of 0.2%-yield strength $R_{p0.2,OT}$ and ultimate tensile strength $R_{m,OT}$, Equ. (4.83)) at $N = 0.5$ cycles. The slope was determined to be 45 for both stress ratios. The similar LCF strengths for $R_\varepsilon = -1$ and $R_\varepsilon = 0$ results from distinct stress rearrangements for impressed mean strain, cf. Fig. 4.179. The stress amplitude at LCF-transition $\sigma_{T,LCF}$ [MPa] and the appropriate load cycles $N_{T,LCF}$ (intersection point of LCF-curve and modeled S/N-curve) can be calculated according to Equ. (4.84) and Equ. (4.85), using the flow stress R_f [MPa] and the fatigue model results, slope k_{MGMST} [-], cycles at transition $N_{T,MGMST}$ [-] and fatigue limit $\sigma_{f,MGMST}$ [MPa].

$$R_{f,OT} = \frac{R_{p0.2,OT} + R_{m,OT}}{2} \qquad \text{Equ. (4.83)}$$

$$\sigma_{T,LCF} = \sqrt[(45-k_{MGMST})]{\frac{0.5\,R_{f,OT}^{45}}{N_{T,MGMST} \cdot \sigma_{f,MGMST}^{k_{MGMST}}}} \qquad \text{Equ. (4.84)}$$

$$N_{T,LCF} = 0.5\left(\frac{\sigma_{T,LCF}}{R_{f,OT}}\right)^{-45} \qquad \text{Equ. (4.85)}$$

This estimation does not serve as an exact model for the low cycle fatigue strength, but approximates the upper limit of the finite life region. This approach is especially useful for elevated operating temperatures. Several examples are discussed in the next chapter.

5. Verification of the developed models

The verification of the presented models was done on both, flat notched specimens sampled from mill-annealed V-shape and fatigue test results of Böhler Schmiedtechnik GmbH & Co KG from specimens sampled from forged components.

5.1. Flat notched specimens from mill-annealed V-shape

Flat specimens with a drill hole, cf. Fig. 3.33, were sampled from a mill-annealed V-shape. The surface roughness of the drill hole (R_a = 0.6µm and R_z = 1.9 µm) was measured with a laser-scanning microscope. Tension/compression fatigue tests were carried out in ambient air and at room temperature with a stress ratio R = 0.1 on a SincoTec Power Swing MOT 100 kN resonant testing machine, Fig. 5.1 (l). The stress distribution at the drill hole was simulated with the aid of FE-analysis for determination of stress concentration factor and relative stress gradient. Fig. 5.1 (r) shows the normal stress distribution at the drill hole, mapped on the flat notched specimen.

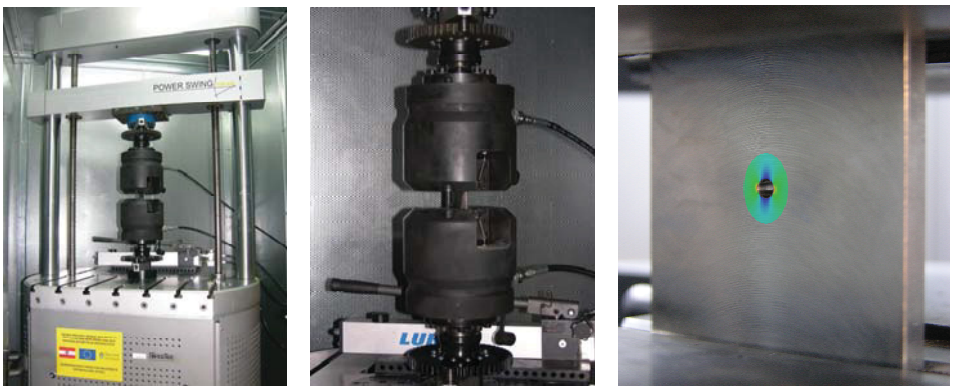

Fig. 5.1: Resonant testing machine (l) and applied flat notched specimen (c, r)

The S/N-curve was predicted based on the new developed models discussed before. The comparison with the experimental data can be found in Fig. 5.2 (l). A typical fracture surface (16x and 40x magnification) is shown in Fig. 5.2 (r). It was observed that the fatigue crack initiates inside of the drill hole.

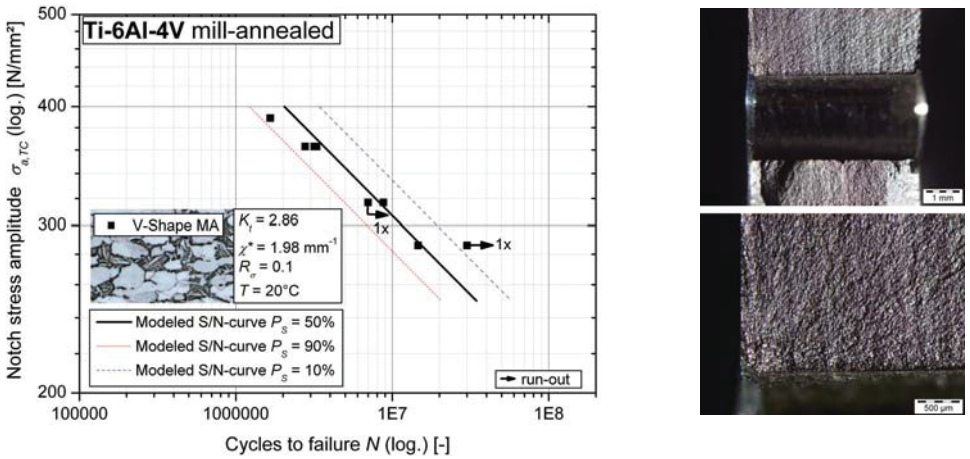

Fig. 5.2: Experimental data and modeled S/N-curves for V-shape mill-annealed (l) and fracture surface (r)

5.2. Fatigue specimens from forged components

Fatigue specimens were sampled from 15 forged components (disks and structural parts) and tested in certified testing laboratories. The fatigue test data was determined either stress- or strain-controlled (converted into stress-based data by utilizing the cyclic stabilized stress values). Different influences on the fatigue behavior were thereby covered, from microstructure and stress ratio to notches and elevated temperature. The machining factors were determined to be uniform for all specimens, what argues for consistent machining in different testing laboratories. In addition, both the ultimate tensile strength and the 0.2%-yield strength at room temperature were determined by the testing laboratories.

The microstructural-based S/N-curves were modeled based on one micrograph per forging. The other influences (relative stress gradient, mean stress, temperature) were considered with the according models presented before. The measured ultimate tensile strength and 0.2%-yield strength at room temperature were modified for the applied testing temperature and used for determination of the LCF regime.

The results for three mill-annealed forgings, one with equiaxed- and two with bimodal-type microstructure, are shown in Fig. 5.3 and Fig. 5.4.

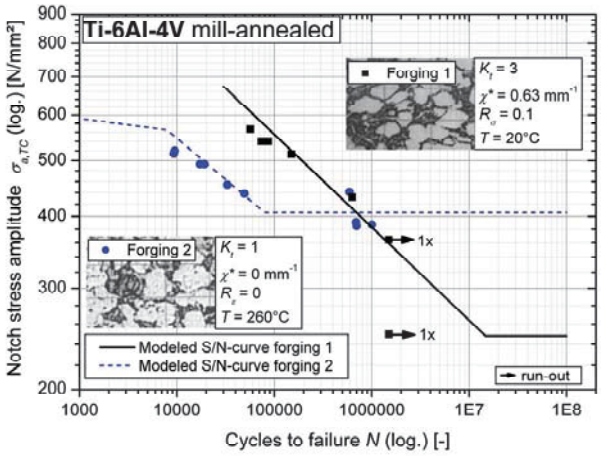

Fig. 5.3: Experimental data and modeled S/N-curves for mill-annealed forgings

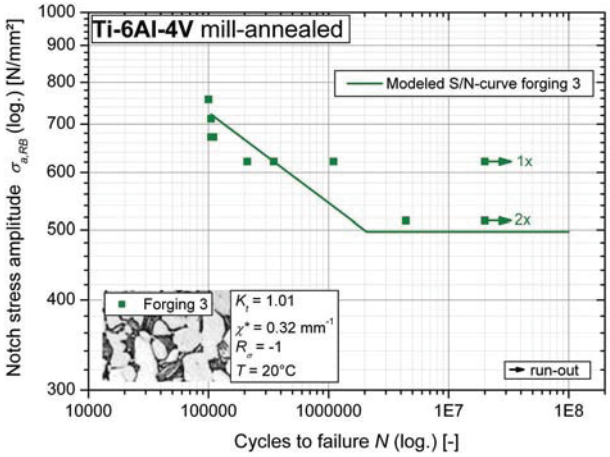

Fig. 5.4: Experimental data and modeled S/N-curve for mill-annealed forging

The results of three solution treated and water-quenched forgings are presented in Fig. 5.5. It was observed that the increase of testing temperature primarily decreases the low cycle fatigue strength. The new developed models for the calculation of the LCF transition in combination with the models for the decrease of tensile strength with increasing temperature are able to predict this behavior.

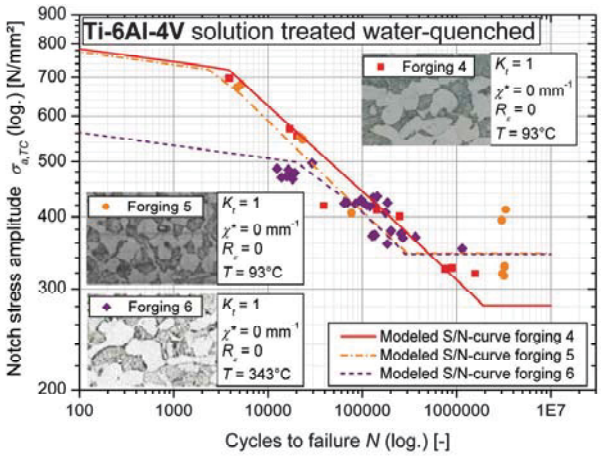

Fig. 5.5: Experimental data and modeled S/N-curves for STWQ forgings

5.3. Conclusion

The comparison of experimental fatigue data and modeled S/N-curves shows a good accordance for several fatigue conditions. It can be concluded that the new developed models enable a microstructural-based lifetime estimation including other important influences on the fatigue behavior of Ti-6Al-4V. The next step is hence to approve the approach on forged components. This will be discussed in the next chapter.

6. Application of the developed models

The developed fatigue models were implemented in a postprocessor for the integration in continuous computational lifetime estimation. The lifetime estimation is the basis for the optimization of processing and geometry of Ti-6Al-4V forgings regarding fatigue-proof and damage tolerant lightweight design. The necessary workflow is exemplarily discussed below on the basis of a developed engine mount.

6.1. Workflow for fatigue-proof damage tolerant lightweight design

The workflow for optimization of Ti-6Al-4V forgings to afford fatigue-proof damage tolerant lightweight design is presented in Fig. 6.1.

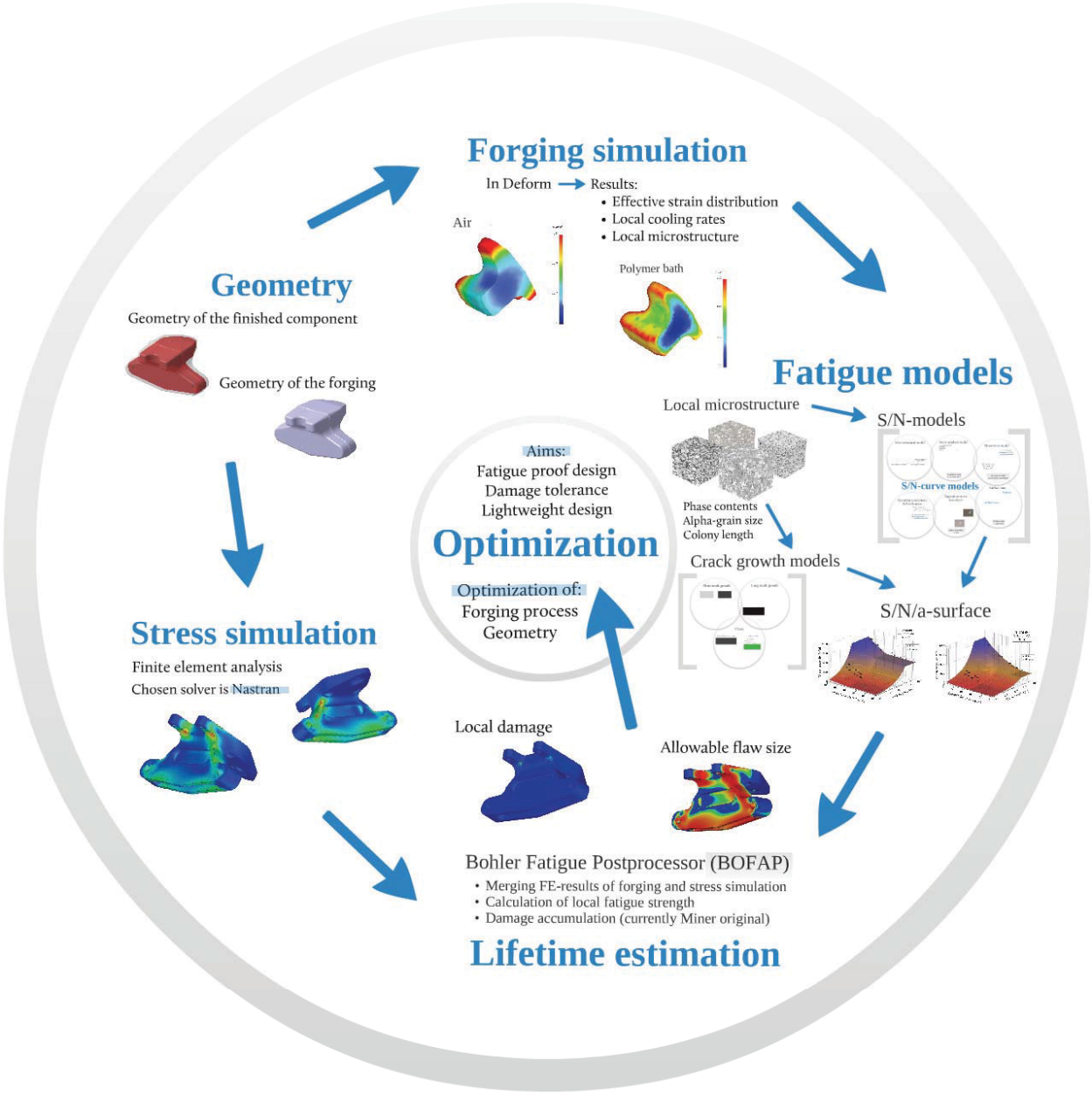

Fig. 6.1: Workflow for optimization of Ti-6Al-4V forgings to afford fatigue-proof damage tolerant lightweight design

Starting from the geometry of a component, a finite element stress analysis and a forging simulation can be performed. Ideally, the starting geometry is thereby the result of a topology optimization tool, for example, TOSCA™. The finite element stress analysis for a given load spectrum provides the stress tensor in every element. The forging simulation in Deform™ affords in addition to effective strain, temperature, cooling rates, etc. also the microstructural parameters in every element of the component by utilizing a user-routine. These microstructural parameters are the input for the developed fatigue models, first and foremost the microstructural-based fatigue model. The fatigue models were implemented in a fatigue postprocessor, which maps the results of the forging simulation on the finite element mesh of the stress analysis and calculates the fatigue strength in every node. The local damage in every node is determined by application of the Palmgren-Miner damage accumulation approach. The results of this lifetime estimation are the basis for the optimization of the forging process and of the shape of the component to achieve optimized durability and lightweight design.

6.2. Geometry

Ideally, the geometry of a component is defined with the aid of topology optimization. Starting from the constructed space under consideration of the applied loads, a topology optimization finds the component design with maximum stiffness or minimum weight. This design has to be adapted to ensure economic producibility and functionality.

An engine mount (dimensions 350 x 260 x 160 mm) was designed by Böhler Schmiedetechnik GmbH & Co KG for application and verification of the developed models. Fig. 6.2 (l) shows the geometry of the finished component, which reacts vertical and lateral loads into the substructure. The mount is required to support a mass of 587.5 kg at a distance of 63.5 mm below the centre of the lower lugs. The assembly of engine mount and aero engine is presented in Fig. 6.2 (r); the engine mount is thereby red-colored.

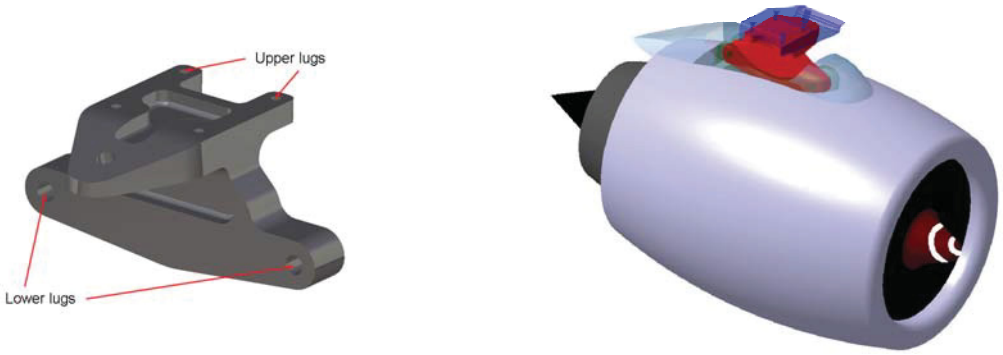

Fig. 6.2: Designed engine mount (l) and assembly of engine mount and aero engine (r)

6.3. Forging simulation

The forging simulation is performed by Böhler Schmiedetechnik GmbH & Co KG with the finite element software tool Deform™. A Deform user-routine is currently developed by Böhler Schmiedetechnik, which predicts the local microstructure in every element of a component in respect of the local thermomechanical processing. An interim link of forging parameters (forging temperature, heat treatment temperature, and cooling rate) and local microstructure was developed, cf. Appendix, by analysis of the microstructure of several heat-treated V-shapes. This interim model was used for fatigue analysis of the engine mount presented below.

The forging simulation of the engine mount was performed by Böhler Schmiedetechnik for solution treating (950°C / 70 min.) with two different cooling types, namely air-cooling and polymer-quenching, respectively. The different cooling types yield in considerable variations of the local cooling rate (determined by linear interpolation between 900°C and 650°C), Fig. 6.3. These local cooling rates are the input for the interim microstructure model (cf. Appendix) and lead to variations of the local microstructural parameters (α+β)-content and colony length.

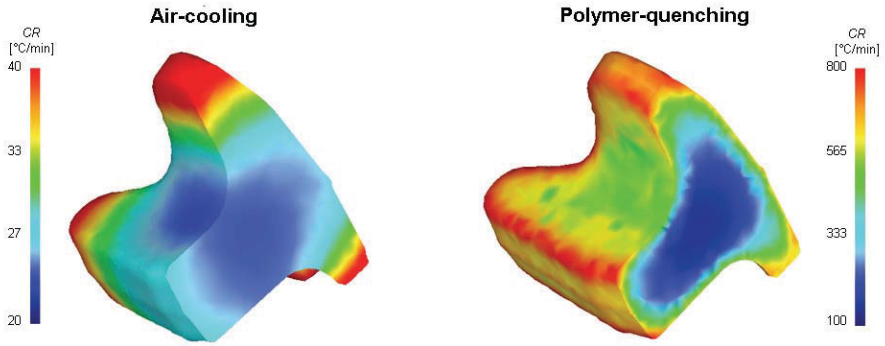

Fig. 6.3: Cooling rate distributions for solution treating with subsequent air-cooling (l) or polymer-quenching (r)

6.4. Finite element stress analysis

A finite element analysis is performed for determination of the stress tensor in every element of a component for a given load case. The stress analysis of the engine mount was done in the software tool Nastran™ for three different load cases. The load cases were chosen in accordance to the Joint Aviation Requirements JAR-25 [88], considering flight loads, ground loads, and emergency landing conditions. Evaluation of these load conditions yield the following critical cases to be considered for this analysis based on the support mass mentioned above: 3g-up, 3g-side, and 6g-down. The according stress distributions for these load cases are shown in Fig. 6.4.

Fig. 6.4: Mises equivalent stress distributions in the engine mount for three different load cases

It was observed that the maximum equivalent stress, 720 MPa, occurs during the 3g-side load case at the notch root at one of the upper lugs. Both other load cases lead to significantly lower maximum equivalent stresses. It can hence be concluded that the 3g-side load case is the critical one regarding fatigue lifetime.

6.5. Fatigue models

The fatigue models developed in this thesis enable the link of local microstructure and fatigue strength, under consideration of several other important influences on the fatigue behavior.

Starting from the local microstructural parameters (α+β)-content, primary α-grain size and (α+β)-colony length, derived from the forging simulation, the following developed fatigue models are used for determination of the local fatigue strength:

- *Microstructural model:* Based on the three microstructural parameters mentioned above, the microstructural-based S/N-curve, Equ. (4.14) to Equ. (4.18), and the long crack growth behavior, Equ. (4.23) to Equ. (4.34), are estimated.
- *Relative stress gradient model:* The influence of the relative stress gradient on the fatigue behavior is determined with Equ. (4.43) to Equ. (4.47), considering the anomalous high notch sensitivity of Ti-6Al-4V.
- *Mean stress model:* The considerable influence of impressed mean stress, due to the anomalous high mean stress sensitivity of Ti-6Al-4V, is estimated with Equ. (4.53) to Equ. (4.63).
- *Surface state model:* The surface state, especially variations of surface roughness and residual stresses, affects the fatigue behavior. This influence is considered with surface state coefficients, Equ. (4.71) to Equ. (4.73).
- *Operating temperature model:* The influence of the operating temperature on the finite life and high cycle fatigue strength is not significant and is estimated with appropriate coefficients, Equ. (4.76) to Equ. (4.78). However, the transition of low cycle fatigue region to finite life region is considerably lowered with increasing temperature and can be estimated according to Equ. (4.83) to Equ. (4.85).
- *Damage tolerance model:* The Chapetti-curve, Equ. (4.3) to Equ. (4.5), in combination with the adapted material parameter for Ti-6Al-4V, Equ. (4.42), and the developed finite life model, Equ. (4.70), is used to estimate the crack growth threshold in respect of crack length and cycles to failure. For a given geometry factor, the stress intensity factor thresholds can be converted according to the basic equation of the linear elastic fracture mechanics, Equ. (4.7), to stress values. A S/N/a-surface can hence be generated, which considers the influence of local flaws on the fatigue behavior.

6.6. Lifetime estimation

The lifetime estimation in the local stress concept is based on damage accumulation. Thereby, the local fatigue behavior (local S/N-curves) and the local stresses are combined with the load spectrum to a damage contribution. The detailed procedure is discussed below.

6.6.1. Critical plane approach

The result of a finite element simulation is a stress tensor. However, a scalar stress value is needed for damage accumulation. One possibility for the transformation of a stress tensor to a scalar stress value for fatigue analysis is the critical plane approach. An immense number of critical plane criteria exists nowadays [90], with the problem, that a selection is increasingly difficult.

The principle of a critical plane approach is that the highest loaded cutting plane in a multiaxial loaded node is critical for fatigue. The stress state of a node is defined with a stress tensor $\underline{\underline{\sigma}}$, Equ. (6.1), consisting of normal stresses σ and shear stresses τ, cf. [75].

$$\underline{\underline{\sigma}} = \begin{pmatrix} \sigma_x & \tau_{xy} & \tau_{xz} \\ \tau_{xy} & \sigma_y & \tau_{yz} \\ \tau_{xz} & \tau_{yz} & \sigma_z \end{pmatrix} \qquad \text{Equ. (6.1)}$$

The transformation of this stress tensor is done in discrete cutting planes. These cutting planes are arranged in equidistant angle increments to each other and are defined with the normal vector $\underline{n}$, Equ. (6.2). Thereby the angles φ and θ define the direction of the normal vector.

$$\underline{n} = \begin{bmatrix} \sin\theta\cos\varphi \\ \sin\theta\sin\varphi \\ \cos\theta \end{bmatrix} \qquad \text{Equ. (6.2)}$$

The stress vector $\underline{\sigma}_c$ of a cutting plane can be determined with Equ. (6.3).

$$\underline{\sigma}_c = \underline{\underline{\sigma}} \cdot \underline{n} \qquad \text{Equ. (6.3)}$$

The scalar normal stress σ_n and the shear stress τ of a cutting plane are given according to Equ. (6.4) and Equ. (6.5).

$$\sigma_n = \underline{\sigma}_c \cdot \underline{n} \qquad \text{Equ. (6.4)}$$

$$\tau = \sqrt{\underline{\sigma}_c^2 - \sigma_n^2} \qquad \text{Equ. (6.5)}$$

These normal and shear stresses have to be converted into an equivalent stress. One commercially used approach is presented in [106], using the sign of the normal stress also for the equivalent stress in a cutting plane. This approach, adapted for Ti-6Al-4V, leads to Equ. (6.6).

$$\sigma_{equ,Ti64} = sign(\sigma_n)\sqrt{0.75\,\sigma_n^2 + 3\,\tau^2} \qquad \text{Equ. (6.6)}$$

This equivalent stress is calculated for all equidistant cutting planes of a node. That plane with the highest equivalent stress is assumed to be the most damaging one, and the according stress amplitude and mean stress are used for damage accumulation.

6.6.2. Maximum principal stress

With respect to crack propagation and damage tolerance, the equivalent stress discussed before should not be used for calculation of stress intensity factors and according stresses (S/N-curve for local flaws). Normal stresses (crack opening mode I) are considerably more unfavorable with respect to crack growth than shear stresses (propagation mode II and mode III). Therefore, it is suggested that the maximum principal stress should be used for the determination of stress intensity factors and according stresses.

At every node with a stress tensor $\underline{\underline{\sigma}}$ there are at least three planes, called principal planes, where the corresponding stress vector is perpendicular to the plane, and where no shear stresses τ are present. The three stresses normal to these principal planes are called principal stresses. These three principal stresses are the eigenvalues of the stress tensor. They can be determined by solving the characteristic equation, Equ. (6.7). The three invariants I_1 to I_3 are thereby calculated according to Equ. (6.8) to Equ. (6.10).

$$-\lambda^3 + I_1 \lambda^2 - I_2 \lambda + I_3 = 0 \qquad \text{Equ. (6.7)}$$

$$I_1 = \sigma_{11} + \sigma_{22} + \sigma_{33} \qquad \text{Equ. (6.8)}$$

$$I_2 = \sigma_{11}\sigma_{22} + \sigma_{22}\sigma_{33} + \sigma_{11}\sigma_{33} - \sigma_{12}^2 - \sigma_{23}^2 - \sigma_{13}^2 \qquad \text{Equ. (6.9)}$$

$$I_3 = \det\left(\underline{\underline{\sigma}}\right) \qquad \text{Equ. (6.10)}$$

The maximum principal stress should be used for damage tolerance calculations. This approach is conservative, because it implies the worst case of crack-to-load arrangement (maximum principal stress perpendicular to crack → pure opening mode I). It should be used in combination with the flawed region of the S/N/a-surface for damage tolerant design.

6.6.3. Load spectrum

A simplified load spectrum for the lifetime estimation (consisting of simple stress reversals) is usually generated from measured complex load-time-histories (variable amplitude loading) by utilization of counting algorithms (for example, the rainflow counting method, cf. [34]).

For the examined aero engine mount, fatigue loads are generated by:

- Ground handling (towing, de-icing, turning, pivoting)
- Taxiing
- Take-off and landing
- Ground-air-ground loads
- Vertical and lateral maneuvers
- Vertical, lateral, forward and aft gusts

The load spectrum for the engine mount was chosen according to the TWIST (Transport Wing Standard) loading sequence, reported in [78]. The TWIST loading sequence was developed to be representative of the stresses in the lower wing skin at the wing root of a transport aircraft, since this has been found to be typically the most fatigue critical location. The TWIST load spectrum based on 40,000 flights is stated in Tab. 6.1.

Nr.	σ_m	σ_a	Cycles
1	1.0	1.600	10
2	1.0	1.500	20
3	1.0	1.300	50
4	1.0	1.150	180
5	1.0	0.995	520
6	1.0	0.840	1,520
7	1.0	0.685	8,000
8	1.0	0.530	41,700
9	1.0	0.375	348,000
10	1.0	0.222	3,586,650
11	-0.3	0.200	40,000
12	-0.3	0.120	3,946,650

Tab. 6.1: TWIST loading sequence for 40,000 flights [78]

6.6.4. Damage accumulation

A simple and common method for the lifetime estimation of variable amplitude loaded components is the Palmgren-Miner rule, also known as linear damage accumulation hypothesis. The input for such a damage accumulation is a S/N-curve and the load spectrum. It is assumed that the damage of one load cycle is $1/N_i$, where N_i are the cycles to failure for a stress amplitude σ_{ai} according to the S/N-curve.
The summation of the damages resulting from all cycles of a load spectrum leads to the damage D, Equ. (6.11), where n_i are the load cycles of one step with stress amplitude σ_{ai} of the load spectrum. The Palmgren-Miner rule states that failure occurs when $D = 1$. [78]

$$D = \sum_i \frac{n_i}{N_i} \qquad \text{Equ. (6.11)}$$

Different types of the Palmgren-Miner rule exist regarding damage contribution of stress amplitudes below the fatigue limit:

- Miner Original: It is assumed that stress amplitudes below the fatigue limit have no damaging effects.
- Miner Modified: A S/N curve below the fatigue limit with a slope $k_{mod} = 2k\text{-}1$ is used for calculation of the damage.
- Miner Elementary: The stress amplitudes in the whole range above and below the fatigue limit are evaluated equally.

For Ti-6Al-4V with its distinct fatigue limit, it can be assumed that Miner Original should be used for damage accumulation. However, the finite life fatigue strength is dominated by fatigue crack growth.

Therefore, the fatigue limit for a damage accumulation according to Miner Original should be approximated with the short crack growth threshold. The easier and conservative approach is to use Miner Elementary. Nevertheless, the Palmgren-Miner approach has to be verified for relevant load spectra, which is a potential research field.

6.6.5. Implementation in a postprocessor

Both, the fatigue models and the damage accumulation were implemented by Böhler Schmiedetechnik GmbH & Co KG in *Fortran* in a postprocessor called BOFAP (Böhler Fatigue Postprocessor). BOFAP maps the results of the forging simulation (local microstructural parameters) on the finite element mesh of the stress analysis.
One example, the distribution of the colony length in the engine mount for two different cooling-types, is presented in Fig. 6.5. It was observed that polymer-quenching leads to larger colonies, what coincides with the findings in the chapter "Microstructural characterization", cf. Fig. 3.27 (l). It can be assumed that this change of the lamellae aspect ratio (the polymer-quenched lamellae are thinner but longer) is caused by the higher (α+β)-content compared to the air-cooling.
The critical plane approach and the eigenvalues of the local stress tensors lead to the equivalent stress amplitude, maximum principal stress and stress ratio in every node of the component.

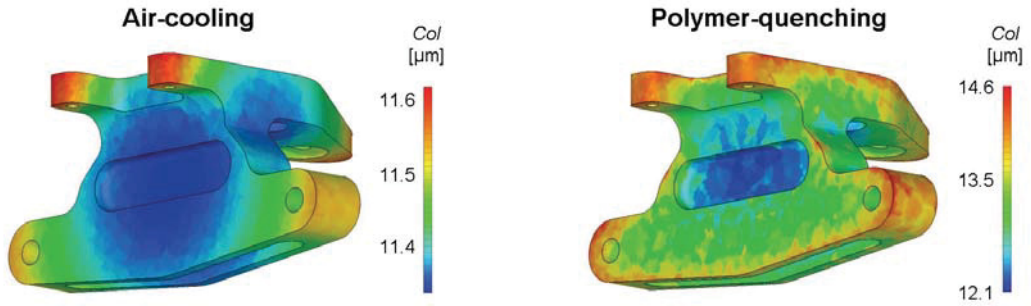

Fig. 6.5: Distribution of colony length for air-cooling (l) and polymer-quenching (r)

The local microstructural parameters are the input for the fatigue models, and the local S/N-curve can be computed. The equivalent stress amplitude and the local S/N-curve are the input for a damage accumulation based on the Palmgren-Miner rule. The result is the damage distribution in the component. The damage distributions for the engine mount are presented in Fig. 6.6. It was observed that the microstructure resulting from polymer-quenching leads to the lower damage, in spite of the larger colony length, cf. Fig. 6.5. This is caused by the higher (α+β)-content (50% compared to 43% for air-cooling) at the fatigue-critical zone and the significant influence of this microstructural parameter on the finite life fatigue strength, cf. Fig. 4.67. The location of the maximum damage corresponds with the highest loaded region of the component, cf. Fig. 6.4 (load case 3g-side).

The calculated damage is based on the TWIST loading sequence discussed before, and is hence related to 40,000 flights. The lifetime of the air-cooled engine mount would therefore be 615,000 flights, that of the polymer-quenched one 690,000 flights; a difference of 12%.

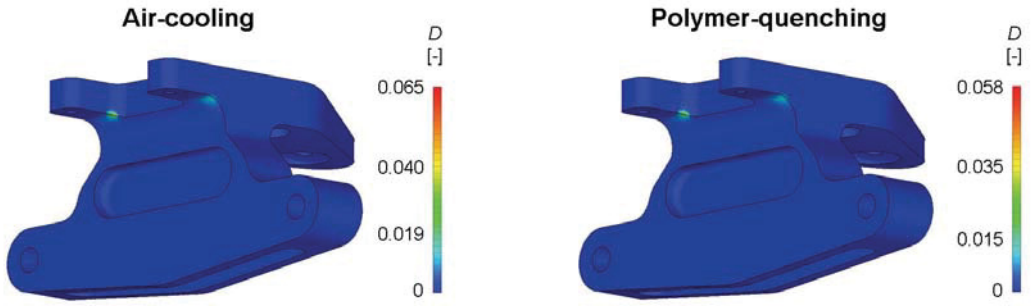

Fig. 6.6: Damage distribution in the engine mount for air-cooling (l) and polymer-quenching (r)

For damage tolerance analysis, a maximum flaw size can be defined, for example, according to the smallest detectable flaw size of non-destructive testing methods (approximately 0.5 mm, cf. [119]). This flaw size serves as input for computation of a local S/N-curve considering the given flaw size, which is used in combination with the local maximum principal stress amplitude for a damage accumulation and estimation of the local damage tolerant lifetime. This analysis was performed for the engine mount, and a maximum damage of 625 was found for both cooling-types. This means, that the inspection interval for damage-tolerance has to be set to 64 flights.

Furthermore, the allowable crack length, for example, for infinite life, can be estimated. The according results for the engine mount are shown in Fig. 6.7. Uncritical regions are blue-colored, which means allowable crack lengths larger 1 mm. Red-colored regions indicate allowable crack lengths smaller zero, which means that infinite life is not possible and a finite life number of load cycles has to be defined. The identical distributions of the allowable crack length for both cooling-types result from the fact that the α-grain size is currently supposed to be independent from cooling rate, cf. Equ. (12.3).

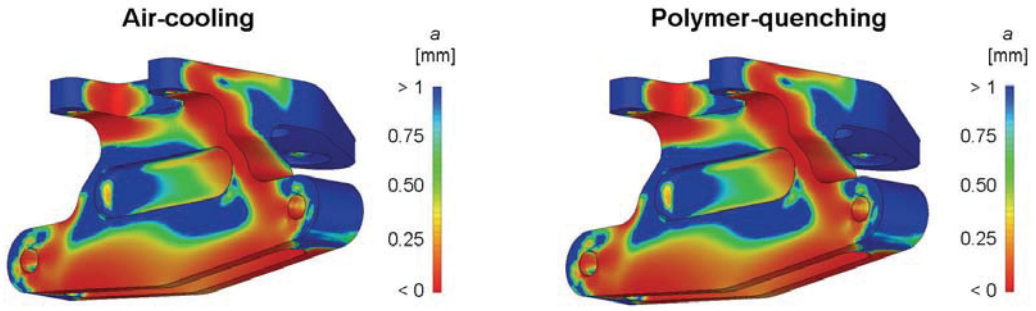

Fig. 6.7: Distribution of the allowable crack length for infinite life for air-cooling (l) and polymer-quenching (r)

These results show the significant difference of S/N-approach and damage tolerant design. The lifetime of the component based on the S/N-approach is over 600,000 flights, which corresponds to the eight-fold design life of an appropriate aircraft. However, to ensure damage tolerance, the engine mount has to be inspected every 64 flights. This inspection interval can be enlarged either by decreasing the smallest detectable flaw size of non-destructive testing, or by optimization of the component, cf. the chapter below. Damage tolerance in combination with infinite life is impossible for this component.

6.7. Optimization

The lifetime or damage tolerance of a component can be optimized in two respects:

- Decrease of the local loading
- Increase of the local fatigue strength

The decrease of the local loading can be achieved by utilizing shape optimization tools. These tools optimize the local shape of a component and decrease that way the stress concentration at stress raisers, for example, geometrical transitions or notches. The results of the computational lifetime estimation in BOFAP serve thereby as input, because those zones of the component with the maximum damage should be optimized. In the case of the examined engine mount, the zone of maximum damage at the upper lugs has potential for shape optimization.

The local fatigue strength of Ti-6Al-4V can be enhanced by optimization of the local microstructure and hence thermomechanical processing. Again, those zones of the component with the maximum damage should be optimized. This can be achieved by adaptation of forging geometry, forging process and subsequent heat treatment. For the engine mount, polymer-quenching after the solution-treatment leads to an enhanced lifetime, plus 12%, compared to the common air-cooling.

It can be concluded that the developed engine mount has potential for fatigue-proof and damage tolerant lightweight design, which is enabled by the developed models for continuous computational optimization of Ti-6Al-4V forgings. Especially in the aerospace industry, the realization of lightweight structural components is a top priority. Weight reduction of structures both increases the potential payload of aircraft and decreases their fuel consumption and CO_2 emission.

7. Conclusion

- The fatigue behavior of Ti-6Al-4V forgings is considerably influenced by microstructure, relative stress gradient, impressed mean stress, type of loading, surface state, operating temperature and flaws.

- It was observed that the influence of microstructure is different for equiaxed-type ($C_{\alpha+\beta} \leq 20\%$) and bimodal-type ($C_{\alpha+\beta} > 25\%$) microstructures. For both types of microstructures, phenomenological models were developed for the estimation of finite life fatigue strength and fatigue limit in respect of characteristic microstructural parameters. The long crack growth threshold is controlled by roughness-induced crack closure and was linked with the primary α-grain size.

- Ti-6Al-4V exhibits almost full notch sensitivity in the infinite life region. This means that the maximum stress in a notch root determines the fatigue limit, independent from a relative stress gradient. A slight supporting effect was determined for the finite life region. Phenomenological models were developed to account for the anomalous high notch sensitivity.

- Impressed mean stress leads to a significant decrease of the high cycle fatigue strength, because the maximum stress determines the fatigue limit. This anomalous mean stress dependence was analyzed and phenomenological models were developed for the estimation of the fatigue strength in the finite and infinite life region in respect of the stress ratio.

- The full mean stress sensitivity is consistent with the high notch sensitivity. This can be attributed to the crack initiation mechanism in Ti-6Al-4V. A crack initiates, if a certain maximum stress is reached to cause cleavage fracture; almost independent from stress ratio or stress gradient. This mechanism controls the fatigue limit of Ti-6Al-4V. In contrast, the finite life region is dominated by the crack propagation behavior.

- Regarding multiaxial loading, the von Mises equivalent stress was determined to be valid for Ti-6Al-4V for the fatigue limit. The use of this equivalent stress for the finite life fatigue region leads to a (conservative) overestimation of shear stresses owing to the disregard of decelerated crack propagation in shear mode.

- The surface state considerably influences the fatigue behavior of Ti-6Al-4V. It was observed that the fatigue limit is thereby mainly affected by surface roughness. In contrast, the fatigue behavior in the finite life region is dominated by residual stresses in the surface layer. This can be explained by the maximum stress controlled crack initiation and crack propagation controlled finite life fatigue strength mentioned above.

- Including the surface state in the lifetime estimation is difficult due to the complex interaction of several influencing variables, especially residual stresses and surface roughness, with other fatigue influences, for example, stress ratio and relative stress gradient. A simple model was hence implemented, using three coefficients for the description of the S/N-curve shift relative to the machined surface state.

- It was determined that shot peening does not compulsorily lead to an increase of fatigue strength. In the finite life region, the effectiveness of a shot peening treatment depends especially on the stress ratio of the load. The fatigue limit (fatigue strength at 10^8 load cycles) is not increased by shot peening.

- Machined square edges result in decreased fatigue strengths. This may arise due to the residual stress state in the edge regions (lower compressive or multiaxial residual tensile stresses). For this reason, chamfered edges are recommended.

- The as-forged surface of Ti-6Al-4V forgings exhibits high residual compressive stresses in the surface layer. A shot peening treatment leads to a significantly higher roughness and only a slight modification in the residual stress distribution. For safety critical regions of shot peened, as-forged surfaces, when no machining is performed, in order to be conservative it can be assumed that the fatigue strength is lowered at concomitant higher manufacturing costs.

- If an as-forged surface borders a machined surface, tensile residual stresses are exposed. This leads to significantly lower fatigue strength. Such transition regions should be shot peened, causing the residual tensile stresses to shift beneath the surface, allowing for increased fatigue strength.

- Regarding damage tolerance, a new approach was introduced, combining the Kitagawa-Takahashi-diagram and the S/N-approach to a S/N/a-surface. The (flaw-less) plain fatigue limit is thereby determined according to the microstructural, stress gradient, and mean stress models. For the infinite life region, the Chapetti-curve is used for estimation of the crack growth threshold in respect of the crack length. The finite life region of the S/N/a-surface is based on the flaw-less modeled S/N-curves and finite life thresholds, which are a function of the load cycles. This approach provides a simple model for design engineers to estimate the damage tolerance of a component for any flaw or damage.

- Fatigue test results of Böhler Schmiedetechnik GmbH & Co KG reveal that temperatures up to 350°C do not significantly affect the fatigue strength, neither in the finite life region nor at the fatigue limit. However, the low cycle fatigue strength is considerably decreased due to the decrease of the tensile strength. Therefore, it is important to determine the decrease of the flow stress at elevated temperatures and calculate the transition from finite life to low cycle fatigue. According models were hence developed.

- The comparison of cyclic stabilized strain-controlled fatigue data and stress-controlled tension/compression test results revealed a good accordance for the finite life region. A model for the estimation of the low cycle fatigue region based on the flow stress was presented.

- The verification of the developed fatigue models was done with fatigue test results of 15 forged components (discs, structural parts) from Böhler Schmiedetechnik GmbH & Co KG. The fatigue tests were performed in certified testing laboratories under different loading conditions (stress ratios, operating temperatures, etc.). A good accordance of modeled S/N-curves and fatigue test data was observed, what confirms the chosen approaches.

- The developed models were implemented by Böhler Schmiedetechnik GmbH & Co KG in a postprocessor. This fatigue postprocessor merges the results of forging simulation (with Deform™) and finite element stress analysis (with Nastran™), and calculates the damage for a given load spectrum.

- The developed models enable fatigue-proof and damage tolerant lightweight design of forged Ti-6Al-4V components by optimization of forging process and geometry, Fig. 7.1. Starting from the geometry of a component, a finite element stress analysis and a forging simulation can be performed. Ideally, the starting geometry is thereby the result of a topology optimization tool, for example, TOSCA™. The forging simulation affords the microstructural parameters in every element of the component. This information in combination with the local stresses and the developed fatigue models enable a computational lifetime estimation. The results of this lifetime estimation are the basis for the optimization of the forging process and of the shape of the component to achieve optimized durability and light weighting.

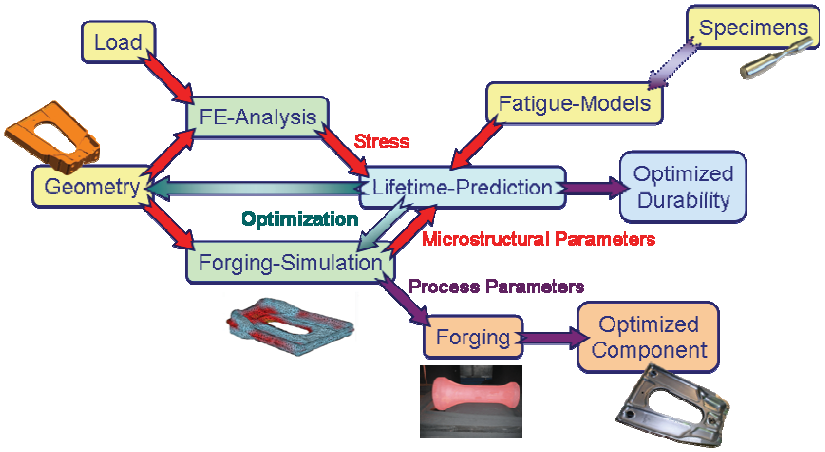

Fig. 7.1: Optimization of Ti-6Al-4V forgings with respect to fatigue behavior and damage tolerance

- The developed approach for the computational optimization of Ti-6Al-4V forgings is a useful contribution to lightweight design of products. Especially in the aerospace industry, the realization of lightweight structural components is a top priority. Weight reduction of structures both increases the potential payload of aircraft and decreases their fuel consumption and CO_2 emission.

8. Outlook

- The next step has to be the verification of the developed models based on multiaxial fatigue tests on forged components. Therefore, the designed engine mount has to be manufactured. Component fatigue tests have to be done on this mount to verify the results of the computational lifetime estimation. After this verification, an optimization tool should be implemented in the interface of fatigue postprocessor and Deform™ for automated optimization of the forging process. Furthermore, a link of fatigue postprocessor and shape optimization tools is conceivable.

- The influence of variable amplitude loading was not investigated in the presented research. However, the currently used Miner-approach for damage accumulation has to be verified for relevant load spectra. Therefore, variable amplitude fatigue tests are suggested for verification.

- An exact estimation of static strength in respect of microstructural parameters is currently missing. Additional tensile tests and K_{IC}-tests on Ti-6Al-4V with varying microstructure are currently performed for development of according models.

- The influence of operating temperature was analyzed based on few test results obtained from Böhler Schmiedetechnik. Additional fatigue tests and tensile tests are necessary to confirm the suggested models. Furthermore, the influence of thermo-mechanical fatigue should be investigated.

- This doctoral thesis was focused on the fatigue behavior of isotropic equiaxed and bimodal Ti-6Al-4V. Lamellar microstructures and the influence of crystallographic texture were excluded, since they do not represent typical forgings. Nevertheless, it would be interesting to include these options in the fatigue postprocessor.

- Another potential research field is a more comprehensive investigation of the influence of surface state and fretting on the fatigue behavior of materials in general and especially Ti-6Al-4V. These influences are currently investigated by Böhler Schmiedetechnik for a detailed consideration in continuous computational lifetime estimation.

- An improvement of the microstructural and residual stress modeling in Deform has to be done, and is part of current research of Böhler Schmiedetechnik.

- Finally, the transferability of the developed fatigue models to other titanium alloys (especially those with similar microstructure) should be analyzed.

9. List of publications

AB…Abstract PA…Paper / written contribution
PO…Poster PR…Presentation

[1] Oberwinkler B.: "Schwingfestigkeit von Ti-6Al-4V - Betrachtung mehrerer Einflussgrößen", Diploma Thesis, University of Leoben, Austria, September 2007 (PA)

[2] Javidi A., Leitner H., Oberwinkler B., Eichlseder W.: "Influence of Shot Peening on the Fatigue Behaviour of Ti-6-4 under Multiaxial Loading", 16th International Federation for Heat Treatment and Surface Engineering (IFHTSE) Congress, Brisbane, Australia, October 2007 (PR)

[3] Leitner H., Oberwinkler B., Gänser H.-P., Stoschka M.: "Life Time Estimation of Mechanically Surface Treated Titanium Components", 7th Int. ASTM/ESIS Symposium on Fatigue and Fracture, Tampa, USA, November 2007 (PR)

[4] Oberwinkler B., Javidi A., Leitner H.: "Schwingfestigkeit von Ti-6Al-4V - Betrachtung mehrerer Einflussgrößen", DGM, Tagung Werkstoffprüfung 2007, Neu-Ulm, Germany, Ed. Pohl M., pp. 145-150, November 2007, ISBN 978-3-514-00753-6 (PA, PR)

[5] Oberwinkler B., Leitner H., Gänser H.-P.: "Life Time Estimation of Highly Loaded Titanium Components with Regard to Automotive Engineering", 2nd Fatigue Symposium Leoben, Austria, Ed. Eichlseder W., pp. 67-75, April 2008, ISBN 978-3-902544-0 (PA)

[6] Oberwinkler B., Leitner H.: "Characterisation of the Fatigue Behaviour of Ti-6Al-4V to Provide a Basis for the Lifetime Estimation", Poster, 2nd Fatigue Symposium Leoben, Austria, April 2008 (PO)

[7] Oberwinkler B., Stoschka M., Riedler M.: "Influence of Microstructure on the Fatigue Behaviour of Ti-6Al-4V", Materials Science and Engineering (MSE), Nürnberg, Germany, September 2008 (PR)

[8] Oberwinkler B.: "Einfluss der Fertigung auf die Schwingfestigkeit von Ti-6Al-4V", DGM Technical Committee Titanium, MTU Aero Engines, Munich, Germany, September 2008 (PR)

[9] Riedler M., Stockinger M., Stoschka M., Oberwinkler B., Tan W.: "Linking Microstructure and Fatigue of Forged Ti-6Al-4V Aerospace Parts", 6th International Conference on Low Cycle Fatigue (LCF6), Berlin, Deutschland, Eds. Portella P.D., Beck T., Okazaki, pp. 129-134, September 2008 (PA, PR)

[10] Oberwinkler B., Leitner H., Stoschka M.: "Influence of Shot Peening on the Fatigue Behaviour of Ti-6Al-4V in Respect of Multiaxial Loading", 10th International Conference on Shot Peening (ICSP10), Tokyo, Japan, Conference Proceedings, Ed. Tosha K., pp. 388-393, September 2008 (PA, PR)

[11] Leitner H., Oberwinkler B., Gänser H.-P., Stoschka M.: "Influence of the Peening Intensity on the Fatigue Behavior of Shot Peened Titanium Components", Journal of ASTM International, Vol. 5, No. 9, pp. 1-10, October 2008 (PA)

[12] Oberwinkler B., Leitner H., Riedler M.: "Bruchmechanische Lebensdauerbewertung von geschmiedeten Bauteilen aus Ti-6Al-4V", DVM, Tagung Werkstoffprüfung 2008, Berlin, Germany, DVM Bericht 642, Eds. Frenz H., Grellmann W., pp. 257-262, December 2008, ISBN 978-3-00-026399-6 (PA, PR)

[13] Leitner H., Oberwinkler B., Stoschka M.: "Tragfähigkeitssteigerung von Leichtbaukonstruktionen durch lokale mechanische Oberflächenverfestigung", 4. Landshuter Leichtbau-Colloquium, Landshut, Germany, February 2009 (PR)

[14] Oberwinkler B., Leitner H., Riedler M.: "Combination of Safe Life and Fail Safe Concepts to Assess the Lifetime of Ti-6Al-4V Forgings", TMS 2009, 138th Annual Meeting & Exhibition, San Francisco, California, Supplemental Proceedings, Vol.1, pp. 77-84, February 2009, ISBN 978-0-87339-738-4 (PA, PR)

[15] Oberwinkler C., Oberwinkler B., Redik S., Eichlseder W.: "Comparison of Short and Long Crack Growth for Titanium and Aluminum Alloys", Poster, TMS 2009, 138th Annual Meeting & Exhibition, San Francisco, California, February 2009 (PO)

[16] Oberwinkler B., Riedler M., Eichlseder W.: "Importance of Residual Stresses Regarding Fatigue of Titanium Forgings", 9th Int. ASTM/ESIS Symposium on Fatigue and Fracture Mechanics, Vancouver, Canada, May 2009 (PR)

[17] Riedler M., Stockinger M., Stoschka M., Oberwinkler B., Tan W., Leitner H.: "Analysis and simulation of heat treatment processes for fatigue and fracture optimization of forged aircraft engine and structural parts", AeroMat 2009, Dayton, Ohio, June 2009 (AB, PR)

[18] Riedler M., Stockinger M., Huber D., Stoschka M., Oberwinkler B., Tan W.: "Computational Fatigue Optimization - Application for purpose-aimed Component and Forging Process Design", European Conference on Materials and Structures in Aerospace, Augsburg, Germany, July 2009 (AB, PR)

[19] Oberwinkler B., Oberwinkler C., Redik S., Leitner H.: "Analysis of Short Crack Growth for Two Representative Light Metals", 12th International Conference on Fracture (ICF12), Ottawa, Canada, July 2009 (PA, PR)

[20] Oberwinkler B., Riedler M., Leitner H., Javidi A.: "Four Point Bending Fatigue Tests of Forged Ti 6Al 4V", MP Materials Testing, Vol. 51, pp. 580-586, September 2009 (PA)

[21] Oberwinkler B.: "Optimierung der Schwingfestigkeit von geschmiedeten Bauteilen aus Ti-6Al-4V", Clausthaler Leichtmetall-Tagung, Clausthal-Zellerfeld, Germany, September 2009 (PR)

[22] Oberwinkler B., Riedler M., Eichlseder W., Gutknecht M.F.: "Light Weight Design of Ti-6Al-4V Forgings", Titanium 2009, Waikoloa, Hawai'i, 25th Annual Conference Proceedings, International Titanium Association, September 2009 (PA, PR)

[23] Oberwinkler B.: "Betriebsfeste und schadenstolerante Auslegung von geschmiedeten Bauteilen aus Ti-6Al-4V", European Structural Integrity Society (ESIS) Austria Meeting, Leoben, Austria, November 2009 (PR)

[24] Oberwinkler B., Riedler M., Eichlseder W.: "Importance of Residual Stresses and Surface Roughness Regarding Fatigue of Titanium Forgings", Journal of ASTM International, Vol. 7, No. 2, February 2010, Paper ID JAI102534 (PA)

[25] Oberwinkler B., Riedler M., Eichlseder W.: "Importance of local microstructure for damage tolerant light weight design of Ti-6Al-4V forgings", International Journal of Fatigue, Vol. 32, Issue 5, pp. 808-814, May 2010, doi:10.1016/j.ijfatigue.2009.06.021 (PA)

10. Bibliography

[26] Adachi S., Wagner L., Lütjering G.: "Influence of microstructure and mean stress on fatigue strength of Ti-6Al-4V", In: Titanium '84 - Science and Technology, Vol. 4, eds. Lütjering G., Zwicker U., Bunk W., pp. 2139-2146, DGM, 1985

[27] Adachi S., Wagner L., Lütjering G.: "Influence of Mean Stress on Fatigue Strength of Ti-6Al-4V", In: Proceedings 7th Int. Conf. on Strength of Metals and Alloys, eds. McQueen H.L., Bailon J.P., Dickson J.I., p. 2117, Pergamon Press, New York, 1986

[28] Adams D.O.: "Flaw Tolerant Safe-Life Methodology", RTO AVT Specialists' Meeting, Greece, 1999

[29] Anderson T.L.: "Fracture mechanics: fundamentals and applications", 3rd Edition, CRC Press, 2005, ISBN 0-84931-656-1

[30] ASTM International: "ASTM E466 - Standard Practice for Conducting Force Controlled Constant Amplitude Axial Fatigue Tests of Metallic Materials", ASTM International, West Conshohocken, PA, USA, 1990

[31] ASTM International: "ASTM E468 - Standard Practice for Presentation of Constant Amplitude Fatigue Test Results for Metallic Materials", ASTM International, West Conshohocken, PA, USA, 2007

[32] ASTM International: "ASTM E647 - Standard Test Method for Measurement of Fatigue Crack Growth Rates", ASTM International, West Conshohocken, PA, USA, 2008

[33] ASTM International: "ASTM E739 - Standard Practice for Statistical Analysis of Linear or Linearized Stress-Life (S-N) and Strain-Life (ε-N) Fatigue Data", ASTM International, West Conshohocken, PA, USA, 1991

[34] ASTM International: "ASTM E1049-85 - Standard Practices for Cycle Counting in Fatigue Analysis", ASTM International, West Conshohocken, PA, USA, 2005

[35] Banerjee D., Williams J. C.: "Microstructure and Slip Character in Titanium Alloys", Defence Science Journal, Vol. 36, No. 2, pp. 191-206, April 1986

[36] Bartlo L.J., Effect of Microstructure on Fatigue of Ti-6Al-4V Bar, ASTM STP 459, 1969, In: Materials Properties Handbook: Titanium Alloys, eds. Boyer R., Welsch G., Collings E.W., p. 538, ASM International, 1994

[37] Baxter G.J., Rainforth W.M., Grabowski L.: "TEM observations of fatigue damage accumulation at the surface of the near-α titanium alloy IMI 834", Acta Materialia, Vol. 44, No. 9, pp. 3453-3463, 1996

[38] Benedetti M., Fontanari V.: "The effect of bi-modal and lamellar microstructures of Ti-6Al-4V on the behavior of fatigue cracks emanating from edge-notches", Fatigue & Fracture of Engineering Materials & Structures, Vol. 27, pp. 1073-1089, 2004

[39] Benson D.K., Grosskreutz J.C., Shaw G.G.: "Mechanisms of fatigue in mill-annealed Ti-6Al-4V at room temperature and 600°F", Metallurgical and Materials Transactions B, Vol. 3, Nr. 5, 1972

[40] Bergner F., Zouhar G.: "A new approach to the correlation between the coefficient and the exponent in the power law equation of fatigue crack growth", International Journal of Fatigue, Vol. 22, pp. 229-239, 2000

[41] Bowen A.W., Titanium '80, Science and Technology, p. 947, 1980, In: Materials Properties Handbook: Titanium Alloys, eds. Boyer R., Welsch G., Collings E.W., ASM International, 1994

[42] Boyer R., Welsch G., Collings E.W.: "Materials Properties Handbook: Titanium Alloys", ASM International, 1994, ISBN 0-87170-481-1

[43] Bridier F., Villechaise P, Mendez J.: "Slip and fatigue crack formation processes in an α/β titanium alloy in relation to crystallographic texture on different scales", Acta Materialia, Vol. 56, pp. 3951-3962, 2008

[44] Cadario A.: "Fretting Fatigue - A Literature Survey", Report 385, KTH Royal Institute of Technology, Stockholm, Sweden, 2005

[45] Calles W.: "Schwingfestigkeit und Gefügeparameter der Legierung TiAl6V4", Roell Amsler Symposium 98/99, World of Dynamic Testing, pp. 147-153, 2000, ISBN 3-89653-883-7

[46] Carboni M., Patriarca L., Regazzi D.: "Determination of ΔK_{th} by compression pre-cracking in a structural steel", Journal of ASTM International, Vol. 6, Issue 9, 2009

[47] Chapetti M.D.: "Fatigue propagation threshold of short cracks under constant amplitude loading", Int. Journal of Fatigue, Vol. 25, pp. 1319-1326, 2003

[48] Chapetti M.D.: "On the fatigue behavior of small cracks induced by foreign-object damage in Ti-6Al-4V", 11th Int. Conference on Fracture, Italy, 2005

[49] Clausen R., Stangenberg J.: "Roughness of Shot-Peened Surfaces - Definition and Measurement", ICSP-7, Warsaw, Poland, 1999, pp. 69-77, International Scientific Committee for Shot Peening, Warrendale, PA, www.shotpeening.org/ICSP

[50] Cohen R.E., Matlock D.K., Krauss G.: "Specimen Edge Effects on Bending Fatigue of Carburized Steel", Journal of Materials Engineering and Performance, Vol.1 (5), pp. 695-704, 1992

[51] Conner B.P., Hutson A.L., Chambon L.: "Observations of fretting fatigue micro-damage of Ti-6Al-4V", Wear, Vol. 255, pp. 259-268, 2003

[52] Cowles B.A.: "High cycel fatigue in aircraft gas turbines - an industry perspective", Int. Journal of Fracture, Vol. 80, pp. 147-163, 1996

[53] De Freitas M., François D.: "Analysis of fatigue crack growth in rotary bend specimens and railway axles", Fatigue & Fracture of Engineering Mater. & Struct., Vol. 18, No. 2, pp. 171-178, 1995

[54] Delahay T.: "Développement d'une méthode probabiliste de calcul en fatigue multiaxiale prenant en compte la répartition volumique des contraintes", PhD Thesis, Université Bordeaux 1, France, 2004

[55] Dengel D.: "Die arcsin√P-Transformation - ein einfaches Verfahren zur grafischen und rechnerischen Auswertung geplanter Wöhlerversuche", Zeitschrift für Werkstofftechnik, 6. Jhrg., Heft 8, pp. 253-288, 1975

[56] Deutsches Institut für Normung: "DIN 50100 - Testing of Materials; Continuous Vibration Test; Definitions, Symbols, Procedure, Evaluation", Beuth, Berlin, Germany, 1978

[57] Deutsches Institut für Normung: "DIN 50113 - Testing of metals; Rotating bar bending fatigue test", Beuth Verlag, Berlin, Germany, 1982

[58] Deutsches Institut für Normung: "DIN 50125 - Testing of metallic materials - Tensile test pieces ", Beuth Verlag, Berlin, Germany, 2009

[59] Deutsches Institut für Normung: "DIN EN ISO 6892-1 - Metallic materials - Tensile testing - Part 1: Method of test at room temperature", Beuth Verlag, Berlin, Germany, 2009

[60] Eichlseder W.: "Rechnerische Lebensdaueranalyse von Nutzfahrzeugkomponenten mit der Finite Elemente Methode", Doctoral Thesis, University of Technology Graz, Austria, 1989

[61] El Haddad M.H., Smith K.N., Topper T.H.: "Fatigue Crack Propagation of Short Cracks", ASME Transactions, Journal of Engineering Materials and Technology, Vol. 101, pp. 42-46, 1979

[62] Evans W.J.: "Optimising mechanical properties in alpha+beta titanium alloys", Materials Science and Engineering A, Vol. A243, pp. 89-96, 1998

[63] Franz H.E., Olbricht A.: "Optimization of Shot Peening to Improve the Fatigue Strength of Ti-6Al-4V", ICSP-3, Shot Peening: Science, Technology, Application, Vol. 2, Garmisch-Partenkirchen, Germany, 1987, International Scientific Committee for Shot Peening, Warrendale, PA, pp. 439–446, www.shotpeening.org/ICSP

[64] Freudenthal A.M.: "New Aspects of Fatigue and Fracture Mechanics", Engineering Fracture Mechanics, Vol. 6, Issue 4, pp. 775-780, 1974

[65] Froes F.H., Friedrich H., Kiese J., Bergoint D.: "Titanium in the Family Automobile: The Cost Challenge", JOM, Vol.56, pp. 40-44, 2004

[66] Fröschl J.: "Fatigue behavior of forged components: Technological effects and multiaxial fatigue", Doctoral Thesis, Montanuniversität Leoben, 2006

[67] Frost N.E., Marsh K.J., Pook L.P.: "Metal fatigue", Dover publications, New York, 1999, ISBN 0-486-40927-9

[68] Fujii H., Takahashi K., Yamashita Y.: "Application of Titanium and Its Alloys for Automobile Parts", Nippon Steel Technical Report, No. 88, pp. 70-75, 2003

[69] Gessinger G.H., Corti C.W.: "Influence of Surface Condition on the Fatigue Strength of Isothermally Forged Ti-6Al-4V", Titanium '80 – Science and Technology, Vol. 3, eds. Kimura H., Izumi O., pp. 1787-1795, TMS-AIME, Japan, 1980

[70] Goswami T.: "Fatigue crack growth behavior of Ti–6Al–4V alloy forging", Materials and Design, Vol. 24, pp. 423–433, 2003

[71] Gottstein G.: "Physikalische Grundlagen der Materialkunde", 2nd Edition, Springer, Berlin, 2001, ISBN 3-540-41961-6

[72] Gough H.J., Pollard W.J., Clenshaw W.J.: "Some Experiments on the Resistance of Metals to Fatigue under Combined Stress", Mem. 2522, Aeronautical Research Council, His Majesty's Stationary Office, London, 1951

[73] Gray III G.T., Lütjering G.: "The effect of microstructure and stress ratio on fatigue crack propagation behavior of Ti-6Al-4V", In: Titanium '84 - Science and Technology, Vol. 4, eds. Lütjering G., Zwicker U., Bunk W., pp. 2251-2258, DGM, 1985

[74] Gray H., Wagner L., and Lütjering G.: "Influence of Surface Treatment on the Fatigue Behavior of Titanium-Alloys at Room and Elevated Temperatures," Sixth World Conference on Titanium, Cannes, France, 1988, pp. 1895–1900, Societe Française de Metallurgie, Les Editions de Physique, Les Ulis, France

[75] Gross D., Hauger W., Schnell W., Wriggers P.: "Technische Mechanik", Band 4, 5. Auflage, Springer, 2004, ISBN 3-540-22099-2

[76] Gudehus H., Zenner H.: "Leitfaden für eine Betriebsfestigkeitsrechnung", 3rd Edition, Verlag Stahleisen, Düsseldorf, 1995, ISBN 3-514-00445-5

[77] Hager C.H. Jr., Sanders J.H., Sharma S.: "Characterization of mixed and gross slip fretting wear regimes in Ti6Al4V interfaces at room temperature", Wear, Vol. 257, pp. 167-180, 2004

[78] Haibach E.: "Betriebsfestigkeit: Verfahren und Daten zur Bauteilberechnung", 2nd Edition, Springer, 2002, ISBN 9783540431428

[79] Hall E.O.: "The deformation and ageing of mild steel: III. Discussion of results", Proc. Phys. Soc., Nr. 381, B64, pp. 747-753, 1951

[80] Hall J.A.: "Fatigue crack initiation in alpha-beta titanium alloys", International Journal of Fatigue, Vol. 19, No. 1, pp. S23-S37, 1997

[81] Haritos G.K., Nicholas T., Lanning D.B.: "Notch size effects in HCF behavior of Ti-6Al-4V", International Journal of Fatigue, Vol. 21, pp. 643-652, 1999

[82] Hawkyard M., Powell B.E., Hussey I., Grabowski L.: "Fatigue crack growth under the conjoint action of major and minor stress cycles", Fatigue & Fracture of Engineering Materials & Structures, Vol. 19, Issue 2-3, pp. 217-227, 1996

[83] Hayes M.: "Connexions between the moduli for anistropic elastic materials", Journal of Elasticity, Vol. 2, Nr. 2, pp. 135-141, 1972

[84] Henry G.: "Fractography and Microfractography", Vol. 5, p. 445, Verlag Stahleisen, Düsseldorf, Germany, 1979

[85] International Organization for Standardization: "ISO 1099:2006 - Metallic materials - Fatigue testing - Axial force-controlled method", Beuth Verlag, Berlin, Germany, 2006

[86] Ivanova S.G., Biederman R.R., Sisson R.D. Jr.: "Investigations of Fatigue Crack Initiation in Ti-6Al-4V During Tensile-Tensile Fatigue", Journal of Materials Engineering and Performance", Vol. 11, pp. 226-231, 2002

[87] Ivanova S.G., Cohen F.S., Biederman R.R., Sisson R.D. Jr.: "Role of microstructure in the mean stress dependence of fatigue strength in Ti-6Al-4V alloy", In: Fatigue Behavior of Titanium Alloys, eds. Boyer R.R., Eylon D., Lütjering G., pp. 39-46, TMS, 1999

[88] Joint Aviation Authorities: "Joint Aviation Requirements", JAR-25, 2004

[89] Kallmeyer A.R., Krgo A., Kurath P.: "Evaluation of Multiaxial Fatigue Life Prediction Methodologies for Ti-6Al-4V", Journal of Engineering Materials and Technology, Vol. 124, pp. 229-237, 2002

[90] Karolczuk A., Macha E.: "A review of critical plane orientations in multiaxial fatigue failure criteria of metallic materials", Int. Journal of Fracture, Vol. 134, pp. 267-304, 2005

[91] Kato Y., Takafuji S.: "Fatigue Properties of Shot-Peened Ti-6Al-4V Alloy at Elevated Temperatures", J. Soc. Mat. Sci. Japan, Vol. 46, No. 10, pp. 1136-1142, 1997

[92] Kato Y., Takafuji S., Kiriyama M.: "Effect of Shot Peening on Fatigue Strength of Ti-6Al-4V Alloy at Elevated Temperatures", Journal of the Society of Materials Science Japan, Vol. 45, No. 1, pp. 43-47, 1996

[93] Kitagawa H., Takahashi S.: "Applicability of fracture mechanics to very small cracks or cracks in the early stage", Proc. of the second int. conference on mech. behaviour of materials, ASM, pp. 627-631, 1976

[94] Knobbe H., Köster P., Christ H.-J., Fritzen C.-P., Riedler M.: "Rissinitiierung und Mikrorissausbreitung in einer geschmiedeten (α+β) Titanlegierung", Clausthaler Leichtmetall-Tagung, Clausthal-Zellerfeld, Germany, 2009

[95] Koster W.P., In: Materials Properties Handbook: Titanium Alloys, eds. Boyer R., Welsch G., Collings E.W., p. 539, ASM International, 1994

[96] Koster W.P., Gatto L.R., Cammett J.T.: "Influence of Shot Peening on Surface Integrity of Some Machined Aerospace Materials", ICSP-1, Paris, France, 1981, pp. 287–293, International Scientific Committee for Shot Peening, Warrendale, PA, www.shotpeening.org/ICSP

[97] Krishnamohanrao Y., Kutumbarao V. V., Rao P. Rama: "Fracture mechanism maps for titanium and its alloys", Acta Metallurgica, Vol. 34, No. 9, pp.1783-1806, 1986

[98] Künkler B., Düber O., Köster P., Krupp U., Fritzen C.-P., Christ H.-J.: "Modelling of short crack propagation - Transition from stage I to stage II", Engineering Fracture Mechanics, Vol. 75, pp. 715-725, 2008

[99] Lanning D.B., Haritos G.K., Nicholas T.: "Influence of stress state on high cycle fatigue of notched Ti-6Al-4V specimens", International Journal of Fatigue, Vol. 21, pp. S87-S95, 1999

[100] Lazzeri L., Mariani U.: "Application of Damage Tolerance principles to the design of helicopters", International Journal of Fatigue, Vol. 31, pp. 1039-1045, 2009

[101] Lindley T.C.: "Fretting fatigue in engineering alloys", Int. Journal of Fatigue, Vol. 19, Supp. No. 1, pp. S39-S49, 1997

[102] Lucas J.J., Konieczny P.P., In: Materials Properties Handbook: Titanium Alloys, eds. Boyer R., Welsch G., Collings E.W., p. 553, ASM International, 1994

[103] Lütjering G.: "Influence of processing on microstructure and mechanical properties of (α+β) titanium alloys", Material Science and Engineering A, Vol. A243, pp. 32-45, 1998

[104] Lütjering G., Gysler A.: "Fatigue", In: Titanium '84 - Science and Technology, Vol. 4, eds. Lütjering G., Zwicker U., Bunk W., pp. 2065-2083, DGM, 1985

[105] Lütjering G., Williams J.C.: "Titanium", 2nd Edition, Springer, 2007, ISBN 978-3-540-71397-5

[106] Magna Powertrain: "FemFAT 4.7 Basic User Manual", 2007

[107] Majidi B.: "Fatigue Life and Short Crack Behavior in Ti-6Al-4V Alloy; Interactions of Foreign Object Damage, Stress, and Temperature", Metallurgical and Materials Transactions A, Vol. 39A, pp. 772-777, 2008

[108] Mall S., Hamrick J.L. II, Nicholas T.: "High cycle fatigue behavior of Ti-6Al-4V with simulated foreign object damage", Mechanics of Materials, Vol. 33, pp. 679-692, 2001

[109] McEvily A.J., Minakawa K.: "On crack closure and the notch size effect in fatigue", Engineering Fracture Mechanics, Vol. 28, Issue 5-6, pp. 519-527, 1987

[110] Miner M.A.: "Cumulative damage in fatigue", Journal of Applied Mechanics, Vol. 12, pp. 159-164, 1945

[111] Morrissey R.J., McDowell D.L., Nicholas T.: "Frequency and stress ratio effects in high cycle fatigue of Ti-6Al-4V", International Journal of Fatigue, Vol. 21, pp. 679-685, Elsevier Science Ltd., 1999

[112] Morrissey R.J., McDowell D.L., Nicholas T.: "Microplasticity in HCF of Ti-6Al-4V", International Journal of Fatigue, Vol. 23, pp. S56-S64, Elsevier Science Ltd., 2001

[113] Morrisey R.J., Nicholas T.: "Fatigue strength of Ti-6Al-4V at very long lives", International Journal of Fatigue, Vol. 27, pp. 1608-1612, 2005

[114] Murakami Y.: "Stress Intensity Factors Handbook", Vol.1, Pergamon Press, 1987, ISBN 0-08-034809-2

[115] Murakami Y.: "Stress Intensity Factors Handbook", Vol.2, Pergamon Press, 1987, ISBN 0-08-034809-2

[116] Nakajima K., Terao K., Miyata T.: "The effect of microstructure on fatigue crack propagation of α+β titanium alloys In-situ observation of short fatigue crack growth", Materials Science and Engineering A, Vol. A243, pp. 176-181, 1998

[117] Nalla R.K., Boyce B.L., Campbell J.P., Peters J.O., Ritchie R.O.: "Influence of Microstructure on High-Cycle Fatigue of Ti-6Al-4V: Bimodal vs. Lamellar Structures", Metallurgical and Materials Transactions A, Vol. 33A, pp. 899-918, March 2002

[118] National Aeronautics and Space Administration: "Image of the Day - January 25, 2007", NASA Earth Observatory, http://earthobservatory.nasa.gov/IOTD

[119] National Aeronautics and Space Administration: "Nondestructive Evaluation Requirements for Fracture-Critical Metallic Components", NASA-STD-5009, National Aeronautics and Space Administration (NASA), Washington, DC, 2008

[120] Nazmy M., Staubli M., Onofrio G., Lupinc V.: "Surface defect tolerance of a cast TiAl alloy in fatigue", Scripta Materialia, Vol. 45, pp. 787-792, 2001

[121] Neal D.F., Blenkinsop P.A.: "Internal Fatigue Origins in α-β Titanium Alloys", Acta Metallurgica, Vol. 24, Issue 1, pp. 59-63, 1976

[122] Neuber H.: "Kerbspannungslehre: Grundlagen für genaue Spannungsrechnungen", Springer, Berlin, 1937

[123] Neuber H.: "Über die Berücksichtigung der Spannungskonzentration bei Festigkeitsberechnungen", Konstruktion 20, Heft 7, pp. 245-251, 1968

[124] Oakley S.Y., Nowell D.: "Prediction of the combined high- and low-cycle fatigue performance of gas turbine blades after foreign object damage", Int. Journal of Fatigue, Vol. 29, pp. 69-80, 2007

[125] Oberwinkler C.: "Virtuelle betriebsfeste Auslegung von Aluminium-Druckgussbauteilen", Doctoral Thesis, Montanuniversität Leoben, Austria, 2009

[126] Paris P., Erdogan F.: "A critical analysis of crack propagation laws", Journal of Basic Engineering, Transactions of the American Society of Mechanical Engineers, Vol. 85, pp. 528-534, 1963

[127] Pearson S.: "Initiation of fatigue cracks in commercial aluminium alloys and the subsequent propagation of very short cracks", Engineering Fracture Mechanics, Vol. 7, pp. 235-247, 1975

[128] Petch N.J.: "The cleavage strength of polycrystals", J. Iron Steel Inst., Vol. 174, pp. 25-28, 1953

[129] Peters J.O., Boyce B.L., Chen X., McNaney J.M., Hutchinson J.W., Ritchie R.O.: "On the application of the Kitagawa-Takahashi diagram to foreign-object damage and high-cycle fatigue", Engineering Fracture Mechanics, Vol. 69, pp. 1425-1446, 2002

[130] Peters M.: "Titan im Aufwind", MB-Revue, Jahreshauptausgabe 2009, Olympia-Verlag AG, Zürich, 2009

[131] Peters M., Gysler A., Lütjering G.: "Influence of Microstructure on the Fatigue Behavior of Ti-6Al-4V", In: Titanium '80 – Science and Technology, Vol. 3, eds. Kimura H., Izumi O., pp. 1777-1786, TMS-AIME, Japan, 1980

[132] Peters M., Gysler A., Lütjering G.: "Influence of texture on fatigue properties of Ti-6Al-4V", Metallurgical and Materials Transactions A, Vol. 15A, pp. 1597-1605, 1984

[133] Peters M., Leyens C: "Titan und Titanlegierungen", 1. Auflage, 1. Nachdruck, WILEY-VCH Verlag, Weinheim, 2007, ISBN 978-3-527-30539-1

[134] Peterson R.E.: "Notch sensitivity", In: Metal fatigue, eds. Sines G., Waisman J.L., pp. 293-306, 1959

[135] Postans P.J., Jeal R.H., In: Titanium '72 - Science and Technology, Vol. 1, eds. Jaffee R.I., Burte H.M., p. 192, Plenum Press, New York, 1973

[136] Powell B.E., Duggan T.V.: "Crack growth in Ti-6Al-4V under the conjoint action of high and low cycle fatigue", Int. Journal of Fatigue, Vol. 9, pp. 195-202, 1987

[137] Powell B.E., Hawkyard M., Grabowski L.: "The growth of cracks in Ti-6Al-4V plate under combined high and low cycle fatigue", Int. Journal of Fatigue, Vol.19, Supp. No. 1, pp. S167-S176, 1997

[138] Prevey P.S., Hornbach D., Mason P.: "Thermal Residual Stress Relaxation and Distortion in Surface Enhanced Gas Turbine Engine Components", Proceedings of the 17th Heat Treating Society Conference and Exposition, eds. Milam D.L. et al., pp. 3-12, ASM, 1998

[139] Prevey P.S., Ravindranath R., Cammett J.T.: "Application of low plasticity burnishing to improve damage tolerance of a Ti-6Al-4V first stage fan blade", Proceedings of the 44th AIAA/ASME/ASCE/AHS Structures, Structural Dynamics & Materials Conf., Norfolk, VA, 2003

[140] Radaj D.: "Ermüdungsfestigkeit: Grundlagen für Leichtbau, Maschinen- und Stahlbau", 2nd Edition, Springer, 2003, ISBN 3540440631

[141] Ramberg W., Osgood W.R.: "Description of Stress-Strain Curves by three Parameters", National Advisory Committee for Aeronautics (NACA), Technical Note No. 902, 1943

[142] Redik S.: "Kurzrisswachstum in AlSi9Cu3 und Ti-6Al-4V - Einfluss kurzer Risse auf die Lebensdauer", Diploma Thesis, Montanuniversität Leoben, Austria, 2009

[143] Riedler M.: "Methodikfindung zur Simulation von thermomechanisch beanspruchten Motorbauteilen aus Aluminiumlegierungen", Fortschrittberichte VDI, Reihe 5, Nr. 718, 2005, ISBN 3-18-371805-7

[144] Roder O., Peters J.O., Thompson A.W., Ritchie R.O.: "Influence of simulated foreign object damage on the high cycle fatigue properties of Ti-6Al-4V for gas turbine blades", Proceedings of the Fourth National Turbine Engine High Cycle Fatigue Conference, Monterey, CA, pp. 41-50, Universal Technology Corp., Dayton, OH, 1999

[145] Rösler J., Harders H., Bäker M.: "Mechanical behaviour of engineering materials: metals, ceramics, polymers, and composites", Springer, 2007, ISBN 978-3-540-73446-8

[146] Rüdinger K., Fischer D.: "Relationship Between Primary Alpha Content, Tensile Properties and High Cycle Fatigue Behaviour of Ti-6Al-4V", In: Titanium '84 - Science and Technology, Vol. 4, eds. Lütjering G., Zwicker U., Bunk W., pp. 2123-2130, DGM, 1985

[147] Ruiz C., Boddington P.H.B., Chen K.C.: "An investigation of fatigue and fretting in a dovetail joint", Experimental Mechanics, Vol. 24, pp. 208-217, 1984

[148] Ruiz C., Chen K.C.: "Life assessment of dovetail joints between blades and disks in aero-engines", Proceedings of International Conference on Fatigue and Structures, London, 1986

[149] Ruiz C., Wang Z.P., Webb P.H.: "Techniques for the characterisation of fretting fatigue damage", In: Standardisation of Fretting Fatigue Test Methods and Equipment, ASTM STP 1159, eds. Attia H.A., Waterhouse R.B., pp. 170-177, 1992

[150] Ruschau J.J., Nicholas T., Thompson S.R.: "Influence of foreign object damage (FOD) on the fatigue life of simulated Ti-6Al-4V airfoils", Int. Journal of Impact Engineering, Vol. 25, pp. 233-250, 2001

[151] Sarrazin-Baudoux C., Lesterlin S., Petit J.: "Atmospheric Influence on Fatigue Crack Propagation in Titanium Alloys at Elevated Temperature", In: Elevated Temperature Effects on Fatigue and Fracture, ASTM STP 1297, eds. Piascik R.S., Gangloff R.P., Saxena A., pp. 117-139, 1997

[152] Schauerte O.: "Titanium in Automotive Production", Advanced Engineering Materials, Vol. 5, Issue 6, pp. 411-418, 2003

[153] Schijve J.: "Fatigue of Structures and Materials", Kluwer Academic Publishers, 2001, ISBN 0-7923-7014-7

[154] Schütz W.: "Über eine Beziehung zwischen der Lebensdauer bei konstanter und bei veränderlicher Beanspruchungsamplitude und ihre Anwendbarkeit auf die Bemessung von Flugzeugbauteilen", Z. für Flugwissenschaften, Vol. 15, H. 11, pp. 407-419, 1967

[155] Schütz W.: "Werkstoffoptimierung für schwingbeanspruchte Bauteile", Materialwissenschaft und Werkstofftechnik, Vol. 2, Issue 4, pp. 189-197, 1971

[156] Shyam A., Allison J.E., Szczepanski C.J., Pollock T.M., Jones J.W.: "Small fatigue crack growth in metallic materials: A model and its application to engineering alloys", Acta Materialia, Vol. 55, pp. 6606-6616, 2007

[157] Sines G., Ohgi G.: "Fatigue Criteria under Combined Stresses or Strains", Journal of Engineering Materials and Technology, Vol. 103, Issue 2, pp. 82-90, 1981

[158] Sinha V., Mercer C., Soboyejo W.O.: "An investigation of short and long fatigue crack growth behaviour of Ti-6Al-4V", Materials Science and Engineering A, Vol. A287, pp. 30-42, 2000

[159] Socie D.: "Critical Plane Approaches for Multiaxial Fatigue Damage Assessment", Advances in Multiaxial Fatigue, ASTM STP 1191, eds. McDowell D.L., Ellis R., pp. 7-36, ASTM, 1993

[160] Sparks R.B., Long J.R., AFML-TR-73-301, 1974, In: Materials Properties Handbook: Titanium Alloys, eds. Boyer R., Welsch G., Collings E.W., p. 538, ASM International, 1994

[161] Stanzl-Tschegg S.: "Fatigue crack growth and thresholds at ultrasonic frequencies", International Journal of Fatigue, Vol. 28, pp. 1456-1464, 2006

[162] Steele R.K., McEvily A.J.: "The High-Cycle Fatigue Behavior of Ti-6Al-4V Alloy", Engineering Fracture Mechanics, Vol. 8, Issue 1, pp. 31-37, 1976

[163] Stockinger M.: "Mikrostrukturelle Simulation des Gesenkschmiedens von Nickelbasis-Legierungen", Doctoral Thesis, University of Technology Graz, Austria, 2003

[164] Stroh A.N.: "A Theory of the Fracture of Metals", Advances in Physics, Vol. 6, Issue 24, pp. 418-465, 1957

[165] Suresh S., Ritchie R.O.: “Propagation of short fatigue cracks”, Int. Met. Rev., Vol. 29, pp. 445-476, 1984

[166] Takafuji S., Kato Y., Tokaji K.: "Fatigue Properties of Shot-Peened Notched Components in Ti-6Al-4V Alloy at Elevated Temperatures", J. Soc. Mat. Sci. Japan, Vol. 49, No. 1, pp. 61-65, 2000

[167] Tanaka K.: "A correlation of ΔK_{th}-value with the exponent, m, in the equation of fatigue crack growth for various steels", International Journal of Fracture, Vol. 15, Nr. 1, pp. 57-68, 1979

[168] Taylor D., Wang G.: "The critical volume method in fatigue analysis", In: Notch effects in fatigue and fracture, eds. Pluvinage G., Gjonaj M., NATO science series II, Vol. 11, pp. 1-22, 2000

[169] Tokaji K.: "High cycle fatigue behaviour of Ti-6Al-4V alloy at elevated temperatures", Scripta Materialia, Vol. 54, pp. 2143-2148, 2006

[170] Tokaji K., Ogawa T., Harada Y., Ando Z.: "Limitations of Linear Elastic Fracture Mechanics in Respect of Small Fatigue Cracks and Microstructure", Fatigue Fract. Eng. Mater. Struct., Vol. 9, No. 1, pp. 1-14, 1986

[171] U.S. Army: "Military Specification - Shot Peening of Metal Parts", MIL-S-13165C, 1998

[172] U.S. Army: "Military Specifications - Peening of Metals", MIL-P-81985, 1974

[173] Vaughan R.E., Chang J.H.: "Life Predictions for High Cycle Dynamic Components Using Damage Tolerance and Small Threshold Cracks", Presented at the Am. Helicopter Soc. 59th Annual Forum, Phoenix, AZ, 2003

[174] Verreman Y., Limodin N.: "Fatigue notch factor and short crack propagation", Engineering Fracture Mechanics, Vol. 75, pp. 1320-1335, 2008

[175] Wagner L., Bigoney J.K.: "Fatigue of Titanium Alloys", In: Titanium and Titanium Alloys, WILEY-VCH Verlag, eds. Leyens C., Peters M., pp. 153-185, 2003, ISBN 3-527-30534-3

[176] Wagner L., Gerdes C., Lütjering G.: “Influence of surface treatment on fatigue strength of Ti-6Al-4V”, 5th International Conference on Ti, Munich, Germany, 1984, In: Titanium '84 - Science and Technology, Vol. 4, eds. Lütjering G., Zwicker U., Bunk W., pp. 2147-2154, DGM, 1985

[177] Wagner L., Gregory J.K.: "Ermüdung von Titanlegierungen", In: Titan und Titanlegierungen, WILEY-VCH Verlag, eds. Peters M., Leyens C., pp. 163-196, 2007, ISBN 978-3-527-30539-1

[178] Wagner L., Gregory J.K., Gysler A., Lütjering G., In: Small Fatigue Cracks - Proceedings of the 2nd Engineering Foundation Int. Fatigue Conference/Workshop, eds. Ritchie R.O., Lankford J., p. 117, TMS-AIME, Warrendale, PA, 1986

[179] Wagner L., Lütjering G.: "Influence of the Shot Peening Parameters on the Surface Layer Properties and the Fatigue Life of Ti-6Al-4V", Shot Peening, American Shot Peening Society, pp. 194-200, 1984

[180] Wagner L., Lütjering G.: "Influence of Shot Peening Treatment on the Fatigue Limit of Ti-6Al-4V", Shot Peening, American Shot Peening Society, pp. 201-207, 1984

[181] Wagner L., Lütjering G.: "Propagation of small fatigue cracks in Ti alloys", In: Titanium '88 - Science and Technology, Vol. 1, eds. Lacombe P., Tricot R., Béranger G., pp. 345-350, Les Ulis Cedex, France, 1988

[182] Weixing Y., Kaiquan X., Yi G.: "On the fatigue notch factor, K_f", International Journal of Fatigue, Vol. 17, pp. 245-251, 1995

[183] Williams J.C., Lütjering G.: "Effect of slip length and slip character on titanium alloys", In: Titanium '80 – science and technology, Vol. 3, eds. Kimura H., Izumi O., pp. 671-681, TMS-AIME, Japan, 1980

[184] Wohlfahrt H.: "Kugelstrahlen und Dauerschwingverhalten", ICSP-1, Paris, 1981, International Scientific Committee for Shot Peening, Warrendale, PA, www.shotpeening.org/ICSP

[185] Zuo J.H., Wang Z.G., Han E.H.: "Effect of microstructure on ultra-high cycle fatigue behavior of Ti-6Al-4V", Material Science and Engineering A, Vol. 473, pp. 147-152, 2008

11. Acronyms, abbreviations and symbols

11.1. Acronyms and abbreviations

AB.....Abstract
AC.....Air-cooling
b .....Bottom
c.....Center
BA.....Beta-annealed
bcc.....Body-centered cubic
BSTG ...Böhler Schmiedetechnik GmbH & Co KG (Bohler Forging)
CP.....Commercially pure
DT .....Damage tolerance
DTD .....Damage tolerant design
EBSD ...Electron backscatter diffraction
FB.....Feedstock billet
FPB .....Four point bending
FC.....Furnace cooling
FCP .....Fatigue crack propagation
fcc.....Face-centered cubic
FE.....Finite element
FOD .....Foreign-object damage
h .....Hour
HCF.....High cycle fatigue
hcp.....Hexagonal close-packed
hkl .....Miller indices
l .....Left
LEFM...Linear elastic fracture mechanics
LC .....Long crack
LCF .....Low cycle fatigue
LOM.....Light optical microscopy
MA .....Mill-annealed
MAX ....Multiaxial
min .....Minute
OT .....Operating temperature
PA .....Paper / written contribution
PO .....Poster
PQ .....Polymer-quenched
PR.....Presentation
r .....Right
RA.....Recrystallisation-annealed
RB .....Rotating bending
RS.....Residual stress
RT .....Room temperature
SC.....Short crack
SCG.....Short crack growth
SEB .....Single edge bending
SEM .....Scanning electron microscope
SIF.....Stress intensity factor
ST.....Solution treated
STA.....Solution treated aged
STOA ...Solution treated over-aged
STPQ....Solution treated polymer-quenched
STWQ ..Solution treated water-quenched
t .....Top
T .....Torsion
TC .....Tension/compression
UHCF...Ultra-high cycle fatigue
Vac .....Vacuum
XRD .....X-ray diffraction

11.2. Symbols

11.2.1. Latin symbols

a .....Crack length
a_0 .....Initial crack length
a_{th} .....Crack length at the transition point of the Kitagawa-curve
A .....Elongation at rupture
A_g.....Uniform strain
A_{gt}.....Total strain at maximum load
A_t .....Total strain at rupture
b .....Fatigue strength exponent
c.....Fatigue ductility exponent
c_{equ}.....Equivalent stress material constant
$c_{S,f}$.....Surface state coefficient for the fatigue limit
$c_{S,FL}$.....Surface state coefficient for the finite life fatigue strength at 10^5 cycles to failure
$c_{S,k}$.....Surface state coefficient for the finite life slope
$c_{T,f}$.....Temperature coefficient for the fatigue limit
$c_{T,FL}$.....Temperature coefficient for the finite life fatigue strength at 10^5 cycles to failure
$c_{T,k}$ .....Temperature coefficient for the finite life slope
C.....Paris-coefficient
$C_{\alpha+\beta}$.....(α+β)-Content
Col.....Colony length
Con.....Connectivity
CR .....Cooling rate
d .....Diameter of something, or microstructural barrier length
d_o .....Micro crack limiting obstruction distance
D.....Grain size, or damage
E .....Young's modulus
f_i.....Modeled values
f_m .....Mean value of the modeled values
I.....Invariant
k.....Slope of S/N-curve in finite life region, or material constant for Chapetti-curve
k_{Ti64}.....Material constant for Chapetti-curve adapted for Ti-6Al-4V
K' .....Cyclic strain hardening coefficient
K_α.....Type of X-ray radiation
K_f.....Fatigue notch factor
K_t.....Theoretical stress concentration factor
ΔK .....Stress intensity factor range
ΔK_C.....Extrinsic component of the crack propagation threshold
ΔK_{CR}.....Extrinsic component of the crack propagation threshold for long cracks
ΔK_{dR} .....Intrinsic component of the crack propagation threshold (microstructural threshold)
ΔK_{th} .....Stress intensity factor threshold range (for long cracks)
m.....Paris-exponent or Schmid factor
M_b.....Bending moment
M_t .....Torsional moment
$\underline{n}$ .....Normal vector or supporting factor
n'.....Cyclic strain hardening exponent
n_i.....Load cycles of one step of a load spectrum
N.....Cycles to failure
N_f.....Cycles to failure
$N_{f/2}$.....Half cycles to failure
N_g .....Crack growth cycles
N_i.....Crack initiation cycles, or cycles to failure for Palmgren-Miner rule
N_T .....Cycles at transition
p .....Parameter resulting from fitting
P_S.....Survival probability
q .....Parameter resulting from fitting
R.....Stress ratio
R^2.....Coefficient of determination

R_a.....Center-line average roughness
R_ε.....Strain ratio
R_m.....Ultimate tensile strength
R_f.....Flow stress
$R_{p0.2}$.....0.2%-Yield strength
$R_{p,c}$.....Compressive yield strength
$R_{p,t}$.....Tensile yield strength
R_z.....Average maximum roughness height
T.....Periodic time
T_F.....Forging temperature
T_{HT}.....Heat treatment temperature
T_N.....Scatter in finite life region
T_S.....Scatter in HCF region
w_{lam}.....α-Lamellae width
Y.....Geometry factor
y_i.....Data set values
y_m.....Data set mean value
z.....Exponent of the modified Gough Pollard equation

11.2.2. Greek symbols

α.....Alpha-phase
α_{IC}.....Interconnected α-grain size
α_p.....Primary α-grain size
β.....Beta-phase
χ^*.....Relative stress gradient
δ.....Slip
ε.....Strain
$\varepsilon_{a,e}$.....Elastic strain amplitude
$\varepsilon_{a,p}$.....Plastic strain amplitude
$\varepsilon_{a,t}$.....Total strain amplitude
ε_f'.....Fatigue ductility coefficient
ε_F.....Elongation at fracture
$\varepsilon_{m,e}$.....Elastic mean strain
$\varepsilon_{m,p}$.....Plastic mean strain
$\varepsilon_{m,t}$.....Total mean strain
φ.....Angle for definition of a normal vector
θ.....Angle of deflection or angle for definition of a normal vector
σ.....Stress
$\underline{\underline{\sigma}}$.....Stress tensor
$\Delta\sigma$.....Stress range
$\Delta\sigma_{fR}$.....Stress ratio dependent plain fatigue limit
$\sigma_{0.2}$.....0.2%-Yield strength
σ_a.....Stress amplitude
$\underline{\sigma_c}$.....Stress vector of a cutting plane
σ_f.....Fatigue strength at 10^8 load cycles (fatigue limit)
$\sigma_{f,n}$.....Fatigue limit of notched specimens
σ_f'.....Fatigue strength coefficient
σ_m.....Mean stress
σ_{max}.....Maximum stress
σ_{min}.....Minimum stress
σ_n.....Normal stress
σ_{nom}.....Nominal stress
σ_t.....Tangential stress
τ.....Shear stress
τ_a.....Shear stress amplitude
τ_f.....Fatigue strength at 10^8 load cycles (fatigue limit)
τ_t.....Shear stress resulting from torsion

12. Appendix

12.1. Residual stress distribution in forgings

The residual stresses in as-forged surface layers were measured using X-ray diffraction (XRD) in combination with the $sin^2\psi$ method, Fig. 12.1 (l). It was observed that both, the peak residual stress (-575 MPa, directly at the surface) and the residual stress distributions are independent from the analyzed heat treatments (mill-annealing or solution treating). The comparison of two different types of forgings (V-shapes and pancakes) reveals that the residual stresses are almost independent from the type and shape of the forging; only the residual stress gradient exhibits slight differences.

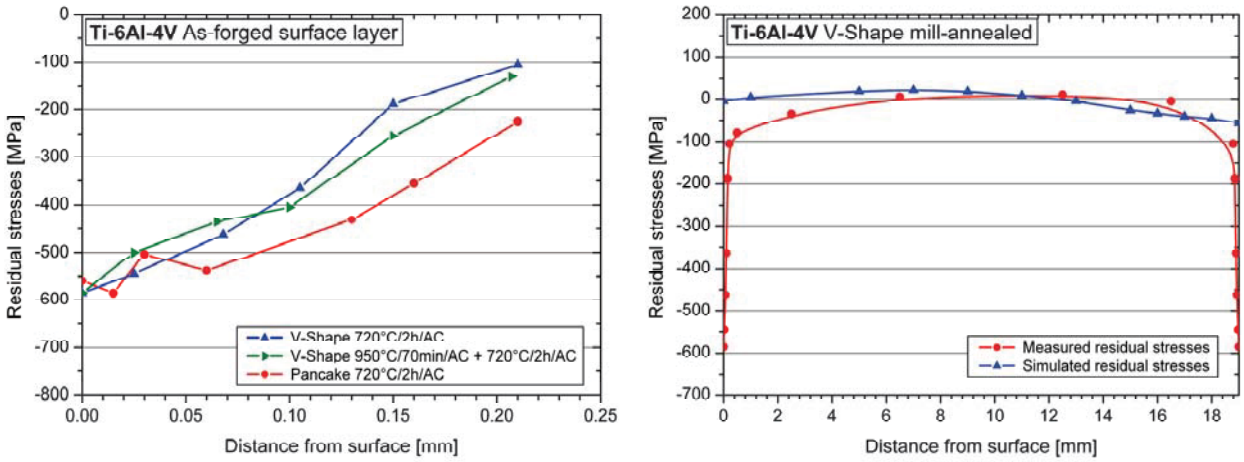

Fig. 12.1: Measured residual stress distributions in as-forged surface layers (l) and residual stress distributions in a mill-annealed V-shape in through-thickness direction (r)

The comparison of simulated (in Deform™) and measured (XRD) residual stress distributions of a mill-annealed V-shape in through-thickness direction is presented in Fig. 12.1 (r). It has to be mentioned that the residual stresses in the surface layer were just measured for one side of the V-shape and (owing to the findings discussed before) assumed to be comparable to those of the other side. It was observed that the FE-simulation is not able to reflect the considerable compressive residual stresses in the surface layer. It can be assumed that this behavior is caused by too large element sizes near the surface. The residual stresses inside of the forging can be estimated by forging simulation. Improvements in the residual stress modeling (phase transformation, precipitations, surface layer) are currently investigated at Böhler Schmiedetechnik.

12.2. Quasi-static loading

Tensile tests according to DIN EN ISO 6892-1 [59] were performed on specimens (cf. Fig. 3.29) sampled from mill-annealed V-shape. The tensile-test results of two specimens of V-shape mill-annealed can be found in Tab. 12.1. The corresponding stress-strain diagram is shown in Fig. 12.2.

	E [MPa]	$R_{p0.2}$ [%]	R_m [%]	A_g [%]	A_{gt} [%]	A [%]	A_t [%]
Nr. V2-4	124,000	925	977	8.0	8.8	19.9	20.5
Nr. V2-2	122,000	926	978	8.9	9.7	19.5	20.1
Mean value	123,000	925	978	8.4	9.2	19.7	20.3

Tab. 12.1: Tensile test results for V-shape mill-annealed

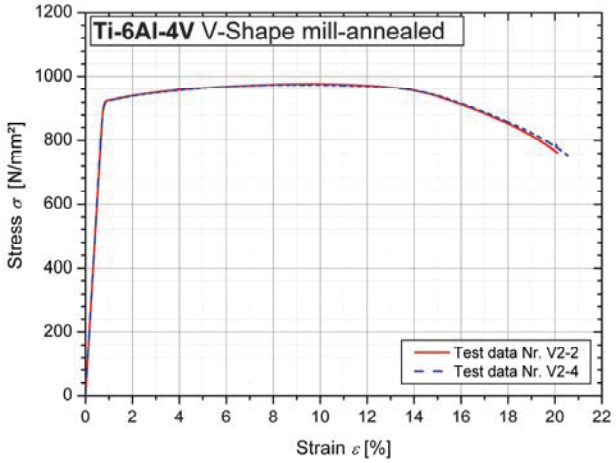

Fig. 12.2: Stress-strain-curves for V-shape mill-annealed

The mill-annealed V-shape exhibits a kind of ideal-elastic ideal-plastic stress-strain behavior. Such a behavior was also found in former research work [1] for lamellar and fine equiaxed Ti-6Al-4V, respectively.

12.3. Fitting parameters of crack growth curves

The parameters resulting from the fitting of the long crack propagation curves with Equ. (4.8) are summarized in Tab. 12.2.

Material	R	p_1	p_2	q_1	q_2
V-Shape MA	-1	-22.70	21.17	0.80	-1.64
	0	-16.83	10.81	0.55	-0.78
	0.3	-16.05	9.42	0.52	-0.65
	0.7	-20.08	7.51	1.30	-0.63
V-Shape ST	-1	-19.96	19.27	0.24	-1.17
	0	-15.94	11.99	0.20	-0.72
	0.3	-18.04	10.99	0.70	-0.80
	0.7	-21.24	9.28	1.39	-0.81
V-Shape STPQ	-1	-19.82	19.25	0.19	-1.14
	0	-18.29	12.30	0.61	-0.87
	0.3	-20.22	11.46	1.07	-0.93
	0.7	-21.89	7.94	1.54	-0.69
Pancake MA	-1	-19.51	18.05	0.31	-1.15
	0	-18.28	11.63	0.74	-0.88
	0.3	-17.36	9.88	0.73	-0.74
	0.7	-18.51	7.03	1.12	-0.57
Pancake ST	-1	-16.94	16.75	-0.18	-0.80
	0	-16.32	11.58	0.36	-0.76
	0.3	-16.96	10.20	0.63	-0.75
	0.7	-19.87	7.61	1.25	-0.63
Pancake RA	-1	-16.21	16.24	-0.31	-0.69
	0	-15.23	11.29	0.11	-0.63
	0.3	-14.57	9.30	0.19	-0.53
	0.7	-19.06	8.15	1.04	-0.63
Pancake BA	-1	-14.70	15.92	-0.62	-0.50
	0	-15.78	12.34	0.19	-0.77
	0.3	-16.67	10.89	0.48	-0.76
	0.7	-16.15	7.14	0.68	-0.50
Feedstock billet	-1	-16.89	18.78	-0.35	-0.85
	0	-14.00	11.50	-0.15	-0.55
	0.3	-12.98	8.89	-0.07	-0.42
	0.7	-17.23	8.10	0.73	-0.57

Tab. 12.2: Fitting parameters of long crack propagation curves

12.4. Matlab-code for S/N/a-surface

```
% © Oberwinkler Bernd
% Montanuniversität Leoben, Austria
% January 2010

% Calculation of a S/N/a-Surface
% for Ti-6Al-4V (example-values for V-shape MA) with Matlab

clear all;
close all;
clc;

DKthSEB = 5.31; %SEB Long Crack Growth Threshold [MPam^0.5]

DSf = 391.2; %Fatigue Limit [MPa] res. from Microstr. & Mean Stress Model

k = 6.2; %According S/N-curve slope

Neck = 69132000; %According cycles at transition

F = 1.12; %Geometry factor for the initial crack [-]

d = 11.2E-6; %Microstructural barrier length [m]

% Meshgrid: (log.) Crack length [m] and (log.) load cycles [-]
[X,Y] = meshgrid(log(1E-6):0.008:log(1E-2), log(1E4):0.008:log(1E9));

m=size(Y);

for i=1:1:m(1,1)
    for j=1:1:m(1,2)

        a0 = exp(X(i,j)); %Crack length

        N = exp(Y(i,j)); %Cycles to failure

        DKdR = F*DSf*(pi*d)^0.5; %Intrinsic threshold

        kc = (1/(20*d))*(DKdR/(DKthSEB-DKdR)); %Material param.

        %Kth = DKdR; %Threshold for microstructurally short cracks

        Kth = DKdR + (DKthSEB - DKdR)*(1-exp(-kc*(a0-d)));
        %General threshold depending on the crack length

        Kfl = 28 * DKthSEB * N^(-0.274); %Finite life threshold

        Sf = DSf; %Fatigue limit

        Sfl = Sf * (N/Neck)^(-1/k); %Finite life fatigue strength

        SfBM = Kth /(F*((pi*a0)^0.5)); %Fracture mech. fatigue limit

        SflBM = Kfl /(F*((pi*a0)^0.5)); %Fract. mech. finite life strength

        if Sf > Sfl %if yes, than infinite life region

            SFat(i,j) = Sf;
```

```
        else %else, finite life region
            SFat(i,j) = Sfl;
        end
        if SfBM > SflBM %if yes, than fract. mech. infinite life region
            SB(i,j) = SfBM;
        else %else, fracture mech. finite life region
            SB(i,j) = SflBM;
        end
        if SFat(i,j) < SB(i,j) %if yes, classical S/N-approach valid
            S(i,j) = SFat(i,j);
        else %else, fracture mechanical region
            S(i,j) = SB(i,j);
        end
    end
end
```

12.5. Linking thermomechanical processing and microstructure

The simulation of the local microstructure in forgings is performed with user-routines in Deform™, cf. [163]. Such a user-routine is currently implemented for Ti-6Al-4V. An interim model was hence developed linking forging temperature, heat treatment temperature and local cooling rate with the necessary microstructural parameters for the fatigue models. This model is based on the microstructural evaluation of several heat treated V-shapes.

The (α+β)-content $C_{\alpha+\beta}$ [%] was linked with the forging temperature T_F [°C], the heat treatment temperature T_{HT} [°C], and the cooling rate CR [°C/min]. A separate link was used for solution treating (T_{HT} / cooling with CR), Equ. (12.1), and mill-annealing (720°C / 2h / AC), Equ. (12.2).

$$ST: \quad C_{\alpha+\beta} = 0.7\,T_F + T_{HT} + 0.5\sqrt{CR} - 1560 \qquad \text{Equ. (12.1)}$$

$$MA: \quad C_{\alpha+\beta} = 0.7\,T_F - 613 \qquad \text{Equ. (12.2)}$$

The primary α-grain size α_p [µm] was linked with the forging temperature T_F [°C] and the heat treatment temperature T_{HT} [°C], Equ. (12.3).

$$\alpha_p = \frac{T_F + 0.5\,T_{HT}}{170} \qquad \text{Equ. (12.3)}$$

The colony-length Col [µm] was related to the (α+β)-content $C_{\alpha+\beta}$ [%], heat treatment temperature T_{HT} [°C], and cooling rate CR [°C/min], cf. Equ. (12.4).

$$Col = \frac{500\,C_{\alpha+\beta} + T_{HT} + CR}{2000} \qquad \text{Equ. (12.4)}$$

13. Curriculum vitae

Dipl.-Ing. Bernd Oberwinkler, born in 1984 in Austria, studied Mechanical Engineering at the Montanuniversität Leoben (Austria) and graduated in 2007 with honors. From 2007 until 2010 he was scientific assistant and PhD student at the Chair of Mechanical Engineering at the Montanuniversität Leoben. In 2008, he received the Johann-Puch-Award for Excellence in Automotive Engineering and the Honor Award of the Austrian Motor Vehicle Association in recognition of his diploma thesis. In addition, he was awarded the Appreciation Prize of the Austrian Federal Minister for Science and Research.